RELIABLE HIGH-SPEED SHORT-RANGE UNDERWATER WIRELESS OPTICAL COMMUNICATION SYSTEMS

RELIABLE HIGH-SPEED SHORT-RANGE UNDERWATER WIRELESS OPTICAL COMMUNICATION SYSTEMS

BY

ABDALLAH GHAZY, B.Eng., M.Sc.

A THESIS
SUBMITTED TO THE DEPARTMENT OF ELECTRICAL & COMPUTER ENGINEERING
AND THE SCHOOL OF GRADUATE STUDIES
OF MCMASTER UNIVERSITY
IN PARTIAL FULFILMENT OF THE REQUIREMENTS
FOR THE DEGREE OF
DOCTOR OF PHILOSOPHY

Doctor of Philosophy (2021) McMaster University
(electrical & computer engineering) Hamilton, Ontario, Canada

TITLE:	Reliable High-Speed Short-Range Underwater Wireless Optical Communication Systems
AUTHOR:	Abdallah Ghazy B.Eng., M.Sc. (Electrical and Computer Engineering) Al-Azhar University, Egypt-Japan University of Science and Technology (EJUST), Cairo, Alexandria, Egypt
SUPERVISOR:	Dr. Steve Hranilovic
NUMBER OF PAGES:	xxiii, 235

Lay Abstract

Compared to acoustic and radio frequency systems, underwater wireless optical communication (UWOC) systems utilize the broad bandwidth available to realize high-speed links. Moreover, UWOC systems can be implemented with a small size and work with low transmitted power. However, UWOC links require alignment between the ends of the communication link, which is challenging due to seawater currents and waves and system mobility. In addition, the speed and range of UWOC links are restricted in practice due to the narrow bandwidth of opto-electronic components, eye safety, and seawater scattering.

To realize reliable high-speed links, in the first part of this thesis, we propose an angular imaging multiple-input multiple-output (A-MIMO) system by which the alignment restriction is relaxed, and the link speed is raised in some scenarios. In contrast to classic imaging MIMO systems, A-MIMO systems are robust against the displacement and link length variations, thanks to sending beams in angle rather than in space. A-MIMO systems are good candidates for mobile-to-fixed communications where the relative displacement dominates the misalignment conditions.

For further enhancement in link reliability and speed, in the second part of this thesis, tracking A-MIMO (TA-MIMO) systems are proposed. TA-MIMO systems inherit tracking features from their optical architecture and infer the relative position and orientation between the ends of links. TA-MIMO systems are promising candidates in buoyed-to-fixed communications where the relative tilt dominates the displacement conditions. In addition to communication applications, TA-MIMO systems offer localization features that are challenging to be realized underwater.

The third part of this thesis proposes a novel sea ice diffusing optical communication (SDOC) system for reliable broadband-broadcast communications under sea ice, e.g., in Arctic and Antarctic zones. SDOC approaches utilize the sea ice sheet that exists above seawaters to diffuse the optical beam omni-directionally from the transmitter to receivers. SDOC systems are promising solutions for real-time signaling exchange between mobile sensors that navigate underneath sea ice sheets.

Abstract

In recent years, the high demand for high-speed communications at short-range applications motivates underwater wireless optical communication (UWOC) systems to be an alternative technology rather than acoustic and radio frequency (RF) technologies. However, UWOC systems require alignment, which is challenging underwater due to currents and waves of seawaters in addition to the system mobility. The speed of UWOC links is restricted in practice due to the narrow bandwidth of opto-electronic components and scattering in seawaters. In addition, the transmitted optical power is restricted by noise and limited transmitted power due to eye-safety standards. In order to tackle these challenges and provide reliable high-speed links, this thesis proposes three new UWOC approaches which are appropriate for point-to-point and broadcast communications.

We propose angular multiple-input multiple-output (A-MIMO) and tracking A-MIMO (TA-MIMO) communication systems for point-to-point links. In the first part of this thesis, A-MIMO systems are proposed and modeled rather than conventional MIMO (C-MIMO) systems. Unlike C-MIMO systems, A-MIMO systems send information in angle rather than in space, thus relaxing the strict requirements of on-axis alignment and fixed channel length are relaxed. The main features of A-MIMO systems are highlighted, and maximum link lengths and angle-of-arrival (AoA) distributions are derived. C-MIMO and A-MIMO systems are simulated using a Monte Carlo numerical ray tracing (MCNRT) method. Numerical results indicate that A-MIMO systems are more robust than C-MIMO systems. As well, A-MIMO systems can be implemented with smaller sizes.

In the second part of this thesis, motivated by the performance of A-MIMO systems, we introduce TA-MIMO systems. TA-MIMO systems inherit tracking advantages from their optical structures by which they infer the relative displacement and tilt between ends of the link. Compared to A-MIMO systems, TA-MIMO systems further enhance the link against tilt misalignment, and they perform localization functions besides communication. The architecture of TA-MIMO systems is described by highlighting their inherent tracking advantages. Comprehensive analytic models for TA-MIMO and A-MIMO links are derived by considering link misalignment, channel impairments, and receiver noise. Closed-form expressions for AoA distributions are derived and verified using a MCNRT method. Utilizing the architecture of TA-MIMO systems, a pointing, localization, and tracking (PLT) scheme is proposed and modeled. Numerical results indicate that TA-MIMO systems outperform A-MIMO and C-MIMO systems when the misalignment is presented by both displacement and tilt.

The third part of this thesis proposes a novel sea ice diffusing optical communication (SDOC) system for reliable broad-band broadcast communications under sea ice, such as in the Arctic and Antarctic zones. SDOC systems utilize the sea ice sheets floating on the sea surface to diffuse optical beams with wide spots and omnidirectional patterns from the transmitter to receivers. SDOC channels are modeled as seawater-sea ice cascaded layers (SSCL) in which the vertical channel is divided into multiple layers based on their optical characteristics. An efficient methodology is proposed to compute channel impulse responses (CIRs), ensuring accuracy and reducing computing time. In order to overcome the limitations of channel and receiver noise, we propose a system architecture that enhances system speeds and ranges. Numerical results reveal that, under a snow-covered sea ice sheet with a thickness of 36 cm, the proposed system can achieve a communication speed of 100 Mbps with ranges up to 3.5 meters with BER less than 10^{-3} and average transmitted power of 100 mW. This work serves as a design guide to broadband-broadcast communications under the frozen oceans. For example, a group of mobile sensors navigating below sea ice sheets in Arctic regions could use SDCOC systems for real-time signaling exchange.

To GOD

For creating and enriching me with his graces.

To my parents

For teaching me be a self-reliance and patient.

To my brothers and sisters

For supporting me since I was born to be graduated and got the B.Eng.

To my kids and wife

For loving and playing with me.

Acknowledgment

Firstly, I would like to thank GOD for his infinite graces.

A special thank to my parents, sisters and brothers who have provided me with unconditional love, encouragement, support, and direction over the years. Without them in contact with me, I would not have reached this far in my academic achievement.

To Hana Ghazy, Ali Ghazy, and Heba Rashad, no words could express how blessed I am to have you in my life, funny kids, and a great wife. Without them being with me in Canada, I would not have the fun and the love.

Then, I would like to thank my supervisor, Prof. Steve Hranilovic, for his help and support during my Ph.D. journey. His uncompromising commitment to the originality and quality of our research output has continuously pushed me out of my comfort zone to become the best researcher that I can be.

I am grateful to Dr. Hiatham Khalaf, our research collaborator in the FOCAL lab, ECE school, McMaster University, Canada, and Prof. Ali Khalighi, our research collaborator from Aix-Marseille University, France, for their valuable insights that helped enrich the work presented in this thesis.

I am thankful to my supervisory committee members, Prof. Jian Kang Zhang, Prof. Shiva Kumar, and Dr. Ratnasingham Tharmarasa, for their insightful discussions during my supervisory meetings.

I would like to thank my current and former colleagues at the FOCAL lab, with special thanks to Dr. Khaqan Majeed, and Eng. Tau Rasethuntsa for their contributions to the research.

Thank you to all the excellent staff at McMaster University. Special thanks to Cheryl Gies, the Graduate Administrative Assistant of the Department of Electrical & Computer Engineering.

I want to take this opportunity to thank Hamilton Downtown Mosque (HDM), where I used to relax and get peace of mind while I was navigating the rough seas of my Ph.D. journey.

Finally, thank all who supported and assisted me until I got the Ph.D. degree.

Contents

List of Figures

List of Tables

Abbreviations

AoA	Angle-of-arrival
AoD	Angle of the diffusing
A-MIMO	Angular imaging multiple-input–multiple-output
AUVs	Autonomous underwater vehicles
AUV-Tx	Autonomous underwater vehicles transmitter
AUV-Rx	Autonomous underwater vehicles receiver
AWGN	Additive white Gaussian noise
BER	Bit-error rate
B2F	Buoyed-to-fixed
CIR	Channel impulse response
CLT	Central limit theorem
CM	Cubic metric
C-MIMO	Conventional imaging multiple-input–multiple-output

DFE	Decision feedback equalizer
FB	Feedback
FF	Feedforward
FFT	Fast Fourier transform
FOV	Field-of-view
F-Q	Four-quad
Gb/s	Gigabits per second
IFFT	Inverse fast Fourier transform
IM/DD	Intensity modulation/direct detection
ISI	Inter-symbol interference
kbps	Kilo bite per seconds
LDs	Laser diodes
LED	Light-emitting diode
LMS	Least mean square
LOS	Line-of-sight
MCNRT	Monte Carlo numerical ray tracing
M2F	Mobile-to-fixed
MIMO	Multiple-input/multiple-output

MPE	Maximum permissible exposure
NLOS	Non-line-of-sight
NRDS	Normalized optical power penalty
OFDM	Orthogonal frequency-division multiplexing
OOK	On-off keying
OTHG	One term Henyey-Greensteen
PD	Photodetector
PDF	Probability distribution function
PDs	Photo-detectors
PIN-PD	PIN Photodetector
PLT	Pointing–localization-tracking
PoA	Position-of-arrival
PoD	Position of the diffusing
RF	Radio frequency
RMS	Root mean square
SDOC	Sea ice diffusing optical communication
SINR	Signal to interference pulse noise ratio
SNR	Signal-to-noise ratio

SSCL	Seawater-sea ice cascaded layers
TA-MIMO	Tracked angular imaging multiple-input–multiple-output
ToD	Time of the diffusing
TRE	Tracking residual error
UWOCs	Underwater wireless optical communications
WOC	Wireless optical communication

Chapter 1

Introduction

Seawater and sea ice cover nearly 79% of the Earth's surface. However, as much as 95% of the underwater environment is not yet discovered, according to the latest survey published by the National Oceanic and Atmospheric Administration (NOAA) [1, 2]. Since the last decade, underwater wireless sensor network (UWSN) technology has been developed to discover underwater environments and explore natural resources on the seabed [3]. Recent applications for UWSNs include and are not limited to; surveillance for coastal security, investigation for natural resources, mapping and discovery unknown regions, data collection and analysis, ecosystem navigation, and early detection warning [4].

Such UWSN contains several components, such as sensors and relays, and they cooperate to achieve the required tasks. For efficient cooperation, the components of the network must be connected via wireless communication systems[1] that can overcome the challenges of underwater channels. Firstly, communication systems should

---

[1] In contrast to wire communication systems, wireless systems offer ease of installation, maintenance, mobility, multi-cast and broadcast accesses, and low cast.

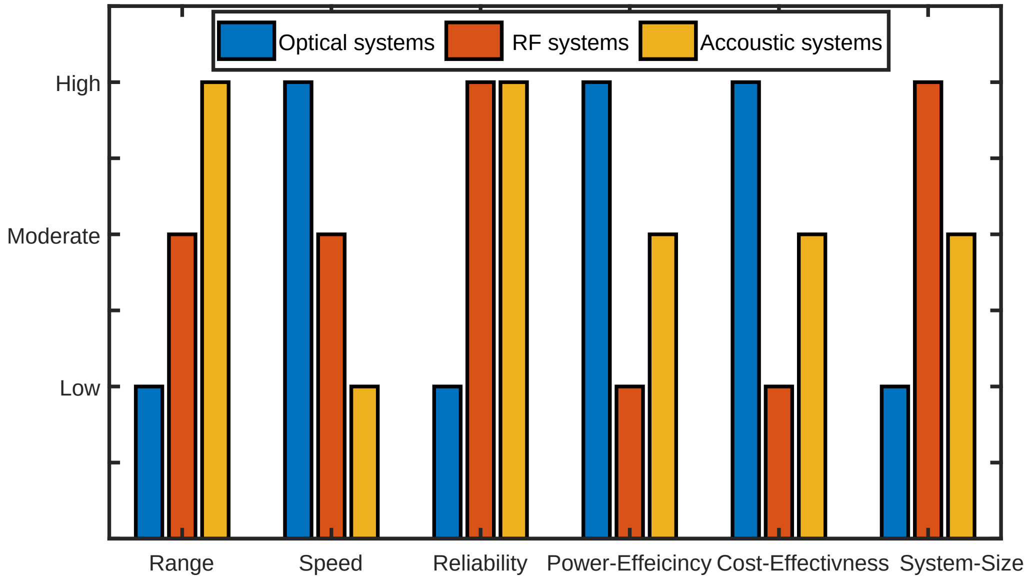

Figure 1.1: Trade off between the wireless communication technologies for UWSNs.

be reliable against misalignment due to the seawater currents and waves and the mobility of the endpoints of the link. High-speed communications are required for data muling (i.e., data collection), video surveillance, or real-time (latency-sensitive) signaling. Power efficiency is also required to ensure battery lifespan is sufficient without interrupting the mission for recharging. Lastly, communication systems should be implemented with small size and light-weight, and this aspect is required for automated underwater vehicles (AUVs) and sensors used in swarming technology[2] [4, 5, 6, 7].

Figure 1.1 contrasts the physical layer of current wireless communications that are used with UWSNs, namely, acoustic, radio frequency (RF), and wireless optical communication (WOC) systems [4, 5]. Acoustic systems use sound waves in the range of 10 Hz-1 MHz, where sound waves can propagate for long distances with low

---

[2] An AUV-swarm is a group of AUVs that navigate underwater and cooperate to achieve a single task.

attenuation in seawaters. Acoustic systems take advantage of long-range communication (up to 20 km). However, they offer low-speed communications, e.g., in the order of a few kbps [4]. Thus, acoustic systems are not appropriate for high-speed or latency-sensitive applications. RF systems use radio waves in the range of GHz, however, these can not propagate for long distances in seawaters due to severe attenuation. Designing the RF systems with lower frequency, MHz range, reduces the attenuation. However, it provides lower speed and increases system sizes[3], and costs [4]. Though RF systems offer higher rates (in tens Mbps) with moderate communication ranges, they are not power-efficient. Thanks to the propagation characteristics of optical beams in seawaters, e.g., broadband and small attenuation, underwater WOC (UWOC) systems are characterized with high speed (e.g., in the order of Gbps rate) and power-efficiency (e.g., in the order of a fraction of Watt). In addition, they are implemented with small size (e.g., on the order of cm to meters) and low-cost [5]. Due to the mentioned reasons, acoustic and RF communication systems are not the best solutions for high-speed short-range UWSNs. However, WOC systems are promising alternative physical layers for underwater communications. Due to the dynamic nature of underwater environments, seawater scattering, and the directivity of optical sources, WOC systems provide short-range communications with low reliability.

In this thesis, motivated by the unique advantages of WOC systems [4, 5], we propose new UWOC architectures that take advantage of high reliability and high speed and can be adopted for short-range applications. Specifically, for reliable high-speed point-to-point communications, we propose angular multiple-input multiple-output (A- MIMO) architectures that relax the conditions of on-axis and fixed-length transmissions between the ends of the communication [8]. Then, for further enhancement,

---

[3] The size of RF systems is related inversely with the operating frequency.

we introduce tracking A-MIMO (TA-MIMO) architectures that relax the condition of perfect orientation between the ends of the communication [9]. For reliable broadband broadcast communications under sea ice sheets, we propose under sea-ice diffusing communication (USDOC) architectures that offer robust communications regardless of dynamic environments under sea ice [10].

The remainder of this chapter is organized as follows. Section 1.1 shows the general architecture of underwater wireless optical sensor networks (UWOSNs). The section focuses on two scenarios for communications; point-point and broadcast communications. Section 1.2 describes the components of underwater optical wireless communication systems. The section introduces the major components of UWOC systems, i.e., optical sources, transmitter optics, receiver optics, photo-detectors, and MIMO architectures. Section 1.3 introduces the challenges of UWOC systems. The section highlights impacts of scattering and absorption in seawater and sea ice and receiver noise. Section 1.4 introduces a literature review and highlights solutions for the key challenges of UWOC systems. Section 1.5 presents the thesis vision and contributions. Then, Section 1.6 presents the outline of the thesis. The publication list and the details of the contributions are provided in 1.7. Finally, the chapter is concluded in Section 1.8.

1.1 Underwater Wireless Optical Sensor Networks

Figure 1.2 shows a general architecture for UWOSNs focusing on high-speed short-range applications. The figure highlights two topologies indicated using blue-dashed ellipses; point-to-point and broadcast communications under seawater surface and undersea ice sheet, respectively. The topologies contain several sensors and relay

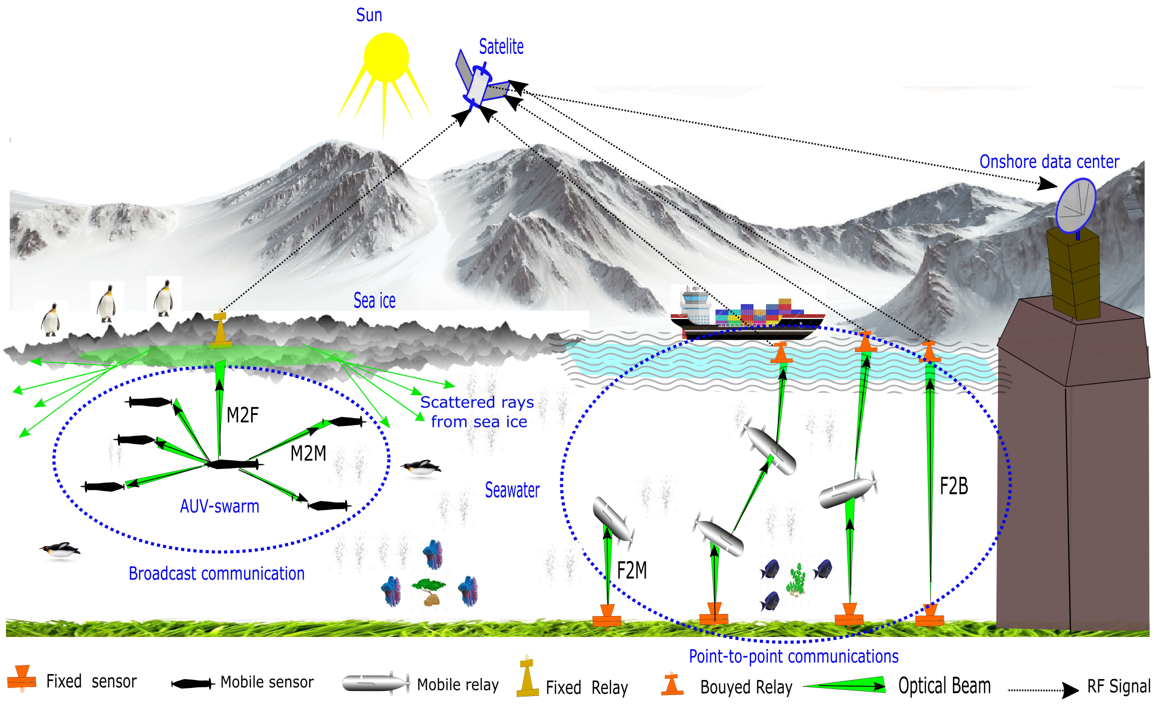

Figure 1.2: A general architecture for UWOSN (some cliparts are reproduced from [11, 12, 13]).

components that cooperate in gathering seawater data and transmitting them to an onshore data center. The sensors are either fixed nodes on the seabed or mobile nodes, i.e., autonomous underwater vehicles (AUVs) that navigate seawater. The relays are mobile nodes, fixed nodes on sea ice, or buoyed nodes on seawater. The sensors gather data from seawater or undersea ice sheets, while the relays transmit the gathered data to a satellite using RF signals. Then, the satellite sends the gathered data to the data center onshore for processing, and analysis [4, 5].

As shown in Fig. 1.2, under seawater, point-to-point communications are presented between fixed nodes and AUVs, and these links are named fixed-to-mobile (F2M) links. F2M links are used in several applications, such as data muling and sensor recharging. Point-to-point communications are also established between fixed sensors and the buoyed relay nodes, and these links are named fixed-to-buoyed (F2B) links. F2B links are used in various applications, e.g., video surveillance and border security [4, 5]. F2B links with short ranges are implemented in shallow seawaters, i.e., a few meters in depth [14]. However, as shown in the figure, some AUVs operate as relays between the fixed and buoyed nodes in deeper seawater [4, 5]. For links under sea ice, broadcast communications are established between a group of AUVs called AUV-swarming. Communications between AUVs are named mobile-to-mobile (M2M) links, as shown in the figure. In such swarms, AUVs navigate under sea ice and cooperate to achieve a single task such as mapping the thickness of sea ice sheets or measuring parameters of sea ices. Usually, the AUVs in a swarm are small in size (e.g., 60 cm×25 cm, [7]) and move together much like a group of fish with inter-distance in the order of meters or less [7]. AUVs use M2M communications to share speed, position, and motion directions to avoid collisions. AUV swarms also use M2M communications to backup the gathered data where some AUVs may be lost or damaged during the mission. In order to send the gathered data to the satellite, AUVs communicate with a relay node fixed on sea ice, and this communication is named mobile-to-fixed (M2F) link, as shown in the figure.

A challenge in implementing UWOSN topologies shown in Fig. 1.2 is the need for alignment between transmitters and receivers due to the high directivity of optical sources. Such alignment is, in practice, challenging in underwater environments due to surface waves, seawater currents, and mobility of the nodes, i.e., AUVs and buoyed nodes. This thesis proposes three new approaches to tackle this challenge; two systems are adopted for point-to-point communications underwater, namely A-MIMO and TA-MIMO approaches. The third approach is adopted for broadcast communications

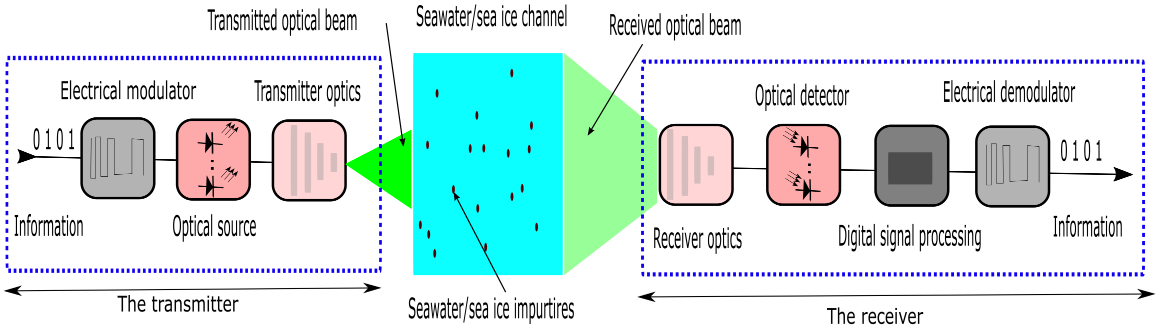

Figure 1.3: A general block diagram for UWOC links with IM/DD modulation.

under sea ice, and it is named SDOC approach.

1.2 Components of UWOC Links

Rather than using coherent modulation schemes[4], UWOC links are implemented commonly using intensity-modulation/direct-detection (IM/DD) modulation schemes. IM/DD systems take advantage of simplicity in implementation, small size, low weight, and cost-effectiveness [4, 5]. Figure 1.3 shows a general block diagram for UWOC links, IM/DD transmitter, receiver, and channel. In the following subsections, we demonstrate the block diagram in more detail.

Transmitter

As shown in Fig. 1.3, an external electrical modulator drives optical sources. Due to its simplicity and compromise between the power and spectrum efficiency, on-off keying (OOK) modulators are commonly used with IM/DD systems [16, 17]. The OOK modulator drives optical sources using a time-varying electrical current,

---

[4] In the literature, few works had investigated coherent modulation systems with underwater applications such as [15].

representing an electrical stream of zeros and ones. The intensity of optical sources is modulated proportionally to the driving current and associated with the transmitted information. Optical sources are realized using light-emitting diodes (LEDs) or laser diodes (LDs). LEDs are non-coherent optical sources with narrow bandwidths in the range of 1-300 MHz and wide linewidths (e.g., tens nm), e.g., phosphor-converted LEDs and micro-LEDs [18, 19, 20]. LED sources emit omni-directional illuminations with large spots. Thus, links that use LEDs are more robust against pointing errors [4, 5, 6]. In contrast to LED sources, LDs are coherent sources which can be modulated with broadband signals (e.g., tens of GHz) and have narrow linewidths (e.g., few nm), e.g., Quantum Cascade and Vertical-Cavity Surface-Emitting Laser (VCSEL) diodes [21, 22, 23]. In addition, LDs emit high directive beams with small spots, and eye-safety standards restrict the transmitted power [24]. Various types of LEDs and LDs sources have unique characteristics (e.g., wavelength, bandwidth, and efficiency) by which they can be adapted for different channels, and applications [25]. For instance, LED and LD sources with ultraviolet (i.e., $100-400$ nm), visible (i.e., $400-700$ nm), and infra-red (i.e., $700-1400$ nm) wavelengths are commonly used in non-line-of-sight outdoor, indoor visible light, and free-space optical communications, respectively [4, 5, 6]. In this thesis, to leverage the benefits of LD sources, using LD sources with bandwidth in the range of GHz and visible green wavelength (i.e., 532 nm) is considered rather than using LED sources.

Optical transmitters are implemented using a single optical source or an array of optical sources, called single input (SI) or multiple-input (MI) transmitters. Though MI transmitters increase the complexity of systems, they provide a spatial degree of freedom to raise communication speeds or provide spatial diversities [26]. After the LD, an assembly of lenses is used to modulate the spatial pattern of the optical beam. For instance, collimator lenses [27] could be used to reduce the divergence of the emitted beam for LOS communications. Diffusers may be used to modulate the directive beam into an omni-directional one for broadcast communications and to satisfy eye-safety requirements. An assembly of the diffuser and collimator lenses could also be arranged to modify the narrow Gaussian beam of LDs into a broader uniform one to relax restrictions of the eye safety [16].

Channel

The ocean body consists of salty water and contains an array of impurities. Most likely, oceans are covered by sheets of sea ice in cold regions such as in the Arctic and Antarctic zones. In winter seasons, sea ice sheets are additionally covered by thick layers of snow [2, 28, 29].

Seawaters are most likely contaminated by dissolved and suspended particles such as dissolved salts, mineral components, colored dissolved organic matter, etc. [28, 30]. These contaminations change the purity of seawater and cause cloudiness and haziness, i.e., turbidity. Increasing the concentration of contaminations leads to an increase in seawater turbidity, which varies by geographical location. For instance, horizontal channels from seawaters to rivers, the turbidity of channels are varied gradually with distance. As well, vertical channels from seabeds to the seawater surfaces, the turbidity of channels changes gradually with depth [31]. Generally, seawaters are classified into four main categories; pure, clear, coastal, and turbid seawaters, where the pure seawaters have the lowest turbidity. However, turbid seawaters are the highest in turbidity [32].

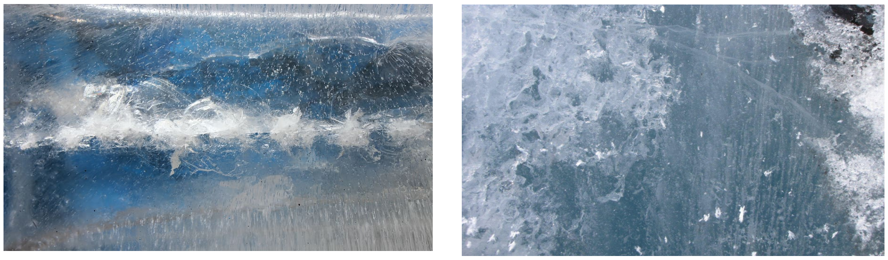

(a) Transparent sea ice. (b) Partial white sea ice.

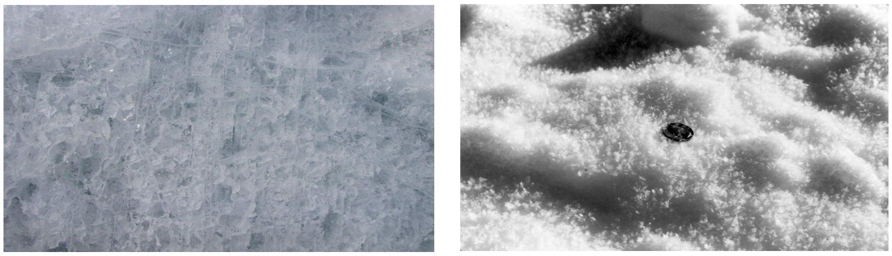

(c) White sea ice. (d) Snow-covered sea ice.

Figure 1.4: Four sea ice samples, namely; (a) transparent, (b) partial, (c) white and (d) snow-covered sea ice sheets. The samples were photographed in the Antarctic region [35].

Sea ice is frozen salty water due to the cooling of the atmosphere, and it is also contaminated by dissolved and suspended salts, i.e., brine pockets and solid salts, and air bubbles. The surrounding environments impact the surface and bottom of sea ice, i.e., the atmosphere impacts surfaces, and seawater impacts the bottom of the ice sheet. Sea ice surfaces are contaminated by black carbon called soot matter, which falls from the atmosphere. During winter seasons, which are present most of the year in the north and south poles, a thick layer of snow covers sea ice surfaces. The snow is a mixed layer of air gaps and snowflakes and is contaminated by soot matter. The bottoms of sea ice sheets and snows are contaminated by green matter called algae arriving from seawaters [33, 34].

The concentration of impurities in sea ice sheets changes the reflectivity of sea ice for incident light, i.e., whiteness. Increasing the concentration of the contaminated particles leads to an increase in sea ice whiteness. For instance, white sea ices reflect most sunlight hitting their surfaces back to the atmosphere. The whiteness of sea ice sheets changes with geographical locations and the depths of the sheets. For instance, to accurately present a vertical channel through sea ice, sea ice slabs should be divided into multiple layers with different whiteness. Generally, according to the whiteness, sea ice sheets are classified into four main types; transparent, partially transparent, white, and snow-covered sea ice sheets. Figure 1.4 shows samples for the sea ice types, and these samples were photographed in the Antarctic region [35]. In the shown photos, the surfaces' impurities and roughness increase from (a)-(d), which can be qualitatively observed from the color of the photo background. In Fig. 1.4a the transparent sea ice is a pure sheet of frozen seawater with fewer impurities, and the surface is less rough. Thus, the whiteness is low, and the seawater can be observed underneath the sheet in the photo (i.e., the blue background of the photo). In Fig. 1.4c, however, the white sea ice is contaminated with many impurities, and the surface is rougher than the transparent sea ice sheet. Thus, the whiteness is higher where the seawater under the sheet can not be observed in the photo. Fig. 1.4d shows the highest whiteness among the four shown samples where a layer of snow covers the ice sheet. Like the impurities and roughness, increasing the thickness of sea ice sheets leads to increasing whiteness [36, 37, 38].

Receiver

At the front end of the receiver, an optics assembly composed of the lens and optical filter is implemented. The lens is adopted according to the transmitter configuration, i.e., SI or MI. For SI transmitters, receivers are equipped with non-imaging lenses to maximize the effective area of the detection, and these end-to-end configurations are called SI-single output (SISO) systems [39]. For MI configurations, receivers are equipped with an array of non-imaging lenses, called non-imaging MI-multiple output (MIMO) systems [40]. As well, receivers may be equipped with a single imaging lens, and these configurations are called imaging MIMO systems [41]. Though SI-MO (SIMO) and MI-SO (MISO) systems could be realized for some benefits [5], however, this thesis focuses only on SISO and MIMO systems. Optical filters are band-pass, and they are used to eliminate background radiations such as solar radiation during daylight. Commercially, lenses and filters are implemented as a single component with a thin coating layer that presents the optical filter, such as a hemispheric concentrator [42].

Following the receiver optics, a photodetector (PD) or an array of PDs is used in SISO or MIMO system cases, respectively [40]. PDs convert the received optical intensity to the electrical current with a distortion related to channel type and receiver noise. The receiver noise depends on PD models; positive-intrinsic-negative semiconductor (PIN), avalanche PD (APD), and photon-multiplier tubes (PMTs) are some examples [43]. HOWEVER, the APD and PMT take advantage of internal gains at the expense of excess noise. The PIN PD is the appropriate PD when background radiations dominate the receiver noise and are, in addition, less expensive [43]. After PDs, trans-impedance amplifiers (TIAs) should be used to convert small photocurrents into significant electrical voltages [17].

In order to enhance system performance, PDs are typically followed by digital signal processing (DSP) such as low pass filters and channel equalizers [16, 44]. Lowpass filters are used to limit the bandwidth of the Gaussian noise, and channel equalizers are employed to eliminate the inter-symbol-interference (ISI) induced on the received signals. The decision feedback equalizer (DFE) scheme adapts itself to channel conditions using training sequences among the available equalizer schemes. Due to dynamic environments underwater, this adaptation is required with communication scenarios such as; F2M, M2F, and M2Ms links, as shown in Fig. 1.2.

1.3 Challenges of UWOC Systems

In contrast to acoustic and RF systems, UWOC systems with IM/DD schemes offer high speed and high power efficiency, and their transceivers are implemented with small sizes [4, 5]. However, the performance of UWOC systems is hampered by; the non-linearity of opto-electronic components, eye safety, channel impairments, system noise, and link misalignment. In the following subsection, we discuss each impairment for UWOC systems in some detail.

Non-Linearity of Opto-Electronic Components

Though LDs can provide broadband communications in the Gbps range, the transmitted power and communication speed are restricted practically due to the non-linearity of opto-electronic components in IM/DD systems, as shown in Fig.1.5. Figure 1.5 shows the relationship between electrical current applied in the input of LD source and optical power emitted from the output. LD sources behave linearly

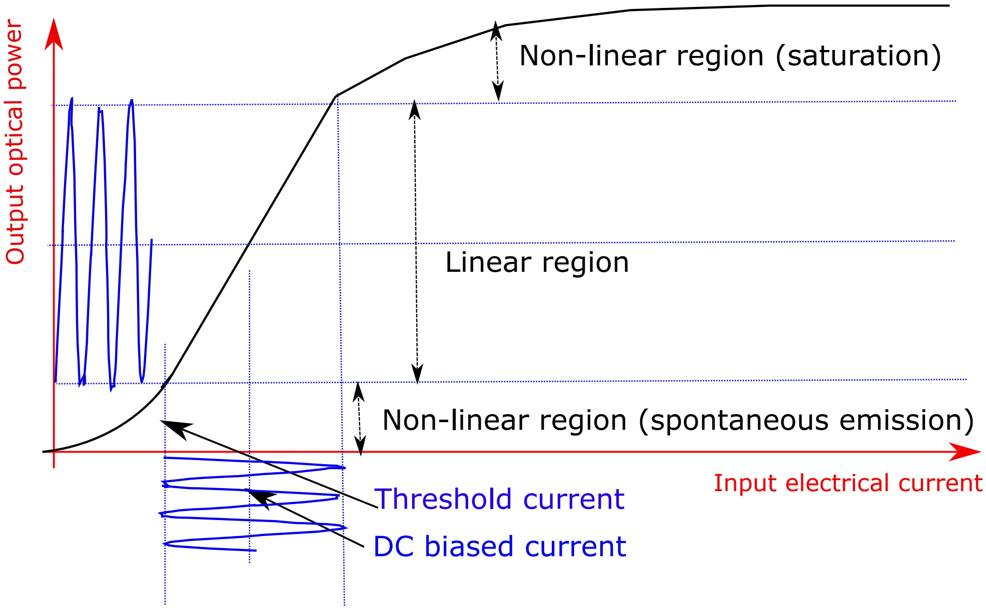

Figure 1.5: Illustration for non-linearity characteristics of LD sources (the figure reproduced from [45]).

within a dynamic range in which the optical intensity of LDs increases proportionally with the driving current, i.e., the linear region in the figure. However, LDs behave non-linearly when the current exceeds that range in which the optical intensity of LDs does not increase with the driving current, i.e., the saturation region in the figure. Moreover, LDs behave non-linearly when the driving current is smaller than a threshold by which the LDs are considered off, i.e., the spontaneous emission region in the figure. The non-linearity of LD sources with IM/DD systems is a phenomenon termed ”clipping” [45, 46]. On the other hand, opto-electronic components practically have narrow bandwidths, limiting LD source’s modulation speed. At high-speed modulation, the modulating optical carrier of LDs suffers from the phenomenon called chirping [47]. Chirping means the optical carrier shifts up and down instantaneously. As compared to coherent systems, due to the effects of noise-clipping and chirping, IM/DD systems are most likely used only for low-speed applications, with limited power, i.e., Mbps and mW ranges, respectively. However, as shown in the next section, multiple-input multiple-output systems, multi-carrier, and high-order modulations are promising avenues to raise the communication speed to the Gbps range. For instance, using the orthogonal frequency division multiplexing (OFDM) scheme, Oubei *et al.* have demonstrated a UWOC link with the data rate of up to 4.8 Gbps over 5.4 m [48].

Eye-Safety

Due to the low absorption in the visible window 400-700 nm, the visible window is the preferable spectrum window for communications underwater [17]. However, due to the high directivity and narrowing of LD beams, the permissible transmitted power of LD sources is restricted by the maximum permissible exposure (MPE) level for eye safety [49, 50]. When using LD sources, eye safety must be taken into account to ensure the safety of humans and animals underwater. Moderate and high-transmitted power values are potentially hazardous. They can cause eye and skin damage to divers underwater and sea creatures. For instance, the power value of laser point source with wavelength 840 nm is restricted to less than 0.24 mW to remain eye-safe, and this laser source is classified as II according to the laser safety of the industry [51]. As well, laser point source with wavelength 530 nm and power level 100 mW is restricted in specific applications, e.g., medical surgery, and this laser source is classified as IIIb according to the laser safety of the industry [51]. The MPE level is associated with wavelengths and beamwidths of LDs. Thus, LD sources with point sources are not recommended for communication purposes [51].

Using transmitter optics (e.g., diffuser cascaded with collimator lenses) with LD sources can convert point beam into a wide beam, which relaxes the restrictions of the MPE to some extent, as discussed in Section 1.2. For instance, using a holographic diffuser, Khoo *et al.* raised the allowable transmitted power from 0.24 mW to 1.1 mW (i.e., five times) for a laser point source at wavelength 840 nm [52]. On the other hand, the underwater channel may mitigate these risks since the scattering in the seawater diffuses the beam of LD, which reduces the risk of the LD beam on the eye and skin [9].

Channel Impairments

The propagation of optical rays in seawater and sea ice is challenging due to the inevitable photon interactions with molecules and other particulate matters [4, 5]. The photon-particle interaction severely absorbs the ray intensity and alters the ray direction, i.e., scattering. Though the absorption can be mitigated by raising the transmitted power, scattering is a significant challenge underwater. The scattering induces multi-path propagation, which leads to pulse dispersion and beams spreading in the receiving side. The pulse dispersion induces ISI during the detection and becomes more severe with high-speed and long-range communications [53, 54, 55]. The beam spreading also limits the communication range where the geometric loss severely attenuates the transmitted power as the link range increases [32].

Absorption and scattering effects increase with the turbidity and whiteness of seawaters and sea ice sheets, respectively [28, 38]. For instance, absorption and scattering impacts are more severe in turbid seawaters than in clear seawaters. Also, absorption and scattering impacts are more significant in snow-covered sea ice sheets than bare-sea ice sheets. In F2B and F2M links (e.g., see Fig.1.2), the link range and communication speed should be short and low to achieve acceptable performance in turbid seawaters, respectively. However, higher speed and more extended range communication are achievable in low turbidity sweaters such as clear and coastal seawater. Undersea ice sheets, such as M2F and M2M links (e.g., see Fig.1.2), the optical beam can propagate from seawaters to the atmosphere through transparent sea ice sheets, which rarely exist on frozen oceans. However, the beam is severely diffused when propagating through snow-covered sea ice sheets that mainly exist during the winter season in the Arctic and Antarctic zones. In contrast to seawaters, sea ice sheets have less absorption and higher scattering due to the high brine pockets and air bubbles [37], especially when sea ice sheets are covered by layers of snow [56].

On the other hand, absorption and scattering effects are wavelength-dependent processes. The optical window of blue-green colors (i.e., $450 - 550$ nm) has relatively low attenuation and is commonly used for underwater communications [17]. For instance, the absorption coefficients for green and red colors are 10^{-4} and 10^{-2} 1/cm, respectively, [4].

Underwater turbulence induces fading on propagating of the optical signals [57, 58, 59, 60]. Unlike absorption effects, which have fixed attenuation, the turbulence-induced fading causes rapid fluctuations in the received signals and raises the error in the detection. The fading effects on the received signals depend on the type of turbulence, i.e., weak, moderate or strong, which is related to the fluctuations in the refractive index of the seawater. The refractive index fluctuates due to random variations in the temperature and salinity of seawaters, i.e., inhomogeneous seawater channels. Small variations in the temperature and salinity lead to low fluctuations in the refractive index and induce weak turbulence. Weak turbulence is associated with short inhomogeneous channels, i.e., less than ten meters [59, 60]. However, high variations in the temperature and salinity lead to high fluctuations in the refractive index and induce strong turbulence. Strong turbulence is associated with long inhomogeneous channels, i.e., more than ten meters [59, 60]. This thesis focuses on short-range channels, i.e., less than 8 meters, and the turbulence effect is ignored where it is dominated by the rest impairments, i.e., absorption, scattering, misalignment, and receiver noises [57, 58, 59, 60].

Receiver Noise

There are a variety of noise sources that impact optical receivers, including; dark current, shot, thermal, and background noises [61]. Dark current is a relatively small electrical current that flows through PD devices when no photon is received. In most cases of PIN PDs, for simplicity, the dark current is ignored as it is dominated by other noise sources [43]. Shot noise is signal-dependent, and is generated due to the quantum-physics of PDs, i.e., random fluctuations of arrival photons [61]. When the number of arriving photons per time slot is slight, such as in turbid seawater and white sea ice channels, the shot noise is modeled using the Poisson probability distribution function (PDF). However, when the number of the arriving photons is large, such as in clear seawater channels, the random behavior of the shot noise is well described as being Gaussian distributed [43].

Thermal noise is generated due to the thermal effect of PD circuits, especially load resistors of TIA modules [61]. Such thermal noise increases with the temperature of the circuits. Underwater, the temperature reaches its highest value at surfaces of seawaters and decreases proportionally with increasing depth of seawaters [43]. However, on undersea ice sheets, the temperature of seawaters is usually less than zero Celsius [37] and increases with increasing the depth of seawaters. Undersea ice, thermal noises are less severe as compared to other noise sources [10].

Background noise arises mainly from solar radiations during the daytime [43]. The background radiation is highly dependent on weather conditions, zenith angle of the sun, surface conditions and sea ice types, and the depth of the receiver [43]. At the same depth under seawater, the background radiation in non-frozen oceans is higher than in frozen oceans due to the sea ice, and cold weather [43, 62]. At the surface, background radiation reaches the maximum value. Due to scattering and absorption in the water medium, the impact of background radiation decays with depth reaching its minimum at the seabed [29].

On the other hand, background radiation depends on the operating wavelength (i.e., optical carrier of the source and the linewidth of the emission spectrum), and it reaches its highest value at the optical window of blue-green color (i.e., $480 - 532$ nm) [62].

Link Misalignment

LDs are directive sources and are commonly used for point-to-point communications such as; F2B, F2M, M2F, and M2M links (see Fig. 1.2). Point-to-point links suffer misalignment errors due to seawater currents and waves, in addition to the mobility of nodes underwater, e.g., AUVs and buoyed nodes. For instance, in F2B links, buoyed nodes are displaced around their center of gravity on seawater surfaces due to sea waves [39]. The strength of sea waves depends on wind speeds in the atmosphere, i.e., higher wind speed means stronger sea waves. In cases of F2M and M2F links, AUVs move intentionally due to mobility or non-intentionally due to currents of seawaters [9]. Undersea ice, seawater currents induce slight misalignment, such as in M2F links, where seawaters are calmer under sea ice sheets [63]. However, underwater, such as F2M links, seawaters are more dynamic. The misalignment error leads to geometric loss, which increases with communication ranges proportionally. A small pointing error over a long communication range induces significant geometric loss [64]. Thus, using LDs can prove challenging for long-range underwater links. Though LEDs offer fewer advantages than LDs sources, they provide more robust links against pointing errors, to some extent, and thanks to illuminations with large spots [5, 4], as discussed in Section 1.2.

For broadcast applications, such as the M2Ms link in Fig. 1.2, transmitters with multi-LED configuration can be employed. In multi-LED configurations, each LED emits a wide beam pointed in a different direction to cover a large area [65]. Though these configurations offer a degree of spatial diversity, they increase system complexity, size, weight, and cost. Using LEDs rather than LDs, such systems also sacrifice key advantages of LD sources, i.e., high-speed modulation and a narrow emission spectrum, as discussed in Section 1.2. Also, which is more critical, multi-LED configurations are susceptible to blockage due to other AUVs [66, 67].

1.4 Literature Review

This section presents solutions proposed in the literature for tackling limitations of UWOC systems mentioned in Section 1.3.

1.4.1 Multiple-input Multiple-out (MIMO) Architectures

As discussed in Section 1.3, due to the non-linearity of opto-electronic components and eye-safety issues, the speed and transmitted power of UWOC links are restricted. These restrictions are associated with SISO architectures discussed in Section 1.2. One possible avenue to address these restrictions is using MIMO architectures. MIMO architectures are implemented using arrays of LD and arrays of PD at transmitters and receivers, respectively, as discussed in Section 1.2. MIMO systems leverage spatial and temporal degrees of freedom. Thus, MIMO systems increase capacities, and properly spaced emitters can transmit more power due to the extended nature of the source while remaining eye-safe. Thus, compared to SISO systems, MIMO systems provide higher capacity, power rating, and power efficiency while maintaining eye safety [8, 9]. However, the payment for the mentioned advantages is an extra hardware-complexity in the transmitter, and receiver implementations [68, 69]. As well, which is more critical, MIMO systems require alignment between ends of links where misalignment results in high spatial inter-channel-interference (SICI) and geometric loss problems [40]. SICI problems occur between adjacent PDs arranged in arrays, reducing the signal-to-interference-plus-noise ratio (SINR), which degrades the capacities of links. Maintaining the alignment between ends of MIMO links is a challenging task underwater [5, 4]. However, tracking techniques could solve this issue, as discussed in the following subsection.

Due to the advantages of MIMO systems, non-imaging MIMO architectures have been investigated underwater under different circumstances [4, 5]. For example, Dong *et al.* [26] studied a 2×2 non-imaging MIMO system considering the impact of inter-channel interference due to water scattering. However, perfect alignment and a fixed channel length were assumed for seeking simplicity. In [39], the capacity of a buoy node was investigated with highlighting the impact of misalignment due to sea waves. The numerical results, shown in [39], indicate that the capacity of the buoy node is degraded with the increase in strength of sea waves. Moreover, in [64], the capacity of a 3×2 non-imaging MIMO buoyed node was studied, focusing on turbulence, scattering, and misalignment impairments.

Though imaging MIMO systems require imaging receivers (i.e., large arrays of pixeled PD with single imaging lenses such as cameras), they offer more features than non-imaging MIMO systems. In [40], Zeng *et al.* evaluated the performance of imaging and non-imaging MIMO systems, showing the potential of the former in reducing SICI problems, background noise, and size of transceivers. Thus, imaging MIMO systems have been proposed for high-speed short-range indoor applications [68]. Underwater, little work has been done on the investigation of imaging MIMO systems [4, 5]. For instance, Li *et al.* [41] showed the effect of layout of LDs and PDs arrays on the performance of a 2×2 imaging MIMO link over 2.4 m assuming perfect alignment.

In contrast to non-imaging MIMO systems, imaging MIMO requires more accurate (i.e., perfect) alignment and compensation of changes in magnification due to channel length variations [69]. Recently, Han *et al.* proposed fixed-scale imaging MIMO architectures for high-speed short-range indoor applications. Fixed-scale imaging MIMO systems are robust against off-axis misalignment, as well as, their magnifications are independent of channel lengths (i.e., fixed magnifications) [70].

1.4.2 Misalignment Mitigation and Link Tracking

The precise pointing between ends of links is required for point-to-point communications, such as F2M, F2B, and M2F links (see Fig. 1.2). However, link misalignment is an inevitable phenomenon underwater where relative shifting (i.e., displacement) and disorientation (i.e., tilt) are expected between ends of links due to dynamic environments [4, 5].

Conventionally, there are three common approaches to relax/maintain the alignment between the ends of links: using an optical source with a wide beamwidth, increasing receiver size, and implementing an active tracking scheme [4, 5, 6]. Using an optical source with a wide beam can be realized either using a stand-alone LED or LD cascaded with a diffusing lens, which converts the narrow beam of LDs into wider ones. Wide beams can effectively increase the illuminated areas, which relax the pointing condition between the ends of links. However, this approach negatively impacts the power budget for point-to-point links. Thus, it is not a power-efficient solution for limited power applications [31, 66, 67]. The second approach employs receivers with larger apertures, and it is implemented either using a sizeable non-imaging lens cascaded with PD or an extensive array of PDs (e.g., PMT) without lens [32]. The first implementation limits the FOVs of receivers, while the second one limits the communication speeds due to the high capacitance of circuits. Large aperture sizes for receivers reduce the geometric loss of misaligned links. However, the increase in background noise and transceiver complexity restricts the applications of this approach [4, 5]. Note that the choice between using the first or second approach depends on the configuration of links. For instance, the first and second approaches could be adopted for F2M and M2F links cases, respectively. In F2M and M2F links, the transmitter and receiver are fixed, respectively, to accommodate relatively larger hardware.

In contrast to the first and second approaches, active tracking schemes maintain the pointing and take advantage of power efficiency. Active tracking schemes are implemented with relatively high power efficiencies and smaller sizes. Though active tracking schemes increase implementation cost, they can be effective in mitigating the impact of pointing errors in AUVs and sensor nodes [4]. In free-space optical (FSO) communications, active tracking schemes are a mature technology, and they are often referred to as ”pointing, acquisition and tracking” (PAT) schemes [71, 72]. PAT schemes are commonly implemented with FSO links for the alignment, and they can be realized with different approaches, among them, using Gimbal-based systems with digital imaging processing [4]. With three angles, Gimbal-based systems rotate transmitters mechanically around their optical axes (i.e., x, y, and z). The angles are estimated using least mean square error (LMSE) algorithms processed on received and reference images. LMSE algorithms estimate the angles that minimize the error between the reference and received images. For instance, Nalbandian *et al.* [73] developed a Gimbal-based system relay on a new rotary actuator technology that achieves perfect pointing performance, and it can be employed for LOS communications such as imaging MIMO systems. Though Gimbal-based systems could be adapted for underwater systems, they depend on mechanical rotation, increasing transceivers sizes and costs [4, 72]. Another approach is mirror-based systems which are light in weight because they use mirrors with small masses, unlike Gimbal-based systems. Though mirror-based systems have high steering speeds and perfect pointing resolutions, they have narrow views restricting their motion with wide angular ranges. For instance,

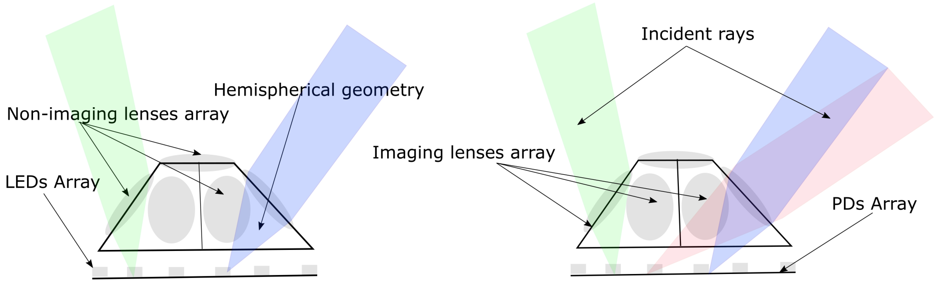

(a) Transmitter architecture. (b) Receiver architecture and angle-to-space mapping.

Figure 1.6: Smart transceiver architecture and angle-to-space mapping (the figure reproduced from [75]).

FSM-300-01 is a mirror-based PAT system for fast Steering, and it is used commercially in many applications such as laser pointing, tracking, FSO, and imaging MIMO systems [74].

Figure 1.6 shows a less bulky and more affordable tracking system [75]. The shown architecture is a part of a smart transceiver, and it was proposed for the underwater. As shown, the transmitters and receivers are implemented with hemispherical geometries using an array of non-imaging lenses with an array of LED, and an array of imaging lenses with an array of PD, respectively. As shown in Fig. 1.6a, each LED is coupled with its non-imaging lens and oriented into an associated direction. The non-imaging lenses converge the broad beams of LEDs into narrow ones with the associated directions, i.e., space-to-angle mapping. As shown in Fig. 1.6b, the imaging lenses map the incident rays into associated PDs according to the arrival angles, i.e., angle-to-space mapping. Due to that mapping, i.e., space-to-angle and angle-to-space, the receiver can estimate the arrival angles and varies FOVs of PDs according to these angles. The transmitter also knows the arrival angles from the

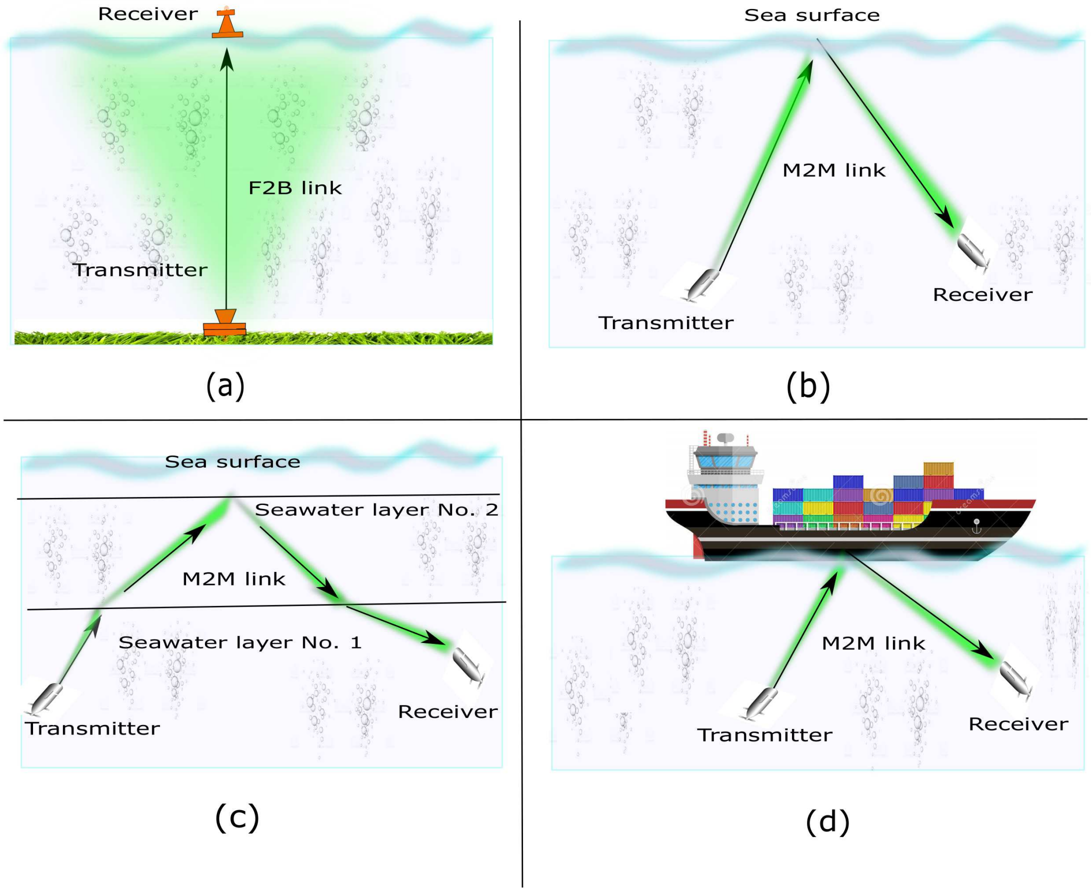

Figure 1.7: Illustration for NLOS configurations proposed in the literature; (a) seawaters are used as diffusing mediums, (b) seawater surfaces are used as reflectors, (c) seawater layers are used as reflectors, and (d) bottoms of ships are used as reflectors, (some cliparts in the figure are reproduced from [11, 12, 13]).

co-located receiver, then steers the beams of LEDs electrically according to the correct directions. In contrast to Gimbal-based systems, smart transceivers depend on electrical rotation, reducing the sizes and costs of underwater systems [75].

1.4.3 Non-Line of Sight (NLOS) Communications

Line-of-sight (LOS) communications between AUVs can suffer outages due to blockage, dynamic conditions of the seawater, and mobility of the AUVs [31, 66, 67]. In such cases, non-line of sight (NLOS) communications are alternative configurations for reaching obscured AUVs and sensors. NLOS communications also offer the advantages of broadcast communications, such as M2Ms links in Fig.1.2, [4, 5]. NLOS communications can be implemented with different configurations which depend on the communication scenarios and environments. In the literature, by exploiting the unique environmental conditions underwater, many configurations have been proposed for NLOS point-to-point communications as shown in Fig. 1.7.

Figure 1.7a, in high turbidity seawaters, the scattering in seawater has been suggested as a means to diffuse optical beams into wider ones with more omni-directional illuminations [76, 77]. Omni-directional illuminations reduce the outage probability, i.e., link disconnection, and enhance communication reliability. This configuration is only feasible for high turbidity seawaters with long-range communications where the multi-scattering components dominate the LOS component, e.g., attenuation length[5] more than 10 [32]. However, it is not an effective configuration in cases of clear/coastal seawaters or short-range communications. Due to severe attenuation in turbid seawaters, this configuration is not power-efficient.

Figure 1.7b, seawater/air interfaces have also been proposed as diffusers for the optical beam from transmitters to receivers when terrains block the LOS paths underwater [78]. In such cases, the links are implemented near the seawater surface, approximately tens of meters under the water surface. Transmitters and receivers

---

[5] The attenuation length is a multiplication of the link length by extinction coefficient of the seawater.

are oriented toward seawater/air interfaces. The spatial pattern of reflected intensity depends on the refractive index of seawaters and the pattern of sea waves on seawater surfaces. Due to the smoothness of sea waves, the spot of the reflected intensity can be relatively small and does not cover a large area, i.e., a few centimeters. Thus, these configurations are used for NLOS point-to-point communications, which is not suited for broadcast communications. This configuration does not depend on the scattering of seawaters, thus, it is suitable for all types of seawater. So, with clear seawaters, this configuration could establish a long-range between two obstructed transceivers in the order of 100 m [78].

Refractive index variation with depths (i.e., the vertical gradient of refractive index) in seawaters has also been proposed to reflect optical beams for NLOS communications, as shown in Fig. 1.7c. The refractive index varies with depth due to seawater temperature, salinity, and pressure [79]. Though the refractive index changes slowly with depth in typical scenarios, significant changes can be seen in long-range links on the order of hundreds of meters [79]. Inspired by geoscience, Anous *et al.* [31] used the concept of layering to discretize the vertical variation in the refractive index with temperature and salinity profiles of seawaters. The concept of layering is commonly used in geoscience to measure the effect of the Atmosphere-Ocean system on global warming [33, 80, 81]. Anous *et al.* proposed a configuration for NLOS point-to-point communications that could be adopted for long-range, in order of tens of hundred meters. Due to slight variation in the refractive index with short and moderate ranges, the proposed configuration is practical only for long-range links, i.e., in the order of hundreds of meters, such as searching for black boxes of aircraft lost in deep seawaters.

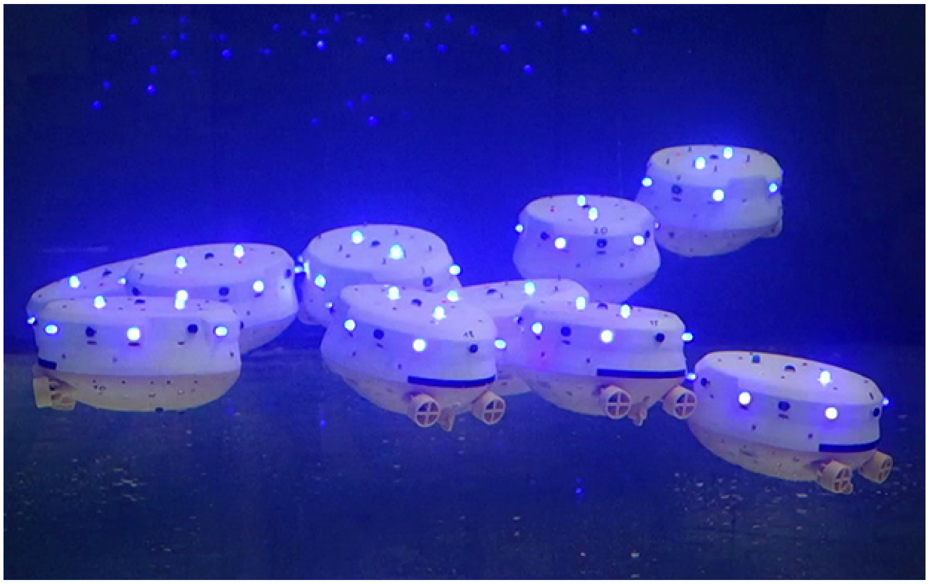

Figure 1.8: NLOS broadcast communication system using 12-LEDs transmitter (the image reproduced from [65])

As shown in Fig. 1.7d, the bottom of ship hulls has also been considered as artificial reflectors for NLOS communications [6]. In such cases, the reflectivity of the ship hull may be enhanced by painting or coating with a reflective coating. This configuration requires the ship to move on seawater along with the communication system underwater, and this requires coordination and localization to maintain orientation in mobile settings.

On the other hand, transceiver configurations can be adjusted to provide NLOS communications. An LD source cascaded with diffusing lens may be used in the transmitter to increase the width of the beam with an omni-directional radiation pattern [6]. For greater reliability, Fig. 1.8 shows a transmitter equipped with a multi-LED source, and each LED is configured with a wide beam and is oriented to a different direction. The shown configuration is a prototype with a 12-LED transceiver, which can be employed for broadcast communication [65]. In contrast to single-LED transmitters, multi-LED transmitters offer relatively reliable communications, however, the model has significant drawbacks. Due to the vulnerability of transceivers to the blockage by other transceivers, the shown approach is not sufficiently reliable. Due to the broad emission spectrum of LED sources, the communication performance is also vulnerable to the effects of background radiation. Intensity background radiation impairs AUVs operating near the seawater surface, especially daylight. On the other hand, LED sources offer relatively low-speed communication, in the order of a few tens Mbps, due to narrow modulation bandwidth, in the order of few tens MHz, [4]. Moreover, implementing a transmitter using multi-LED raises the system complexity and cost. These transmitters are not fit for small devices such as AUVs employed as swarms under sea ice [82].

There is no superior technique among the mentioned NLOS configurations; however, the suited one depends on environments and communication scenarios.

1.5 Thesis Vision and Contributions

The previous sections have provided a survey along with a literature review for underwater tracking and NLOS approaches for short-range communications. Then, we demonstrated the recent solutions proposed for tackling the weaknesses. Based on the previous survey, this section shows the thesis vision, and articulates the thesis contributions, and compares them to the approaches survey in Sec. 1.4.

1.5.1 Thesis Vision

The overall vision of this thesis is the development of novel approaches to enable realizable for reliable high-speed short-distance UWOC systems while considering the practicality, eco-friendliness, and power efficiency conditions. We can state the thesis vision in the following five points:

1. Reliable Communication Systems:
   Misalignment, blockage, and shadowing are inevitable phenomena underwater due to seawater currents and waves, communication system mobility, underwater terrains, and widespread fish and marine life groups. This thesis focuses on system reliability as the primary requirement for underwater communication systems [8, 9, 10].

2. High-Speed Communication Systems:
   Recently, UWSNs have paid much attention to real-time (i.e., small-latency) applications more than last decades. For example, real-time, high-quality video streaming is used for border security and ecosystem monitoring. Real-time signaling is used for exchanging traffic information between AUVs to avoid vehicle collisions. In this thesis, we focus on high-speed communications on the order of Gpbs and latency in the range of nanoseconds [8, 9, 10].

3. Short-Range Communications:
   Though, UWOC systems can offer relatively long-range communications on the order of hundreds of meters, for instance, using LED sources with highly-sensitive receivers [4, 5]. However, the scope of this thesis is focused on short-range communications in the order of a few meters, e.g., 7 meters. Several

applications can be adopted for short-range communication, such as shallow sea waters, data muling, and AUV swarm [9, 14, 48, 83]. Precisely, in AUV swarms, AUVs navigate with short inter-distance in the order of 1-meter [7, 84].

4. Eco-Friendly Systems:

   Sea animals often move in large groups, and there is a chance for interacting with components of UWOSNs. Divers usually are in touch with the elements of UWOSNs for adjustment, maintenance, or replacement. These used cases have the inherent hazards of laser-eye or laser-skin interaction and may lead to injury. Given the importance of maintaining our natural environment, it is essential that any wide deployment of UWOSN is safe for both humans and wildlife [4, 5]. In this thesis, we consider standards of the eye-safety to provide safe conditions for divers and sea animals. We limit the transmitted optical intensity by the threshold of maximum permissible exposure (MPE) [49, 50].

5. Power-Efficient Communication Systems:

   The size of batteries and energy storage components on AUVs and sensors are limited due to the strict size and width restrictions inherent to underwater systems [7, 83]. Recharging batteries underwater is a difficult task considering the complex environment of oceans and the widespread of sensor nodes [6]. Thus, it is not efficient to recharge the battery much frequently, and the efficient use for the power has to be assumed. This thesis aims to propose WOC systems that take advantage of power efficiency.

1.5.2 Thesis Contributions

In this subsection, the thesis contributions are shown to guide the research and industry societies to new directions in UWOC systems. The thesis provides three promising trends for reliable high-speed point-to-point and broadcasts communications as follows:

1. Imaging MIMO systems offer several benefits, as mentioned in Subsection 1.4.1. This thesis utilizes these benefits and proposes angular imaging MIMO (A-MIMO) systems for reliable point-to-point UWOCs. A-MIMO systems are motivated by fixed-scale imaging MIMO systems indoor applications [70], [85]. A-MIMO systems send beams in angle rather than space, so the on-axis and fixed channel length transmissions are not required. In contrast to classic imaging MIMO (C-MIMO) systems mentioned in Subsection 1.4.1, A-MIMO systems are reliable against the relative displacement between ends of links, e.g., data muling between AUVs and fixed sensors on the seabed (F2M links shown in Fig. 1.2). Rather than using tracking schemes that increase the sizes and costs of communication systems, as mentioned in Subsection 1.4.2, A-MIMO systems provide simple and low-cost reliable communication systems [8, 9].

2. Motivated by promising results obtained from A-MIMO systems, tracking angular MIMO (TA-MIMO) systems are proposed for more reliable high-speed point-to-point UWOCs [9]. TA-MIMO systems inherit the tracking characteristics from their optical architecture, i.e., space-to-angle and angle-space mapping. In addition to the benefits of A-MIMO systems, TA-MIMO systems are robust against the relative tilt between ends of links, e.g., links between fixed sensors on the seabed and buoyed nodes on seawater (F2B links shown in Fig.

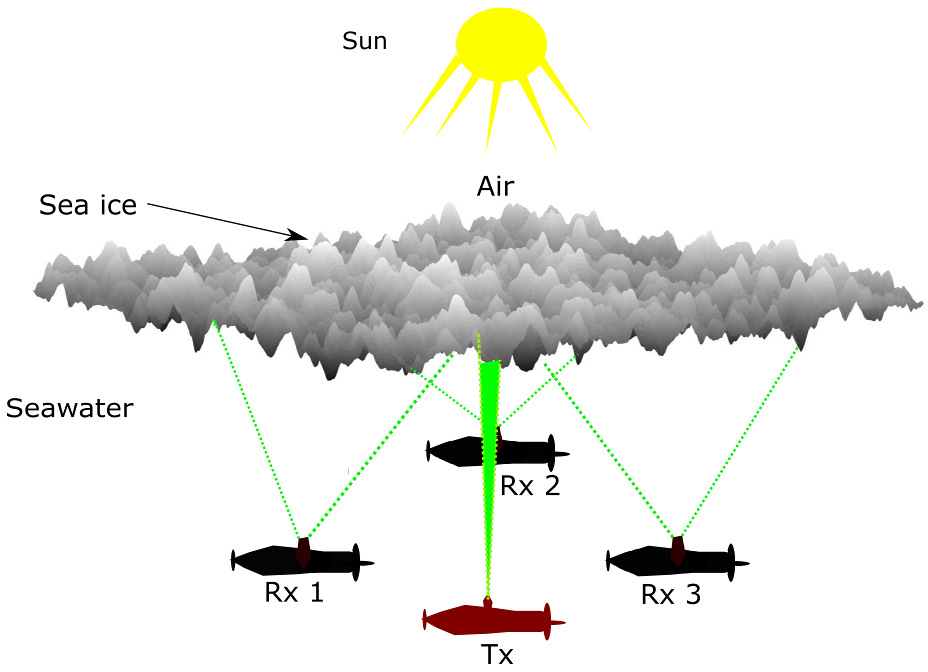

Figure 1.9: SDOC approach: single LD transmitter with sea ice as diffusing surface (Tx and Rx indicate to transmitter and receiver, respectively).

1.2). In addition to reliable communications, TA-MIMO systems can be used for localization functions that are challenging underwater. In contrast to tracking schemes mentioned in Subsection 1.4.2 and classic localization schemes [6], TA-MIMO systems could be employed for several purposes; communications, tracking, and localization [9].

3. For reliable NLOS broadband broadcast communications under sea ice, we propose sea ice diffusing optical communication (SDOC) systems rather than multi-LED transmitters. As shown in Fig. 1.9, SDOC systems utilize sea ice sheets above transceivers to diffuse the optical beam from the transmitter (Tx) to receivers (Rxs). Sea ice sheets diffuse the optical beam with a wide omnidirectional pattern and thanks to dense scattering, interior sea ice, and snow,

as discussed in Section 1.2. SDOC systems are reliable since they do not require alignment between the Tx and Rxs, and they are robust against blockage and shadowing. In contrast to multi-LED systems as mentioned in Section 1.2 and Subsection 1.4.3, SDOC systems utilize the merits of LD sources. In addition, SDOC systems are implemented with simple hardware, which is the primary requirement for small sensors and AUVs. The system takes advantage of high-speed, narrow-spectrum-emission, simplicity in the implementation, small hardware, and cost-effectiveness. In contrast to all previous NLOS configurations mentioned in Subsection 1.4.3, SDOC systems can be utilized for all communication scenarios; point-to-point, multicast, and broadcast communications [10].

1.6 Thesis Outline

This thesis introduces A-MIMO, TA-MIMO, and SDOC systems to fulfill the vision and contributions for short-range underwater links in Sec. 1.5 and overcome many of the conventional drawbacks of the optical systems pointed out in Sec. 1.3. A-MIMO, TA-MIMO, and SDOC links are modeled analytically, and then system designs are proposed to enhance link performances by considering realistic assumptions. Numerically, channel performances are investigated, and the system performances are evaluated, highlighting significant results. This thesis is written following regulations for a “sandwich” format. In addition to the introduction, it contains two self-contained chapters, a conclusion, and three appendices. Each chapter consists of an abstract, an introduction, a body, a conclusion, and necessary appendices. The references from all chapters are compiled in the bibliography list at the end of the thesis. The organization of the thesis is as follows.

In **Chapter 2**, for the first time, A-MIMO systems are proposed as a promising candidate for reliable high-speed point-to-point communications, such as F2M and M2F links. Compared to C-MIMO systems, A-MIMO systems send the optical beams in angle rather than space, significantly relaxing the on-axis requirement. In addition, sending the beams in angle fixes the image magnification regardless of the variation in link range. These two features are essential for underwater environments, where maintaining alignment between the ends of the links is challenging, as discussed in Section 1.3. In this chapter, we describe the architecture of A-MIMO systems and highlight their inherent characteristics in contrast to C-MIMO systems. The maximum communication range is derived as a function in the parameters of system architecture. The polar and azimuthal angle of arrival (AoA) distributions are derived in closed-form equations for the LOS components. A Monte Carol method is introduced for the underwater channel, and it is used to compute AoA distributions for multiple scattering components. Then, the AoA distributions are shown numerically in clear and coastal seawaters. For comparing A-MIMO and C-MIMO systems, channel capacities of 9×9 MIMO systems are evaluated versus off-axis transmission and link length variation conditions. The numerical results show that A-MIMO systems maintain the link capacity against the misalignment conditions far better than C-MIMO systems while using smaller transceivers. Numerically, with 10 cm off-axis, A-MIMO systems outperform C-MIMO by 25% and 20% extra channel capacity in clear and coastal seawaters, respectively. A-MIMO systems should be adopted to short-range applications, where the increase in link range raises the size of those systems.

In **Chapter 3**, TA-MIMO systems are proposed for more reliable and higher-speed point-to-point links for the first time. Compared to A-MIMO systems, TA-MIMO systems offer tracking ability between ends of the link in addition to the communication function. Due to their optical architectures, TA-MIMO systems estimate the relative misalignment, displacement, and tilt between the transmitter and the receiver. A comprehensive model for TA-MIMO and A-MIMO links is derived by considering link misalignment, channel impairments, and receiver noise. AoA distributions of the received signal on the lens and their position of arrival (PoA) distributions on the focal plane of the detector are modeled. Closed-form expressions for AoA distributions are obtained and verified using Monte-Carlo simulation. The pointing-localization-tracking (PLT) scheme is modeled for TA-MIMO systems, and distributions of residual tracking errors are calculated. Then, the channel capacity is estimated for 49×49 MIMO links with two communication scenarios; F2B, which is dominated by angular (i.e., tilt) misalignment, and F2M, which is dominated by off-axis (i.e., displacement) misalignment. Numerical results indicate that in F2B scenarios, A-MIMO systems are sensitive to angular misalignment; however, TA-MIMO systems outperform C-MIMO systems. In the case of F2M scenarios, A-MIMO systems significantly outperform C-MIMO systems when off-axis misalignment is presented. Specifically, with 6m/sec wind speed, TA-MIMO links outperform C-MIMO links by 25% and 50% extra capacity in clear and coastal seawaters, respectively. TA-MIMO systems should be adopted to short-range applications, like AMIMO systems, requiring high-resolution imaging receivers. In addition, PLT schemes require a training sequence, which slightly reduces the link throughput.

In contrast to the previous chapters, **Chapter 4** satisfies the thesis vision for NLOS broadcast communications under sea ice. As discussed in Sec. 1.4, many

NLOS point-to-point approaches are proposed for different environments underwater, however, undersea ice environment has not been considered previously. **Chapter 4** proposes SDOC systems for broadband-broadcast communications under sea ice sheets. For example, groups of AUVs navigate under sea ice sheets to map the thickness of sea ices or measure the temperature and salinity underneath sea ices. We utilize sea ice above the AUVs to diffuse the optical beam sent from the AUV transmitter omni-directionally to AUV receivers. Channels of SDOC approaches are modeled using seawater-sea ice cascaded layers (SSCL), where the vertical channel is divided into multiple layers based on their optical characteristics. Using the SSCL model, snow-covered and bare sea ice sheets with a thickness of 36 cm and 12 cm, respectively, are modeled using data measured in the literature. SDOC links are modeled with upward and downward transmissions (Tx to sea ice and sea ice to Rxs). The two-step modeling facilitates the link modeling and reduces the computation time. The diffusing pattern, resulting from the upward-transmission, is computed using a Monte Carlo numerical ray-tracing (MCNRT) technique. A quasi-analytic equation is derived for the channel impulse response function in receiver configuration, location, and orientation. To overcome the limitations of solar radiation and inter-symbol interference, we engineer a transceivers architecture for SDOC approaches. Numerically, the diffusing pattern, CIR, DC gain, and time delay spread are investigated for the channel in different cases. Furthermore, the bit error rate performance, power penalty, and maximum achievable bit rate are evaluated architecture under different scenarios for the proposed transceiver. Numerical results test the proposed systems under the snow-covered and bare sea ice sheets. The proposed systems achieved communication speeds of 100 Mbps with ranges up to 3.5 meters and 3 meters in the former and later sea ice sheets, respectively, with BER less than 10^{-3} and an average transmitted power of 100 mW.

Chapter 5 concludes the thesis and outlines the potential research avenues that could be motivated by this work and extend it.

Further details for the derivations in **Chapter 3** are introduced in **Appendix A**. For **Chapter 4**, the details of SSCL models and Table 4.1 are given in **Appendix B**, and additional numerical results for SDOC channels are shown in **Appendix C**.

1.7 Description of Contributions to Publications

This thesis has been prepared in the "sandwich thesis" format. This section describes the contribution of each of the co-authors to work.

Chapter 2: **Angular MIMO for Underwater Wireless Optical Communications: Channel Modeling and Capacity**

Authors: Abdallah S. Ghazy, Steve Hranilovic, and M. A. Khalighi

The idea of A-MIMO came up during supervisory meetings between Abdallah Ghazy and Dr. Steve Hranilovic, who encouraged Abdallah to follow this research direction. Abdallah Ghazy then formulated the underwater MIMO system model, developed the system block diagram, and carried out all analyses and simulations in this paper. He also plotted all graphs and did all the writing of this paper while receiving feedback and suggestions from Dr. Hranilovic. Once a paper draft was completed, Dr. Khalighi reviewed the paper and provided his feedback and suggestions. Abdallah Ghazy continued to edit the paper based on this feedback, while Dr. Hranilovic helped with the final editing of the paper and guided the research. This work was presented in [8]. The material in this chapter was published in the proceedings IEEE Canadian Workshop on Information Theory (Hamilton, Ontario, Canada, June 2019) [8]. The IEEE holds the copyright of the material in this chapter. The material is re-used with the permission of the IEEE, and this statement is included at the IEEE's request.

Chapter 3: **Angular MIMO for Underwater Wireless Optical Communications: Link Modelling and Tracking**

Authors: Abdallah S. Ghazy, Steve Hranilovic, and Mohammad-Ali Khalighi

Abdallah Ghazy and Dr. Steve Hranilovic had been motivated by the promising results they obtained from the A-MIMO systems. So, they thought about the idea of TA-MIMO during supervisory meetings, and Dr. Steve Hranilovic encouraged Abdallah to follow this research direction. Abdallah then formulated the underwater TA-MIMO system model, developed the system block diagram, and carried out all analyses and simulations in this paper. He also plotted all graphs and did all the writing of this paper while receiving feedback and suggestions from Dr.Hranilovic. Once a paper draft was completed, Dr. Khalighi reviewed the paper and provided his feedback and suggestions. Abdallah continued to edit the paper based on this feedback, while Dr. Hranilovic helped with the final editing of the paper and guiding the research. This work was presented in [9], the material in this chapter was published in IEEE Journal of Oceanic Engineering (Volume: 46, Number: 4, Pages: 1391-1407, March 2021) [9]. The IEEE holds the copyright of the material in this chapter. The material is re-used with the permission of the IEEE, and this statement is included at the IEEE's request.

Chapter 4: **Under-Sea Ice Diffusing Optical Communication**

Authors: Abdallah S. Ghazy, Haitham S. Khallaf, Steve Hranilovic, and
Mohammad-Ali Khalighi

The idea of SDOC systems came up during supervisory meetings between Abdallah Ghazy and Dr. Steve Hranilovic, who encouraged Abdallah to follow this research direction. Abdallah set out to study sea ice characteristics and their modeling. Abdallah then proceeded to channel modeling. He then performed all the analysis and simulations, obtained all the graphs, and did all the writing of the paper. Dr. Haitham Khallaf reviewed the paper draft, helped with the final editing, and guided feedback and suggestions to improve the paper. Dr. Khalighi and Dr. Steve Hranilovic reviewed the paper and provided comments and suggestions in the initial phase of the problem layout and before the paper submission. This work was presented in [10], the material in this chapter was published in IEEE Access (Volume: 9, Pages: 159652-159671, January 2021) [10]. The IEEE holds the copyright of the material in this chapter. The material is re-used with the permission of the IEEE, and this statement is included at the IEEE's request.

1.8 Conclusion

This chapter highlighted the challenges of underwater wireless optical communication and related solutions in the existing literature. In contrast to the literature, this chapter presented the thesis vision to overcome the challenges in underwater systems. According to that vision, the thesis proposed three novel systems: A-MIMO, TA-MIMO, and SDOC systems. A-MIMO and TA-MIMO systems are proposed for reliable high-speed point-to-point communications. A-MIMO systems are promising candidates when the relative displacement is presented between ends of the link, such as data muling links between fixed sensors on seabed and AUVs. However, TA-MIMO systems are promising approaches when the relative displacement and tilt are presented between ends of the links, such as video links between AUVs and buoyed nodes on the sea surface. SDOC systems are proposed for reliable high-speed broadcast communications under sea ices. SDOC systems are promising solutions for AUV-swarm deployed under sea ice, e.g., AUV used to map the thickness of sea ice sheets or measure sea ice parameters in Arctic and Antarctic zones. The proposed systems should be adopted for short-range applications, where increases in the link range lead to an increase in the sizes of those systems. The following chapters discuss and model the proposed systems with profound insight.

Chapter 2

Angular MIMO for Underwater Wireless Optical Communications: Channel Modelling and Capacity

In this chapter, to satisfy the thesis vision as discussed in Sec. 1.5, we propose A-MIMO systems for reliable point-to-point communications. As illustrated in Sec. 1.1 and shown in Fig. 1.2, A-MIMO systems could be used in high-speed short-range communications such as F2M and M2F links. A-MIMO systems mitigate the non-linearity of opto-electronic components in IM/DD modulations and relax eye-safety restrictions. Also, A-MIMO links relax the perfect alignment condition between ends of the link, which is essential in the case of C-MIMO links, as discussed in Sec. 1.4.1. The architecture of A-MIMO systems is described by highlighting the difference with C-MIMO systems. The maximum length for A-MIMO links is derived as a function in dimensions of the optical architecture. In order to consider multiple scattering, channels are modeled using the MCNRT method. AoA distributions are obtained for LOS and multiple scattering components analytically and numerically, respectively. The instance channel capacities for 9×9 A-MIMO and C-MIMO systems are evaluated in clear and coastal seawater with two scenarios; displacement and link length variation transmissions.

The work in this chapter has appeared in the Proceeding of *2019 IEEE Canadian Workshop for Information Theory (CWIT), (Pages: 1-6, June 2019) [8].* IEEE owns the copyright of the material in this chapter, and it is permitted to be re-used in the thesis.

Abstract An alternative architecture for imaging multiple-input/multiple-output (MIMO) underwater wireless optical communications (UWOCs) is proposed which relies on the transmission in *angle* rather than directly in *space*. The angular MIMO (A-MIMO) system has advantages over conventional underwater MIMO systems (C-MIMO) in that the image magnification is invariant to link range, and angular transmission greatly relaxes the alignment requirements of such links. These features are especially important for underwater wireless sensor networks (UWSNs), where the maintaining alignment between underwater vehicles and floating sensors nodes may be difficult in such dynamic environments. In this paper, we describe the architecture of A-MIMO for underwater channels and numerically characterize it in clear and coastal seawater conditions. For comparison a C-MIMO underwater system with similar parameters is also characterized and the channel capacities for A-MIMO and a C-MIMO are contrasted against link distances and misalignment errors. The numerical results show that A-MIMO maintains the link capacity against the misalignment conditions far better than C-MIMO while using a smaller size transceiver.

2.1 Introduction

Wireless communications using light are among the only broadband connectivity solutions for underwater wireless sensor networks (UWSNs). Whereas, radio links are highly attenuated underwater and acoustic links are intrinsically low bandwidth, underwater wireless optical communication (UWOC) links are highly directive, require lower energy consumption and have a significantly higher bandwidth. For example, UWOC links have been demonstrated at ranges of several to tens of meters at rates of gigabits/second [4]. However, impurities in the seawater reduce link reliability by attenuating and scattering optical signals. Signal scattering induces multipath distortion, which may generate temporal inter-symbol interference (TISI) and spatial inter-channel interference (SICI) problems [26]. These channel impairments limit the range and rate of UWSNs links [32].

In order to improve the spectral efficiency of optical wireless channels, imaging mulitple-input/multiple-output (MIMO) systems have been considered using arrays of lasers or light emitting diodes (LDs/LEDs) and arrays of photodetectors (PDs). A typical imaging MIMO configuration for optical wireless channels, termed *conventional MIMO* (C-MIMO), consists of an array of emitters and an imaging receiver, as shown in Figure 2.1. There has been significant work in designing and characterizing imaging receivers for MIMO systems for short range communication in the atmosphere. For example, Zeng *et al.* evaluated the performance of imaging and non-imaging MIMO systems, and showed that imaging MIMO systems can offer better uncorrelated channel matrices [40]. A key limitation of such MIMO systems is their requirement for perfect alignment, and the system is implemented according to associated channel length. Therefore, the distance and alignment between the transmitters and receivers of imaging MIMO systems must be tightly controlled to avoid SICI problems which cause a degradation in system capacity [69]. A recently proposed fixed scale optical wireless MIMO architecture [70], relaxes these constraints by sending data directly in angle rather than in space and has been characterized in a free-space channel.

For UWOC channels, little work has been done on the design of non-imaging MIMO systems [4]. In [26], a 2 × 2 MIMO system was investigated under the effects of SICI and with perfect alignment and fixed length are assumed. In [39, 64], the capacity of a buoy based downlink is studied considering the impacts of misalignment induced by the wavy surface of seawater. The capacity of a 2×2 MIMO non-imaging system is characterized for different misalignment conditions at different wind speeds. In a follow-up paper, Zhang *et al.* evaluated the performance of 3×2 MIMO buoy-based downlink capacity considering turbulence, scattering and misalignment impairments [39, 64]. However, to our best knowledge, there has been no work to date on the development of imaging transceivers for UWOCs. In UWSNs, autonomous underwater/remotely operated vehicles (AUVs/ROVs) are used to communicate with fixed/floated sensor nodes for data harvesting purposes. In these kinds of UWSNs, channels are dynamic due to acoustic waves, mobility of AUVs/ROVs and motion of sensor nodes. Accordingly, it is difficult for C-MIMO to provide a reliable communication link for such applications.

In this paper, motivated by [70], we propose an imaging angular MIMO (A-MIMO) architecture for UWOC for potential application to UWSNs. The A-MIMO system transmits data in the angular domain, and has a fixed magnification regardless of channel length, and it is robust against off axis transmission. The architecture is briefly reviewed, and channel modelling of angle of arrival is shown using numerical simulations. Also, the capacity of A-MIMO systems is contrasted with C-MIMO in a realistic setting in clear and coastal seawater channels.

The balance of the paper is organized as the follows. In Section 2.2, the model of A-MIMO architecture is introduced and compared with C-MIMO. Section 2.3 presents the channel modelling of A-MIMO, modelling assumptions and the link capacity. In Section 2.4, the distributions of arrival angles for A-MIMO system are obtained numerically using a Monte Carlo ray tracing (MCRT) solver [86]. Also, the numerical

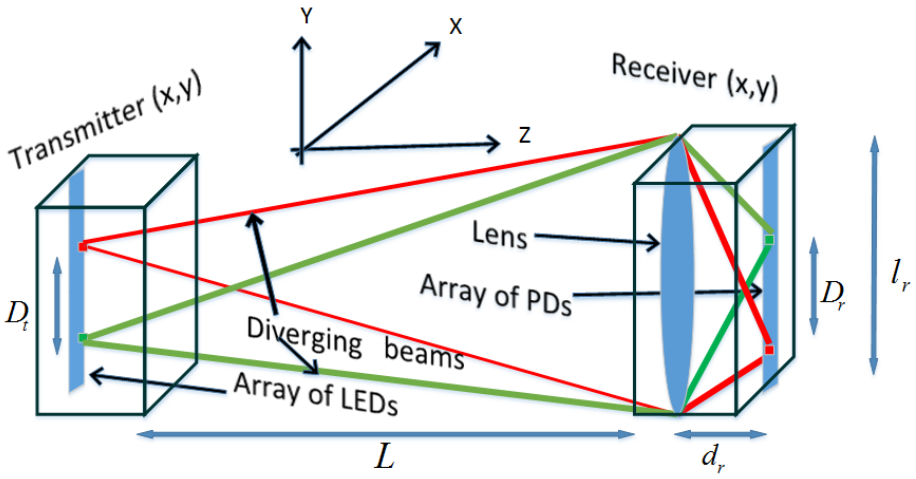

Figure 2.1: Conventional MIMO (C-MIMO) architecture.

results of link capacity of A-MIMO and C-MIMO systems are provided for clear and coastal seawaters under misalignment (off axis transmission) and dynamic channel length conditions.

2.2 Angular MIMO (A-MIMO) System

In general, MIMO optical wireless systems are implemented using an array of LDs emitters and PDs in the transmitter and receiver respectively. Figure 2.1 shows the setup of the C-MIMO system. The transmitter consists of an array of M_t LDs spaced on a square grid with spacing D_t between the centre of the emitters. Similarly, the receiver is implemented by a square array of M_r PDs spaced D_r apart from centre-to-centre. A convex lens of focal length f_r and diameter l_r is placed at distance $d_r = \frac{f_r L}{f_r - L}$ from the array to produce an image on the photodetectors. Assuming a thin lens, the

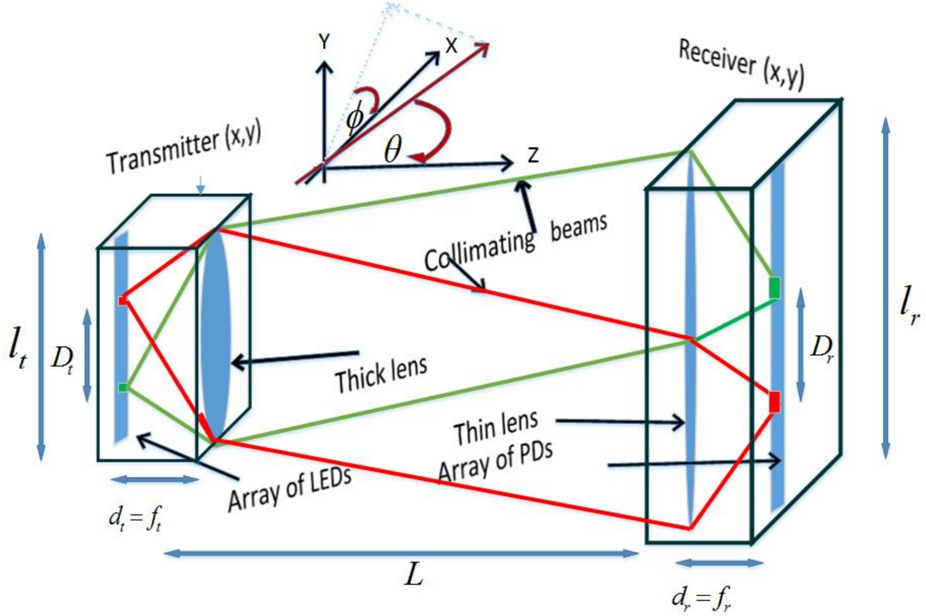

Figure 2.2: Angular MIMO (A-MIMO) architecture.

magnification, M_C is calculated as [87]

$$M_C := \frac{D_r}{D_t} = \frac{f_r}{L - f_r}. \tag{2.2.1}$$

where L is the channel length. Notice that the magnification is inversely proportional to the channel length when $L >> f_r$. Therefore, the scale of the image (i.e., the projection of the LDs array on the PD array) varies according to changes in L which leads to SICI. In order to avoid SICI, C-MIMO systems require a fixed distance and perfect alignment between the transmitters and receivers which is difficult to achieve between AUVs/ROVs and floating sensor nodes in UWSNs.

A fixed scale MIMO scheme has been proposed for imaging MIMO optical wireless systems which offers a fixed magnification (regardless the channel length) and reduces the requirements of on-axis transmission [70]. Figure 2.2 shows the setup of an A-MIMO system, where the transmitter is implemented by an array of M_t LDs with a collimating lens with diameter l_t and focal length f_t located at distance $d_t = f_t$ from the LDs array as shown. Also, the receiver is realized by an array of M_r PDs with an imaging lens of diameter l_r and focal length f_r located at distance $d_r = f_r$ from the LDs array as shown in the figure. In A-MIMO, the magnification in this configuration is fixed and equal to [87]

$$M_A := \frac{D_r}{D_t} = \frac{f_r}{f_t}. \tag{2.2.2}$$

Clearly, the magnification does not change with channel length. This is a key advantage of A-MIMO systems over C-MIMO systems as SICI is avoided because of the fixed magnification. Also, angular rather than spatial transmission provides inherent robustness to off axis transmission for this architecture. The A-MIMO architecture resembles an extended microscope objective where the receiver is focused at infinity. Alternatively, one may view the transmit lens as performing space-to-angle mapping while the receive lens performs the inverse operation [70]. Precisely, the transmit lens maps the i^{th} LD (position x,y) into associated launch polar and azimuth angles $(\theta_{0,i}, \phi_{0,i})$. The transmitter sends a collection of collimated (cylindrical) beams to the receiver at different polar and azimuthal angles for every $i \in \{1, 2, ..., M_t\}$, as shown in the Fig. 2.2. The receiver lens can be thought of doing the inverse mapping, i.e, from angle to space. That is, the arriving collimated beams from angles (θ_j, ϕ_j) are mapped to the associated j^{th} PDs (positions x,y), where $j \in \{1, 2, ..., M_r\}$. This mapping (position to angle and vice versa) offers fixed location for the image on the receiving plane based on the angle of reception regardless on or off axis transmission. Therefore, misalignment in the xy-plane between transmitter and receiver axis does not lead to SICI problems.

On the other hand, while the scale of the image on the receive plane is preserved in A-MIMO, the number of channels available will scale as the angular subtense of the receiver from the transmitter decreases with range. This is termed *truncation by windowing*, and the window area of the received image, A_w, is given by [70]:

$$A_w = \pi \times \frac{(f_r\ (l_r + l_t))^2}{4\ L^2}. \tag{2.2.3}$$

This equation shows that increasing the channel length leads to decreasing the window area and this generates the image truncation, which causes in reduction of the link capacity. According to Eq. (2.2.3), for given transceiver setting with square array ($\sqrt{M_t} \times \sqrt{M_t}$) of LDs and square array ($\sqrt{M_r} \times \sqrt{M_r}$) of PDs, the primitive channel length is upper bounded by:

$$L \leq \frac{f_r\ (l_r + l_t)}{D_r\ \sqrt{M_r}} = \frac{f_t\ (l_r + l_t)}{D_t\ \sqrt{M_t}} \tag{2.2.4}$$

within this range, image of the LDs array is fully projected on PDs array without image truncation. Clearly, the use of larger focal length and large transmitter/receiver aperture diameters partially mitigates this problem, at the cost of implementation complexity.

2.3 Channel Modelling and Link Capacity

2.3.1 Context

In A-MIMO, each LD transmits data in unique polar and azimuth angles while the PDs at the receiver are associated with particular range of received angle according to its detection area. Thus, data are transmitted in different angles between the transmitter and receiver. However, the impurities of seawater distort and alter direction of propagation of the emitted beams.

Physically, seawater scatters light due to dissolved organic and non-dissolved inorganic matters. In non-pure seawater conditions, particles scatter the emitted collimated beams in A-MIMO systems in random directions potentially limiting system performance. This randomization of angles of arrival caused by scattering can lead to SICI in detection, resulting in a reduction in channel capacity and link availability. Thus, the statistics of angle of arrival for each emitted stream are essential to quantify the performance of A-MIMO systems. Accordingly, in this section, the power distributions in polar and azimuth arrival angles for given launch angles $\theta_{0,i}$ and $\phi_{0,i}$, $P_i(\theta|\theta_{0,i})$ and $P_i(\phi|\phi_{0,i})$, are investigated.

In previous work, there exist models of time and spatial arrival of aquatic communication environments using MCRT, quasi-analytic models, radiative transfer equation (RTE) and stochastic models [4]. Some authors have developed practical equations that can be used in MCRT to generate trusted results [28]. Also, [88] provides a comprehensive stochastic model of channel impulse response at different water conditions and transceiver parameters. In [89], authors use RTEs in order to calculate the path loss. Also, [66] shows the channel impulse response of shadowing and blockage channel by using a commercial optics solver. However, to the best of our knowledge, there is no existing work characterizing the angular arrival statistics in an underwater setting. In the following subsections, the distributions of arrival angle and MIMO link capacity are obtained by using a commercial MCRT tool [86].

2.3.2 Aquatic Channel Characteristics and Angle of Arrival Distributions

Impurities in water such as organic and solid matters cause absorption and scattering of the emitted optical signals. As is conventional in such channels, define the absorption cofficient a and scattering coefficient b with albedo defined as $w = b/c$ and total extinction $c = a + b$ [28]. Notice that the albedo is a first order measure of the reduction in channel bandwidth while c quantifies the total power loss due to absorption and scattering.

In low albedo environments ($w < 1$) (i.e., pure seawater), the aquatic channel offers low scattering of the collimated beams for A-MIMO systems. In this case, the arrival angle distribution for given launching angle can be well approximated following Beer-Lambert law as

$$\begin{aligned} P_i(\theta|\theta_{0,i}) &= \sum_{i=1}^{M_t} P_{t,i}\ G_i\ \exp\left[\frac{-Lc}{\cos(\theta_{0,i})}\right]\delta(\theta-\theta_{0,i}) \\ P_i(\phi|\phi_{0,i}) &= \sum_{i=1}^{M_t} P_{t,i}\ G_i\ \exp\left[\frac{-Lc}{\cos(\theta_{0,i})}\right]\delta(\phi-\phi_{0,i}) \end{aligned} \tag{2.3.1}$$

where, G_i and $P_{t,i}$ are the geometric loss and transmitted optical power associated by i^{th} LED respectively.

In the case of higher albedo ($w > 1$), as in non-pure water, the scattering components become dominant. This case is typical in most coastal and turbid seawater conditions. In this case, the angle of the scattered light is randomized according to the phase scattering function, $B(\theta)$, of the seawater. There are many forms for $B(\theta)$ to model the scattering polar angle θ. A popular and tractable model for $B(\theta)$ is the one term Henyey-Greenstein (OTHG) model and is defined by [90]

$$B(\theta) = \frac{1-g^2}{4\pi(1+g^2-2g\cos(\theta))^{(3/2)}} \ , \quad g = \overline{\cos(\theta)} \tag{2.3.2}$$

where, g depends on the water type. The azimuthal angle of scattering, ϕ, is assumed to be uniform following [91], that is,

$$p(\phi) = \frac{1}{2\pi}. \tag{2.3.3}$$

At high attenuation length (i.e., large Lc), multiple scattering events take place. That is, a photon may scatter multiple times between the transmitter and receiver. Each scattering event further increases the randomness in the arrival angle. Additionally, scattering leads to the likelihood of additional loss (i.e., weight reduction in the MCRT by $W_{k+1} = b/c \cdot W_k$, where $W_0 = 1$ [91]). It can be shown that the propagation distance, η, between the consecutive scattering events is well modelled by the negative exponential distribution [91]

$$p(\eta) = c \ \exp(-c \ \eta). \tag{2.3.4}$$

Accordingly, four computational steps describe the ray tracing from transmitter to receiver in the aquatic channel via the MCRT algorithm: travel distance, polar angle of scattering, azimuth angle of scattering and weight loss. At each step, a random variable is generated according to its associated distribution Eqs. (2.3.2-2.3.4). In the following section, the angle of arrival distributions for A-MIMO link is obtained in clear and coastal seawaters by using an MCRT solver [86].

2.3.3 Link Capacity of MIMO System

MIMO systems add degrees of freedom to the aquatic channel thereby increasing channel capacity and have been considered in underwater environments for high speed communication [39, 64]. Given the small wavelength of light relative to radio systems, there is the potential to integrate large arrays of transmitters and receivers resulting in larger gains using the added degrees of freedom in MIMO optical wireless systems [40]. In this work, the UWOC is modelled as linear with additive noise MIMO receiver, the received electrical current is given by

$$Y = \Re\ H\ X + n \tag{2.3.5}$$

where, Y is received electrical current vector ($M_r \times 1$), $\Re$ is receiver responsitivity, H is gain matrix of the channel ($M_r \times M_t$), X is transmitted optical power vector ($M_t \times 1$) and n noise vector ($M_r \times 1$). For simplicity, we assume that the total transmitted power P_t is equally divided between all LDs. To estimate the capacity of this link, consider the capacity of the Gaussian noise channel where n is modelled as zero mean independent identical Gaussian noise [39, 64]

$$C = \frac{1}{2}\ \log_2 \left(\det \left[I + \left(\frac{\Re\ P_t}{M_t \sigma_n} \right)^2 H\ H^T \right] \right) \tag{2.3.6}$$

in bits/channel use, where I is identity matrix $(M_r \times M_r)$, σ_n^2 noise variance and H^T is transpose of H.

The additive white Gaussian noise (AWGN) MIMO capacity in (2.3.6) is an accurate estimate when the non-negativity constraint of the channel is satisfied by a sufficient bias signal and non-linear clipping noise is minimized. Notice that the capacity in (2.3.6) will depend on the spacing between LDs/PDs in transmitter/receiver $\{D_t, D_r\}$, the radiation profile of LDs, the field-of-view (FOV) of PDs and the attenuation and scattering of the aquatic channel. In the following section, the channel gain matrix H of A-MIMO and C-MIMO systems are computed by using an MCRT solver and their capacities compute via Eq. (2.3.6) are contrasted.

2.4 Numerical Results

2.4.1 Context

A commerical MCRT solver [86] is used to calculate the numerical results of underwater propagation. In an MCRT simulation, optical rays are propagated from the source to the receiver according to the distributions of seawater, Eqs. (2.3.2-2.3.4), and using system parameters that are shown in Table 2.1. In all cases a 9×9 A-MIMO and C-MIMO setup is considered in both clear and coastal seawaters with a nominal link length $L \approx 5$ m. The associated parameters for clear and coastal seawaters are

Table 2.1: Parameters of MCRT Set up for A-MIMO and C-MIMO systems

Transmitter parameters	**C-MIMO**	**A-MIMO**
Diameter of the lens (l_t)	N/A	0.1 m
Focal length of the lens (f_t)	N/A	0.365 m
No. of LDs (M_t)	9	
Distance between the centres of the LDs (D_t)	0.1 m	0.01 m
Distance between LEDs array and the lens (d_t)	N/A	0.365 m
Optical transmitted power (P_t)	1 W	
Working wave length	532 nm	
Gaussian Beam waist	5.5 mm	
Divergence angle of Gaussian Beam	2^o	
Receiver parameters	**C-MIMO**	**A-MIMO**
Diameter of the lens (l_r)	0.5 m	
Focal length of the lens (f_r)	0.72 m	0.365 m
No. of PDs (M_r)	9	
Distance between the centres of the PDs (D_r)	0.01 m	
Distance between PDs array and the lens (d_r)	0.5 m	0.365 m
Receiver field of view (FOV)	180^o	
Receiver responsitivity ($\Re$)	0.8 A/W	
Thermal noise variance (σ^2)	10^{-6} A^2	
Channel parameters	**Clear**	**Coastal**
Water absorption (a)	0.07 m^{-1}	0.089 m^{-1}
Water scattering (b)	0.08 m^{-1}	0.216 m^{-1}
Channel length (L) range	$1 - 9$ m	

taken from earlier work [4]. In this section, angle of arrival distributions are obtained for A-MIMO in different seawater conditions. Additionally, the channel matrix H for C-MIMO and A-MIMO is computed, and the capacity is estimated according to Eq. (2.3.6) for clear and coastal seawaters channels.

2.4.2 C-MIMO and A-MIMO System Setups

In order to have a fair comparison between C-MIMO and A-MIMO systems, the parameters of LD sources, lens of the receiver ($l_r = 0.5$ m) and the total PD detection area ($D_r^2 = 1$ cm^2) are the same in both systems as shown in the table. For C-MIMO, the spacing of the transmitter LDs is set to 0.1 m to ensure an overall detection area is less than 0.3×0.3 m^2. According to Eq. (2.2.1), the focal length of the receiver lens in C-MIMO and the position of the receiver d_r are selected to ensure that image is projected on the PDs array for the nominal transmission distance $L \approx 5$ m. For the A-MIMO system, the overall magnification of the system is set to be unity and $D_r = D_t$. Also, $f_r = f_t$ and $(l_t + l_r)$ of the lenses are set to project the transmitted image on the receiver without truncation (windowing effect) for the channel range $L < 7.5$ m, according to Eq. (2.2.4). This setting gives C-MIMO an advantage over A-MIMO since the spacing of transmitters is larger in the conventional case giving rise to less SICO at the receiver.

2.4.3 Results: Distributions of Angle of Arrival

As shown in Fig. 2.2, for the A-MIMO system each of nine LDs launches a collimated beam with associated polar and azimuth angles toward the receiver (i.e, position to angle mapping). Figures 2.3 and 2.4 shows the distributions of polar and

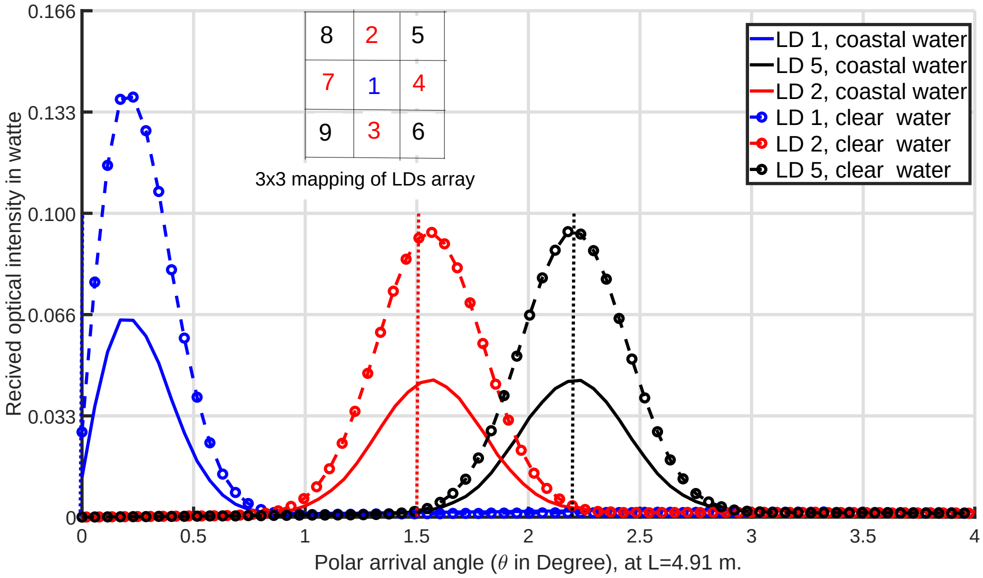

Figure 2.3: Distributions of arrival polar angle for nine LDs of 9×9 A-MIMO system in clear and coastal water channels at L=4.91m. Also, mapping of the LDs on the transmitter array is shown.

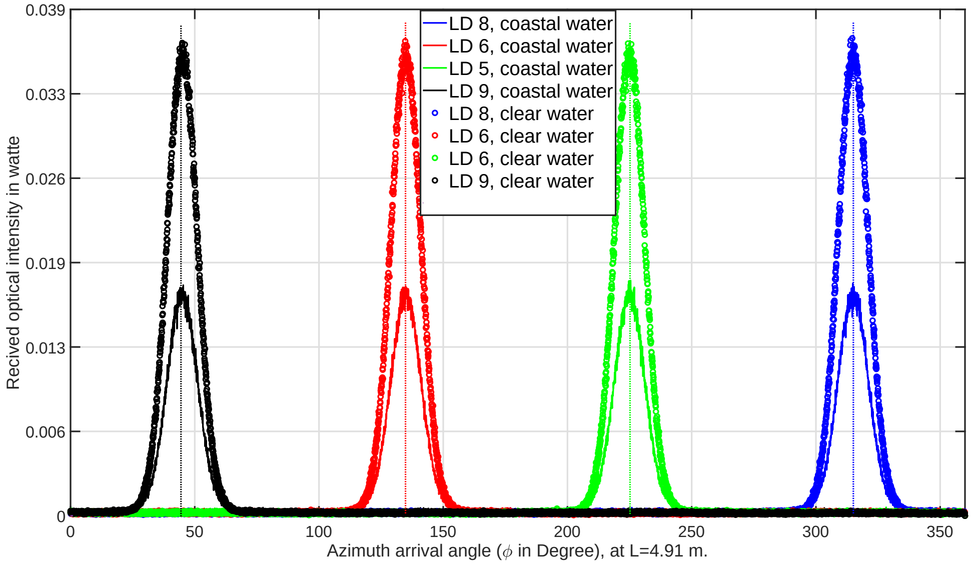

Figure 2.4: Distributions of arrival azimuth angle for LDs No. $\{5, 6, 8, 9\}$ of 9×9 A-MIMO system in clear and coastal water channels at L=4.91m.

azimuthal arrival angles as simulated on the normal of receiver lens and at nominal channel length of 5 m. From the figures, the peaks indicate the line-of-sight (LOS) components in both polar and azimuth angles. However the dispersion of these distributions is due to the multiple scattering components ($w > 1$). Also, the angles are more dispersed in coastal seawater channel compared to clear seawater channel. Clearly, the coastal seawater induces a relative larger distortion in the received angular signal with a larger power loss. Thus, the probability of SICI problems are less in clear seawater channel and this reflects on the capacity performance, as discussed in the following subsection. LD 1 is located on the centre of the transmitter array, and launches at $0°$ polar angle and null azimuth angle. LDs $\{5, 6, 8, 9\}$ are located on the same outer circle on x-y plane, therefore they launch beams at the same $2.21°$ polar angle, as indicated in the peak of the black curve in Fig. 2.3. However, those four LDs launch the beams at different azimuth angles of $\{225°, 135°, 315°, 45°\}$ respectively, as shown in the peaks of the curves of Fig. (2.4). Also, LDs $\{2, 3, 4, 7\}$ are located on the same inner circle and launch their collimated beams at a $1.5°$ polar angle, as shown in the peak of the red curve in Fig. 2.3, and azimuthal angles $\{270°, 90°, 180°, 0°\}$ respectively. Notice also that the received signal is relatively larger for those LDs near the optical axis (i.e. LD 1) and decreases as distance from the axis increases (i.e., θ increases).

2.4.4 Results: Link Capacity

Figures 2.5 and 2.6 show the capacity performance for the 9×9 A-MIMO and C-MIMO systems versus changes in channel length in z-axis and misalignment in the y-axis respectively.

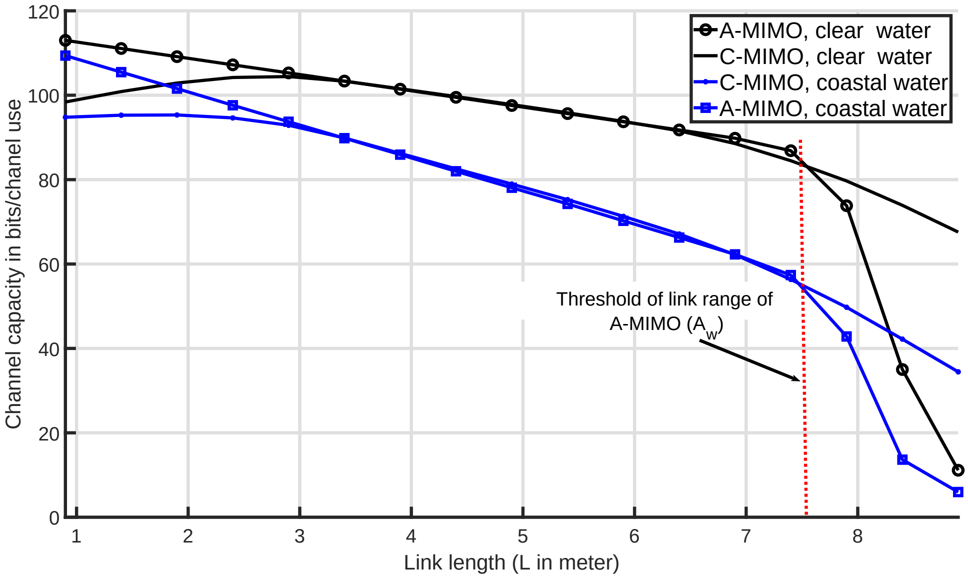

Figure 2.5: System capacity of 9×9 A-MIMO and C-MIMO architectures versus the variation in channel length ($1\ m \leq L \leq 9\ m$) in clear and coastal seawater channels.

Figure 2.5 shows the capacity behaviour for clear and coastal seawaters channels when both transmitter and receiver and aligned on-axis.

Notice that for $L < 7.5$ m, A-MIMO has performance similar or marginally better than C-MIMO. The C-MIMO is designed for a given distance (5 m) and defocusing errors limit the long term performance. Notice also that A-MIMO suffers from window truncation beyond $L = 7.5$ m which greatly limits performance. Numerically at $L = 2$ m, A-MIMO and C-MIMO achieve $C_{\text{A−MIMO}} = 110$ bits/channel use and $C_{\text{C−MIMO}} = 105$ bits/channel use in clear seawater, and $C_{\text{A−MIMO}} = 100$ bits/channel use and $C_{\text{C−MIMO}} = 95$ bits/channel use in coastal seawater. The capacity of A-MIMO is nearly the same as C-MIMO for the ranges of interest.

Figure 2.6 presents the capacity at $L \approx 5$ m, shows the capacity variation for C-MIMO and A-MIMO systems with a misalignment of the optical axes of Δy. The

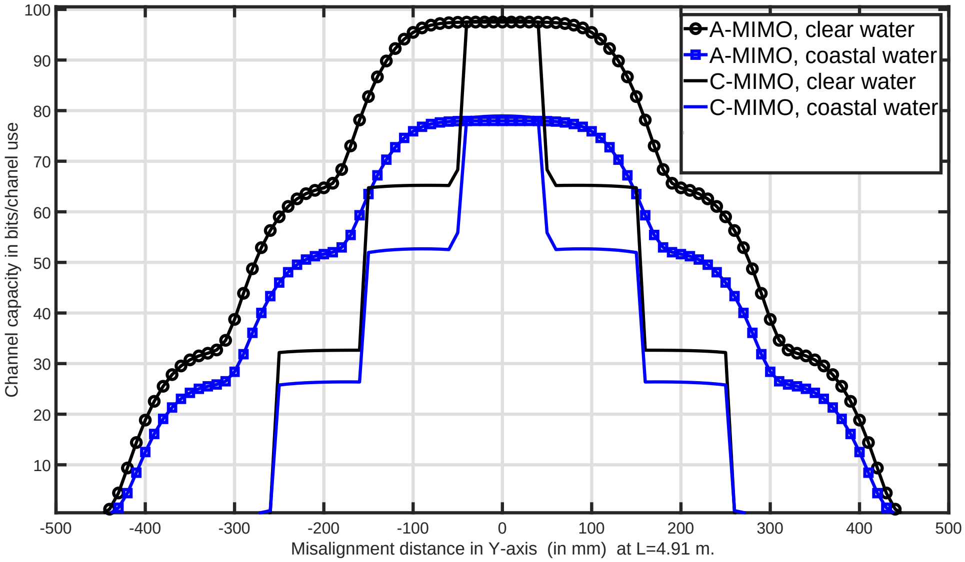

Figure 2.6: System capacity of 9×9 A-MIMO and C-MIMO architectures versus the misalignment in y-axis (or x-axis) in clear and coastal seawater channels at $L = 4.91\ m$.

capacity is nearly the same between A-MIMO and C-MIMO in when aligned, i.e., $\Delta y = 0$. Additionally, the performance is symmetric in Δy axis due to the symmetry of the design of A-MIMO and C-MIMO architectures on the centre of the coordinate $(x = 0\ , y = 0)$. When $\Delta y \neq 0$, the capacity of C-MIMO links more severely impacted than for A-MIMO for both seawater conditions. The reduction in the link capacity of C-MIMO system is due to the sensitivity of this architecture to misalignment. However, the reduction in the link capacity of A-MIMO system due to image truncation in y-axis. Notice that the results in Fig. 2.6 apply equally well to the case of misalignments in the x-axis due to the symmetry of the setup. Numerically, A-MIMO and C-MIMO achieve $C_{\text{A}-\text{MIMO}} = C_{\text{C}-\text{MIMO}} = 97$ bits/channel use in clear seawater, and achieve $C_{\text{A}-\text{MIMO}} = C_{\text{C}-\text{MIMO}} = 78$ bits/channel use in coastal seawater, at $\Delta y = 0$. Notice that for misalignment $\Delta y = 0.05$ m, A-MIMO maintains the its capacity, however the capacity of C-MIMO is more sensitive to misalignment and drops to $C_{\mathrm{C-MIMO}} = 67$ bits/channel use and $C_{\mathrm{C-MIMO}} = 52$ bits/channel in clear and coastal seawaters respectively. Also, link availability of C-MIMO is dropped at $\Delta y \geq 0.25\, m$, while the link availability of A-MIMO link is dropped at $\Delta y \geq 0.45\, m$ in clear and coastal seawaters as shown.

In general, at the same transmitted power, seawater conditions, and receiver noise, the proposed 9×9 A-MIMO architecture offers higher capacity performance in dynamic environments in contrast to C-MIMO system. Also, this improvement is achieved at smaller transceiver size, as shown in the table, which reflects on system feasibility. Thus, A-MIMO is recommended as a new imaging MIMO candidate for data harvesting purposes in UWSNs. In practice, the dimensions of the 9×9 A-MIMO system considered here are comparable to similar payloads already integrated on current ROVs [92].

2.5 Conclusions

In this paper, an angular imaging MIMO architecture has been proposed in contrast to conventional imaging MIMO architecture for UWSN. In angular MIMO, the information is associated to angle rather than position. This approach has many inherent benefits including fixed scale imaging and robustness to misalignment errors. These advantages may be essential to realizing efficient imaging MIMO links in dynamic seawater channels for data harvesting purposes in UWSNs. Also, the distributions of angle arrivals has been shown numerically using an MCRT technique. The results have shown that angular MIMO has maintained the link capacity against misalignment and channel length variations in contrast to conventional MIMO systems. Ongoing work includes testing A-MIMO in a practical scenarios of sea wave motion as well as improved analytical modelling of the angle of arrival distributions for A-MIMO.

Chapter 3

Angular MIMO for Underwater Wireless Optical Communications: Link Modelling and Tracking

In Chapter 2, A-MIMO systems are simulated with considering for multiple scattering. Due to the challenge of multiple scattering, no analytical model is provided for A-MIMO links. A-MIMO systems are also evaluated using low resolution imaging MIMO links (i.e., 9×9). Capacity performances are only evaluated under instantaneous displacement and length variations; however, capacity performances are not evaluated under inclination and rotation conditions. In this chapter and motivated by the promising results shown in Chapter 2, A-MIMO systems are investigated with more deep insight and simulated under more practical conditions. This chapter introduces two significant contributions; a new tracking scheme is added to A-MIMO systems to yield TA-MIMO systems to provide more reliable communications. Comprehensive analytical models are also derived for A-MIMO and TA-MIMO links assuming single scattering. In addition to the advantages mentioned in Chapter 2, TA-MIMO links offer the advantage of high-speed communications with tracking by utilizing their imaging receivers. The tracking advantage is inherited from the optical architecture of the systems, and it yields a simple and accurate tracking scheme, namely, the PLT scheme. The PLT scheme is modeled and tested under realistic F2B and F2M scenarios. For simple analysis, closed-form expressions are derived for AoA distributions. The closed-form expressions are verified numerically using a MCNRT method. The average channel capacity is shown for high-resolution imaging MIMO link, 49 × 49 link, contrasting C-MIMO, A-MIMO, and TA-MIMO systems in clear and coastal seawater.

Appendix A shows further details for the closed-form expressions of AoA distributions.

This chapter's work appears in the *IEEE Journal of Oceanic Engineering, (Pages: 1-17, January 2021) [9].* IEEE owns the copyright of the material in **this chapter** and **Appendix A**, and it is permitted to be re-used in the thesis.

Abstract Angular imaging multiple-input/multiple-output (A-MIMO) is investigated for short-range, high-speed underwater wireless optical communications (UWOCs) where, unlike conventional imaging MIMO (C-MIMO), data are transmitted in an angle rather than in space. In this approach, the strict requirements of on-axis alignment and fixed channel length are relaxed. This technique also allows for simpler estimation of the relative misalignment between the transmitter and the receiver from the received image. For the first time, we derive a comprehensive model for the underwater A-MIMO link by taking into account link misalignment, background noise, as well as seawater absorption and scattering. Power distributions at the receiver are modeled by the angle-of-arrival (AoA) of the received signal on the lens and its position-of-arrival (PoA) on the focal plane of the detector. We further propose and model a tracked A-MIMO (TA-MIMO) system that maintains the alignment between the two ends of the link, for which the distribution of the residual tracking error is calculated. The UWOC channel capacity is then estimated for buoyed-to-fixed (B2F) (which has dominant angular misalignments) and mobile-to-fixed (M2F) (which has dominant off-axis misalignment) communication scenarios. Numerical results indicate that in the B2F scenario, A-MIMO is sensitive to angular misalignments; however, TA-MIMO outperforms C-MIMO. In the case of M2F links, A-MIMO greatly outperforms C-MIMO when off-axis misalignments are present. This work serves as a design guide to determine the selection of A-MIMO, TA-MIMO or C-MIMO receivers depending on the misalignment conditions for a particular underwater application.

3.1 Introduction

Underwater acoustic communication is an intrinsically low data-rate transmission technology, offering communication speeds on the order of kilobits/second (kbps). Underwater wireless optical communication (UWOC) is a promising candidate for high data-rate applications with rates that can approach gigabits/second (Gbps)[4, 17, 93, 94]. This technology takes advantage of the directivity of optical beams, low energy consumption, and relatively small size transceivers inherent to free-space optics. However, the capacity of UWOC links is in practice limited by the high optical beam attenuation in seawater and the limited bandwidth of the opto-electronic components [5, 95]. The use of multiple-input multiple-output (MIMO) techniques in underwater scenarios is one possible avenue to address some of these isseus. A MIMO optical wireless system is implemented using an array of emitters and detectors at the transmitter and receiver, respectively. Leveraging spatial and temporal degrees of freedom, such optical wireless MIMO systems increase the system capacity. In addition, will properly spaced emitters such systems can transmit larger total optical power due to the extended nature of the source while remaining eye-safe. However, the advantages of such MIMO architectures come at the cost of increased system complexity [68, 69].

In atmospheric wireless optical communications links, imaging MIMO has been proposed for high-speed short-range indoor applications [68]. A typical imaging MIMO configuration, termed here conventional MIMO (C-MIMO), consists of an array of emitters and an imaging receiver. In [40], Zeng *et al.* evaluated the performance of imaging and non-imaging MIMO systems, showing the potential of the former in reducing spatial inter-channel interference problems. However, imaging

MIMO systems require perfect alignment and compensation of changes in magnification due to channel length variations [69]. Recently, a fixed-scale imaging MIMO architecture was proposed in [70] for short-range indoor applications, with robustness against off-axis misalignment as well as fixed magnification, independent of the channel length [70].

Comparatively, little work has been done on the investigation of MIMO approaches for high-speed short range UWOC links [4]. In [26], a 2×2 non-imaging MIMO system was investigated considering the impact of inter-channel interference. However, perfect alignment and a fixed channel length were assumed. In [39, 64], the capacity of a buoy node was studied focusing on the impact of misalignment induced by sea waves at different wind speeds. In a follow-up paper [39, 64], the capacity of a 3×2 non-imaging MIMO buoyed node was investigated under turbulence, scattering and misalignment impairments. For underwater imaging MIMO systems, Li *et al.* [41] showed the effect of inter-spacing between laser diodes (LDs) and photo-detectors (PDs) on the performance of a 2×2 imaging C-MIMO link over 2.4 m under perfect alignment conditions. A common thread through these studies is that severe misalignment losses due to sea waves or currents are identified as key impairments to C-MIMO UWOC links.

Recently, Xu *et al.* [96] and Ghazy *et al.* [8] applied the fixed-scale architecture of [70] to UWOC links. In particular, the authors in [96] numerically quantified the bit-error rate (BER) performance of the fixed scale MIMO system underwater over a 1 m range. In [8], Ghazy *et al.* proposed angular MIMO (A-MIMO) using the architecture of the fixed-scale MIMO system. There in, the capacity performance of (9×9) A-MIMO and C-MIMO systems are contrasted under off-axis misalignment and variation of a channel length.

For the first time, we extend our work in [8] by deriving a comprehensive model and presenting a design for short-range high-capacity underwater A-MIMO systems where data are transmitted in angle rather than in space. Additionally, a tracking scheme is proposed and its performance quantified using the unique features of the A-MIMO system to yield a tracked A-MIMO (TA-MIMO) system. More specifically, in contrast to [8, 96], here we derive detailed link modelling, which provides useful insight into the design of underwater A-MIMO and TA-MIMO systems from both channel capacity and tracking perspectives. The main contributions of this paper are summarized as follows:

- A comprehensive model for underwater A-MIMO links is derived considering both angle of arrival (AoA) and position of arrival (PoA) distributions.
- Closed-form polar and azimuthal AoA distributions are derived for the central source at on-axis alignment conditions.
- The derived equations for AoA distributions are verified through Monte Carlo numerical ray tracing (MCNRT) simulations [86, 97].
- Based on the optical properties and geometry of the A-MIMO architecture, a new tracking scheme is proposed and modelled, termed pointing-localization-tracking (PLT) scheme, and its efficiency is demonstrated through numerical results.
- The distribution of the tracking residual errors (TRE) is calculated using MC-NRT method for the cases of a buoyed-to-fixed (B2F) communication model.

- For the case of B2F and mobile-to-fixed (M2F) communication scenarios, the average capacity of a 49×49 link using A-MIMO, TA-MIMO, and C-MIMO techniques, are contrasted.

The remainder of the paper is organized as follows. Section 3.2 describes the optical architecture of an A-MIMO link and its intrinsic characteristics. Section 3.3 focuses on A-MIMO link modelling, where AoA and PoA distributions are derived with closed-form expressions for special cases. Section 3.4 presents the capacity of A-MIMO and C-MIMO links under two realistic B2F and M2F communication scenarios. In Section 3.5, intrinsic localization features of A-MIMO systems are demonstrated. A PLT scheme is proposed and TRE distributions are computed using MCNRT. Afterwards, in Section 3.6, the numerical results on link modelling are presented, and the capacity of A-MIMO, TA-MIMO, and C-MIMO links are contrasted for the cases of clear and coastal seawaters. The paper concludes in Section 3.7 with directions for future work.

Notation: In this article, vectors and matrices are denoted by bold-face lower and upper-case letters, respectively. Probability distribution functions are denoted by $p(\cdot)$. A Gaussian random variable with zero mean and σ^2 variance is denoted by $\mathcal{N}(0, \sigma^2)$. Also, the complex conjugate of $G(\cdot)$ is written as $G^*(\cdot)$.

3.2 Angular MIMO

Imaging MIMO systems are well suited to high-speed short-range underwater applications [8, 41, 96]. Practical examples of such links include buoys and autonomous underwater vehicles (AUVs) as will be discussed in Section 3.4. C-MIMO systems require perfect alignment and a fixed magnification between the two ends of the link, which is difficult to maintain in practice [8, 96]. In the following, we present the key advantages of underwater A-MIMO systems that relax these two key impairments of C-MIMO.

3.2.1 Description of A-MIMO Systems

Consider a general $(M_t \times M_r)$ A-MIMO structure. At the transmitter, M_t LDs are used, arranged on a square array of $(\sqrt{M_t} \times \sqrt{M_t})$, with the spacing D_t between the centres of the LDs. The centre of the m_t^{th} LD, $m_t \in (1, 2, ..., M_t)$, is obtained by $\dot{x}_{m_t} = D_t\,(2\,i - (\sqrt{M_t} + 1))$ and $\dot{y}_{m_t} = D_t\,(2\,j - (\sqrt{M_t} + 1))$. Note that m_t is related to $\{i, j\} \in (1, 2, ..., \sqrt{M_t})$ through $m_t = (j + (i - 1)\,\sqrt{M_t})$. Likewise, at the receiver, located at a nominal range of L_o, the M_r PDs are arranged on a square array of $(\sqrt{M_r} \times \sqrt{M_r})$, with spacing D_r between their centers. The centre of the m_r^{th} PD, $m_r \in (1, 2, ..., M_r)$, is given by $\dot{x}_{m_r} = D_r\,(2\,i - (\sqrt{M_r} + 1))$ and $\dot{y}_{m_r} = D_r\,(2\,j - (\sqrt{M_r} + 1))$. Here, m_r is related to $\{i, j\} \in (1, 2, ..., \sqrt{M_r})$ by $m_r = (j + (i - 1)\,\sqrt{M_r})$. Figures 3.1 and 3.2 illustrate the system architecture of a (3×3) A-MIMO link for the two cases of perfectly-aligned and misaligned transmitter and receiver, respectively (we have taken $M_t = M_r = 3$ just to simplify the illustration). The receiver axes (X_r, Y_r, Z_r) are fixed at $(0, 0, 0)$ and considered as reference. The considered transmitter axes (X_t, Y_t, Z_t) are then either aligned or misaligned. The definition of the different parameters, angles, etc. are summarized in Table 3.1.

At the transmitter, the LD array produces an image $g_t(\dot{x}_t, \dot{y}_t)$, where $(\dot{x}_t, \dot{y}_t)$ is the position in the plane of the LD array. Moreover, a convex lens (e.g., a Fresnel lens) with focal length f_t and diameter l_t is placed at a distance d_t from the array, where $d_t = f_t$. This lens collimates the beam of the m_t^{th} LD and transmits it in the direction

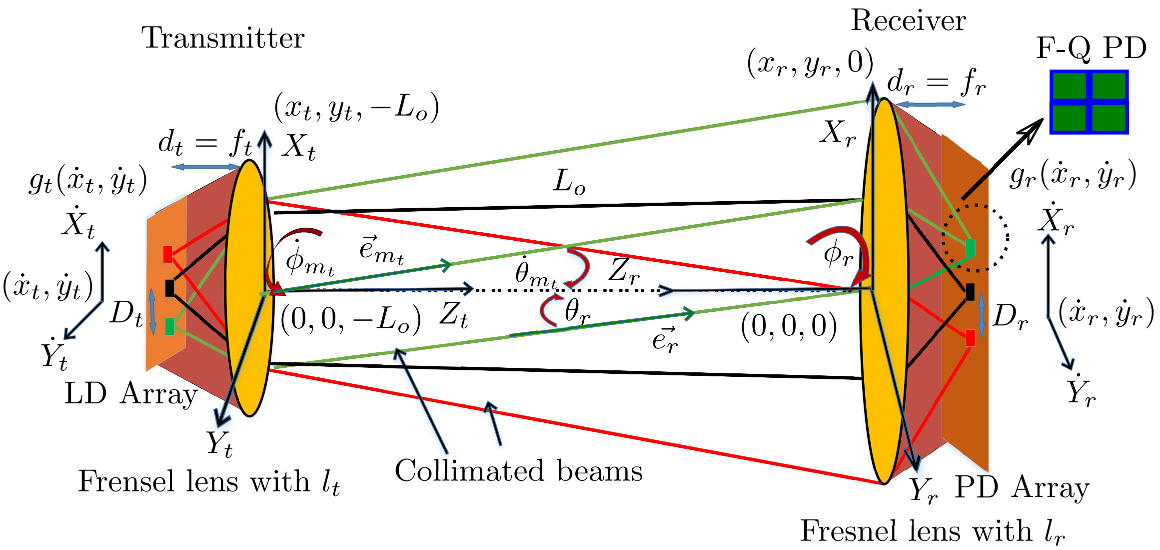

Figure 3.1: Architecture of a 3 × 3 A-MIMO system with parameters given in Table 3.1.

of the unit vector $\vec{e}_{m_t}$, specified by polar and azimuthal angles ($\dot{\theta}_{m_t}$,$\dot{\phi}_{m_t}$), defined with respect to the transmitter axes. For instance, the transmitted unit vector associated with the green LD is shown by a green arrow in Fig. 3.1. In the transmitter lens plane, each ray is sent from position (x_t,y_t, $-L_o$) according to the receiver axes as shown in the figure.

At the receiver side, a convex lens with focal length f_r and diameter l_r is placed at distance $d_r = f_r$ from the PD array. The incident ray arrivals at position (x_r,y_r, 0) are shown in Fig. 3.1. The lens receives each beam with direction along with the unit vector $\vec{e_r}$, specified by polar and azimuthal angles (θ_r,ϕ_r). Then, the lens projects the received image $g_r(\dot{x}_r, \dot{y}_r)$ on the PD array, i.e., the ($\dot{x}_r$,$\dot{y}_r$) plane. For tracking purposes, each pixel (i.e., PD) in the array is oversampled by a factor of D_r^2/δ^2, where δ indicates the inter-spacing between the sub-pixels (i.e. sub-PDs). For instance, as illustrated in Fig.3.1, the PD is oversampled by a factor of 4, using a 2 × 2 sub-PD

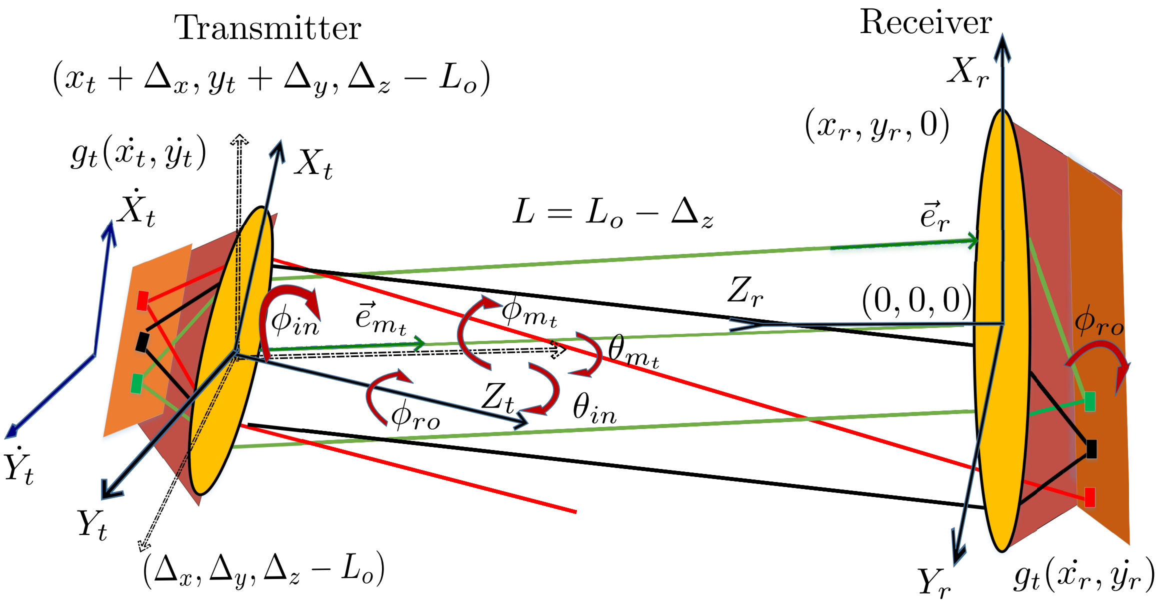

Figure 3.2: Beam axes and orientations for the case of a misaligned 3 × 3 A-MIMO system. The definition of the different parameters are provided in Table 3.1.

array. Such a PD is known as four-quad (F-Q) PD, commonly used for tracking purposes [98].

Consider Fig. 3.2 which illustrates the case of misaligned system. As shown, the transmitter axes are shifted in three directions by Δ_x, Δ_y, and Δ_z. Also, the orientation of the transmitter axes are misaligned by three angles, namely, polar and azimuthal inclination angles (θ_{in},ϕ_{in}) and rotation angle ϕ_{ro}. Notice that θ_{in}, ϕ_{in} and ϕ_{ro} are the angles between axes Z_t and Z_r, rotation around Z_r, and rotation around Z_t, respectively. This misalignment causes the basis of angle measurements at the transmitter and at the receiver to differ. Thus, though $\vec{e}_{m_t}$ is defined by angles

($\dot{\theta}_{m_t}$,$\dot{\phi}_{m_t}$) relative to the transmitter axes as shown in Fig. 3.1, and it is written as

$$\begin{aligned}\vec{e}_{m_t} &= \vec{x}_t \sin(\dot{\theta}_{m_t})\cos(\dot{\phi}_{m_t}) + \vec{y}_t \sin(\dot{\theta}_{m_t})\sin(\dot{\phi}_{m_t}) \\ &\quad + \vec{z}_t \cos(\dot{\theta}_{m_t}),\end{aligned} \tag{3.2.1}$$

$\vec{e}_{m_t}$ is also characterized by angles (θ_{m_t},ϕ_{m_t}) relative to the receiver axes as shown in Fig. 3.2, and can be equivalently written as

$$\begin{aligned}\vec{e}_{m_t} &= \vec{x}_r \sin(\theta_{m_t})\cos(\phi_{m_t}) + \vec{y}_r \sin(\theta_{m_t})\sin(\phi_{m_t}) \\ &\quad + \vec{z}_r \cos(\theta_{m_t}),\end{aligned} \tag{3.2.2}$$

where ($\vec{x}_t$, $\vec{y}_t$, $\vec{z}_t$) and ($\vec{x}_r$, $\vec{y}_r$, $\vec{z}_r$) are the unit vectors relative to the axes of the transmitter and the receiver, respectively. Similarly, the received direction vector can be expressed as

$$\vec{e}_r = \vec{x}_r \sin(\theta_r)\cos(\phi_r) + \vec{y}_r \sin(\theta_r)\sin(\phi_r) + \vec{z}_r \cos(\theta_r). \tag{3.2.3}$$

3.2.2 Characteristics of Angular MIMO Systems

Though C-MIMO systems are similar to their A-MIMO counterparts in architecture, the collimating (i.e. convex) lens at the transmitter of A-MIMO greatly changes system characteristics. In particular, in a C-MIMO system, the magnification [1] of

---

[1] The magnification scale M is given by $M := \frac{I_r}{I_t}$, where I_r and I_t are the length of the received and transmitted images, respectively.

Table 3.1: A-MIMO Link Parameters

M_t	Number of LDs at the transmitter.
D_t	Inter spacing between centres of LDs.
d_t	Distance between LD array and the transmitter lens.
f_t	Focal length of the transmitter lens.
l_t	Diameter of the transmitter lens.
$(\dot{x}_t, \dot{y}_t)$	Location in the plane of LD array relative to the transmitter axis.
$(\dot{x}_{m_t}, \dot{y}_{m_t})$	Center of the ${m_t}^{\text{th}}$ LD.
$g_t(\dot{x}_t, \dot{y}_t)$	Transmitted image.
(x_t, y_t)	Location of the ray on the transmit lens relative to the link axis.
$(\dot{\theta}_{m_t}, \dot{\phi}_{m_t})$	Polar and azimuthal angles of the transmitted beam associated with ${m_t}^{\text{th}}$ LD relative to the transmitter axis.
$(\theta_{m_t}, \phi_{m_t})$	Polar and azimuthal angles of the transmitted beams associated with ${m_t}^{\text{th}}$ LD and relative to the link axis.
M_r	Number of PDs at the receiver.
D_r	Inter spacing between centres of PDs.
d_r	Distance between the PD array and the receiver lens.
f_r	Focal length of the receiver lens.
l_r	Diameter of the receiver lens.
$(\dot{x}_r, \dot{y}_r)$	Location in the plane of PD array relative to the link axis.
$(\dot{x}_{m_r}, \dot{y}_{m_r})$	Center of the ${m_r}^{\text{th}}$ PD.
δ	Inter-spacing between sub-PDs in the PD.
$g_r(\dot{x}_r, \dot{y}_r)$	Received image.
(x_r, y_r)	Arrival positions of the rays in the receiver side relative to the link axis.
(θ_r, ϕ_r)	Polar and azimuthal angles of the received beams relative to the link axis.
L_o	Nominal length of the link.
(Δ_x, Δ_y)	Off-axis between the transmitter axis and the link axis.
Δ_z	Variation in the channel length.
(θ_{in}, ϕ_{in})	Polar and azimuthal inclination angles of the transmitter relative to the link axis.
ϕ_{ro}	Rotation angle of the transmitter around the Z_t axis.

the system will change with the range of the link making the received image larger when the transmitter is close and smaller with it is further away. The magnification for a C-MIMO architecture is given by [87]

$$M_C = \frac{f_r}{L - f_r}, \tag{3.2.4}$$

where $L = L_o - \Delta_z$ is the total channel length. Notice that the magnification is inversely proportional to the channel length when $L >> f_r$. In contrast to C-MIMO, A-MIMO systems have a fixed magnification, given by [87]

$$M_A = \frac{f_r}{f_t}. \tag{3.2.5}$$

This *fixed-magnification* means that the scale of the received image is independent of the link range, which is the first key advantage of A-MIMO systems.

A-MIMO systems can be viewed as transmitting data in the angular domain rather than in space, which is termed *space-to-angle mapping* [70]. As indicated in Fig. 3.1, the transmitter lens maps the beam of m_t^{th} LD at position ($\dot{x}_{m_t}$,$\dot{y}_{m_t}$) to associated polar and azimuthal transmitted angles $(\dot{\theta}_{m_t}, \dot{\phi}_{m_t})$ as

$$\begin{aligned} \dot{\theta}_{m_t} &= \arctan\left(\sqrt{\dot{x}_{m_t}^2 + \dot{y}_{m_t}^2}/f_t\right), \\ \dot{\phi}_{m_t} &= \begin{cases} \arccos\left(\dot{x}_{m_t}/\sqrt{\dot{x}_{m_t}^2 + \dot{y}_{m_t}^2}\right), & \text{if} \quad \dot{y}_{m_t} < 0\,, \\ \arccos\left(\dot{x}_{m_t}/\sqrt{\dot{x}_{m_t}^2 + \dot{y}_{m_t}^2}\right) + \pi, & \text{if} \quad \dot{y}_{m_t} \geq 0\,. \end{cases} \end{aligned} \tag{3.2.6}$$

Notice that all LDs that are located at the same distance from the centre have the same polar transmitted angle but are distinguished by different azimuthal angles.

Thus, the transmitter can be viewed as sending M_t collimated beams to the receiver multiplexed spatially at M_t unique polar and azimuthal angles.

The orientation misalignment causes launching angles $(\dot{\theta}_{m_t},\dot{\phi}_{m_t})$ and $(\theta_{m_t},\phi_{m_t})$ to differ. In this case, for given $(\theta_{in}, \phi_{in}, \phi_{ro})$, angles $(\theta_{m_t},\phi_{m_t})$ are calculated from $(\dot{\theta}_{m_t},\dot{\phi}_{m_t})$ as follows: Let $\mathbf{e}_{m_t}$ be (3×1) vector, represented in (X_t, Y_t, Z_t) as $\mathbf{e}_{m_t}=[\sin(\dot{\theta}_{m_t})\cos(\dot{\phi}_{m_t}); \sin(\dot{\theta}_{m_t})\ \sin(\dot{\phi}_{m_t}); \cos(\dot{\theta}_{m_t})]$. Then, $\mathbf{e}_{m_t}$ is rotated around (Y_t, X_t, Z_t) axes by three angles: $\theta_y = \arcsin\left(\cos(\phi_{in})\ \sin(\theta_{in})\right)$,$\theta_x = \arcsin\left(\sin(\phi_{in})\ \sin(\theta_{in})/\cos(\theta_y)\right)$ and $\theta_z = \phi_{ro}$ respectively. Thus, θ_{m_t} and ϕ_{m_t} are calculated by

$$\begin{aligned}\theta_{m_t} &= \arccos\left([0,0,1]\,\mathbf{R}_z(\theta_z)\,\mathbf{R}_x(\theta_x)\,\mathbf{R}_y(\theta_y)\,\mathbf{e}_{m_t}\right),\\ \phi_{m_t} &= \arcsin\left(\frac{[0,1,0]}{\sin(\theta_{m_t})}\,\mathbf{R}_z(\theta_z)\,\mathbf{R}_x(\theta_x)\,\mathbf{R}_y(\theta_y)\,\mathbf{e}_{m_t}\right),\end{aligned} \tag{3.2.7}$$

where $\mathbf{R}_z(\theta_z)$, $\mathbf{R}_x(\theta_x)$ and $\mathbf{R}_y(\theta_y)$ are (3×3) rotation matrices around (Z_t, X_t, Y_t) axes respectively [99]. At the receiver, the *angle-to-space mapping* is done by the lens, which maps the received collimated beams at angle (θ_r, ϕ_r) to the position $(\dot{x}_r,\dot{y}_r)$ on the PD plane, see Fig. 3.1. Using geometric optics and Eq. (3.2.6), the position $(\dot{x}_r,\dot{y}_r)$ is obtained by

$$\begin{aligned}\dot{x}_r &= f_r\ \tan(\theta_r)\ \cos(\phi_r),\\ \dot{y}_r &= \begin{cases}\sqrt{\left(f_r\tan(\theta_r)\right)^2 - \dot{x}_r^2}, & \text{if}\quad 0 \le \phi_r \le \pi,\\ -\sqrt{\left(f_r\tan(\theta_r)\right)^2 - \dot{x}_r^2}, & \text{if}\quad \pi \le \phi_r \le 2\,\pi.\end{cases}\end{aligned} \tag{3.2.8}$$

Notice that, in case of perfect orientation (i.e., $\dot{\theta}_{m_t} = \theta_{m_t}$, $\dot{\phi}_{m_t} = \phi_{m_t}$), the *space-to-angle* mapping makes A-MIMO links resilient to shifting of the transmitter axes (i.e., Δ_x, Δ_y, Δ_z). These affine translations of the transmitter relative to the receiver do not change the angle of reception and thus the received image is unaffected. This is the second key advantage of the A-MIMO over C-MIMO architecture. In practice, this advantage of A-MIMO links is limited by transceiver design constraints. Indeed, the performance of A-MIMO links is invariant to off-axis and channel length variation as long as $\Delta_x^2 + \Delta_y^2 \ll {l_r}^2$ and $L < L_{th}$ are satisfied, respectively. The channel length threshold L_{th} depends on the size of the PD array and lens parameters and can be calculated by [8]

$$L_{th} = \frac{f_r \ (l_r + l_t)}{D_r \ \sqrt{M_r}}. \tag{3.2.9}$$

In practice, the performance of A-MIMO links is degraded when $L > L_{th}$. To illustrate, consider Fig. 3.1, if L_o is increased too much, the red and green beams will be truncated and not detected. However, the central beam (in black) is received regardless of L_o. This process is termed *window truncation* [70] by which the received image is truncated by a circular aperture. In practice, L_{th} can be extended by increasing the transceiver size (e.g. f_r, l_r and l_t) as given in Eq. (3.2.9) [8]. Thus, given this limitation of window truncation for long ranges, A-MIMO systems are best suited to short-range applications.

In the case of orientation misalignment, i.e. $\dot{\theta}_{m_t} \neq \theta_{m_t}$, $\dot{\phi}_{m_t} \neq \phi_{m_t}$, the angles of the received ray will be shifted relative to the receiver optical axis and thus the received image will also be shifted. For example, the inclination by angles (θ_{in}, ϕ_{in}) and rotation by angle ϕ_{ro} lead to shifting and rotating of the received image, as shown in Fig. 3.2. An interesting point is that the geometric optics relationships inherent to A-MIMO can be used to estimate the misalignment parameters from the received image, as we will show in Section 3.5.

3.3 Underwater A-MIMO Link Modelling

In this section, a mathematical model is derived for an underwater A-MIMO link, taking into account link misalignment, scattering, beam attenuation, and background noise. For beam attenuation in seawater, we consider beam attenuation and single scattering, which is valid for short-range, low-turbidity UWOC [24, 32, 88]. In the case of short-range communications considered here, it is reasonable to ignore the impact of turbulence since the variation in the refractive index of the seawater is negligible. Also, due to the use of relatively large receive apertures at the receiving side, aperture averaging will further reduce the impact of any turbulence [100]. In the following analysis, the AoA distribution of the received signal is derived first. Then, the probability density function (PDF) of PoA is obtained from the AoA PDF using the random variable transformation (RVT) theory. Using the latter, the channel matrix and the received image are calculated.

3.3.1 AoA Distribution

Figure 3.3 illustrates transmitter with displacement and disorientation with respect to the receiver. Consider that the optical beam from the $m_t{}^{\text{th}}$ LD has the

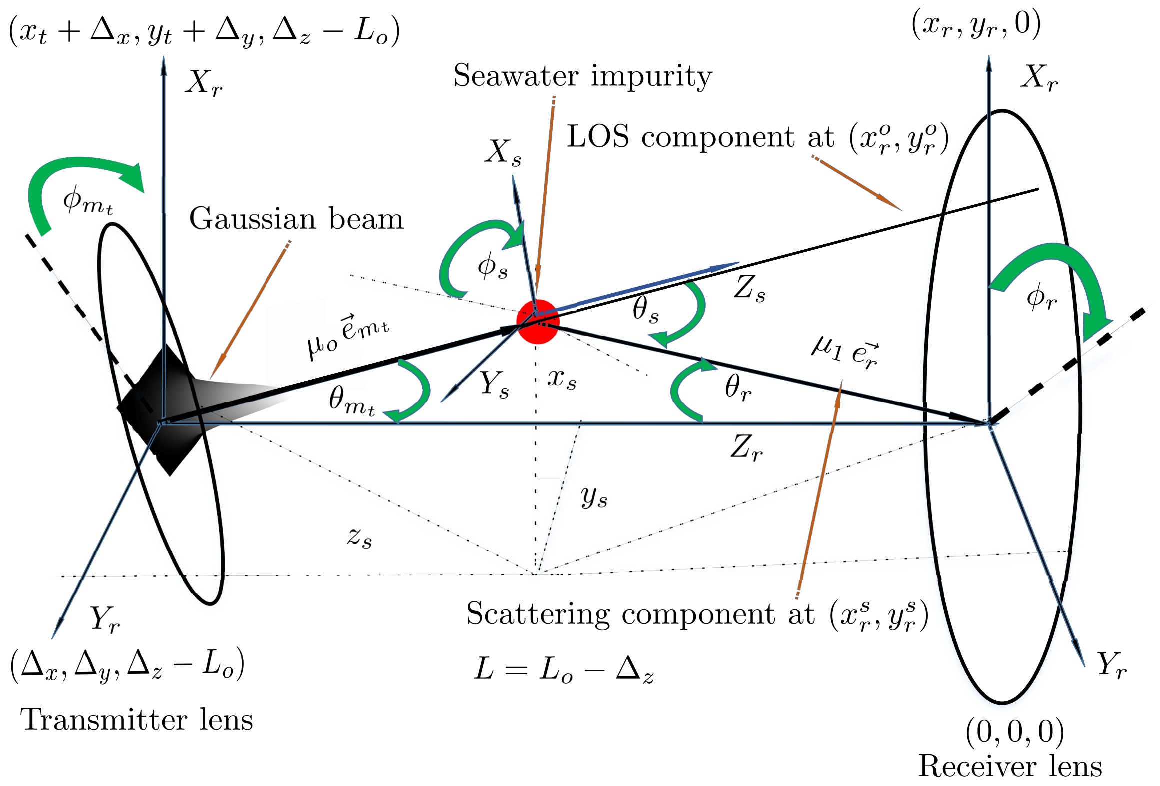

Figure 3.3: Beam scattering model for an A-MIMO link, under single scattering assumption.

optical power P_o with a Gaussian beam profile [101]

$$I_{m_t}(x_t, y_t) = I_o \exp\left(\frac{-2\left((x_t - x_{m_t})^2 + (y_t - y_{m_t})^2\right)}{w_o^2}\right) \tag{3.3.1}$$

where w_o and (x_{m_t}, y_{m_t}) are the beam waist and beam centre coordinates, respectively. Moreover, the radius of the beam width on the transmitter lens is $w = w_o\sqrt{(1 + \lambda\, d_t/(\pi\, w_o{}^2))^2}$ with λ being the wavelength. In order to simplify the analysis, we assume that $w_o \ll D_t$, which allows approximating the $m_t{}^{\text{th}}$ LD as a point-source at position $(\dot{x}_{m_t}, \dot{y}_{m_t})$.

Seawater impurities in underwater channels cause absorption and scattering of the transmitted optical beam. The extinction ratio $c = a + b$ and albedo coefficient $W = b/c$ quantify the total power loss and single scattering, respectively, where a and b are the absorption and scattering coefficients, respectively [28]. Under a single scattering assumption, a transmitted ray is scattered at most once during its propagation between the transmitter and the receiver. More precisely, a ray sent in the direction $\vec{e}_{m_t}$, after propagating over a given distance, is attenuated and randomly scattered to a new direction $\vec{e}_r$, which can be divided into line-of-sight (LOS) and scattered components, as shown in Fig. 3.3. For the LOS component, the amplitude of the optical ray is attenuated according to the Beer-Lambert law, however, its direction is maintained (i.e., $\vec{e}_{m_t} = \vec{e}_r$) arriving at position (x_r^o, y_r^o) as shown in the figure. For the scattered component, scattering leads to the likelihood of loss by a factor b/c. The likelihood of ray-impurity interaction[2] after propagating over a distance μ_0, is modelled by an exponential PDF [88, 102]

$$p_\mu(\mu_0) = c \exp(-c\ \mu_0). \tag{3.3.2}$$

Upon scattering, an incident ray arriving from the direction $\vec{e}_{m_t}$ will have its direction $\vec{e}_r$ changed randomly according to polar and azimuthal scattering angles (θ_s, ϕ_s). A common probabilistic model for θ_s is given by [90]

$$p_{\theta_s}(\theta_s) = \frac{1 - g^2}{4\pi(1 + g^2 - 2g\cos(\theta_s))^{(3/2)}}\ , \quad g = \overline{\cos(\theta_s)} \tag{3.3.3}$$

where, the average cosine g depends on the seawater type. Also, azimuthal scattering

---

[2] The ray-impurity interaction is either an absorption or scattering event. The absorption event results when ray losses all energy (i.e. ray termination), while the scattering event occurs when the ray changes its direction (i.e. ray deflection) [102].

angle is typically described by the uniform PDF [91]

$$p_{\phi_s}(\phi_s) = \frac{1}{2\pi}. \tag{3.3.4}$$

For the given scattering angle (θ_s, ϕ_s), $\vec{e}_r$ is calculated from $\vec{e}_{m_t}$ using Eq. (3.2.7), by replacing the orientation misalignment angles $(\theta_{in}, \phi_{in}, \phi_{ro})$ by $(\theta_s, \phi_s, 0)$ in the definitions of θ_x, θ_y, and θ_z. After being scattered, the ray travels a distance μ_1 in the direction $\vec{e}_r$ before arriving at the receiver at the position (x_r^s, y_r^s), as shown in Fig. 3.3. The ray is effectively detected if PoA is located within the receiver lens aperture. However, the ray may contribute to spatial inter-channel interference (i.e. cross-talk) depending on which PD it is incident. Mathematically, a ray arriving at position (x_r, y_r) is effectively received provided that $(x_r^2 + y_r^2) \leq l_r^2/4$. For the ${m_t}^{th}$ LD, the corresponding geometric loss, denoted by G_{m_t}, which takes the window truncation into account, is given by

$$G_{m_t}(x_r, y_r) = \begin{cases} 1, & \text{if} \quad (x_r^2 + y_r^2) \leq l_r^2/4 \\ 0, & \text{otherwise.} \end{cases} \tag{3.3.5}$$

In short-range, low-albedo waters (e.g., $W = 0.053$ in case of pure seawaters) the impact of scattering is small [28]. Thus, the AoA PDF of the received power can be well approximated by a linear combination of LOS components from each LD. For an $(\sqrt{M_t} \times \sqrt{M_t})$ LD array, the AoA distribution of the received signal can be approximated as

$$\begin{aligned} P_{\theta_r,\phi_r}(\theta_r,\phi_r) \approx & \sum_{m_t=1}^{M_t} \exp\left(\frac{-Lc}{\cos(\theta_{m_t})}\right) \int_{x_{tn}}^{x_{tp}} \int_{y_{tn}}^{y_{tp}} I_{m_t}(x_t,y_t) \\ & \times G_{m_t}(x_r^o, y_r^o)\, dy_t\, dx_t\, \delta(\theta_r-\theta_{m_t}, \phi_r-\phi_{m_t}). \end{aligned} \tag{3.3.6}$$

In Eq. (3.3.6), the exponential term is the path loss according to the Beer-Lambert law [91]. The limits of the integrals are defined as: $x_{t_n} = -l_t/2+\Delta_x$, $x_{t_p} = l_t/2+\Delta_x$, $y_{t_n} = -l_t/2+\Delta_y$ and $y_{t_p} = l_t/2+\Delta_y$. The arrival position of the LOS ray is shown in Fig. 3.3, which it is given by $x_r^o = x_t+\Delta_x+L\,\tan(\theta_t)\,\cos(\phi_t)$, and $y_r^o = y_t+\Delta_y+L\,\tan(\theta_t)\,\sin(\phi_t)$. Define $\delta(\theta_r-\theta_{m_t},\phi_r-\phi_{m_t})$ as the Dirac-delta function, taking its non-zero value at the associated launching angles. Note that for the case of relatively high-albedo seawaters, multiple scattering can become significant, especially for relatively long-range links [88]. In the following analysis, we consider only the LOS and single scattering components that dominate short-range links, which allows a tractable mathematical analysis of the link misalignment.

In order to calculate the single scattering component, for a transmitted ray in direction $\vec{e}_{m_t}$ and scattered at point (x_s,y_s,z_s) with scattering angle θ_s (see Fig. 3), we have [39, 64]

$$\begin{aligned} x_s &= \mu_0\,\sin(\theta_{m_t})\,\cos(\phi_{m_t}), & y_s &= \mu_0\,\sin(\theta_{m_t})\,\sin(\phi_{m_t}), \\ z_s &= -\mu_0\,\cos(\theta_{m_t}), & \theta_s &= \arccos\left(\vec{e}_{m_t}.\vec{e}_r\right). \end{aligned} \tag{3.3.7}$$

The arrival position of the scattered ray $(x_r^s, y_r^s, 0)$ in the receiving side is [39, 64]

$$\begin{aligned}
x_r^s &= x_t + \Delta_x + x_s + \mu_1 \sin(\theta_r) \cos(\phi_r), \\
y_r^s &= y_t + \Delta_y + y_s + \mu_1 \sin(\theta_r) \sin(\phi_r), \\
0 &= L_o - \Delta_z + z_s - \mu_1 \cos(\theta_r).
\end{aligned} \tag{3.3.8}$$

Using Eqs. (3.3.1)-(3.3.8), the AoA distribution of LOS and scattering components is derived by using a similar approach as in [88]. Accordingly, the AoA distribution of received signal from the m_t^{th} LD is given as

$$\begin{aligned}
&P_{\theta_r,\phi_r}(\theta_r, \phi_r | \theta_{m_t}, \phi_{m_t}) = \int_{x_{tn}}^{x_{tp}} \int_{y_{tn}}^{y_{tp}} I_{m_t}(x_t, y_t) \Bigg(\frac{b}{4\pi} \times \\
&p_{\phi_s}(\phi_s)\, p_{\theta_s}(\arccos(\vec{e}_{m_t}.\vec{e}_r)) \sin(\arccos(\vec{e}_{m_t}.\vec{e}_r)) \\
&\times \int_0^{l_{\mu_o}} \exp(-c\,\mu_0)\, \exp(-c\,\mu_1)\;\; G_{m_t}(x_r^s, y_r^s)\, d\mu_0 \\
&+ \exp\left(\frac{-c\;L}{\cos(\theta_{m_t})}\right) \times G_{m_t}(x_r^o, y_r^o)\; \delta(\theta_r - \theta_{m_t}, \phi_r - \phi_{m_t}) \Bigg) \\
&\qquad\qquad dy_t\; dx_t,
\end{aligned} \tag{3.3.9}$$

where $l_{\mu_o} = L/\cos(\theta_{m_t})$ and $P_{\theta_r,\phi_r}(\theta_r, \phi_r | \theta_{m_t}, \phi_{m_t})$ has units of W/rad^2. The first and the second terms in Eq. (3.3.9) refer to the scattered and LOS components, respectively.

A simpler AoA expression can be derived from Eq. (3.3.9) assuming that the beam spot on the transmitter lens is very small, i.e., $w << l_t$, allowing the LD to be well approximated as a single-ray source. For the central LD under perfect beam alignment (i.e., $x_t = y_t = 0$ and $\Delta_x = \Delta_y = 0$), Eq. (3.3.9) can be simplified as

$$\begin{aligned} P_{\theta_r,\phi_r}(\theta_r, \phi_r|\theta_{m_t}, \phi_{m_t}) &= \frac{P_o\, b\,(1-g^2)\, \sin(\arccos(\vec{e}_{m_t}.\vec{e}_r))}{8\pi^2(1+\ g^2 - 2\, g\,(\vec{e}_{m_t}.\vec{e}_r))^{3/2}} \\ \times\, & \frac{\exp(-c\, L\, \sec(\theta_r))\,(\exp(\nu\ f_2(\theta_r,\phi_r)) - \exp(\nu\ f_1(\theta_r,\phi_r)))}{c\ (\cos(\theta_{m_t})\ \sec(\theta_r) - 1)} \\ +\, & P_o\, \exp\left(\frac{-c\ L}{\cos(\theta_{m_t})}\right)\, G_{m_t}\,(x_r^o, y_r^o)\ \delta(\theta_r - \theta_{m_t}, \phi_r - \phi_{m_t}), \end{aligned} \tag{3.3.10}$$

where $\nu = c\,(\cos(\theta_{m_t})\ \sec(\theta_r) - 1)$.

Integrating Eq. (3.3.10) over ϕ_r gives the polar AoA distribution as

$$\begin{aligned} P_{\theta_r}(\theta_r|\theta_{m_t}) &= P_o \exp\left(\frac{-c\ L}{\cos(\theta_{m_t})}\right)\, G_{m_t}\,(x_r^o, y_r^o)\ \delta(\theta_r - \theta_{m_t}) \\ +\, & \frac{P_o\, b\ (1-g^2)\ \sin(\arccos(\vec{e}_{m_t}.\vec{e}_r))\ \exp(-c\, L\ \sec(\theta_r))}{8\pi^2\ c\,(1+\ g^2 - 2\ g\ (\vec{e}_{m_t}.\vec{e}_r))^{3/2}\,(\cos(\theta_{m_t})\ \sec(\theta_r) - 1)} \\ \times\, & \int_0^{2\pi} (\exp(\nu\, f_2(\theta_r,\phi_r)) - \exp(\nu\, f_1(\theta_r,\phi_r)))\ d\phi_r. \end{aligned} \tag{3.3.11}$$

In particular, for zero launching angle (i.e. $\theta_{m_t} = 0$), Eq. (3.3.11) is simplified as

$$\begin{aligned} P_{\theta_r}(\theta_r|\theta_{m_t} = 0) &= \frac{P_o\, b\,(1-g^2)\ \sin(\theta_r)\ \exp(-c\ L\ \sec(\theta_r))}{c\,(\sec(\theta_r) - 1)(1+\ g^2 - 2\, g\ \cos(\theta_r))^{3/2}} \\ \frac{1}{4\,\pi} & \left(\exp\left(c\ \frac{f_2(\theta_r)}{(\sec(\theta_r) - 1)^{-1}}\right) - \exp\left(c\ \frac{f_1(\theta_r)}{(\sec(\theta_r) - 1)^{-1}}\right)\right) \\ +\, & P_o\ \exp\left(\frac{-c\ L}{\cos(\theta_{m_t})}\right)\, G_{m_t}\,(x_r^o, y_r^o)\ \delta(\theta_r - \theta_{m_t}, \phi_r - \phi_{m_t}). \end{aligned} \tag{3.3.12}$$

Similarly, the azimuthal AoA distribution can be obtained from Eq. (3.3.10) as

$$
\begin{aligned}
&P_{\phi_r}(\phi_r|\theta_{m_t},\phi_{m_t}) = \\
&P_o \Bigg(\exp\left(\frac{-c\;L}{\cos(\theta_{m_t})}\right)\; G_{m_t}\left(x_r^o, y_r^o\right)\; \delta(\phi_r - \phi_{m_t}) \; + \\
&\frac{b\,(1-g^2)}{8\pi^2\,c} \int_0^{\pi/2} \frac{\sin(\arccos\left(\vec{e}_{m_t}.\vec{e}_r\right))\; \exp\left(-c\,L\;\sec(\theta_r)\right)}{(1+\;g^2 - 2\,g\;(\vec{e}_{m_t}.\vec{e}_r))^{3/2}} \\
&\times \frac{(\exp\left(\nu\;\,f_2(\theta_r,\phi_r)\right) - \exp(\nu\;\,f_1(\theta_r,\phi_r)))}{(\cos(\theta_{m_t})\;\sec(\theta_r) - 1)}\; d\theta_r \Bigg)\,.
\end{aligned}
\tag{3.3.13}
$$

Equation (3.3.13) can be approximated in a closed-form using Eq. (3.3.12) for $\theta_{m_t} = 0$ as

$$
\begin{aligned}
&P_{\phi_r}(\phi_r|\theta_{m_t} = 0) \approx \frac{P_o\,b\;\exp(-c\,L)}{11.63\,\pi\,c} \times \\
&\Bigg(1.45 \times 10^3 - \sum_{i=1}^{2} \xi_i\left(\mathit{\Gamma}(\gamma_i,\alpha_i) - \mathit{\Gamma}(\gamma_i,\beta_i)\right) \\
&+ \frac{2258.5}{\sqrt{c\,L}} \left(\operatorname{erf}\left(\sqrt{\frac{c\,L}{2}}\operatorname{arccot}\left(\frac{c\,L}{l_r}\right)\right) - \operatorname{erf}\left(\frac{\sqrt{c\,L}}{81.03}\right)\right) \\
&- \frac{7208}{c\,l_r}\left(\exp\left(\frac{-c\,l_r}{19.1}\right) - \exp\left(\frac{-c\,l_r}{4}\operatorname{arccot}\left(\frac{2\,L}{l_r}\right)\right)\right)\Bigg)\,,
\end{aligned}
\tag{3.3.14}
$$

where, the incomplete-gamma function $\mathit{\Gamma}(\gamma,\alpha)$ and the error function $\operatorname{erf}(u)$ are defined as: $\mathit{\Gamma}(\gamma,\alpha) = \int_\alpha^\infty t^{\gamma-1}\,\exp(-t)\,dt$ and $\operatorname{erf}(u) = \dfrac{2}{\sqrt{\pi}}\int_0^u \exp(-t^2)\,dt$. Also, the coefficients of incomplete-gamma functions are defend as: $\xi_1 = -603.47\,(c\,L)^{0.26}$, $\xi_2 = 76.07\,(c\,l_r)^{0.52}$, $\gamma_1 = -0.26$, $\gamma_2 = -0.52$, $\alpha_1 = c\,l/2\,\left(\cot^{-1}\left(2\,L/l_r\right)\right)^2$, $\alpha_2 = c\,l_r/19.12$, $\beta_1 = c\,L/114.6$ and $\beta_2 = c\,l_r/4\cot^{-1}\left(2\,L/l_r\right)$.

Notice that, though Eq. (3.3.9) is the exact distribution of the AOA, Eqs. (3.3.10)-(3.3.14) provide simpler closed-forms, which are more convenient to use. Detailed proofs of Eqs. (3.3.10), (3.3.12) and (3.3.14) are provided in Appendix A. In Section 3.6 the accuracy of Eqs. (3.3.10-3.3.14) is verified using MCNRT simulations.

3.3.2 PoA Distribution

Recall that for A-MIMO systems, the receiver lens maps the AoA to a PoA on the focal plane of the imaging receiver and onto the PD array. In order to simplify the derivation of PoA, the field of view (FOV) of the PDs is assumed to be full angle [3], i.e., 180^o. Thus, the received power of PoA distribution from the m_t^{th} LD is derived from Eqs. (3.3.9) and (3.2.8) as

$$P_{\dot{x}_r,\dot{y}_r}(\dot{x}_r,\dot{y}_r|\theta_{m_t},\phi_{m_t}) = \frac{f_r\ P_{\theta_r,\phi_r}(\dot{x}_r,\dot{y}_r|\theta_{m_t},\phi_{m_t})}{(f_r^2+\dot{x}_r^2+\dot{y}_r^2)\sqrt{(\dot{x}_r^2+\dot{y}_r^2)}}, \tag{3.3.15}$$

where the distribution is in units of W/m^2. Also, the focal plane of the imaging receiver is defined by the square region $-\sqrt{M_r}\,D_r/2 \leq \{\dot{x}_r,\dot{y}_r\} \leq \sqrt{M_r}\,D_r/2$.

Using Eq. (3.3.15), the channel gain between the m_t^{th} LD and the m_r^{th} PD can be calculated as

$$h_{m_r,m_t}(\boldsymbol{\Delta}) = \frac{1}{P_o}\int_{x_{r_n}}^{x_{r_p}}\int_{y_{r_n}}^{y_{r_p}} P_{\dot{x}_r,\dot{y}_r}(\dot{x}_r,\dot{y}_r|\theta_{m_t},\phi_{m_t})d\dot{y}_r d\dot{x}_r, \tag{3.3.16}$$

where $\boldsymbol{\Delta} := [\theta_{in};\phi_{in};\phi_{ro};\Delta_x;\Delta_y;\Delta_z]$ is the (6×1) misalignment vector, and the limits of the integral are defined as $x_{r_n} = \dot{x}_{m_r} - D_r/2$, $x_{r_p} = \dot{x}_{m_r} + D_r/2$, $y_{r_n} = \dot{y}_{m_r} - D_r/2$ and $y_{r_p} = \dot{y}_{m_r} + D_r/2$. For an $(M_t \times M_r)$ A-MIMO system, the channel gains can be

---

[3] The full FOV maximizes the channel gain, however it is not ideal in case of high background noise. In the presented work, in order to reduce the effects of the background noise, an optical filter is implemented with the receiver lens.

arranged in a channel matrix **H** defined as

$$\mathbf{H}(\boldsymbol{\Delta}) = \begin{bmatrix} h_{11} & h_{12} & \dots & h_{1,M_t} \\ h_{21} & h_{22} & \dots & h_{2,M_t} \\ \vdots & \vdots & h_{m_r,m_t} & \vdots \\ h_{M_r,1} & h_{M_r,2} & \dots & h_{M_r,M_t} \end{bmatrix}. \tag{3.3.17}$$

The correlation of the channel matrix depends on the transceiver parameters (i.e., D_t, l_t, D_r and l_r) and the channel conditions (i.e., a, b and L). For example, increasing the inter-spacing between LDs/PDs leads to a reduced spatial inter-channel interference, which reduces the channel correlation. As well, increasing the channel length or seawater turbidity leads to an increase in spatial inter-channel interference, which increases the channel correlation.

Due to displacement and orientation misalignments the received image is a truncated, shifted and rotated version of the image at the transmitter focal plane. Additionally, absorption and scattering due to seawater will result in an attenuated and blurred received image. For the $(\sqrt{M_t} \times \sqrt{M_t})$ LD array, using Eq. (3.3.15), the received image is a summation of M_t received PoA distributions and noise $n(\dot{x}_r, \dot{y}_r)$

$$g_r(\dot{x}_r, \dot{y}_r) = \sum_{m_t=1}^{M_t} P_{\dot{x}_r,\dot{y}_r}(\dot{x}_r, \dot{y}_r|\theta_{m_t}, \phi_{m_t}) + n(\dot{x}_r, \dot{y}_r). \tag{3.3.18}$$

The noise term $n(\dot{x}_r, \dot{y}_r)$ is the summation of the internal and external noises, denoted by $n_{in}(\dot{x}_r, \dot{y}_r)$ and $n_{ex}(\dot{x}_r, \dot{y}_r)$, respectively. The former includes thermal, shot and dark noises, whereas the latter refers to the background noise [43]. For the background noise, we consider the worst-case analysis proposed in [43, Eq. (9)], corresponding to a vertical link with unobstructed sunlight from the zenith. Using

Eq. (3.2.6), we have

$$n_{ex}(\dot{x}_r, \dot{y}_r) = \frac{\pi\, l_r^2\, \lambda_\Delta\, E_s}{4\, \exp\left(K_d\, L_h\right)}\, \cos\left(\arctan\left(\frac{\sqrt{\dot{x}_r^2 + \dot{y}_r^2}}{f_r}\right)\right), \tag{3.3.19}$$

where, E_s is the solar intensity and L_h is the depth of the receiver. The light diffusion coefficient, K_d, is related to water type and the water turbidity W. As well, λ_Δ is the optical bandwidth of the passband receiver optical filter, centred at the wavelength of the LD. The use of an optical filter is very effective in order to mitigate background noise especially when the orientation of the receiver is upwards [43].

For simplicity, assume that the receiver noise is signal independent, and use an additive white Gaussian noise (AWGN) model for $n(\dot{x}_r, \dot{y}_r)$ [53].

3.4 Channel Capacity and Misalignment Models

Considering the AWGN model, the $(M_r \times 1)$ vector $\mathbf{y}$ of the receiver photo-currents, is given by:

$$\mathbf{y} = \Re\; \mathbf{H}(\boldsymbol{\Delta})\; \mathbf{x} + \mathbf{n} \tag{3.4.1}$$

where, $\Re$ is the PD responsitivity, $\mathbf{x}$ is the $(M_t \times 1)$ transmitted optical power vector and $\boldsymbol{\Delta}$ is defined in Eq. (3.3.16). Also, $\mathbf{n} = [n_1; n_2; ...; n_{m_r}; ...; n_{M_r}]$ is the $(M_r \times 1)$ noise vector where the noise element n_{m_r} is quantified as

$$n_{m_r} = \int_{x_{r_n}}^{x_{r_p}} \int_{y_{r_n}}^{y_{r_p}} \left(n_{ex}(\dot{x}_r,\, \dot{y}_r) + n_{in}(\dot{x}_r, \dot{y}_r)\right)\; d\dot{y}_r\; d\dot{x}_r, \tag{3.4.2}$$

where the integration is taken over each PD as in Eq. (3.3.16). In the case where the channel state information is not available at the transmitter (e.g., unknown seawater parameters), the total transmitted average optical power P_t is divided equally among all LDs (i.e., $P_o = P_t/M_t$). For an imaging receiver with independent identical Gaussian noise elements with zero mean and variance σ_n^2 (i.e., $n_{m_r} \sim \mathcal{N}(0, \sigma_n^2)$), the link capacity in bits/channel-use is obtained as [103]

$$C(\mathbf{\Delta}) = \frac{1}{2}\ \log_2\left(\det\left(\mathbf{I} + \left(\frac{\Re\ P_o}{\sigma_n}\right)^2 \mathbf{H}(\mathbf{\Delta})\ \mathbf{H}(\mathbf{\Delta})^T\right)\right), \tag{3.4.3}$$

where $\mathbf{I}$ is the identity matrix and $(.)^T$ denotes matrix transposition.

Equation (3.4.3) implicitly assumes DCO-OFDM (DC-biased optical orthogonal frequency division multiplexing) signalling, which is a spectrally efficient technique to overcome the bandwidth limitation of the optoelectronic components [48, 104]. In the following, the link capacity is evaluated for B2F and M2F communication scenarios.

3.4.1 B2F Communication Model

Figure 3.4 illustrates a typical B2F communication scenario where one transceiver is tied to a buoyed node on the sea surface and the other one is fixed on the seabed. Such links are commonly used in low depth seawaters, e.g., for high-speed communication with underwater sensor networks [14]. Here, surface waves disrupt the orientation of the buoyed node, causing random inclination and rotation angles. For simplicity, in this scenario it is assumed that the changes in X_t, Y_t and Z_t are negligible, that is, we consider $\Delta_x = \Delta_y = \Delta_z = 0$.

Cox *et al.* developed in [105] a model for seawater waves based on an isotropic

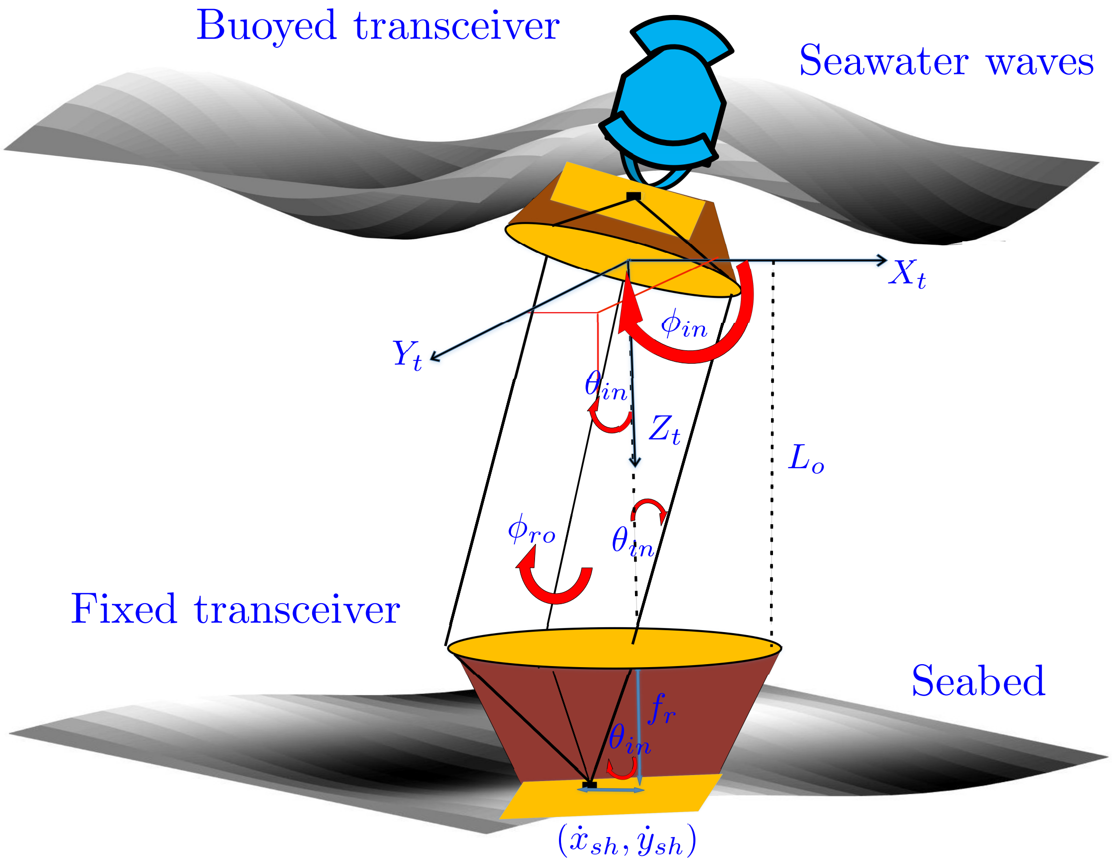

Figure 3.4: Buoyed-to-Fixed (B2F) communication model: Inclination and rotation angles $(\theta_{in}, \phi_{in}, \phi_{ro})$ due to waves of seawaters (i.e. surface slop).

Gaussian distribution. According to this model, only θ_{in} and ϕ_{in} orientation misalignments are considered and described by a joint PDF. Here, we extend the Cox model to include an independent and uniform rotation misalignment of ϕ_{ro} resulting in the following PDF,

$$\begin{aligned} p_{\theta_{in},\phi_{in},\phi_{ro}}(\theta_{in}, \phi_{in}, \phi_{ro}) = \frac{\tan(\theta_{in})\ \sec^2(\theta_{in})}{(2\pi)^2\sigma_{in}^2} \\ \times \exp\left(-\frac{\tan^2(\theta_{in})}{2\sigma_{in}^2}\right), \end{aligned} \tag{3.4.4}$$

where σ_{in}^2 is the variance of the slope of the sea surface (i.e., sea waves), which increases linearly with wind speed U in m/sec through the relationship $\sigma_{in}^2 = 0.003 + 0.00512\ U$ for $0\,\text{m/sec} \leq U \geq 16\text{m/sec}$ [105]. In order to simplify capacity calculations two scenarios are considered separately, denoted by $S1$ and $S2$, assuming $\phi_{in} = 0$ and $\phi_{ro} = 0$, respectively. Using Eqs. (3.4.3) and (3.4.4), the average capacity of A-MIMO and C-MIMO links can be obtained as

$$\overline{C}(U) = \int_0^{2\pi} \int_0^{\pi/2} C(\mathbf{\Delta})\ p_{\theta_{in},\phi_\chi}(\theta_{in}, \phi_\chi)\, d\theta_{in}\, d\phi_\chi \ , \tag{3.4.5}$$

where ϕ_χ is equal to ϕ_{ro} and ϕ_{in} for scenarios $S1$ and $S2$, respectively.

3.4.2 M2F Communication Model

Figure 3.5 illustrates a typical M2F communication scenario, where one of the transceivers is fixed on an AUV and the other one on the seabed. Such M2F links are commonly used for linking AUVs with an underwater sensor network located on the seabed, e.g., for underwater mining or for monitoring gas/oil pipelines [106]. Here, sea currents can disrupt the alignment between the AUV and the fixed sensor node, causing the AUV to be displaced in the three axes as shown in Fig. 3.5. For simplicity, in this scenario perfect angular orientation between the two nodes is assumed, i.e., $\theta_{in} = \phi_{in} = \phi_{ro} = 0$.

Assume that the AUV oscillates around its centre-gravity in the three axes of X_t, Y_t, and Z_t, and model the corresponding displacements Δ_x, Δ_y, and Δ_z by independently distributed Gaussian random variables [107], i.e., $\{\Delta_x, \Delta_y\} \sim \mathcal{N}(0, \sigma_{xy}^2)$, and $\Delta_z \sim \mathcal{N}(-L_o, \sigma_z^2)$. Note that σ_z and σ_{xy} are the standard deviations of the link distance variations and off-axis misalignments, respectively.

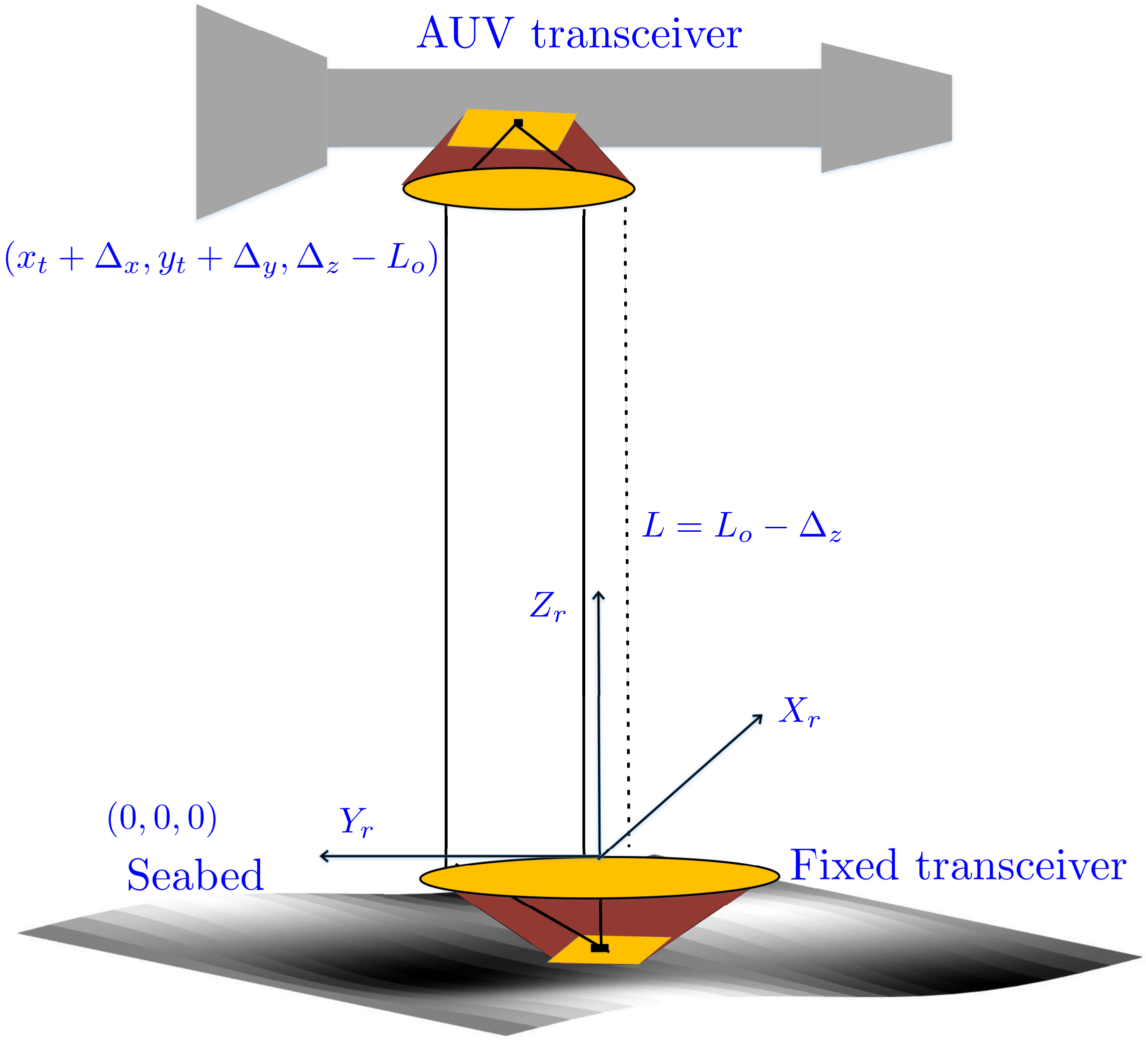

Figure 3.5: M2F communication model showing off-axis transmission with displacement (Δ_x, Δ_y) and channel length variation (Δ_z).

In order to simplify capacity calculation, we consider two different scenarios, denoted by $S3$ and $S4$, where the $S3$ assumes a fixed channel length (i.e., $\Delta_z = 0$), and $S4$ assumes on-axis transmission (i.e., $\Delta_x = \Delta_y = 0$).

In case of scenario $S3$, the average link capacity is calculated as

$$\overline{C}(\sigma_{xy}) = \int_{-\infty}^{\infty}\int_{-\infty}^{\infty} \frac{C(\boldsymbol{\Delta})}{2\,\pi\,\sigma_{xy}^2} \exp\left(\frac{-(\Delta_x^2+\Delta_y^2)}{(2\sigma_{xy}^2)}\right) d\Delta_x\, d\Delta_y. \tag{3.4.6}$$

Also, in case of scenario $S4$, the average link capacity is

$$\overline{C}(\sigma_z) = \int_{-\infty}^{\infty} \frac{C(\boldsymbol{\Delta})}{\sqrt{2\,\pi\,\sigma_z^2}} \exp\left(-\frac{(\Delta_z+L_o)^2}{(2\sigma_z^2)}\right) d\Delta_z. \tag{3.4.7}$$

Both B2F and M2F links considered here have ranges less than L_{th} in Eq. (3.2.9) to guarantee high capacity communication unaffected by window truncation.

3.5 Tracked Angular MIMO (TA-MIMO) Systems

Given that link alignment between the transmitter and the receiver is a major challenge in practice, in this section, a PLT solution for the A-MIMO technique is presented, termed tracked A-MIMO (TA-MIMO). Leveraging the inherent geometric optics properties of A-MIMO systems, this PLT solution utilizes a $\left(D_r\sqrt{M_r}/\delta \times D_r\sqrt{M_r}/\delta\right)$ sub-pixel array to estimate rotation, shifting, and truncation of the received image. In the following subsections, the estimation of rotation, shifting and truncation of the received image are first introduced. Afterwards, the capacity of TA-MIMO links is calculated for the given distribution of tracking residual errors (TREs).

3.5.1 Image Rotation and Shifting

In the case of perfect beam alignment, the received image in an A-MIMO link is an inverted and distorted version of the transmitted image due to receiver lens and channel impairments, respectively. However, in the case of a misaligned link, the received image is additionally rotated or shifted relative to ϕ_{ro} or (θ_{in}, ϕ_{in}) angles. As shown in Fig. 3.4, a rotation in the optical axis of the transmitter by ϕ_{ro} leads to the rotation of the received image by the same value. Also, an inclination of the transmitter by (θ_{in}, ϕ_{in}) causes in a shift in the centre of the received image from the origin of the PD array $(0, 0)$ to a new position $(\dot{x}_{sh}, \dot{y}_{sh})$. In the following, a classical image registration algorithm [108, 109] is adopted to estimate the rotation and inclination angles for the A-MIMO link.

Rotation Angle

Assume that the transmitted image can be identified using pilot symbols, where the receiver can distinguish between the spots of the different LDs without ambiguity. Let $g_o(\dot{x}_r, \dot{y}_r)$ be the received "reference" image under perfect alignment, and $g_r(\dot{x}_r, \dot{y}_r)$ denote the received image at misaligned orientation. In the PLT scheme, the value of the rotation angle can be estimated using phase correlation between $g_o(\dot{x}_r, \dot{y}_r)$ and $g_r(\dot{x}_r, \dot{y}_r)$ in log-polar Fourier transform domain. Thus, ϕ_{ro} can be estimated regardless of the values of (θ_{in}, ϕ_{in}) which reduces the TRE [108, 109].

To obtain the log-polar Fourier transform, the magnitude spectrum of $g_o(\dot{x}_r, \dot{y}_r)$ and $g_r(\dot{x}_r, \dot{y}_r)$ are obtained by using fast Fourier transform (FFT) to yield $|G_o(w_x, w_y)|$ and $|G_r(w_x, w_y)|$, respectively. Then, the spectrum is converted to polar coordinates with log scale for the radius to yield $|G_o(\rho, \phi)|$ and $|G_r(\rho, \phi)|$. Finally, the spectrum in log-polar domain, $G_r(w_\rho, w_\phi)$ and $G_o(w_\rho, w_\phi)$, are calculated from $|G_o(\rho, \phi)|$ and $|G_r(\rho, \phi)|$ using FFT again. The estimate of rotation angle is obtained by calculating the phase correlation between $G_r(w_\rho, w_\phi)$ and $G_o(w_\rho, w_\phi)$ as [110]

$$\hat{\phi}_{ro} = \arg\max_{\phi} : \ \mathbf{F^{-1}} \left\{ \frac{G_o(w_\rho, w_\phi)\ G_r^*(w_\rho, w_\phi)}{|G_o(w_\rho, w_\phi)|\ |G_r^*(w_\rho, w_\phi)|} \right\}, \tag{3.5.1}$$

where, $\mathbf{F^{-1}}$ denotes inverse FFT. Equation (3.5.1) estimates ϕ_{ro} with 180^o ambiguity, that is, the estimated rotation value is either $\hat{\phi}_{ro}$ or $\hat{\phi}_{ro} + \pi$. Therefore, the phase correlation between the reference image and the received one with rotations $\hat{\phi}_{ro}$ and $\hat{\phi}_{ro} + \pi$ should be compared; the rotated image associated to the larger phase correlation will be the correct image [108]. The resulting image from this step is named "compensated" image $g_c(\dot{x}_r, \dot{y}_r)$, which is used in the next step.

Inclination Angles

After estimating and compensating the rotational misalignment, the image shift due to inclination can be also estimated using cross correlation between the original and compensated images as in [109]. As a result, $(\dot{x}_{sh}, \dot{y}_{sh})$ can be estimated as [110]

$$(\hat{\dot{x}}_{sh}, \hat{\dot{y}}_{sh}) = \arg\max_{\dot{x}_r, \dot{y}_r} : \ \mathbf{F^{-1}} \{G_o(w_x, w_y)\ G_c^*(w_x, w_y)\}, \tag{3.5.2}$$

where $G_o(w_x, w_y)$ and $G_c^*(w_x, w_y)$ are FFT and conjugate FFT in the Cartesian coordinates for the original image and the compensated one, respectively. Geometrically, as illustrated in Fig. 3.4, the inclination angles can be calculated using estimated values $(\hat{\dot{x}}_{sh}, \hat{\dot{y}}_{sh})$ and Eq. (3.2.6) as

$$\begin{aligned} \hat{\theta}_{in} &= \arctan\left(\frac{\hat{r}_{sh}}{f_r}\right), \ \ \hat{r}_{sh} = \sqrt{\hat{\dot{x}}_{sh}^{\,2} + \hat{\dot{y}}_{sh}^{\,2}}, \\ \hat{\phi}_{in} &= \begin{cases} \arccos\left(\hat{\dot{x}}_{sh}/\hat{r}_{sh}\right), & \text{if} \quad \hat{\dot{y}}_{sh} < 0\,, \\ \arccos\left(\hat{\dot{x}}_{sh}/\hat{r}_{sh}\right) + \pi, & \text{if} \quad \hat{\dot{y}}_{sh} \geq 0\,. \end{cases} \end{aligned} \tag{3.5.3}$$

Using Eqs. (3.5.1)-(3.5.3), the orientation of the TA-MIMO link can be tracked and maintained.

3.5.2 Image Truncation

As discussed in Section 3.2, in A-MIMO links the received image is not truncated as long as $L \leq L_{th}$. Under this condition, since the system magnification is fixed, the PLT scheme is not able to estimate the channel length or off-axis deviation. However, when $L > L_{th}$, the received image is truncated by a circle of area A_w at centre $(\dot{x}_c, \dot{y}_c)$, which can be estimated (e.g., using [111]) and used to infer the off-axis shift and distance between the transmitter and the receiver. Given the estimated area for the received image, $\hat{A}_w$, the channel length can be estimated as [70]

$$\hat{L} = \pi \times \frac{(f_r\ (l_r + l_t))}{\sqrt{4/\pi\ \hat{A}_w}}, \quad \hat{L} \geq L_{th}\,. \tag{3.5.4}$$

Using the estimated centre $(\hat{x}_c, \hat{y}_c)$ and the channel length, the shift values in the transmitter axes can be estimated by [85]

$$\hat{\Delta}_z = \hat{L} - L_o, \quad \hat{\Delta}_x = \frac{\hat{L}\,\hat{x}_c}{f_r}, \quad \hat{\Delta}_y = \frac{\hat{L}\,\hat{y}_c}{f_r}. \tag{3.5.5}$$

Using Eqs. (3.5.4) and (3.5.5), the on-axis alignment and the channel length of TA-MIMO link can be tracked.

Figure 3.6 presents a flowchart summarizing the PLT scheme, which concurrently estimates the orientation and the off-axis misalignments. In order to consider TREs, we define the vector $\boldsymbol{\Delta}_{TRE}$ as

$$\begin{aligned} \boldsymbol{\Delta}_{TRE} &= [\theta_e; \phi_{e_i}; \phi_{e_r}; x_e; y_e; z_e], \\ \theta_e = |\theta_{in} - \hat{\theta}_{in}|, \quad \phi_{e_i} &= |\phi_{in} - \hat{\phi}_{in}|, \quad \phi_{e_r} = |\phi_{ro} - \hat{\phi}_{ro}|, \\ x_e = |\Delta_x - \hat{\Delta}_x|, \quad y_e &= |\Delta_y - \hat{\Delta}_y|, \quad z_e = \Delta_z - \hat{\Delta}_z. \end{aligned} \tag{3.5.6}$$

one disadvantage of this approach is that the TREs will largely depend on the resolution of the imaging receiver (i.e., the number of sub-PDs per PD array). In addition, small TREs in ϕ_{ro} and L may lead to relatively larger TREs in (θ_{in}, ϕ_{in}) and (Δ_x, Δ_y), respectively. These tradeoffs are further investigated through numerical simulations in Section 3.6.

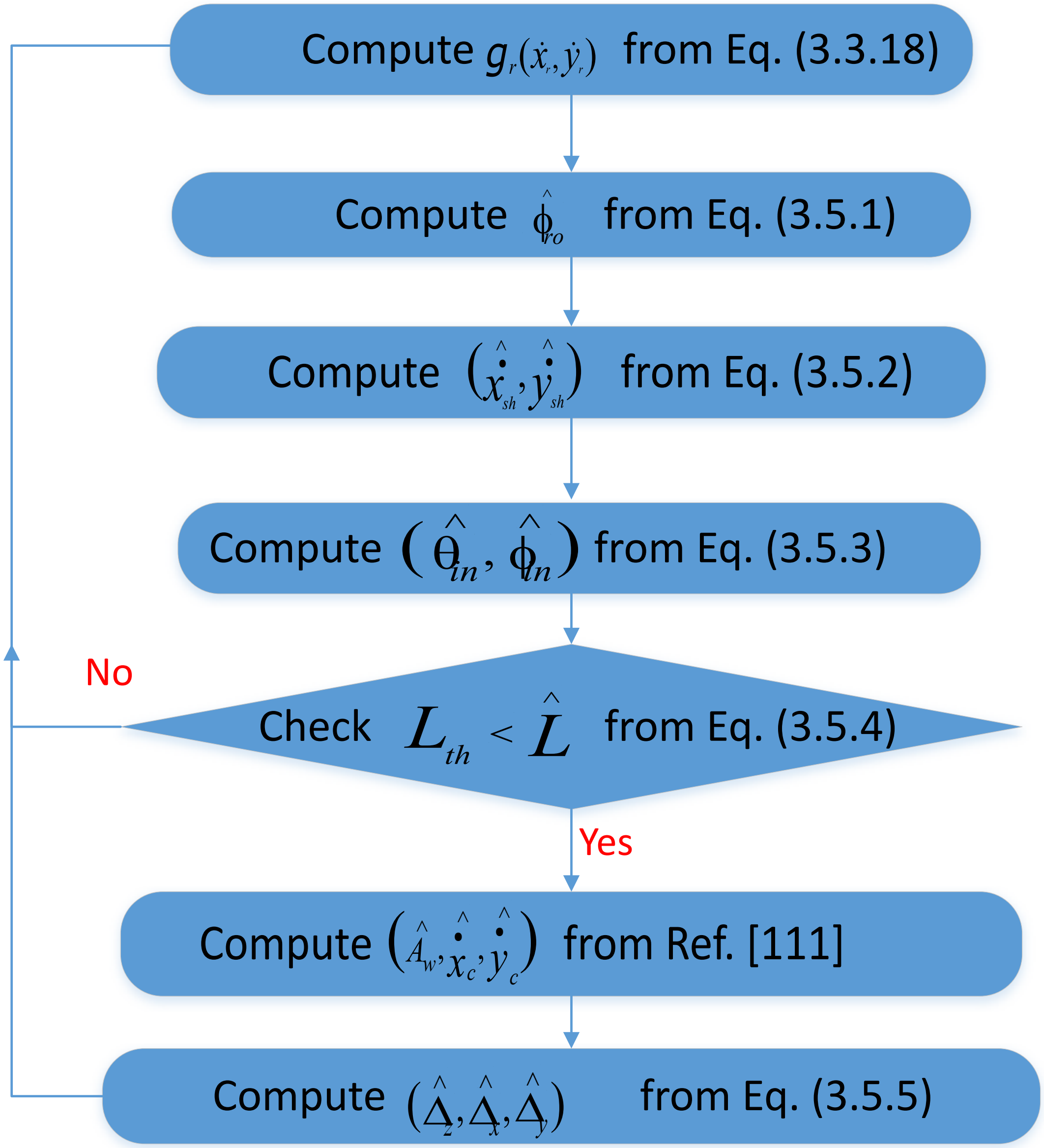

Figure 3.6: Flowchart of the proposed PLT scheme for TA-MIMO systems.

3.5.3 Capacity of TA-MIMO links

For the B2F communication model, the average capacity of TA-MIMO link is calculated as

$$\overline{C}(U) = \int_0^{2\pi} \int_0^{\pi/2} C(\mathbf{\Delta}_{TRE}) \, p_{\theta_e,\phi_{e_\chi}}(\theta_e, \phi_{e_\chi}) \, d\theta_e \, d\phi_{e_\chi}, \tag{3.5.7}$$

where $p_{\theta_e,\phi_{e_\chi}}(\theta_e, \phi_{e_\chi})$ is the joint PDF of TREs, and ϕ_{e_χ} equals ϕ_{e_r} and ϕ_{e_i} for scenarios $S1$ and $S2$, respectively. Note that, $p_{\theta_e,\phi_{e_\chi}}(\theta_e, \phi_{e_\chi})$ is calculated using Eqs. (3.3.18), (3.4.4) and (3.5.1)-(3.5.6). The accuracy of $p_{\theta_e,\phi_{e_\chi}}(\theta_e, \phi_{e_\chi})$ will be later verified via numerical simulations in Section 3.6.

For the M2F communication model, the inherent advantages of the A-MIMO approach do not require a tracking system when only displacement misalignments are present, as will be shown in Section 3.6.

3.6 Numerical Results

In this section, we provide numerical results for AoA, PoA and TRE distributions. Also, we evaluate the capacity of a 49 × 49 link using A-MIMO, TA-MIMO and C-MIMO techniques for B2F and M2F communication scenarios.

The main parameters used in the simulations are summarized in Table 3.2. Both clear and coastal seawaters are considered with a nominal channel length of $L_o = 5\,\mathrm{m}$ which is less than the window truncation threshold of $L_{th} = 6$ m. This channel length is less than the associated mean path length [4] of the multiple scattering [102] in clear and coastal seawaters, which equals 13.5 and 6.6 m, respectively. Here, it is assumed

---

[4] The mean path length is obtained by averaging μ using the PDF in Eq. (3.3.2), and it is equal to $1/c$ and $2/c$ for the single and multiple scattering, respectively.

Table 3.2: Parameters of A-MIMO and TA-MIMO Links [8, 112]

Transmitter parameters		
Diameter of the lens (l_t)	0.1 m	
Focal length of the lens (f_t)	0.365 m	
Magnification scale (M_A)	1	
No. of LDs (M_t)	49	
Distance between the centres of the LDs (D_t)	5 mm	
Average transmitted optical power of each LD (P_o)	20.41 mW	
LD wavelength (λ)	532 nm	
Waist of Gaussian beam (w_o)	0.075 mm	
Divergence angle of Gaussian beam	2.25 mrad	
Receiver parameters		
Diameter of the lens (l_r)	0.5 m	
No. of PDs (M_r)	49	
Distance between the centres of the PDs (D_r)	5 mm	
Field of view of PD (θ_{FoV})	180^o	
Responsitivity of PD ($\Re$)	0.8 A/W	
Receiver Gaussian noise variance (σ_n^2)	10^{-6} A^2	
Resolution of the imaging receiver (δ)	0.49 mm	
Area of the imaging receiver (i.e., PD array)	$\{35 \times 35\}$ mm^2	
Channel parameters	**Clear water**	**Coastal water**
Water absorption coefficient (a)	0.069 m^{-1}	0.088 m^{-1}
Water scattering coefficient (b)	0.08 m^{-1}	0.216 m^{-1}
Water extinction coefficient (c)	0.149 m^{-1}	0.304 m^{-1}
Average cosine of scattering (g)	0.919	
Nominal channel length (L_o)	5 m	

that the parameters of the clear and coastal seawaters (i.e., a, b and g) are fixed with the seawater depth (for instance, see [113]). To make a fair comparison between A-MIMO, TA-MIMO, and C-MIMO systems, the same array parameters (i.e., M_t, D_t, M_r, D_r, and l_r) are used with identical LDs and PDs, as specified in Table 3.2 and described in the next subsection.

3.6.1 A-MIMO and TA-MIMO Link Setup

Figure 3.7 shows the layout of the considered A-MIMO and TA-MIMO transmitters. A 7×7 LD array with inter spacing of 5 mm is considered, with diameter and focal length of transmitter lens set to $l_t = 0.10$ m and $f_t = 0.365\,\mathrm{m}$, respectively. The transmitted power from each LD is $P_o = 20.41$ mW, giving a total transmit power [5] of $P_t = 1$ W. Each LD is considered to have a Gaussian beam profile with small beam waist and beam width to satisfy the assumptions of Section 3.3 (i.e., $w_o \ll D_t$ and $w \ll l_t$). The launching polar and azimuthal angles are associated to the position of LDs, as shown in the figure. On the receiver side, a 7×7 PD array is considered with inter spacing of 5 mm, with the receiver lens of diameter $l_r = 0.5$ m and focal length $f_r = 0.365\,\mathrm{m}$. Not that, although a receiver lens with diameter 0.5 m is relatively large, it is chosen here to illustrate the potential capacity increases with underwater optical MIMO systems corrupted by severe misalignment conditions [6]. For relatively less severe misalignment conditions, as considered in [39, 64, 96], a smaller receiver

---

[5] Though eye-safety is not explicitly considered here or in the related literature, it is an important feature of any wireless optical system. In the atmospheric wireless optical communications, eye-safety limits are well specified and depend strongly on wavelength and beam shape [51]. In practice, in underwater systems, large scattering, absorption and beam divergence would likely provide a more relaxed optical power limit at typical operating ranges.

[6] (e.g., off-axis up to 0.3 meter and wind speed up to 6 meter/second, resulting in polar inclination angle up to 10^o in the following).

lens can be used. For the case of TA-MIMO, the PD array is oversampled with the resolution $\delta = 0.49\,\text{mm}$ which means that a 71×71 sub-pixel array is considered for the tracking purposes.

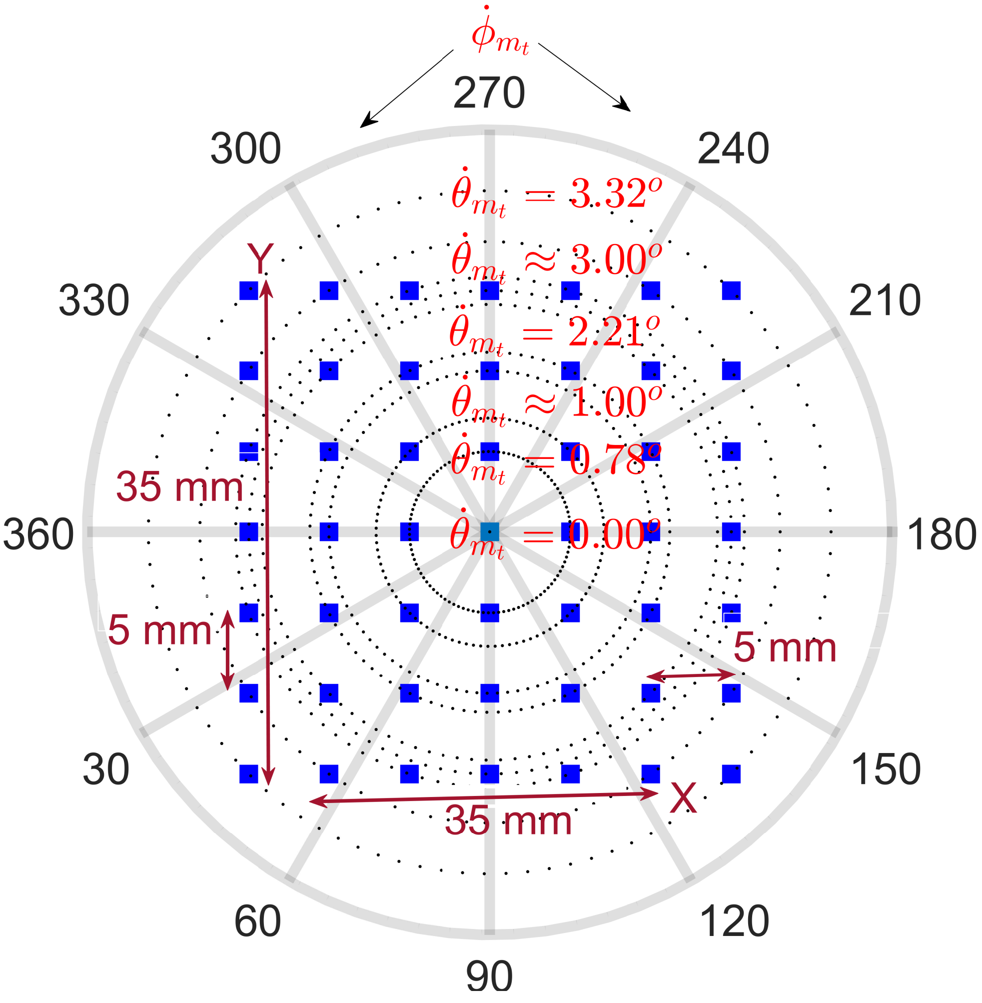

Figure 3.7: *Space-to-angle* mapping ($\dot{\theta}_{m_t}$,$\dot{\phi}_{m_t}$) for a 7×7 LD array of the A-MIMO and TA-MIMO transmitters.

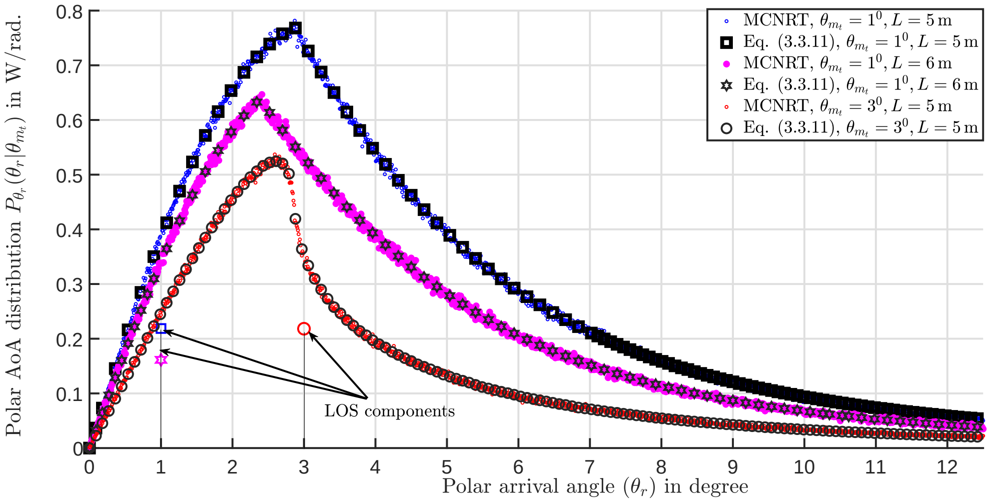

Figure 3.8: Polar AoA distributions (obtained using Eq. (3.3.11)) in coastal seawaters with three settings for the transmitted polar angle (θ_{m_t}) and link length (L).

3.6.2 Results of Polar and Azimuthal AoA Distributions

Figures 3.8-3.10 illustrate the polar and azimuthal AoA distributions in W/rad for the A-MIMO and TA-MIMO links. The LOS component in the figure is not superimposed with single scattering component to show its absolute intensity. The results are obtained analytically (using Eqs. (3.3.11)-(3.3.14)) and verified through MCNRT simulations (Eqs. (3.3.2)-(3.3.4)) with the number of samples equal to $N_s = 10^6$. Figure 3.8 shows polar AoA distributions calculated using Eq. (3.3.11) for the case of coastal seawaters with three settings of; (i) $\theta_{m_t} = 1^o, L = 5\,\mathrm{m}$ (ii) $\theta_{m_t} = 3^o, L = 5\,\mathrm{m}$ and (iii) $\theta_{m_t} = 1^o, L = 6\,\mathrm{m}$. In these settings, the amplitude of the LOS component, as well as peak and dispersion of the distributions decrease with increase in the launching angle and the channel length. Numerically, the amplitude of LOS components are equal to 0.23, 0.23, and 0.18 W/rad, and the PDF peaks are equal to 0.77, 0.52, and 0.65 W/rad for settings (i), (ii), and (iii), respectively. Figure

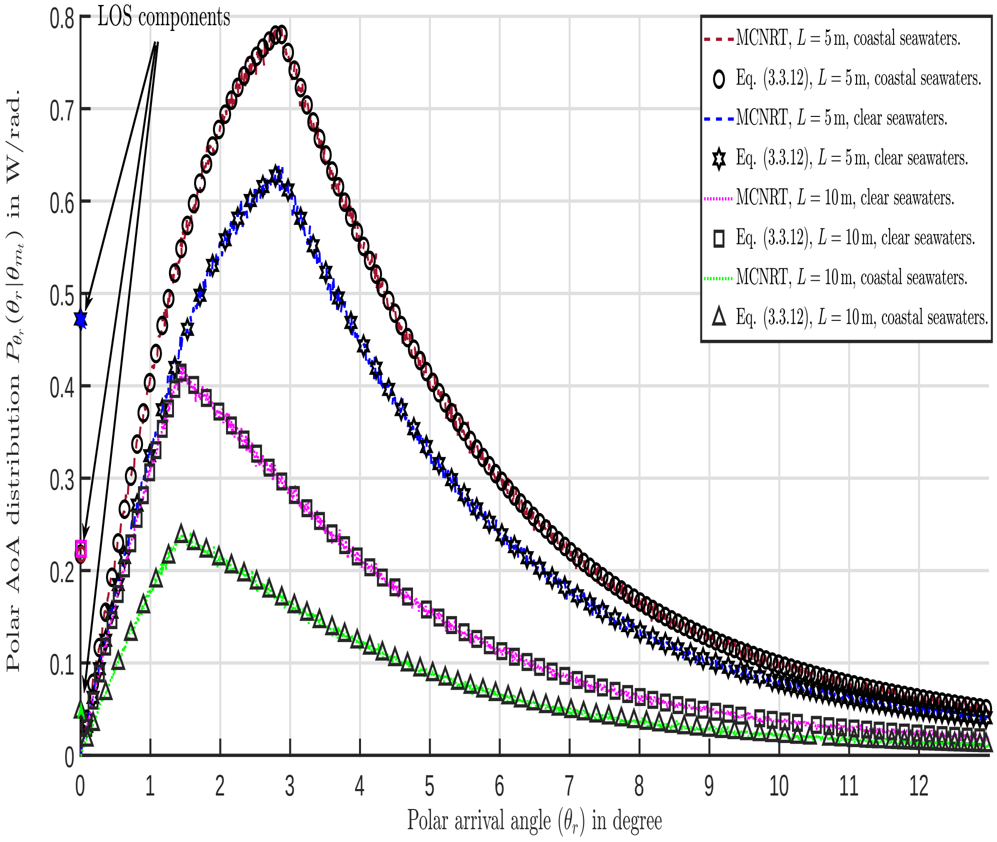

Figure 3.9: Polar AoA distributions with $\theta_{m_t} = 0^o$ (obtained using Eq. (3.3.12)) in clear and coastal seawaters and for link lengths $L = \{5, 10\}$ m.

3.9 shows polar AoA distributions at zero polar launching angle ($\theta_{m_t} = 0$) calculated using Eq. (3.3.12) for clear and coastal seawaters with channel lengths $L = 5$ and 10 m. The effect of seawater type on the LOS component, and peak and dispersion of the distribution can be observed. As expected, the power of the LOS component is larger in clear seawaters, as compared to coastal seawaters. Furthermore, the peak and the dispersion of the distribution are smaller for the case of clear seawaters. Numerically, the amplitude of the LOS components equal 0.47 and 0.21 W/rad, and the peaks equal 0.63 and 0.78 W/rad, for clear and coastal seawaters, respectively, at

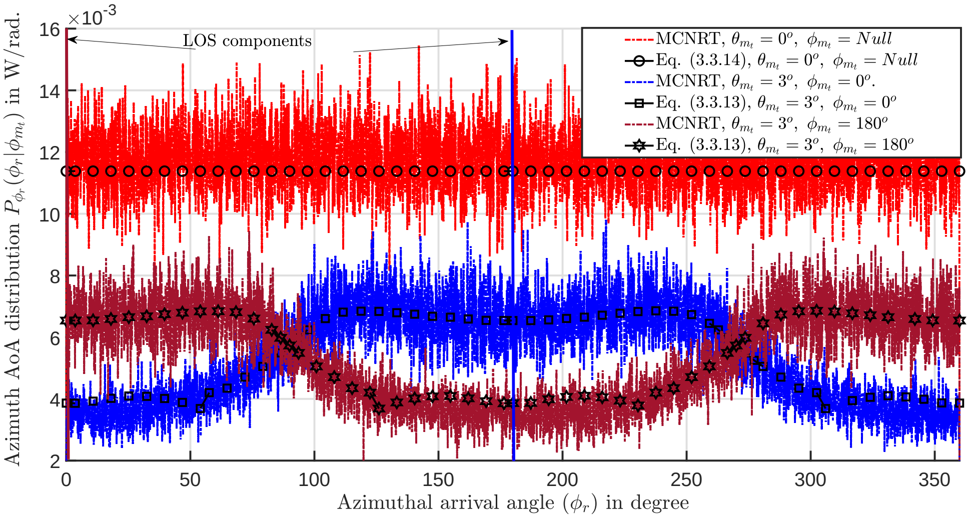

Figure 3.10: Azimuthal AoA distributions (obtained by Eq. (3.3.13)) in coastal seawaters at nominal channel length of 5 m with three settings for polar and azimuthal transmitted angles.

the nominal channel length of $L = 5$ m.

Figure 3.10 shows the azimuthal AoA distributions, calculated using Eq. (3.3.13) for coastal seawaters with the nominal channel length of 5 m and for three settings of: (i) $\theta_{m_t} = 0^o$, (ii) $\theta_{m_t} = 3^o, \phi_{m_t} = 0^o$, and (iii) $\theta_{m_t} = 3^o, \phi_{m_t} = 180^o$. For setting (i), the received distribution is uniform with the value 12×10^{-3} W/rad, while the approximate expression of Eq. (3.3.14) gives 9×10^{-3} W/rad. For settings (ii) and (iii), the corresponding LOS and scattering components are equal due to the symmetry of the transmitter, with peaks around 7×10^{-3} W/rad. Note that, the distributions of settings (ii) and (iii) are relatively lower compared with setting (i), which due to a higher geometric loss for the latter. Lastly, we notice from Figs. 3.8-3.10 that a good agreement between analytical and MCNRT simulation-based results.

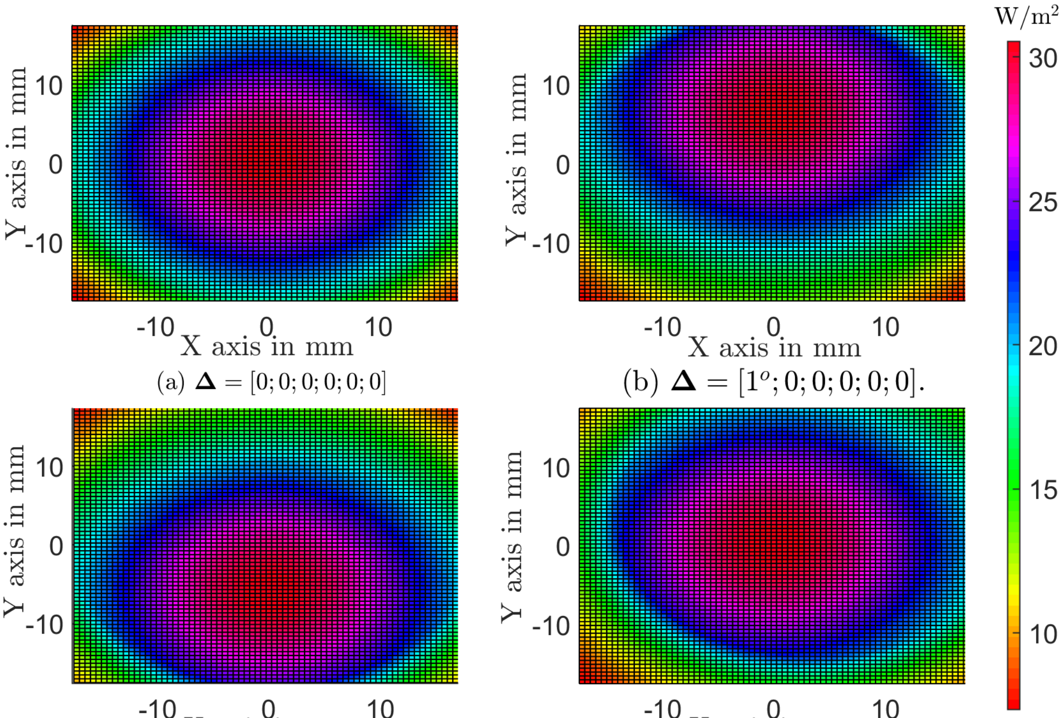

(a) $\boldsymbol{\Delta} = [0; 0; 0; 0; 0; 0]$

(b) $\boldsymbol{\Delta} = [1^o; 0; 0; 0; 0; 0]$.

(c) $\boldsymbol{\Delta} = [1^o; 180^o; 0; 0; 0; 0]$.

(d) $\boldsymbol{\Delta} = [0; 0; 0; 50\,\text{mm}; 50\,\text{mm}; 0]$.

Figure 3.11: PoA distributions (obtained from Eq. (3.3.15) with $\dot{\theta}_{m_t} = 0$) in coastal seawaters at nominal channel length of 5 m with four misalignment conditions (a)-(d).

3.6.3 PoA and TRE Distributions

Figures 3.11, 3.12 and 3.13 illustrate the PoA distribution, the TRE, and the TRE distribution for the TA-MIMO link, respectively. Also, the main results of these figures are summarized in Table III.

The PoA distributions in Figure 3.11 are obtained by using Eq. (3.3.15) for the central LD ($\dot{\theta}_{m_t} = 0$) in coastal seawaters with the nominal channel length. Four conditions are considered: (a) Perfect alignment ($\boldsymbol{\Delta} = [0; 0; 0; 0; 0; 0]$), ($b$) Polar angle misalignment ($\boldsymbol{\Delta} = [1^o; 0; 0; 0; 0; 0]$), ($c$) Azimuthal angle misalignment ($\boldsymbol{\Delta} = [1^o; 180^o; 0; 0; 0; 0]$), and ($d$) Off-axis misalignment ($\boldsymbol{\Delta} = [0; 0; 0; 50\,\text{mm}; 50\,\text{mm}; 0]$),

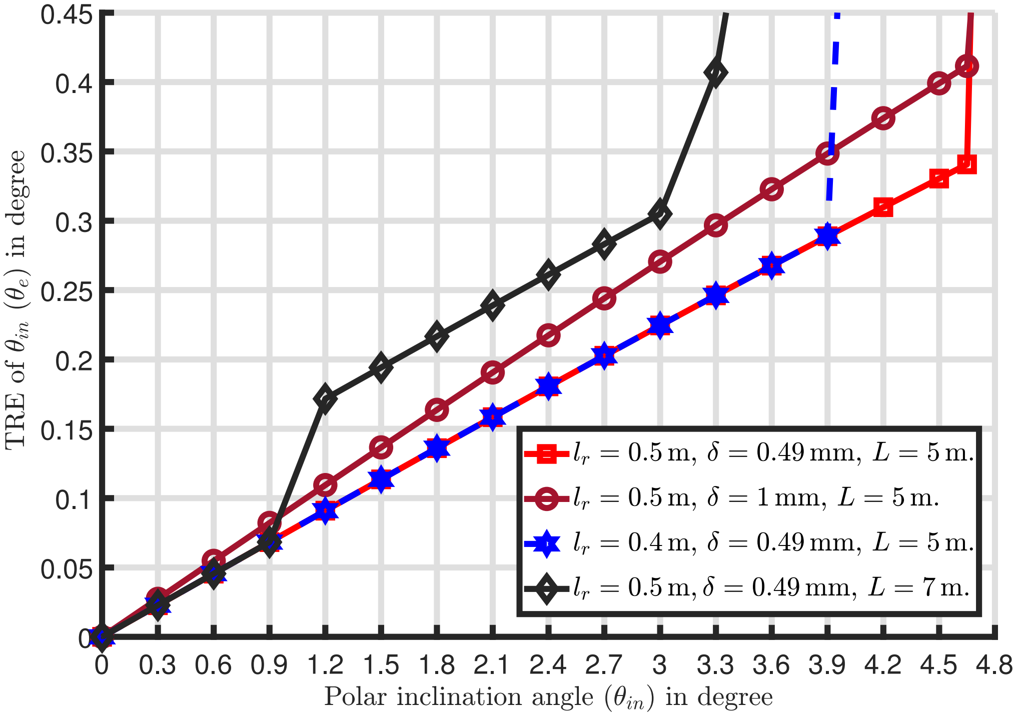

Figure 3.12: Instance TRE of the polar inclination angle (θ_e, obtained by Eq. (3.5.6)) in coastal seawaters with four scenarios for l_r, δ and L.

corresponding to sub-figures (a), (b), (c) and (d), respectively. Notice that the received image is shifted as a result of polar and azimuthal misalignment, as given in Eq. (3.5.3). In case of the off-axis misalignment, the received image endures minimal changes as a consequence of *space-to-angle* mapping. Note that, the small difference between the cases of (a) and (d) is mainly due to slight difference between the scattering and geometric loss conditions for these cases.

Figure 3.12 shows the TRE θ_e at a given inclination misalignment angle θ_{in} in coastal seawaters. The results are obtained by using Eq. (3.5.6) with $\boldsymbol{\Delta} = [\theta_{in}; 0; 0; 0; 0; 0]$. As shown, four scenarios are considered; *(i)* $l_r = 0.5\,\text{m}$, $\delta = 0.49\,\text{mm}$, $L = 5\,\text{m}$, *(ii)* $l_r = 0.5\,\text{m}$, $\delta = 1\,\text{mm}$, $L = 5\,\text{m}$, *(iii)* $l_r = 0.4\,\text{m}$, $\delta = 0.49\,\text{mm}$, $L = 5\,\text{m}$, and

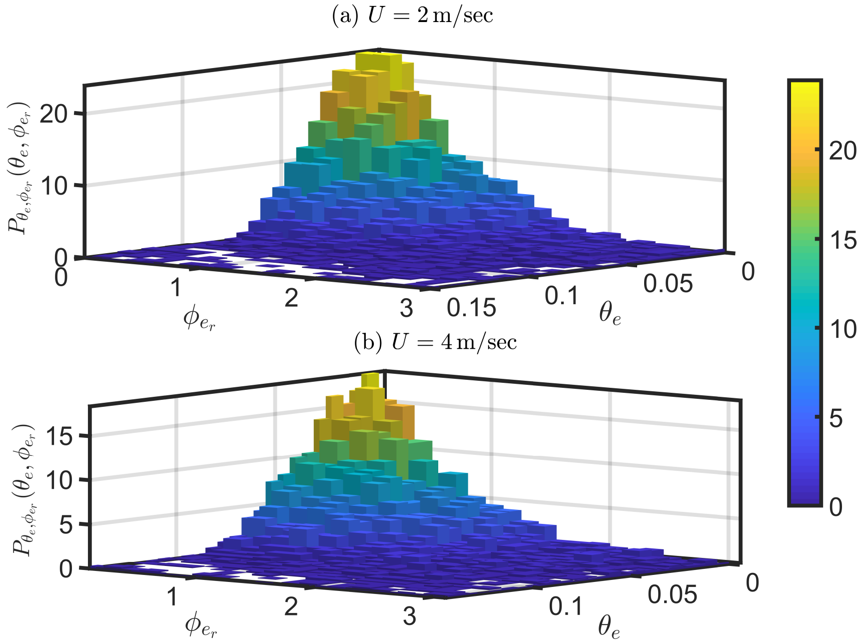

Figure 3.13: Joint probability distributions of TRE ($p_{\theta_e,\phi_{e_r}}(\theta_e, \phi_{e_r})$) for B2F-$S1$ scenario at two wind speeds: (a) $U = 2\,\mathrm{m/sec}$ and (b) $U = 4\,\mathrm{m/sec}$.

(iv) $l_r = 0.5\,\mathrm{m}$, $\delta = 0.49\,\mathrm{mm}$, $L = 7\,\mathrm{m}$. Scenario (i) has the largest lens size, the best resolution (i.e., the lowest value for δ), and the smallest channel length. Thus, this scenario achieves the best performance, i.e., the lowest TRE, among all other scenarios, as can be seen in the figure. The impact of receiver aperture size is apparent by comparing scenarios (i) and (iii). Notice that the larger l_r is, the greater is the range of inclinations θ_{in} that can be estimated since aperture truncation is relaxed as it can be seen from Eq. (3.2.9). Figure 3.13 and Table 3.3 show respectively the joint and marginal PDFs of TRE for scenario $S1$ of the B2F model. The distributions are computed using MCNRT method (Eqs. (3.3.18), (3.4.4) and (3.5.1)-(3.5.6)) under the assumption $\boldsymbol{\Delta} = [\theta_{in}; 0; \phi_{ro}; 0; 0; 0]$ with the number of samples of $N_s = 16000$. The uncertainty due to the relatively small N_s is bounded in Table 3.3 with upper and lower 99% confidence intervals [114].

Table 3.3: Marginal probability distributions of TRE for B2F-$S1$ scenario at three wind speeds

Parameters of $p_{\theta_e}(\theta_e)$ and $p_{\phi_{e_r}}(\phi_{e_r})$	**Wind speed (U) in m/sec**		
	2	4	6
Mean of θ_e	0.08^o	0.12^o	0.34^o
Mode of θ_e	0.03^o	0.03^o	0.1^o
Standard deviation of θ_e	0.23^o	0.25^o	1.05^o
Standard error in mean of θ_e	$\pm0.0045^o$	$\pm0.0049^o$	$\pm0.0207^o$
Mean of ϕ_{e_r}	4^o	6.75^o	10.04^o
Mode of ϕ_{e_r}	1^o	2^o	2^o
Standard deviation of ϕ_{e_r}	10.23^o	12.32^o	13.5^o
Standard error in mean of ϕ_{e_r}	$\pm0.202^o$	$\pm0.2434^o$	$\pm0.266^o$

In Fig. 3.13, the joint PDFs of TRE are evaluated at two wind speeds of $U =$ 2 and 4 m/sec. As shown, $p_{\theta_e,\phi_{e_r}}(\theta_e, \phi_{e_r})$ approaches 2-D negative exponential PDF, where, reasonably, the mean and variance at $U = 4\,$m/sec are higher than those at $U = 2\,$m/sec. To better see the impact of the wind speed on TRE, Table 3.3 presents means, modes, (i.e., peaks) and standard deviations of $p_{\theta_e}(\theta_e)$ and $p_{\phi_{e_r}}(\phi_{e_r})$ distributions for three wind speeds of $U = \{2, 4, 6\}\,$m/sec. Notice that these parameters increase with U. For example, there is a factor of 4 difference between these values for $U = 6\,$m/sec and $U = 2\,$m/sec. Also, the mean and mode parameters of $p_{\phi_{e_r}}(\phi_{e_r})$ at $U = 6\,$m/sec are almost twice those at $U = 2\,$m/sec.

3.6.4 Link Capacity for B2F and M2F Models

Figures 3.14-3.17 show the link capacity of 49 × 49 A-MIMO, TA-MIMO and C-MIMO systems for B2F and M2F communication models. The capacity is calculated using Eqs. (3.4.5)-(3.4.7) and (3.5.7), which are approximated through numerical integration. Errors between the actual and approximate values are bounded according

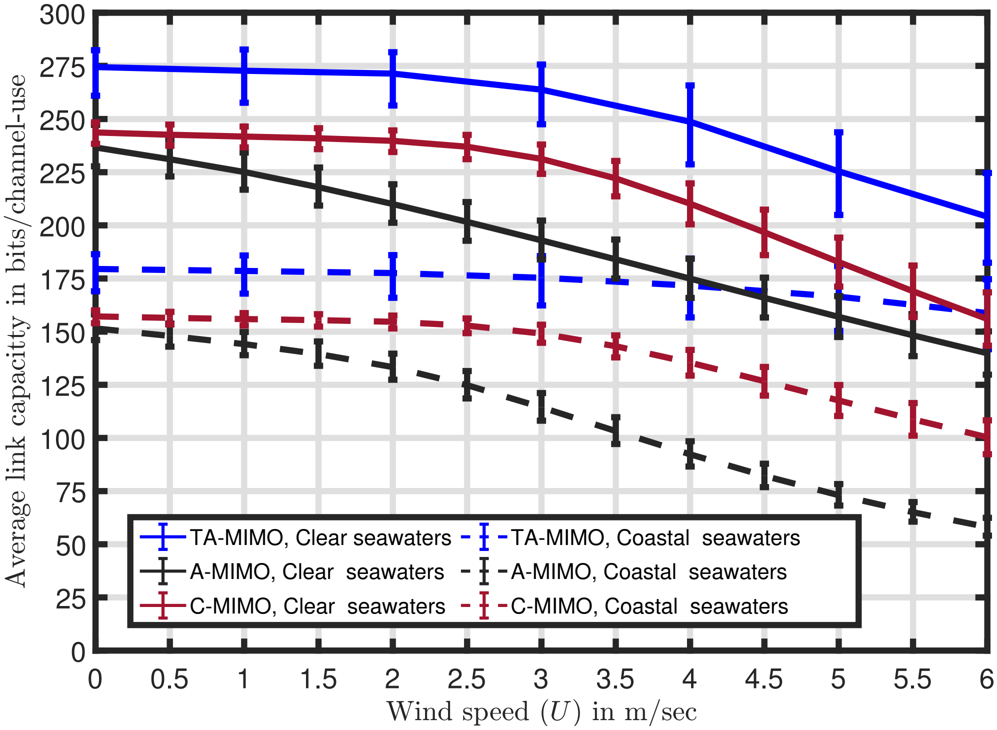

Figure 3.14: Average capacity versus wind speed for scenario of B2F-$S1$ in clear and coastal seawaters with the nominal channel length of 5 m.

to upper and lower Riemann sum theory [115], as shown by error bars in the figures. Under perfect alignment conditions, i.e., $\boldsymbol{\Delta} = [0; 0; 0; 0; 0; 0]$, all links achieve roughly the same capacity of 290 and 185 bits/channel-use in clear and coastal seawaters, respectively.

For the B2F communication model, Figs. 3.14 and 3.15 show the capacity performance versus the wind speed ($U = [0, 6]$ m/sec) in scenarios $S1$ and $S2$, respectively. As shown, the capacity is degraded with increase in the wind speed, causing more orientation misalignments. As expected, the TA-MIMO system gives the best performance, whereas the lowest capacity is achieved for the A-MIMO system. In fact, for A-MIMO and C-MIMO links, the performance degrades faster with wind speed in the

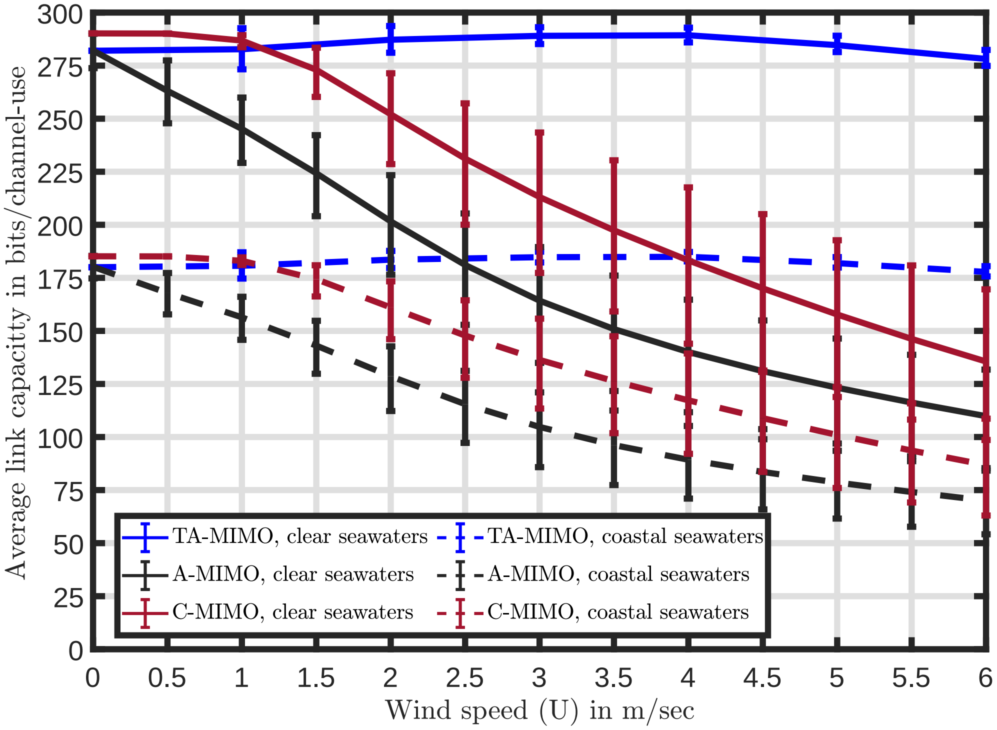

Figure 3.15: Average capacity versus wind speed for scenario of B2F-$S2$ in clear and coastal seawaters with the nominal channel length (i.e. $L = L_o$).

case of scenario $S2$, compared with $S1$. For the TA-MIMO link, the performance is nearly unchanged in the case of scenario $S2$ relative to $S1$. This may be interpreted by the fact that a small TRE ϕ_{e_r} leads to a relatively large TRE θ_e, as mentioned in Section 3.5. For instance, from Fig. 3.14, TA-MIMO, C-MIMO, and A-MIMO systems achieve capacity values of 263 ± 13, 230 ± 5 and 185 ± 13 bits/channel-use, respectively, at $U = 3\,\text{m/sec}$ in clear seawaters. In coastal seawaters, these capacity values decrease to 175 ± 7, 150 ± 5 and 113 ± 10 bits/channel-use, respectively. Also, from Fig. 3.15, TA-MIMO, C-MIMO, and A-MIMO systems achieve capacity values of 285 ± 5, 213 ± 5 and 163 ± 12 bits/channel-use, respectively, at $U = 3\,\text{m/sec}$ in clear seawaters. For coastal seawaters, these capacity values decrease to 180 ± 5, 137 ± 5

and 110 ± 12 bits/channel-use, respectively.

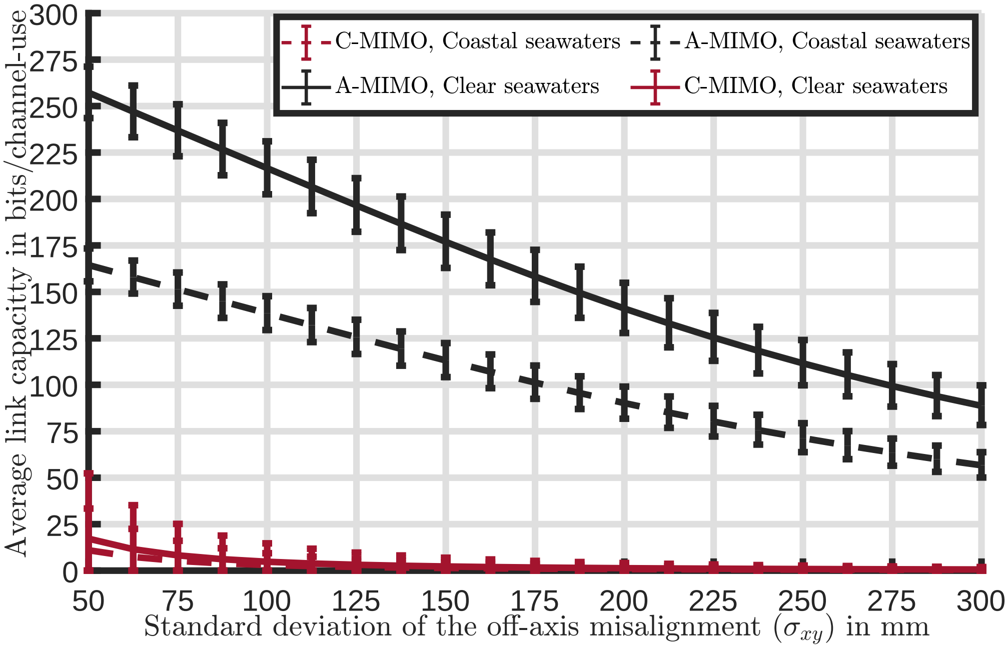

Figure 3.16: Average capacity versus off-axis misalignment standard deviation for scenario M2F-$S3$ in clear and coastal seawaters with the nominal channel length of 5 m.

For the M2F communication model [7], Figs. 3.16 and 3.17 compare the capacity of A-MIMO and C-MIMO systems for scenarios $S3$ and $S4$, respectively. Figure 3.16 shows the capacity versus standard deviation of the off-axis misalignment,σ_{xy}. Notice that at $\sigma_{xy} = 75\,\text{mm}$, the A-MIMO system achieves capacity values 237 ± 25 and 150 ± 7 bits/channel-use in clear and coastal seawaters, respectively, whereas the corresponding C-MIMO capacity values are much lower, i.e., 14 ± 12.5 and 10 ± 9 bits/channel-use. As well, at off-axis misalignment of 300 mm, the A-MIMO system achieves capacity values 55 ± 12.5 and 80 ± 12.5 bits/channel-use in clear and

---

[7] Note that, no numerical results are presented for TA-MIMO in cases of the M2F scenarios, where $L_o < L_{th}$ and no misalignment parameter can be inferred at that length as shown in Fig. 3.6.

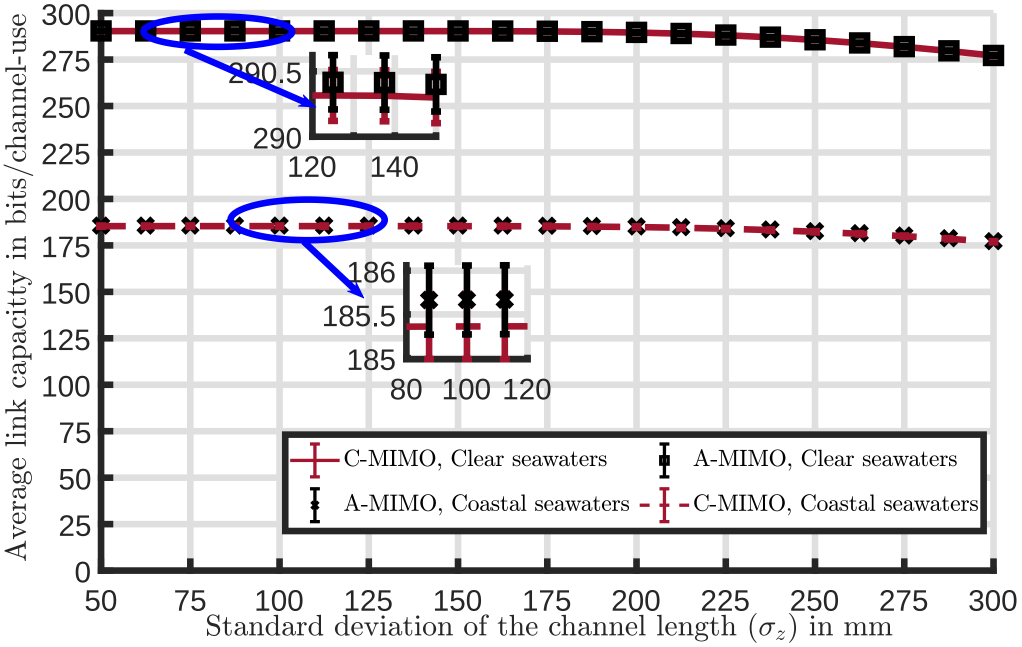

Figure 3.17: Average capacity versus channel length standard deviation for scenario of M2F-$S4$ in clear and coastal seawaters (with mean channel length L_o)

coastal seawaters, respectively, whereas the corresponding C-MIMO capacity values are $1 \pm .5$ bit/channel-use. Note additionally that the capacity decrease for A-MIMO link is due to the increased geometric loss and not due to the off-axis misalignment. These results clearly show that A-MIMO outperforms C-MIMO due to its inherent angle-to-space mapping. Figure 3.17 shows the capacity performance versus standard deviation of the channel length σ_z. The capacity performance is almost fixed for $\sigma_z \leq 225\,\text{mm}$. However, there is a drop of nearly 13 bits/channel-use at $\sigma_z = 300\,\text{mm}$ with respect to the fixed channel length case, i.e., $\sigma_z = 0$. In short range applications, as considered here, the performances of A-MIMO and C-MIMO links are roughly the same in the case of perfect on-axis alignment (i.e., $\sigma_{xy} = 0$). However, the A-MIMO system slightly outperforms C-MIMO, as shown in the enlarged plots. Lastly, note that here we considered scenarios S3 and S4 in order to show the impact of off-axis misalignment and channel length variations independently. However, in a realistic scenario, a M2F system will be displaced in the three axes (i.e. off-axis and length variation) concurrently. The link performance in this realistic scenario can be inferred from the results of Figs. 3.16 and 3.17 together.

3.7 Conclusions and Discussions

In this paper, A-MIMO technique was proposed for short-range high-speed underwater applications, which is more robust against axes-displacement in contrast to C-MIMO technique. The architecture of A-MIMO results in a simple PLT scheme to yield the TA-MIMO system, which estimates the link misalignment. Additionally, a comprehensive link modelling was presented for A-MIMO and TA-MIMO, which is quite useful for the system design.

The presented numerical results demonstrated that C-MIMO generally outperform A-MIMO in the case where angular misalignment dominate, such as those prevalent in the B2F scenario. However, by using the angular information present, the TA-MIMO system can improve over C-MIMO to give high channel capacities. The A-MIMO system, however, greatly outperforms C-MIMO when off-axis misalignment dominate (e.g., in the M2F scenario). By sending information in angular domain, the A-MIMO system is robust against off-axis shifts, and the corresponding capacity remains relatively insensitive to small variations in the channel length.

In realistic scenarios, where both angular and off-axis displacements are present, the choice between A-MIMO and C-MIMO systems depends on the link misalignment conditions. For instance, if the link displacement dominates the misalignment, A-MIMO was shown here to be a good approach to achieve a higher capacity performance. In addition, TA-MIMO is a good choice when both angular misalignment and off-axis displacements are present, so long as the added complexity is tolerable.

The challenges of the implementation of A-MIMO/TA-MIMO systems include the transceiver size, which must be carefully chosen depending on the communication range and the link misalignment. The TA-MIMO system requires a high-resolution PD array, which is associated with the accuracy of the estimation for the relative misalignment between the ends of the link. Lastly, like C-MIMO systems, A-MIMO/TA-MIMO systems are not appropriate solutions in severe scattering channels (i.e., high turbidity seawaters) due to the incurred inter-channel interference.

3.8 Acknowledgements

The authors would like to thank Mr. Khaqan Majeed and Mr. Tau Rasethuntsa for their efforts in proofreading the manuscript.

Chapter 4

Under-Sea Ice Diffusing Optical Communication

Due to the importance of the ice-ocean system on global warming phenomena, earth scientists are interested in deploying AUV swarm underneath sea ice sheets for measuring and observing missions, as mentioned in Section 1.1. Rather than using multi-LED systems [65] as mentioned in Section 1.4, here, sea ice diffusing optical communication (SDOC) systems are proposed for reliable broadband-broadcast communications. SDOC systems are appropriate for high-speed short-range applications for M2Ms links, as illustrated in Sec. 1.1. SDOC systems are diffusing approaches utilizing the nature of sea ice sheets, as discussed in Sec. 1.4.1, and this eliminates the alignment condition between ends of links. SDOC systems also utilize LDs speed and relax the eye-safety restrictions by expanding the laser beam using the transmitter's optics, as explained in Sec. 1.2. SDOC systems are among the first approaches for broadband-broadcast communication proposed for underwater. SDOC channels are modeled using vertical cascaded layers of seawater, sea ice, snow then atmosphere.

SDOC links are modeled in a specific way that simplifies the computation and guarantees the robustness of the results. A new architecture is proposed for SDOC systems to eliminate the impacts of channels and receiver noise. Channel performances are investigated, and system performances are evaluated assuming different communication scenarios consider reasonable assumptions.

The work in this chapter was published in the *journal of IEEE Access [10].* IEEE owns the copyright of the material in this chapter, and it is re-used in the thesis.

Note that additional contributions are provided in **Appendices B and C**. Specifically, **Appendix B** shows details of SSCL models, Table 4.1, and dependency of SSCL models on temperature and salinity values. **Appendix C** shows additional numerical results for impacts of transceiver configurations on channel and system performances. **Appendices B and C** have not been published, and this thesis only owns the copyright of the material in these appendices.

Abstract In this paper, we propose a novel approach to establish a reliable high-speed broadcast communication link between a group of autonomous underwater vehicles (AUVs) swarm under-sea ice. We utilize the fact that sea ice exists above the AUVs to diffuse the optical beam sent from AUV transmitter. We model this channel using a new seawater-sea ice cascaded layers (SSCL) model in which the vertical channel is divided into multiple layers based on their optical characteristics. The diffusing pattern of the SSCL model is computed using Monte Carlo numerical ray-tracing technique. We derive a quasi-analytic equation for the channel impulse response (CIR) which is valid for AUV receivers with different configurations, locations and orientations. The communication performance of underwater sea ice diffusing system is quantified via bit error rate performance, power penalty and and maximum achievable bit rate. Our results reveal that, for a snow-covered sea ice sheet with thickness of 36 cm and bare sea ice sheet with thickness 12 cm, the proposed system can achieve a broadcast communication rate of 100 Mbps with ranges up to 3.5 meters and 3 meters, respectively, with BER less than 10^{-3} and average transmitted power of 100 mW.

4.1 Introduction

Sea ice regions are key zones as they play an important role in climate change and ecosystems of the Earth [116]. They cover roughly 7% and 15% of the earth and the sea-waters, respectively. To understand this rapidly changing environment, researchers have been working on measuring campaigns such as mapping thickness of the sea ice sheets and measuring ice characteristics (e.g., the temperature and salinity) [117, 118]. In addition, it is important to observe, monitor, and protect this ecosystem (e.g., detecting and removing oil spills) [119]. Due to their reliability, cost-effectiveness, and ability to improve human safety, autonomous underwater vehicles (AUVs) are commonly used in under sea ice measurements [117, 118, 119].

A reliable communication link between the AUVs is essential in order for them to work collaboratively to tackle complex tasks, such as the case of cooperative agents in AUV swarms [84, 7, 83]. For any technologies deployed on AUVs, limitations on the size, weight and power consumption are critical [82]. Acoustic, radio frequency, and optical communications are the three main wireless communication systems used in underwater purposes. Compared to both acoustic and radio frequency systems, optical wireless communication (OWC) systems achieve higher transmission data-rate, better power efficiency, and smaller size on the order of cubic centimeters [4, 118].

The mobility of the AUVs, the nature of the sea ice terrain, and presence of the marine groups (e.g., bears, seals, penguins) can degrade the performance of line-of-sight (LOS) OWC systems because of high misalignment and blockage probabilities [66, 67]. While, non-line-of-sight (NLOS) links based on omni-directional sources such as light emitted diodes (LEDs) offer relatively higher reliability, they provide relatively lower speed communication due to their limited modulation bandwidth. In indoor environments, broadcast OWC systems have been proposed where the ceiling, walls and floor have been employed as diffuse reflectors of the optical signal [120]. There has been much work on the optimizing of the diffusing pattern, and the system complexity of such indoor systems to reduce the effects of interference and background noise [121, 122, 123, 124]. Recently, the application of diffusing communication links to underwater scenarios has started to be considered [4]. Arnon *et al.* [78] and Liu *et al.* [125] proposed using seawater-air interface as reflective surface and turbidity seawaters as scattering mediums for NLOS communications, respectively. Anous *et al.* [31] modeled a vertical underwater link taking into account the in-homogeneous nature of the seawater environment with the depth for both LOS and NLOS scenarios. Anous *et al.* used the concept of the layering to discretize the vertical variation in the temperature and salinity profiles of the seawaters. This discretized modeling approach of using multi-layers representing the vertical variation in the temperature, salinity and pressures profiles is commonplace in such systems and widely used in the geoscience literature (e.g., [33, 80, 81, 126, 127]).

In this paper, we propose the concept of *sea ice diffusing optical communications* (SDOCs) where the sea ice is utilized as a diffusing surface with a LD source to establish high-speed short-distance broadcast communication links between the AUVs. Link reliability is improved due to the multiple reflections/scattering from the sea ice and thanks to high impurities contaminating ice mediums and snow caps covering the sea ice sheets. To the best knowledge of the authors, this is the first introduction of this approach in the literature. The main contributions in this paper are summarized as follows:

- For the first time, we introduce a new approach in which the ice sheet is utilized as a diffusing surface to establish reliable diffusing-based broadcast link between underwater AUVs.

- The channel is presented using a seawater-sea ice cascaded layers (SSCL) model where the ice and snow are divided into layers according to the variations in their temperature and salinity profiles.

- In order to obtain transmitter to receiver channel impulse response (CIR), we propose a new simulation methodology consisting of two-steps. In the first step, a Monte Carlo numerical ray tracing (MCNRT) method is used to numerically obtain the ice sheet diffusing pattern. In the second step, the CIR is derived analytically considering the configuration, position and orientation of the AUVs. This methodology reduces the computation time of the CIR, where the first step is computed once, regardless of the number of the receivers, while the second step is only repeated for each receiver.

- An appropriate transceiver is proposed by which the SDOC system achieves a high speed and longer communication range with low bit error rate (BER).
- We numerically investigate the CIR for different sea ices, seawater, and receiver configurations. As well, the performance of the SDOC system is evaluated considering the BER, normalized optical power penalty (NOPP), and maximum achievable bit rate.

The balance of the paper is organized as follows. In Section 4.2, we introduce the SDOC approach and the SSCL channel model. In Section 4.3, we use the MCNRT method to model the upward transmission, then derive a quasi-analytic equation for the CIR. We introduce and model the proposed transceiver architecture in Section 4.4. In Section 4.5, we numerically investigate the channel characteristics and system performance. Finally, conclusions are given in Section 4.6.

4.2 Proposed Sea Ice Diffusing Optical Communication (SDOC) Approach

In this section we introduce the SDOC link as a new approach to establish communication between AUVs operating under sea ice. We discuss the temperature and salinity profile of the sea ice. Then, we introduce a new approach to model optical characteristics of the sea ice.

4.2.1 SDOC Architecture

As shown in Fig. 4.1, we consider a group of AUVs, for example an AUVs-swarm[1], navigating several meters beneath a sheet of sea ice. The AUVs move together in the coordinated fashion with a separation of a few meters. In the proposed approach a broadcast communication link between the AUV transmitter (AUV-Tx) and the AUV receivers (AUV-Rxs) is accomplished in two steps: upward and downward transmissions. In the upward transmission, the AUV-Tx sends a narrow collimated laser beam toward the sea ice. Due to impurities (particles)[2], the transmitted beam is subject to intense scattering at the surface and during propagation in the interior of the ice sheet. Inside the sea ice, a portion of the power will be transmitted through the sheet and lost to the atmosphere. Alternatively, the transmitted light may be trapped in the interior of the sheet where it is absorbed. Finally, a portion of the incident light will be diffused back from the ice sheet into the water. This diffused light which escapes the ice sheet is the useful signal which is used to establish the broadcast

---

[1] Such a swarm typically employs a number of AUVs, however for simplicity, just five AUVs are shown in Fig. 4.1.

[2] In this paper, the term of impurity and particle refer to any of: solid matter, dissolved matter, brine pockets, solid salt, air bubbles or air gaps.

communication link. Given that the light is diffused inside the sheet, as shown in the green ellipse in Fig. 4.1, a wide coverage area is possible. The AUV-Tx can control the position of the diffusing spot by adjusting the direction of the laser beam, i.e., polar and azimuthal launching angles. For instance, if the AUV-Rxs are distributed symmetrically around the AUV-Tx, the beam should be vertically oriented toward the ice sheet to offer a fair coverage for all AUV-Rxs, as shown for the case in Fig. 4.1. However, if the AUV-Rxs are biased to one side, the AUV-Tx can orient its beam toward the direction of the AUV-Rxs to improve link quality. In the downward transmission from the ice sheet, the diffused beam propagates in the seawater and covers the AUV-Rxs with a large spot. Regardless of the position and orientation of the AUV-Rxs, each AUV-Rx receives a portion of this diffused beam, and the AUV-Tx establishes a broadcast communication with the AUV-Rxs.

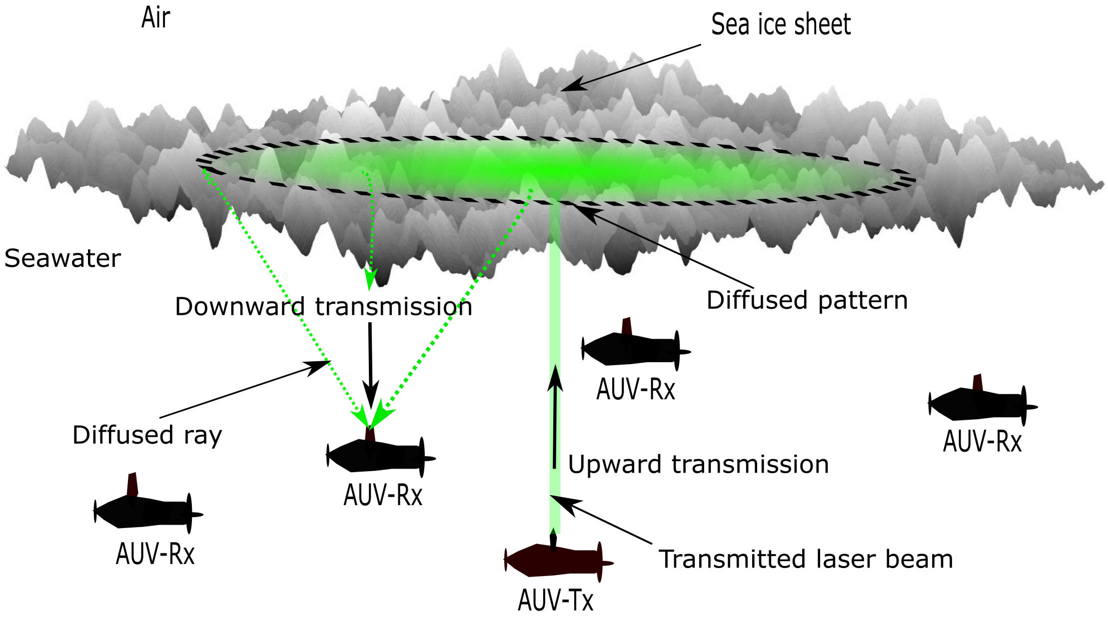

Figure 4.1: A topology for the SDOC approach: AUVs navigate underneath a sea ice and communicate with up and downward transmissions.

The intensity of the diffused optical signal that emanates from the sea ice to the seawater depends on the density of impurities which contaminate the ice sheet as well as the sea ice surface roughness. The optical characteristics (e.g., absorption and scattering coefficients) of the ice sheet are highly affected by changes in impurity density which depend on ice sheet temperature and salinity [37, 128]. Temperature and salinity affect the freezing process of the sea ice which can introduce contaminants such as brine pockets, solid salts, and air bubbles. Given the high values for the temperature and salinity, the ice is most likely contaminated by particles and air bubbles [128]. For sea ice covered by snow, the optical properties will be impacted by temperature changes as well as the gaps between snowflake particles [37].

An example of the measured temperature and salinity profiles shown in Fig. 4.2. This figure represents the temperature and salinity of a 36 cm snow-covered sea ice sheet with 3 cm of snow cap and 33 cm of ice. The shown profiles are measured between November 2007 and June 2008 in the southern Beaufort Sea–Amundsen Gulf, Canadian Arctic [129][3]. As shown in Fig. 4.2, the temperature $T(z)$ and salinity $S(z)$ change with the depth z inside the ice sheet. The two curves in Fig. 4.2 can be well fitted by the following equations

$$T(z) = 0.2668\, z - 10.74 \tag{4.2.1}$$

$$\begin{aligned} S(z) = {} & -3.24 \times 10^{-7}\, z^6 + 3.58 \times 10^{-5}\, z^5 - 1.47 \times 10^{-3} \\ & \times z^4 + 2.74 \times 10^{-2}\, z^3 - 0.205\, z^2 - 0.095\, z + 13.63\,, \end{aligned} \tag{4.2.2}$$

where T is the temperature in Celsius (^oC), S is the salinity in part per thousand

---

[3] Although the given profiles are for specific ice sheet, they hold the common linear relationship and C-shape for temperature T and salinity S, respectively [130].

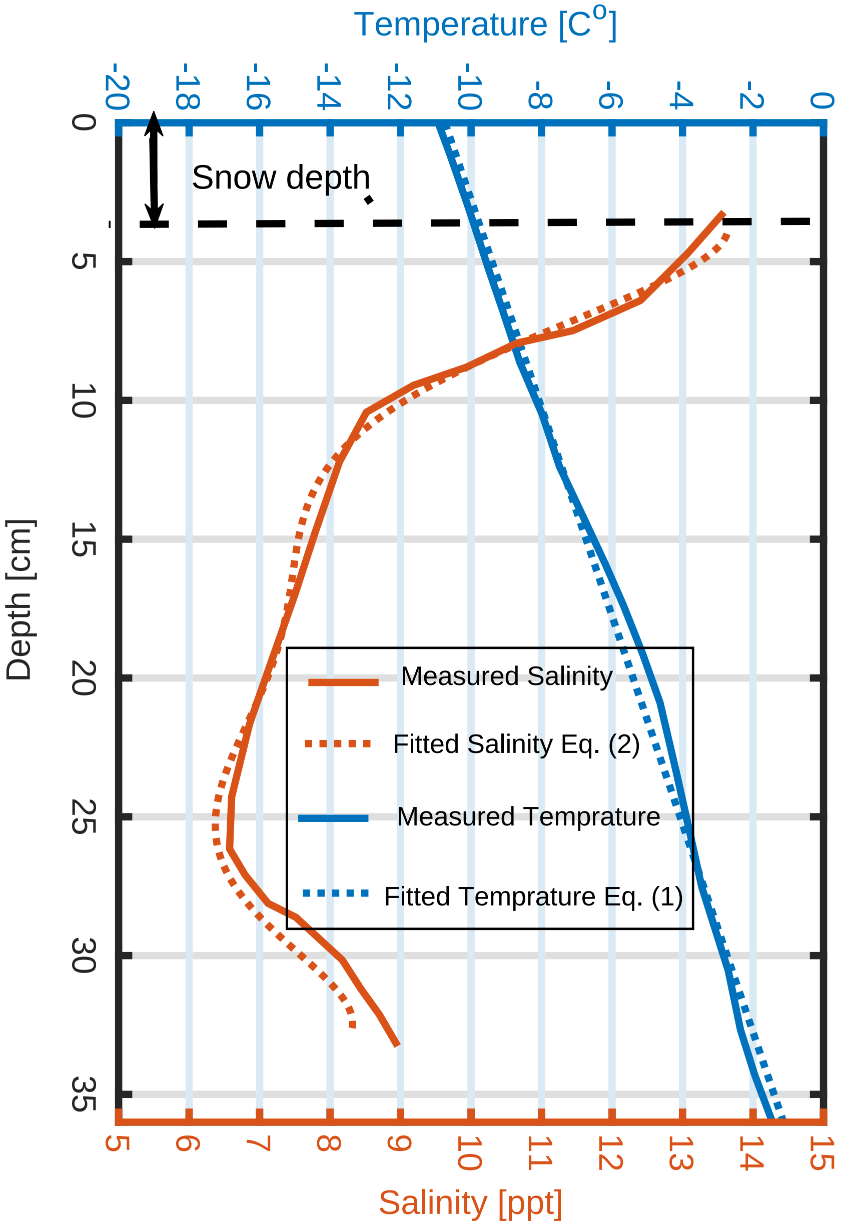

Figure 4.2: The temperature and salinity profiles versus the sea ice depth for a snow-covered sea ice sheet as measured by [129].

(ppt), and $0 \leq z \leq 36$ cm. The equations are shown in the figure, and there is good agreement between the measured and the fitted profiles [4].

Another example is a 12 cm bare-sea ice sheet whose temperature and salinity profiles are shown in [131, Fig. 3]. The sheet is young laboratory-grown saline sea ice. The two profiles of the sheet can be well fitted in $T(z)$ and $S(z)$ functions as[5]

$$T(z) = 1.176\, z - 15.61\,, \quad 0 \leq z \leq 12\text{cm} \tag{4.2.3}$$

$$S(z) = 0.05003\, z^2 - 0.7432\, z + 8.203\ . \tag{4.2.4}$$

These two ice sheet examples will be used later in the numerical results as case studies.

As shown in Fig. 4.2, the top surface of the sea ice is lower in the temperature than the bottom due to a cooling of the atmosphere and a warming of the seawater. As well, the salinity at the top and bottom is much higher than at the middle of the sea ice sheet. The vertical variations in the temperature and salinity with the thickness of the ice sheet result in changes in particle densities, which impact the channel optical characteristics. Given that the scattering inside the ice sheet is extensive and varies through the thickness of the ice sheet, channel modeling is challenging. In the following we introduce a simplified channel model.

4.2.2 Seawater-Sea ice Cascaded Layers (SSCL) Channel Model

In this subsection, inspired by the geoscience literature [37, 128], we propose a SSCL channel model for upward transmission in the SDOC approach. By SSCL, the

---

[4] The corresponding goodness of the fit criteria are; R-square= $\{0.9916, 0.9931\}$ for the temperature and salinity curves, respectively.

[5] The corresponding goodness of the fit criteria are; R-square= $\{0.9997, 0.9788\}$ for the temperature and salinity curves, respectively.

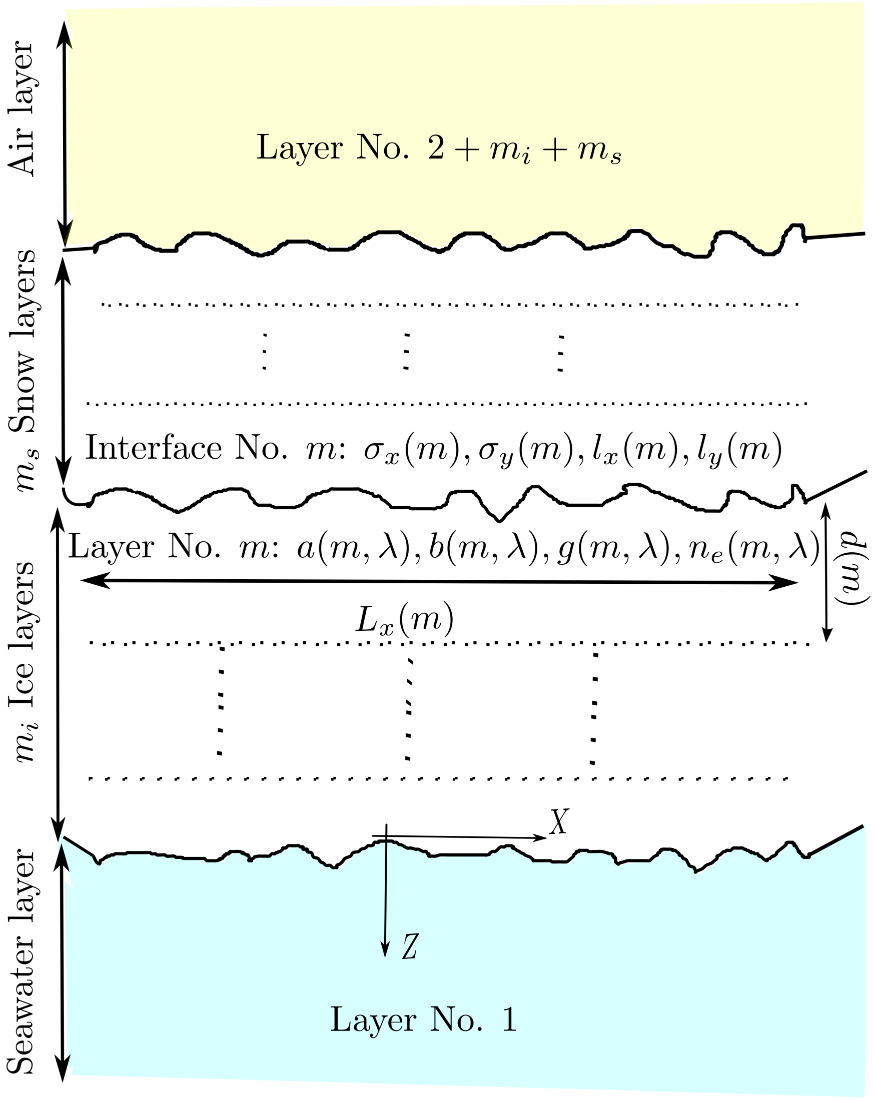

Figure 4.3: The SSCL channel model.

vertical upward transmission link is modelled using cascaded layers of the seawater, ice, snow, and the air as shown in Fig. 4.3. Each of the layers of seawater and air are presented using a single layer since in the scale of few meters range, the particle densities do not change greatly with the depth [80, 81], [132, Ch. 3]. However, as mentioned in the previous subsection, the optical characteristics inside the ice sheet change continuously with the depth. Thus, we divide the ice sheet and snow layers into m_i and m_s of cascaded layers, respectively, over which the temperature and salinity are approximated as being uniform and presented using the average temperature $T(m)$ and average salinity $S(m)$. The thickness of each layer (and consequentially the number of layers) depends on the thickness of the sea ice sheet[6] and the rates of change of the temperature and salinity profiles with the depth. Each layer in the SSCL model is characterized by thickness $d(m)$, lengths of $L_x(m)$ and $L_y(m)$ in x and y axes, respectively, and two rough interfaces between layer and the adjacent ones. By considering a constant temperature and salinity inside each layer, the particle density and the optical characteristics i.e., absorption coefficient $a(m)$, scattering coefficient $b(m)$, and effective refractive index $n_e(m)$ are also constant for each layer in the SSCL model.

Table 4.1: Summary of references used to quantify the surface roughness and optical parameters of the SSCL model.

Surface Scatter Model				
Medium	**Interface Roughness**	**Fixed Particle Density with z?**	**Thickness**	**Layers Numbers**
Seawater and atmosphere		Yes ([80, 81], [132, Ch. 3])	Meters range [80], [132]	Single layer

[134, 135, 136, 137]

Continued on the next page

---

[6] The thickness of the sheet depends on the climate and the location of the sea ice. For instance, Worby *et al.* [133] reported the mean and standard deviation of the ice and snow thickness in Arctic, e.g., 0.87 ± 0.91 and 0.16 ± 0.2 metres, respectively, with a correlation length in kilometre range.

Continued from previous page

Ice and snow		No ([80, 81])	Centimeter range [133, 138]	Multi layers [33, 80, 81]
Particle Scatter Model				
Mixture Particles $j = \{1, 2, ..., J_m\}$	**Absorption Coefficient** $a(m)$	**Scattering Coefficient** $b(m)$	**Asymmetry Parameter** $g(m)$	**Refractive Index** $n(m)$
Seawater Layer $(m = 1)$				
Pure water	[139, Tab. 3]	[140, First term in Eq. (19)]	[141]	[142, Tab. 1]
Chlorophyll-a	[143, Second term in Eq. (16)]	[140, Second term in Eq. (19)]	[141]	[34]
Yellow substance	[144, Eq. (1)]	≈ Zero	Null	[34]
Equivalent Seawater	Eq. (4.2.5)	Eq. (4.2.6)	Eq. (4.2.8)	Eq. (4.2.9)
m_i **Ice Layers** $(m = [2, 3, ..., m_i + 1])$				
Pure ice	[145, Fig. 3]	≈ Zero	*Null*	[142, Tab. 1]

Continued on the next page

Continued from previous page

Brine pocket	$\approx$ Zero	[37, 128]	[38, Fig. 7 (b)]	[38, Fig. 7]
Air bubble	$\approx$ Zero	[33, 37, 128]	[38, Fig. 7 (b)]	[38, Fig. 7 a]
Solid salt	$\approx$Zero	[37, 128, 146]	[38, Fig. 7 (b)]	[38, Fig. 7 a]
Algae	[37, Fig. 7]	$\approx$ Zero	Null	Ref. [34]
Soot	[34, Fig. 13]	$\approx$ Zero	Null	[147]
Equivalent ice	Eq. (4.2.5)	Eq. (4.2.6)	Eq. (4.2.8)	Eq. (4.2.9)
m_s **Snow Layers** $(m = [m_i + 2, ..., m_i + m_s + 1])$				
Air	$\approx$ Zero	$\approx$Zero	Null	≈ 1
Snow grains	[145, Fig. 3]	Eqs. [37], [37]	[56, Fig. 4]	[142, Tab. 1]
Algal impurities	[37, Fig. 9]	$\approx$ Zero	Null	[34]
Non-algal impurities	[37, Fig. 9]	$\approx$ Zero	Null	[34]
Soot	[34, Fig. 13 (a)]	$\approx$ Zero	Null	Ref. [147]
Equivalent snow	Eq. (4.2.5)	Eq. (4.2.6)	Eq. (4.2.8)	Eq. (4.2.9)
Atmosphere Layer $(m = m_i + m_s + 2)$				

Continued on the next page

Continued from previous page

Gases (i.e. free space)	$\approx$ Zero	$\approx$ Zero	Null	1
Snowflakes	[148, Eq. (7)]	[149, Eq. (13)]	[150, Eq. (7)]	[142, Tab. 1]
Rain drops	[148, Eq. (6)]	[151, Eq. (7)]	[152, 153]	[142, Tab. 1]
Fog droplets	[148, Eq. (4)]	[154, Eq. (9)]	[152, 153]	[132, Eq. (27.6)]
Equivalent atmosphere	Eq. (4.2.5)	Eq. (4.2.6)	Eq. (4.2.8)	Eq. (4.2.9)

As shown in Table 4.2.2, each layer in the SSCL model is composed of a mixture of particles, i.e., a hosting medium with additional impurities. For instance, ice layers are composed of the pure ice as a hosting medium with a mixture of particles (e.g., brine pockets, air bubble, solid salt, algae and soot). However, snow layers are composed of air as a hosting medium with a fewer numbers of mixture particles (e.g., snow grains, algal and non-algal particles and soot). Due to these particles, the optical ray propagating inside the m^{th} layer of the SSCL model suffers from absorption and scattering effects. The absorption coefficient, $a(m)$, is the weighted summation of the contribution from the mixture components as [29]

$$a(m) = f_{v_o}\, a_o(m) + \sum_{j=1}^{J_m} f_{v_j}\, a_j(m)\,, \tag{4.2.5}$$

where a_o and f_{v_o} are the absorption coefficient and the volume fraction of the hosting medium, respectively. As well, a_j and f_{v_j} are the absorption coefficient and the volume fraction associated with the j^{th} particle, respectively, where $f_{v_o}+\sum_{j=1}^{J_m} f_{v_j} = 1$. Symbol J_m is the number of mixture particles in layer m, and the value of J_m depends on the hosting medium of the layers and its surrounding environment. The hosting medium does not contribute to the scattering effect, thus, the scattering coefficients for each layer, $b(m)$, are weighted summations of the contribution from the impurity components only as [29]

$$b(m) = \sum_{j=1}^{J_m} f_{v_j}\, b_j(m) \tag{4.2.6}$$

where b_j is the scattering coefficient associated with the j^{th} particle.

Based on the assumptions given in [37, 153], the one term Henyey-Greensteen (OTHG) function is a good approximation to the phase scattering function [90]

$$p_{\theta_s}(\theta_s, m) = \frac{1}{4\,\pi} \frac{1 - g(m)^2}{(1 + g(m)^2 - 2\,g(m)\ \cos(\theta_s))^{3/2}}, \tag{4.2.7}$$

where $g(m)$ is the asymmetry factor and θ_s is a scattering angle. The asymmetry factor is obtained using the weighted sum as [29]

$$g(m) = \frac{1}{b_m(m)} \sum_{j=1}^{J_m} b_j(m)\, g_j(m)\,, \tag{4.2.8}$$

where g_j is the asymmetry factor of the j^{th} particle. The effective refractive index of the layer is computed using the volume fraction f_{v_j} as [155]

$$n_e(m) = f_{v_o}\, n_o(m) + \sum_{j=1}^{J_m} f_{v_j}\, n_j(m)\,, \tag{4.2.9}$$

where n_o is the refractive index of the hosting medium, and n_j is the refractive index of the j^{th} particle.

The interfaces between the adjacent layers are assumed to be rough surfaces which leads to optical surface scattering at the entrance of each layer. The surface roughness of the interface is presented with the random height in the z direction for each point (x, y), which can be well described in the x and y directions using the two-dimensional Gaussian distribution as measured in [134, 135]. To generate a realization of the ice surface, a two dimensional Gaussian random variable is generated with independent components in x and y according to [156]

$$p_{z_m}(z) = \frac{\exp\left(-\left[\dfrac{z^2}{2\,\sigma_x(m)^2} + \dfrac{z^2}{2\,\sigma_y(m)^2}\right]\right)}{\sqrt{2\,\pi\,\sigma_x(m)^2\,\sigma_y(m)^2}} \tag{4.2.10}$$

where z is the height at (x, y) point, and $\sigma_x(m)$ and $\sigma_y(m)$ are the RMS values in x and y directions[7], respectively. As measured in [134, 135], the correlation between heights over the surface is well approximated using the two-dimensional generalized power-law function. Thus, to represent the correlation in space of the surface, the Gaussian realization can be filtered by a generalized power-law function. This function is given

---

[7] The experimental measurements in the Arctic and Antarctic regions revealed that the roughness parameters, RMS and correlation length, are in the millimetre and the centimetre ranges, respectively [136, 137].

with one dimension in [136] and can be generalized to two dimensions $p_{\rho_m}(\rho_x, \rho_y)$ as

$$p_{\rho_m}(\rho_x, \rho_y) = \exp\left(-\left[\left(\frac{\rho_x}{l_x(m)}\right)^{\xi} + \left(\frac{\rho_y}{l_y(m)}\right)^{\xi}\right]\right) , \tag{4.2.11}$$

where ρ_x and ρ_y are the distances between correlated points in x and y directions, respectively, $l_x(m)$ and $l_y(m)$ are the correlation lengths in x and y directions, respectively. The value of ξ depends on the geographical location of the sea ice sheet, and is equal to 1 and 2 in cases of exponential-correlated and Gaussian-correlated surfaces, respectively. Note that, the surface roughness includes parts of the ice suspended in seawater. Due to the low density of these parts, they typically float up toward the ice sheet and settle on its bottom surface [116].

For the reader convenience, a summary of the equations and parameter values needed to quantify surface and optical parameters of the SSCL layers are given in Table 4.2.2. The compositions of each layer in the SSCL model are given in the table with references and equations needed to calculate the optical characteristics of each material.

4.3 The SDOC Link Model

In this section, we obtain an expression for the CIR of links between the AUV-Tx and the AUV-Rxs considering the effects of scattering, attenuation, as well as AUV-Rxs configuration, position and orientation. Here, we introduce a new methodology that consists of two steps to obtain the CIR. In the first step, due to dense scattering occurring in the interior of the sea ice sheet, the upward transmission is evaluated numerically using an MCNRT approach. The MCNRT method obtains the diffusing

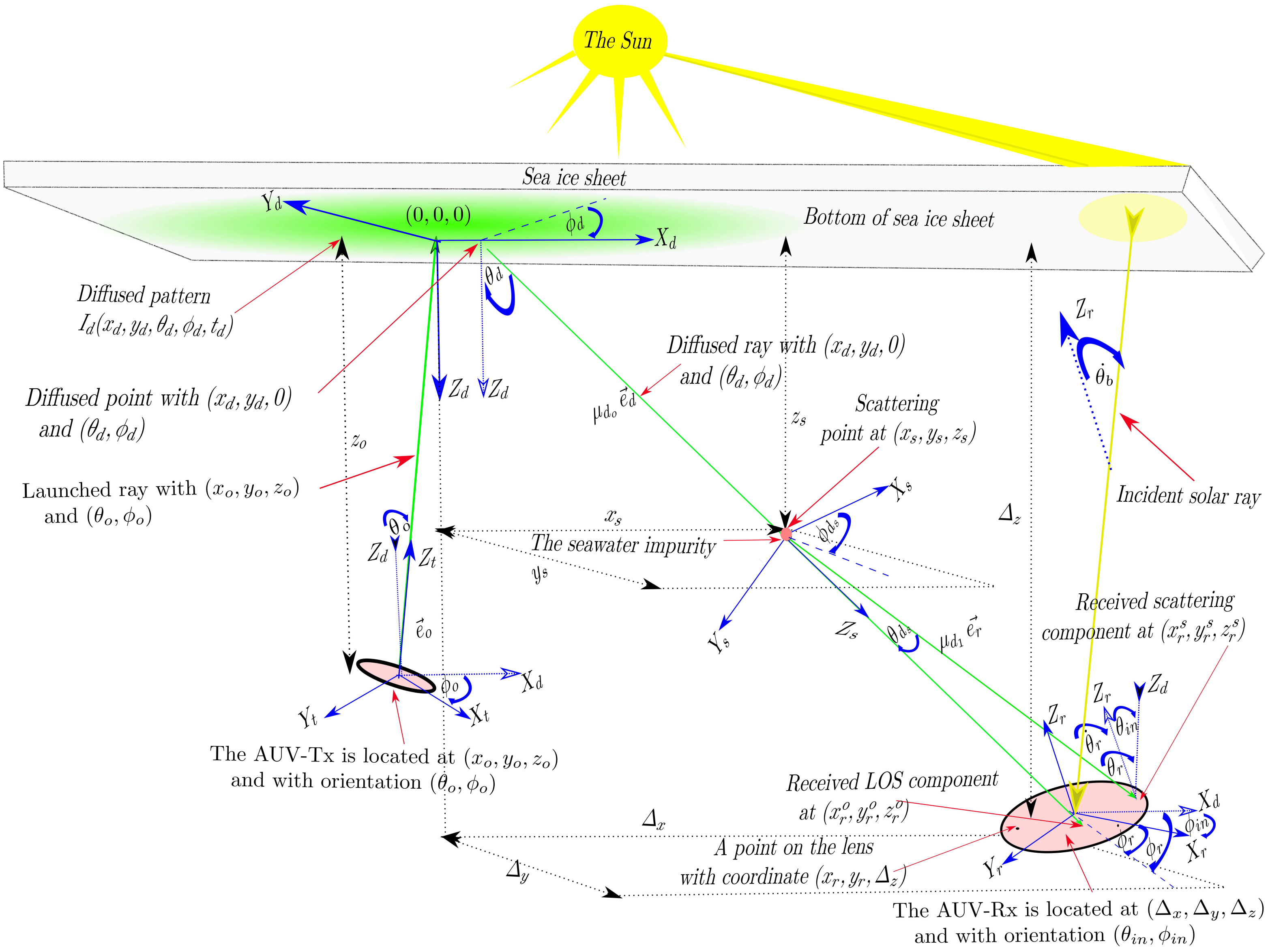

Figure 4.4: A model for the AUV-Tx to an AUV-Rx link (note that, the scattering in the seawater is only shown in the downward transmission for the sake of illustration simplicity.).

pattern (e.g., the green ellipse in Figs. 4.1 and 4.4) that feeds the AUV-Rxs. In the second step, the downward transmission from the bottom of the sea ice sheet to an AUV-Rx is modeled analytically under a single scattering assumption in the seawater layer. This two-step methodology reduces computational complexity where the upward transmission is evaluated once regardless the number of the AUV-Rxs. As well, the CIR equation is a function of the configuration, position and orientation of the AUV-Rxs.

Figure 4.4 shows a link model between AUV-Tx and an AUV-Rx. The distances and angles are measured relative to the diffusing axes, (X_d, Y_d, Z_d), which is centered at the bottom of the sea ice sheet. Relative to these axes, we assume that the AUV-Tx is located at (x_o, y_o, z_o) position and with aperture orientation polar and azimuth angles (θ_o, ϕ_o). While the AUV-Rx is located at $(\Delta_x, \Delta_y, \Delta_z)$ position with aperture polar and azimuthal inclination angles (θ_{in}, ϕ_{in}). Thus, the AUV-Rx position can be described using the position and orientation (PO) vector (5×1) as $\mathbf{\Delta_r} := [\Delta_x; \Delta_y; \Delta_z; \theta_{in}; \phi_{in}]$. The AUV-Rx is equipped with a lens with diameter D_r and field of view (FOV) of θ_{FOV}.

4.3.1 Upward Transmission Model

As shown in Fig. 4.4, the AUV-Tx launches an optical beam with profile I_o, power P_o, wavelength λ_o, and beam width W_o toward the sea ice. The center of the beam is presented by a ray $\vec{e}_o$ with directions (θ_o, ϕ_o) and a photon packet weight

w_o (equivalent to optical intensity). Angles (θ_o, ϕ_o) correspond to intended and non-intended orientation for the optical beam. An intended orientation when is the AUV-Tx directs the optical beam with a specific direction toward the ice sheet. A non-intended orientation occurs disturbances in the environment such as sea currents and waves. Without loss of generality, we assume the spot of the beam on the bottom of the sea ice is centered at the origin, i.e., $(0, 0, 0)$. Thus, the position (x,y) of the AUV-Tx is obtained as $x_o = z_o \sin(\theta_o) \cos(\phi_o)$ and $y_o = z_o \sin(\theta_o) \sin(\phi_o)$. The depth and orientation of the AUV-Tx are noted in a PO vector (3×1) as $\mathbf{\Delta_t} = [z_o; \theta_o; \phi_o]$.

Given the challenge of using analytic approaches to obtain the diffusing pattern produced from the ice sheet in the upward transmission, an MCRT method is used instead. In MCNRT, many optical rays $\vec{e}_o$ are launched from the AUV-Tx to ensure the reliability of the result. The launched rays are diffused due to the surface and particle scattering taken place between and in the layers of the SSCL channel, respectively. The seawater, sea ice, snow and atmosphere layers contribute in producing the diffusing pattern, however, the sea ice and snow layers are the dominant contributors. The surface and particle scattering are simulated using geometric equations and numerical random process with associated PDFs, respectively, as given in the following subsections.

Surface Scattering

Surface scattering occurs when the optical ray strikes the rough interface between the m^{th} layer with refractive index $n_e(m)$ and the $(m+1)^{th}$ layer with refractive index $n_e(m+1)$ in upward propagation. Since $n_e(m) \neq n_e(m+1)$, the optical ray $\vec{e}_o$ incident on the interface with an angle $\theta_i(m)$ is split into a reflected ray $\vec{e}_1$ to the m^{th} layer with an angle $\theta_r(m)$, where $\theta_i(m) = \theta_r(m)$, and a transmitted (i.e., refracted) ray $\vec{e}_2$ to the $(m+1)^{th}$ layer with an angle $\theta_t(m+1)$. The angle of transmitted ray between the m^{th} and $(m+1)^{th}$ layers is given by [157]

$$\theta_t(m+1) = \arcsin\left(\frac{n_e(m)}{n_e(m+1)} \sin\left(\theta_i(m)\right)\right), \tag{4.3.1}$$

where, $\theta_i(m)$, $\theta_t(m+1)$, and $\theta_r(m)$ are measured relative to the local normal of the incident point which has a random direction due the randomness of the surface roughness. The reflection coefficient is computed for non polarized-light[8] using angles $\theta_i(m)$ and $\theta_t(m+1)$ as [157]

$$\begin{aligned} R_s(m) =& 0.5 \left[\left(\frac{\sin(\theta_i(m) - \theta_t(m+1))}{\sin(\theta_i(m) + \theta_t(m+1))} \right)^2 + \right. \\ & \left. \left(\frac{\tan(\theta_t(m+1) - \theta_i(m))}{\tan(\theta_i(m) + \theta_t(m+1))} \right)^2 \right], \end{aligned} \tag{4.3.2}$$

and the corresponding transmission coefficient is obtained as $T_s(m+1) = 1 - R_s(m)$. Accordingly, the reflected and transmitted rays, $\vec{e}_1$ and $\vec{e}_2$, propagate in m^{th} and $(m+1)^{th}$ layers with packet weights $w_1(m) = w_o \times R_s$ and $w_1(m+1) = w_o \times T_s$, respectively.

Particle Scattering

After the optical ray $\vec{e}_1$ enters the m^{th} layer, it will propagate a random distance

---

[8] Modelling using non-polarized light is typical case of scattered light.

$\mu_{u_o}(m)$ with a likelihood of particle scattering $p_\mu(\mu_{u_0}, m)$ given as [158]

$$p_\mu(\mu_{u_0}, m) = c(m)\ \exp[-c(m)\ \mu_{u_o}(m)]. \tag{4.3.3}$$

and the random distance is generated as [158]

$$\mu_{u_o}(m) = -\frac{\log(1-u_\mu)}{c(m)}, \tag{4.3.4}$$

where u_μ is a uniform random variable, $u_\mu \sim U[0,1]$, and $c(m,\lambda)$ is the extinction coefficient of the m^{th} layer representing the loss in the power of the ray. The value of the extinction coefficient $c(m,\lambda)$ is computed as

$$c(m) = a(m) + b(m)\,. \tag{4.3.5}$$

When a scattering event occurs, the weight of the photon packet is dropped to [158]

$$w_3(m) = w_1(m)\frac{b(m)}{c(m)}. \tag{4.3.6}$$

Upon scattering, the optical ray arriving from the direction $\vec{e}_1$ will have a new direction $\vec{e}_3$ determined randomly according to polar and azimuthal scattering angles $(\theta_{u_s}, \phi_{u_s})$. The angle $\theta_{u_s}(m)$ is generated from the OTHG PDF in Eq. (4.2.7) as [158]

$$u_\theta = \int_0^{\theta_{u_s}(m)} p_{\theta_s}(\theta_s, m)\,\sin(\theta_s)\,d\theta_s, \tag{4.3.7}$$

where $u_\theta \sim U[0,1]$. Also, the azimuthal scattering angle ϕ_{u_s} is typically described by a uniform PDF, and it is generated as [90]

$$p_{\phi_s}(\phi_{u_s}) = \frac{1}{2\,\pi}\,, \quad \phi_{u_s} = 2\pi\, u_\phi \tag{4.3.8}$$

where $u_\phi \sim U[0,1]$. After scattering, the ray travels a new distance μ_{u_1} with a new direction $\vec{e}_3$ before the next scattering occurs with likelihood $p_\mu(\mu_{u_1}, m)$. Compared to the seawater and the atmosphere, particle scattering takes place much more frequently in snow and sea ice layers. Typically, the optical ray is scattered few times in the seawater or atmosphere layer, however, hundreds of scattering events can typically take place in the sea ice or snow layers.

The MCNRT traces the optical rays until they are either absorbed, trapped in the ice layer, escape to the atmosphere, or diffuse back into the seawater. The diffused rays only contribute in the obtained diffusing pattern for the upward transmission and the remainder of the rays are considered as lost. For a given position and orientation for the AUV-Tx, $\mathbf{\Delta_t}$, the normalized diffusing pattern is obtained with the intensity I_d as a function of the space, angles and time as follows

$$I_d(x_d, y_d, \theta_d, \phi_d, t_d|\mathbf{\Delta_t}) = \text{MCNRT}\{\text{SSCL}, \mathbf{\Delta_t}, I_o, \lambda_o, W_o\} \tag{4.3.9}$$

where, as shown in Fig. 4.4, the intensity I_d is measured on the bottom of the sea ice surface at position x_d and y_d, with polar θ_d, azimuth ϕ_d angles, and time t_d. As well, the DC gain of the upward transmission G_u is computed using I_d as

$$G_u = \int_{-L_x/2}^{L_x/2}\int_{-L_y/2}^{L_y/2}\int_{0}^{\pi/2}\int_{0}^{2\pi}\int_{0}^{\infty} I_d(x_d, y_d, \theta_d, \phi_d, t_d) \, dt_d \, d\phi_d \, d\theta_d \, dy_d \, dx_d \, , \tag{4.3.10}$$

where $L_x = \max\{L_x(m=2), ..., L_x(m_i + m_s + 1)\}$ and $L_y = \max\{L_y(m=2), ..., L_y(m_i + m_s + 1)\}$ are the considered lengths of the SSCL channel in x and y axes, respectively.

4.3.2 Downward Transmission Model

Figure 4.4 shows a model for the downward transmission which corresponds to the link from the bottom of the sea ice to the AUV-Rx through the seawater channel. A diffused ray emitted from a position $(x_d, y_d, 0)$ in the direction of $\vec{e}_d$ is represented in the figure, where $\vec{e}_d$ is defined as

$$\vec{e}_d = \vec{x}_d \sin(\theta_d)\cos(\phi_d) + \vec{y}_d \sin(\theta_d)\sin(\phi_d) + \vec{z}_d \cos(\theta_d), \tag{4.3.11}$$

where $(\vec{x}_d, \vec{y}_d, \vec{z}_d)$ are the unit vectors in the direction of (X_d, Y_d, Z_d) axes. The impurities in the seawater cause absorption and scattering for the diffused ray $\vec{e}_d$. Under a single scattering assumption, which is reasonable here because the link is short, $\vec{e}_d$ arrives to the AUV-Rx either with LOS (i.e., non-scattering) or after one scattering with the direction $\vec{e}_r$. In the LOS path, the direction is maintained (i.e. $\vec{e}_d = \vec{e}_r$) and the ray arrives with arrival position (x_r^o, y_r^o, z_r^o).

In the scattering path, let (x_s, y_s, z_s) denote the position of the scattering event relative to (X_d, Y_d, Z_d) axes, and with polar and azimuthal scattering angles $(\theta_{d_s}, \phi_{d_s})$

relative to the axes of the scattering (X_s, Y_s, Z_s), as shown in Fig. 4.4. The scattering angles θ_{d_s} and ϕ_{d_s} are computed using Eqs. (4.3.7) and (4.3.8) by replacing angles θ_{u_s} and ϕ_{u_s} with angles θ_{d_s} and ϕ_{d_s}, respectively. The scattered ray arrives to the receiver with polar and azimuthal arrival angles (θ_r,ϕ_r) measured relative to the sea ice axes, (X_d, Y_d, Z_d). For given scattering angles $(\theta_{d_s}, \phi_{d_s})$, the arrival angles ($\theta_r$,$\phi_r$) are computed from ($\theta_d$,$\phi_d$) as follows. Let $\mathbf{e}_d$ be (3×1) vector, represented in (X_d, Y_d, Z_d) as $\mathbf{e}_d$=$[\sin(\theta_d)\,\cos(\phi_d); \sin(\theta_d)\,\sin(\phi_d); \cos(\theta_d)]$. Then, $\mathbf{e}_d$ is rotated around (Y_s, X_s, Z_s) axes by two angles: $\theta_y = \arcsin\left(\cos(\phi_{d_s})\,\sin(\theta_{d_s})\right)$ and $\theta_x = \arcsin\left(\sin(\phi_{d_s})\,\sin(\theta_{d_s})/\cos(\theta_y)\right)$ respectively. Thus, θ_r and ϕ_r are computed as

$$\begin{aligned} \theta_r &= \arccos\left([0,0,1]\,\mathbf{R}_x(\theta_x)\,\mathbf{R}_y(\theta_y)\,\mathbf{e}_d\right), \\ \phi_r &= \arcsin\left(\frac{[0,1,0]}{\sin(\theta_d)}\,\mathbf{R}_x(\theta_x)\,\mathbf{R}_y(\theta_y)\,\mathbf{e}_d\right), \end{aligned} \tag{4.3.12}$$

where $\mathbf{R}_x(\theta_x)$ and $\mathbf{R}_y(\theta_y)$ are (3×3) rotation matrices around(X_d and Y_d axes, respectively [99]. The arrival vector $\vec{e}_r$ is expressed with respect to the axes of the sea ice as

$$\vec{e}_r = \vec{x}_d \sin(\theta_r)\cos(\phi_r) + \vec{y}_d \sin(\theta_r)\sin(\phi_r) + \vec{z}_d \cos(\theta_r)\,. \tag{4.3.13}$$

Vector $\vec{e}_r$ is also characterized by arrivals angles $(\dot{\theta}_r, \dot{\phi}_r)$ measured relative to the axes, (X_r, Y_r, Z_r), as shown in the Fig. 4.4, and can be equivalently written as

$$\vec{e}_r = \vec{x}_r \sin(\dot{\theta}_r)\cos(\dot{\phi}_r) + \vec{y}_r \sin(\dot{\theta}_r)\sin(\dot{\phi}_r) + \vec{z}_r \cos(\dot{\theta}_r)\,, \tag{4.3.14}$$

where $(\vec{x}_r, \vec{y}_r, \vec{z}_r)$ are the unit vectors relative to the Rx axes (X_r, Y_r, Z_r). For the given angles (θ_r, ϕ_r), the angles $(\dot{\theta_r}, \dot{\phi_r})$ are calculated from Eq. (4.3.12) by replacing $\mathbf{e}_d$ with $\mathbf{e}_r$=[$\sin(\theta_r)\ \cos(\phi_r)$; $\sin(\theta_r)\ \sin(\phi_r); \cos(\theta_r)$] and substituting $\theta_y = \arcsin\left(\cos(\phi_{in})\ \sin(\theta_{in})\right)$ and $\theta_x = \arcsin\left(\sin(\phi_{in})\ \sin(\theta_{in})/\cos(\theta_y)\right)$. The scattered ray arrives at arrival position (x_r^s, y_r^s, z_r^s) over the aperture of the AUV-Rx.

The arriving ray from the LOS or scattering path is detected if the position of arrival (x_r, y_r, z_r) is located on the lens of the AUV-Rx with arrival angles $(\dot{\theta_r}, \dot{\phi_r})$ less than half angle of the FOV. This can be compactly represented as the geometric loss G_g and it is written as

$$G_g\left(\mathbf{\Delta_r}\right) = \begin{cases} 1, \text{ if } (x_r, y_r, z_r) \in f_p(D_r, \mathbf{\Delta_r}) \text{ and } \dot{\theta_r} \leq \dfrac{\theta_{FOV}}{2} \\ 0, \quad \text{otherwise}\,, \end{cases} \tag{4.3.15}$$

where $f_p(D_r, \mathbf{\Delta_r})$ represents the spatial extent of the AUV-Rx lens with respect to the sea ice axes (X_d, Y_d, Z_d).

Case 1: Low Scattering Seawater

Consider the case of seawaters with small scattering coefficient (e.g., pure seawater) where the impact of scattering is negligible. In this case, only the LOS component need to be considered [88, 159]. In the LOS path, the direction is maintained (i.e. $\vec{e}_d = \vec{e}_r$), and the amplitude of the optical ray is attenuated according to the Beer-Lambert law. The LOS ray arrives with arrival position (x_r^o, y_r^o, z_r^o), shown in Fig.

4.4, and is computed as [9]

$$
\begin{aligned}
x_r^o &= x_d + \Delta_z \tan(\theta_d) \cos(\phi_d), \\
y_r^o &= y_d + \Delta_z \tan(\theta_d) \sin(\phi_d), \\
z_r^o &= \Delta_z.
\end{aligned}
\tag{4.3.16}
$$

For rays diffused from a single point on the bottom of the sea ice $(x_d, y_d, 0)$, the CIR can be well approximated by a linear combination of LOS components as

$$
\begin{aligned}
P^o(t_r, x_d, y_d) \approx P_o \int_0^{\infty} \int_0^{2\pi} \int_0^{\pi/2} & \left[\exp\left(-l_r^o c\right) \, G_g\left(\mathbf{\Delta_r}\right)\right. \\
I_d(x_d, y_d, \theta_d, \phi_d, t_d) \, \delta & \left.\left(t_r - (t_d + \frac{l_r^o}{\nu})\right)\right] \, d\theta_d \, d\phi_d \, dt_d
\end{aligned}
\tag{4.3.17}
$$

where the length of the LOS path is computed geometrically from the figure as $l_r^o = \sqrt{(x_d - x_r^o)^2 + (y_d - y_r^o)^2 + (z_d - z_r^o)^2}$. The symbols t_r and ν are the arrival time and the light speed in the seawater, respectively, and $\delta(.)$ is the Dirac-delta function.

Case 2: High Scattering Seawater

For the case of seawaters with relatively high scattering coefficient (e.g., clear and coastal seawaters), single scattering is significant relative to the LOS [88, 159]. Thus, both of the LOS and single scattering components are taken into account. Figure 4.4 shows the diffused ray traveling in the direction $\vec{e}_d$ for a distance μ_{d_o} then is scattered in the direction $\vec{e}_r$ and travel a distance μ_{d_1} before arriving the lens. The scattering position (x_s, y_s, z_s) and angle θ_{d_s} are given by [63]

$$\begin{aligned} x_s &= x_d + \mu_{d_0}\,\sin(\theta_d)\,\cos(\phi_d), \quad z_s = \mu_{d_0}\,\cos(\theta_d), \\ y_s &= y_d + \mu_{d_0}\,\sin(\theta_d)\,\sin(\phi_d), \quad \theta_{d_s} = \arccos\left(\vec{e}_d.\vec{e}_r\right)\,. \end{aligned} \tag{4.3.18}$$

This scattering results in a reduction in the photon packet weight of the ray $\vec{e}_r$ by a factor of b/c relative to the packet of the ray $\vec{e}_d$. After scattering and traveling a distance μ_{d_1}, the ray arrives to a position (x_r^s, y_r^s, z_r^s) which is obtained as [63]

$$\begin{aligned} x_r^s &= x_s + \mu_{d_1}\,\sin(\theta_r)\,\cos(\phi_r), \\ y_r^s &= y_s + \mu_{d_1}\,\sin(\theta_r)\,\sin(\phi_r), \\ z_r^s &= z_s + \mu_{d_1}\,\cos(\theta_r)\,. \end{aligned} \tag{4.3.19}$$

Using Eqs. (4.3.11)-(4.3.19), the CIR of single scattering components is derived by using a similar approach as in [88]. For rays diffused from a single point on the bottom of the sea ice $(x_d, y_d, 0)$, the CIR of received signal after single scattering is given as

$$\begin{aligned} &P^s(t_r, x_d, y_d) = P_o \int_0^{\infty}\int_0^{2\pi}\int_0^{\pi/2} I_d(x_d, y_d, \theta_d, \phi_d, t_d) \\ &\Bigg[\frac{b}{2\pi}\ \times \int_0^{2\pi}\int_0^{\pi/2} p_{\phi_s}(\phi_{d_s})\, p_{\theta_s}(\arccos\left(\vec{e}_d.\vec{e}_r\right))\ \times \\ &\sin(\arccos\left(\vec{e}_d.\vec{e}_r\right)) \int_0^{l_r^s} \exp\left(-c\, l_r^s\right)\ G_g\left(\mathbf{\Delta_r}\right)\ \times \\ &\delta\left(t_r - \left(t_d + \frac{l_r^s}{\nu}\right)\right) d\mu_0\, d\theta_r\, d\phi_{d_s}\Bigg]\, d\theta_d\, d\phi_d\, dt_d, \end{aligned} \tag{4.3.20}$$

where the length of the single scattering path is computed as $l_r^s = \mu_{d_o} + \mu_{d_1}$, and μ_{d_1} is computed using Eqs. (4.3.19) and (4.3.18) as

$$\mu_{d_1} = \frac{\Delta_z - \mu_{d_o}\cos(\theta_d)}{\cos(\theta_r)}. \tag{4.3.21}$$

The overall CIR is the summation of the LOS and scattering components, and it is computed using Eqs. (4.3.17) and (4.3.20) as

$$P(t_r, x_d, y_d) = P^o(t_r, x_d, y_d) + P^s(t_r, x_d, y_d). \tag{4.3.22}$$

The CIR for the link between the AUV-Tx and an AUV-Rx with PO vector $\mathbf{\Delta_r}$ is computed by integration over all the points on the bottom of the sea ice (x_d, y_d) as

$$\begin{aligned} P(t_r|\mathbf{\Delta_r}) = \int_{-L_y/2}^{L_y/2}\int_{-L_x/2}^{L_x/2} &[P^o(t_r, x_d, y_d|\mathbf{\Delta_r}) + \\ &P^s(t_r, x_d, y_d|\mathbf{\Delta_r})]\; dx_d\, dy_d \ , \end{aligned} \tag{4.3.23}$$

Equation (4.3.23) can be used to determine the link budget and the induced pulse dispersion. The DC gain of a downward transmission (i.e., AUV-Tx to an AUV-Rx link) is obtained from CIR as [160]

$$h_o(\mathbf{\Delta_r}) = \frac{1}{P_o}\left(\int_0^{\infty} P(t_r|\mathbf{\Delta_r})\, dt_r\right) , \tag{4.3.24}$$

where P_o is the transmitted power as defined in the link model. As well, RMS of the pulse spreading is computed as [160]

$$\tau_{RMS}(\mathbf{\Delta_r}) = \sqrt{\frac{\int_0^\infty (t_r - \tau_o)^2 P(t_r|\mathbf{\Delta_r})^2 \, dt_r}{\int_0^\infty P(t_r|\mathbf{\Delta_r})^2 \, dt_r}}, \tag{4.3.25}$$

where, τ_o is the mean excess delay given by [160]

$$\tau_o(\mathbf{\Delta_r}) = \frac{\int_0^\infty t_r \, P(t_r|\mathbf{\Delta_r})^2 \, dt_r}{\int_0^\infty P(t_r|\mathbf{\Delta_r})^2 \, dt_r}. \tag{4.3.26}$$

The system of Equations, (4.3.11)-(4.3.26), are used to quantify the link performance between the AUV-Tx and the AUV-Rxs as shown in Section 4.5.

4.4 A System Design for SDOC Approach

Though the proposed SDOC approach provides a broadcast communication link without requirement for alignment, its performance is limited by the high channel attenuation and inter-symbol interference (ISI) due to multipath propagation. The ISI is induced mainly by the sea ice sheet in the upward transmission, but also, in the downward transmission due to the scattering occurring in the seawater. In addition, the performance can be degraded by background radiations due to the fact that the AUVs navigate near the bottom of the sea ice and the orientation of the receivers are aligned upwards, as shown in Fig. 4.4. In this section, inspired by indoor OWC systems [120, 121, 122, 123, 124], we propose appropriate Tx and Rx architectures to tackle these limitations. This communication architecture can be considered as a first prototype step in the development of such links. We also discuss practical implementation considerations of SDOC links.

4.4.1 System Model

Figure 4.5 shows the overall block diagram of the proposed SDOC system, as described in the following.

Transmitter

The proposed architecture is shown in Fig. 4.5a. For simplicity, the transmitted data are encoded using intensity modulation direct detection (IM/DD) with non-return-to-zero OOK (NRZ-OOK) modulation scheme [16]. As well, for simplicity, we consider the LD to be switched fully on and off corresponding to ones and zeros of the OOK symbols, respectively, i.e., zero extinction ratio. The OOK symbol duration is T_b, the transmitted data rate is $R_b = 1/T_b$, the electrical bandwidth $B \approx R_b$, the average transmitted optical power is $P_o = p_p/2$, where p_p denotes the transmitted optical power during the on slots. Consider a LD with green wavelength ($\lambda_o = 532$ nm) given its relatively low attenuation in seawater [161]. A beam expander is the LD implemented using two lenses, one lens for beam diverging and other one for beam collimating. This collimated wide beamwidth optical beam helps in transmitting more optical power while keeping the constraint of the maximum permissible exposure (MPE) optical power on the eye [9] regarding eye safety.

---

[9] The typical optical powers used in underwater communication experiments are on the order of fraction of Watt [4], and are far below levels needed to alter the ice surface [162]. Though direct human contact with UAVs is possible, safety must also be considered to preserve wildlife which may interact with these optical emissions [49].

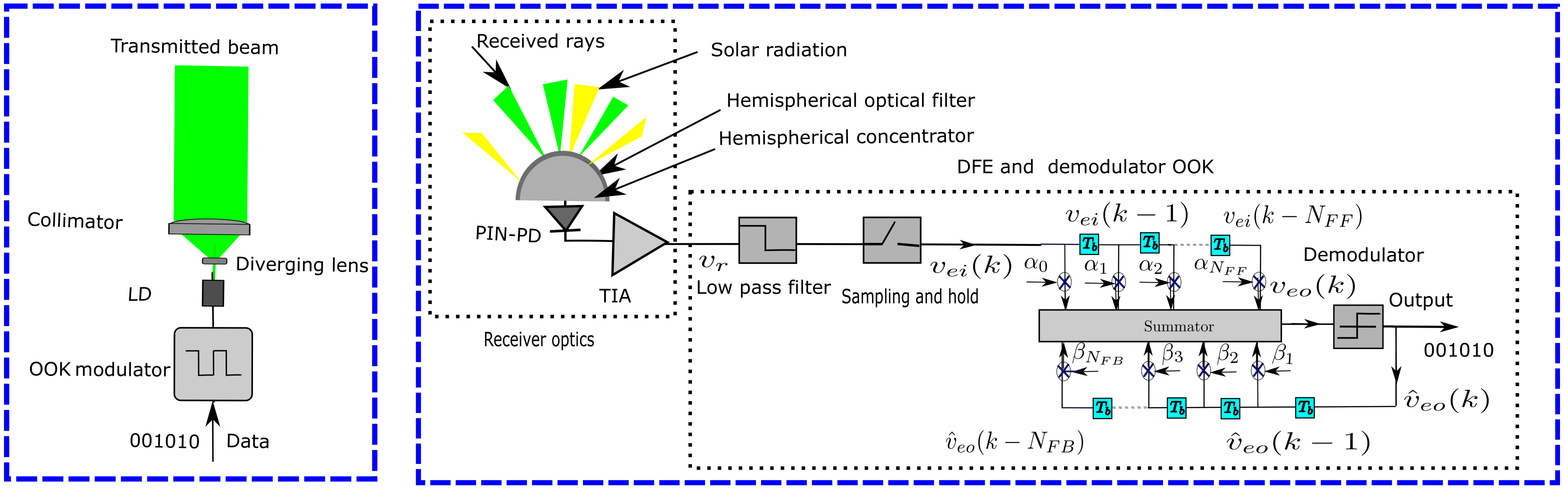

(a) AUV-Tx

(b) AUV-Rx

Figure 4.5: The proposed system architecture for the SDOC approach.

Receiver Optoelectronics

The proposed Rx architecture is shown in Fig. 4.5b. First, the AUV-Rx uses a hemispheric concentrator which is implemented using a hemispherical non-imaging lens coated by a bandpass optical filter as shown. Such a lens with a relatively large diameter, D_r, and a wide FOV, θ_{FOV}, is desired to collect much of diffused rays to compensate SDOC high channel attenuation. As well, an optical filter with narrow bandwidth, $\Delta\lambda$, is preferred to eliminate the incoming background radiation from the sun during the daytime. The concentrator is an essential component in the SDOC approach especially with high background radiation levels at $\lambda_o = 532$ nm [62]. The concentrator is quantified by its gain G_c which depends on its refractive index, n_c, and the FOV as [163]

$$G_c(\dot{\theta}_b) = \begin{cases} \dfrac{n_c^2}{\sin(\theta_{FOV}/2)^2} \quad \textbf{if} \quad \dot{\theta}_b \leq \theta_{FOV}/2\,, \\ 0 \quad \textbf{if} \quad \dot{\theta}_b > \theta_{FOV}/2\,, \end{cases} \tag{4.4.1}$$

where $\dot{\theta}_b$ is the incident angle of the background ray upon the concentrator and it is measured relative to the optical axis of the Rx, Z_r, as shown in Fig. 4.4. As well, the optical band pass filter is quantified by its transmission coefficient $T(\dot{\theta}_b)$ which depends on the incident angle of the received ray. Such hemispheric concentrators are commercially available and have been used in optical diffusing communication systems for indoor applications[10]. The concentrator enlarges the effective area of the PD, A_{ef}, which means capturing solar noise. The effective area of the PD is obtained

---

[10] The optical concentrator and filter with the mentioned specifications can be implemented [42]. However, some customization may be required for use in underwater applications [27].

as [163]

$$A_{ef}(\dot{\theta}_b) = \begin{cases} A_{PD}\, T(\dot{\theta}_b)\, G_c(\dot{\theta}_b)\, \cos(\dot{\theta}_b) \ \textbf{ if } \ \dot{\theta}_b \leq \theta_{FOV}/2 \\ 0 \quad \textbf{if} \quad \dot{\theta}_b > \theta_{FOV}/2 \end{cases} \tag{4.4.2}$$

where A_{PD} denotes the physical active area of the PD. Here, for simplicity, the dependence of the effective area on the incident angle $\dot{\theta}_b$ is represented by replacing $A_{ef}(\dot{\theta}_b)$ by its average $\overline{A_{ef}}$ over the incident angle, while making two assumptions. Firstly, we assume that the function $T(\dot{\theta}_b)$ can be replaced by its average, $\overline{T}$, over all incident angles. This assumption holds, especially, when the incident optical ray arrives within a wide range of the angles which is the typical case of diffusing communications [163]. Secondly, we assume a uniform PDF for $\dot{\theta}_b$. Then, the average Rx effective area is obtained as

$$\overline{A_{ef}} = \frac{2}{\pi} \int_0^{\theta_{FOV/2}} A_{ef}(\dot{\theta}_b)\, d\dot{\theta}_b = \frac{2\, A_{PD}\, \overline{T}\, {n_c}^2}{\pi\, \sin(\theta_{FOV}/2)}\,. \tag{4.4.3}$$

Note that, enlarging the FOV decreases the the average effective area of the Rx.

After the hemispherical concentrator, a silicon PIN photodiode (PIN-PD) with a trans-impedance amplifier (TIA) is used. The PIN-PD converts the collected optical rays to an electrical current proportionally to its responsitivity $\Re$ and A_{PD}. Then, the TIA converts the small current to a high voltage proportionally to its load resistance R_L. In contrast to avalanche photodiodes, photo-multiplier tube and SiPM PDs, the silicon PIN-PD achieves a better performance when the background radiation is much high and dominants the receiver noises [43, 164].

Channel Equalization

Using the described setup, the Rx can overcome the effects of high channel attenuation and background noise. A low pass filter (LPF) is employed after the TIA to eliminate any out-of-band noise, where the filter bandwidth is adjusted according to the actual data rate. The bandwidth of the filter is adopted according to the link speed to maximize the system performance. The output signal of the LPF is sampled with sampling rate T_s, where $T_s < T_b/2$ to avoid aliasing [165]. The sampled signal is then processed by a discrete-time channel equalizer to reduce the impact of ISI. Among the available equalization schemes, the digital decision feedback equalizer (DFE) is chosen due to the mobility of the AUVs [44]. With proper training, the DFE can adapt itself to the changing channel conditions and the PO vector. As well, the DFE coupled with the least mean squares (LMS) algorithm has the advantage of simplicity and is a good choice for non-fading dispersive channels [44]. As shown in Fig. 4.5b, the DFE has two input branches namely, feed forward (FF) and feedback (FB). The input through the FF is the electrical signal from the output of the sampler $v_{ei}(k)$, where k indicates to the index of the received sample. While, the input through the FB is the output of the OOK demodulator $\hat{v}_{eo}(k)$, where $\hat{v}_{eo}(k) \in \{1, 0\}$. The output of the equalizer is the summation of the weighted inputs as follows [44]

$$\begin{aligned} v_{eo}(k\,T_b) = \sum_{j_F=0}^{N_{FF}} \alpha_{j_F}\, v_{ei}(k\,T_b - j_F\,T_b) + \sum_{j_B=1}^{N_{FB}} \beta_{j_B} \\ \times \hat{v}_{eo}(k\,T_b - j_B\,T_b)\,, \end{aligned} \tag{4.4.4}$$

where α_{j_F} and β_{j_B} are the FF and FB weighting coefficients, respectively. Symbols N_{FF} and N_{FB} indicates the number of the tabs used in the FF and FB filters, respectively. The DFE has two operation modes, training and tracking modes. In the training mode, the Tx sends a training sequence which is known to the Rx. The DFE adopts the LMS algorithm to obtain the optimal values for α_{j_F} and β_{j_B} [44]. In the tracking mode, the DFE uses the optimal values obtained for the gains vector to eliminate the effect of ISI in the transmitted OOK symbols. In the next subsection, we discuss the effect of non-ideal performance of the DFE and the different noise sources on the SINR of the SDOC system.

4.4.2 Signal-to-Interference-Plus-Noise Ratio Analysis

During training, the filter coefficients are adapted based on output of OOK decision device and the training sequence [165]. In the tracking mode, assuming that training was successful, error propagation at the output of the decision device should be minimized. Assuming an absence of decision errors, a simple linear model of the the DFE output voltage can be approximated as

$$\begin{aligned} v_{eo}(k\,T_s, \mathbf{\Delta_r}) \approx\ & \underbrace{v_n(k\,T_s, \mathbf{\Delta_r})}_{\text{noise}} + \\ & \underbrace{P_{DFE}(k\,T_s) \otimes \left(R_L\,\Re\left[p(\tau) * P(\tau, \mathbf{\Delta_r})\right]|_{\tau_s = kT_s}\right)}_{\text{signal + residual ISI}} \end{aligned} \tag{4.4.5}$$

where, v_n is the sampled noise voltage, and $\mathbf{\Delta_r}$ is PO vector of the AUV-Rx as defined in the previous section, $P_{DFE}(k\,T_s)$ is the sampled system impulse response of the DFE, $\otimes$ is the discrete convolution operator, $*$ is continuous convolution and $p(t)$ is the instantaneous transmitted optical optical power. The signal in Eq. (4.4.5) can be decomposed as the sum of the desired signal, denoted by $v_s(\mathbf{\Delta_r})$, and the residual ISI denoted by $v_{isi}(\Delta_r)$ where,

$$\begin{aligned} v_s(\mathbf{\Delta_r}) \approx v_n(k\,T_s, \mathbf{\Delta_r}) \,+ & \sum_{k=\tau_d/T_s}^{(T_b+\tau_d)/T_s} P_{DFE}(k\,T_s) \otimes (R_L\,\Re \\ & \times\; [p(\tau) * P(\tau, \mathbf{\Delta_r})]\,|_{\tau_s=kT_s}) \;, \end{aligned} \tag{4.4.6}$$

where τ_d is the time delay of the channel and T_b and τ_d are assumed to be multiples of T_s. Also,

$$\begin{aligned} v_{isi}(\mathbf{\Delta_r}) \approx v_n(k\,T_s, \mathbf{\Delta_r}) \,+ & \sum_{k=(T_b+\tau_d)/T_s}^{\infty} P_{DFE}(k\,T_s) \otimes (\\ & \times\; R_L\,\Re\; [p(\tau) * P(\tau, \mathbf{\Delta_r})]\,|_{\tau_s=kT_s}) \;. \end{aligned} \tag{4.4.7}$$

The noise contribution in (4.4.5) includes the effects of the thermal v_{th} and shot v_{sh} noises, i.e., $v_n = v_{th} + v_{sh}$. The thermal noise v_{th} is well described by zero mean Gaussian distribution with variance σ_{th}^2 given as [61, 166]

$$\sigma_{th}^2 = 4\,R_L K[T(m=1) + 273.15]B, \tag{4.4.8}$$

where, K is the Boltzmann constant and $T(m=1)$ is the temperature of the seawater layer in Celsius as defined in Sec. 4.2.2. Usually, the temperature of the seawater underneath sea ice is $T(m=1) \leq 0\ ^oC$, as shown in Fig. 4.2. On the other hand, the shot noise is associated with the superposition of the desired signal voltage v_s, the ISI distortion voltage v_{isi}, and the background radiation voltage v_{sun}. Due to the high intensity of the solar radiation, the shot noise can be modeled using Gaussian random process with variance given as [61]

$$\sigma^2_{sh}(\mathbf{\Delta_r};\Lambda) = 2\,R_L\,q\,[\Lambda\,v_s(\mathbf{\Delta_r}) + v_{isi}(\mathbf{\Delta_r}) + v_{sun}(\mathbf{\Delta_r})]\,B, \tag{4.4.9}$$

where q is the electron charge in electron-volt units and $\Lambda = 1$ and $\Lambda = 0$ with on and off of the OOK symbols, respectively. The value of v_{sun} is quantified as [43]

$$v_{sun}(\mathbf{\Delta_r}) = \begin{cases} \dfrac{R_L \Re\,(1-G_u)\,\Delta\lambda\,E_s\,\overline{A_{ef}}\,\cos(\theta_{inc})}{\exp(K_d\,\Delta_z)} \\ 0 \quad \textbf{if} \quad \theta_{inc} > \theta_{FOV}/2 \end{cases} \tag{4.4.10}$$

where, the E_s is the spectral solar intensity with unit Watt/(m^2. nm), and K_d is the light diffusion coefficient in the seawater. The value of E_s depends on the weather conditions, as well the zenith angle of the sun [62]. The zenith angle is in range 25^o to 90^o in Arctic and Antarctic regions where frozen oceans exist, and it records a minimum value during the summer seasons [167]. The light diffusing coefficient is related to the seawater parameters by $K_d = a(m=1) + 0.03\,b(m=1)$. The factor of $(1-G_u)$ represents the transmission coefficient of the sea ice sheet. This means a thicker sea ice sheet assists in raising the gain of the upward transmission and in reducing the received background radiations.

The mean η_Λ and the variance σ^2_Λ, $\Lambda \in \{0,1\}$, of the total signal and noise affects system performance are given as

$$\begin{cases} \eta_\Lambda(\mathbf{\Delta_r};\Lambda) = \Lambda\,v_s(\mathbf{\Delta_r}) + v_{isi}(\mathbf{\Delta_r}) + v_{sun}(\mathbf{\Delta_r}) \\ \sigma^2_\Lambda(\mathbf{\Delta_r};\Lambda) = \sigma^2_{isi}(\mathbf{\Delta_r}) + \sigma^2_{sh}(\mathbf{\Delta_r};\Lambda) + \sigma^2_{th} \end{cases} \tag{4.4.11}$$

where σ_{isi}^2 is the variance of ISI signals and it is equal to $R_L\, v_{isi}^2/4$. Thus, the instantaneous SINR, $\gamma(\mathbf{\Delta_r})$, is obtained as

$$\gamma(\mathbf{\Delta_r}) = \frac{[\eta_1(\mathbf{\Delta_r}) - \eta_0(\mathbf{\Delta_r})]^2}{[\sigma_1(\mathbf{\Delta_r}) + \sigma_0(\mathbf{\Delta_r})]^2} = \frac{v_s^2(\mathbf{\Delta_r})}{[\sigma_1(\mathbf{\Delta_r}) + \sigma_0(\mathbf{\Delta_r})]^2}\,. \tag{4.4.12}$$

In the numerical results, we consider three configurations for the AUV-Rxs, namely, unequalized AUV-Rx (Rx-UE), AUV-Rx with DFE (Rx-E), and AUV-Rx with perfect DFE (Rx-PE). The BER of the Rx-E and Rx-UE systems are evaluated numerically using Monte Carlo simulations. However, the BER of the Rx-PE system is evaluated by eliminating the effect of ISI from (4.4.12), i.e. $v_{isi} = 0$, then using the well known AWGN channel as [168]

$$p_e(\mathbf{\Delta_r}) = Q\left(\sqrt{\gamma(\mathbf{\Delta_r})}\right) \tag{4.4.13}$$

where $Q(x) = 1/\sqrt{2\pi}\int_x^\infty \exp(-[z/\sqrt{2}]^2)\, dz$.

4.5 Numerical Results and Discussions

In this section, we numerically evaluate the diffusing patterns of upward transmission, the CIRs of downward transmission, and overall system performance. We assume that the AUV-Tx is located at depth $z_o = 2$ m, and perfectly orientated to the bottom of the sea ice, i.e., $\theta_0 = \phi_o = 0$ and $(x_o, y_o) = (0, 0)$. The AUV-Tx is equipped with a laser source which emits a collimated beam I_o with uniform intensity, wavelength $\lambda_o = 532$ nm, average transmitted power $P_o \leq 200$ mW, and a width of $W_o = 5$ cm to maintain eye-safety. However, we assume the AUV-Rx moves in the x-y plane where the length of the downward transmission does not exceed the limit of the single scattering assumption. Note that the single scattering assumption is valid

Table 4.2: The parameters of seawater bare sea ice and seawater snow-covered sea ice cascaded models.

(a) The Cl-B and Co-B SSCL channels.

Layer No. (m)	$a(m)$ [1/m]	$b(m)$ [1/m]	$g(m)$	$n_e(m)$
$m = 6$ (Clear Air, $T = -14$ C^o, $S \approx 0$ ppt)	0	0	0	1
$m = 5$ (Ice, $T = -13.56$ C^o, $S = 7.19$ ppt)	0.563	480.473	0.9894	1.3494 - 0.0395i
$m = 4$ (Ice, $T = -9.635$ C^o, $S = 5.91$ ppt)	0.492	422.4211	0.9906	1.3496 - 0.0395i
$m = 3$ (Ice, $T = -6.38$ C^o, $S = 5.53$ ppt)	0.483	473.9	0.9923	1.3499 - 0.0395i
$m = 2$ (Ice, $T = -2.6$ C^o, $S = 5.91$ ppt)	0.721	996.81	0.9946	1.3504 - 0.0395i
$m = 1$ (Clear Seawater, $T = 0$ C^o, $S = 5.91$ ppt)	0.069	0.08	0.8708	1.333
$m = 1$ (Coastal Seawater $T = 0$ C^o, $S = 5.91$ ppt)	0.088	0.216	0.9470	1.333

(b) The Cl-S and Co-S SSCL channels.

Layer No. (m)	$a(m)$ [1/m]	$b(m)$ [1/m]	$g(m)$	$n_e(m)$
$m = 9$ (Clear Air, $T = -12$ C^o, $S \approx 0$ ppt)	0	0	0	1
$m = 8$ (Snow, $T = -11.5$ C^o, $S \approx 0$ ppt)	0.282	3.1593×10^3	0.8878	1.1620- 0.0395i
$m = 7$ (Ice, $T = -10.06$ C^o, $S = 11.9$ ppt)	0.532	845.81	0.9900	1.3445 - 0.0395i
$m = 6$ (Ice, $T = -8.56$ C^o, $S = 8.99$ ppt)	0.4661	645.03	0.9903	1.3451 - 0.0395i
$m = 5$ (Ice, $T = -6.57$ C^o, $S = 7.77$ ppt)	0.463	652.64	0.9913	1.3453 - 0.0395i
$m = 4$ (Ice, $T = -4.65$ C^o, $S = 6.66$ ppt)	0.451	760.68	0.9926	1.3455 - 0.0395i
$m = 3$ (Ice, $T = -3.63$ C^o, $S = 7.961$ ppt)	0.4532	724.321	0.9930	1.3454 - 0.0395i
$m = 2$ (Ice, $T = -2.34$ C^o, $S = 7.97$ ppt)	0.684	1334.457	0.9943	1.3457 - 0.0395i
$m = 1$ (Clear Seawater, $T = 0$ C^o, $S = 7.97$ ppt)	0.069	0.08	0.8708	1.333
$m = 1$ (Coastal Seawater $T = 0$ C^o, $S = 7.97$ ppt)	0.088	0.216	0.9470	1.333

(c) The roughness parameters for the interfaces between the layers of the SSCL channel models [136, 137].

The Interface	$\sigma_{x_m} = \sigma_{y_m}$ [mm]	$l_{x_m} = l_{y_m}$ [mm]	The Interface	$\sigma_{x_m} = \sigma_{y_m}$ [mm]	$l_{x_m} = l_{y_m}$ [mm]
Snow-Air	1.2	50	Ice-Snow	2	75
Ice-Air	5	120	Seawater-Ice	2.2	100

with lengths 13.5 and 6.6 m for clear and coastal seawaters, respectively [9]. Note that in in the following results, the particular values for parameters of the AUV-Rx were not optimized for communication performance but were chosen to demonstrate the range of operating conditions of the SSCL channel.

We consider four SSCL channels, namely, a clear and coastal seawater with a snow-covered sea ice sheet (Cl-S and Co-S channels) and the clear and coastal seawater with a bare sea ice sheet (Cl-B and Co-B channels). The snow-covered sea ice sheet has a thickness of 36 cm and it well described by Eqs. (1), (2). The bare sea ice sheet has thickness 12 cm and its temperature and salinity profiles are described by Eqs. (3), (4). We use Eqs. (4.2.2)-(4.2.9) and Table 4.2.2 to calculate the optical and roughness parameters associated with each SSCL layer, where the results are given in Table 4.2.

The bare-ice cases are divided into 6 layers while the snow-covered cases are divided into 9 layers [11]. In all cases, each layer is assigned with the average values of the salinity and temperature using Eqs. (1)-(4), as shown in Tables 4.2a and 4.2b. Clear weather above the sea ice sheets is assumed, which is the typical case during sunny days. As shown in Tables 4.2a and 4.2b, the scattering coefficients of the snow-covered sea ice sheet and coastal seawater are higher than that for bare sea ice sheet and clear seawater, respectively. In addition, it is clear that the changes in the refractive indices and asymmetry parameters are small. In Table 4.2c, the RMS of the roughness and correlation length, are assumed in millimetre and centimetre ranges, respectively, as measured in [136, 137]. As well, we assume isotropic layers (i.e., $\sigma_x(m) = \sigma_y(m)$ and $l_x(m) = l_y(m)$), and the interfaces are Gaussian-correlated (i.e., $\xi = 2$) [134, 135].

---

[11] This is done as a compromise between the accuracy and the computational complexity of the MCNRT method.

The interfaces between the ice layers are assumed smooth due to fact that the variation in the effective refractive indices are negligible in the presented cases. To ensure an accurate realization for the SSCL model, the roughness is sampled with intervals and lengths with values $\delta_x(m) = \delta_y(m) = 0.1\, l_x(m)$ and $L_x(m) = L_y(m) = 60\, l_x(m)$ [169].

4.5.1 Results for Upward Transmission

Figure 4.6 shows the marginalized diffusing patterns[12] for the Cl-B and Cl-S channels with the orange and maroon colors, respectively. The diffusing pattern is measured at the bottom of the sea ice, i.e., $\Delta_z = 0$, with DC gains of $G_u = 0.26$ and 0.37 for Cl-B and Cl-S channels, respectively. These results were obtained by running the MCNRT using the ZeMax Opticstudio software [86] over 10^6 iterations. Note that we have verified that increasing the number of iterations to 10^7 resulted in almost identical results.

Figures 4.6a and 4.6b show the marginalized diffusing patterns versus the polar and the azimuthal angles, $I_{d\downarrow\theta}$ and $I_{d\downarrow\phi}$, respectively. As shown in these figures, the marginalized intensity is uniform with respect to (w.r.t.) ϕ_d, however, it is oriented w.r.t. θ_d with a peak at $\theta_d \approx 45^o$. The orientation indicates non-specular diffusing due to the dense scattering occurred in the sea ice and snow. The value of 45^o is interrupted as the follows; each diffusing point on the sea ice is an identical random variable described by Eq. (4.3.7), and the diffusing pattern is a summation of that diffusing points. Assuming the central limit theory, $I_{d\downarrow\theta}$ approaches the Gaussian with mean 45^o which the mean of the range; 0-90 degrees. In addition, the marginalized

---

[12] The marginalized diffusing pattern with x_d variable, for instance, is obtained by integrating Eq. (4.3.9) over all remaining variables.

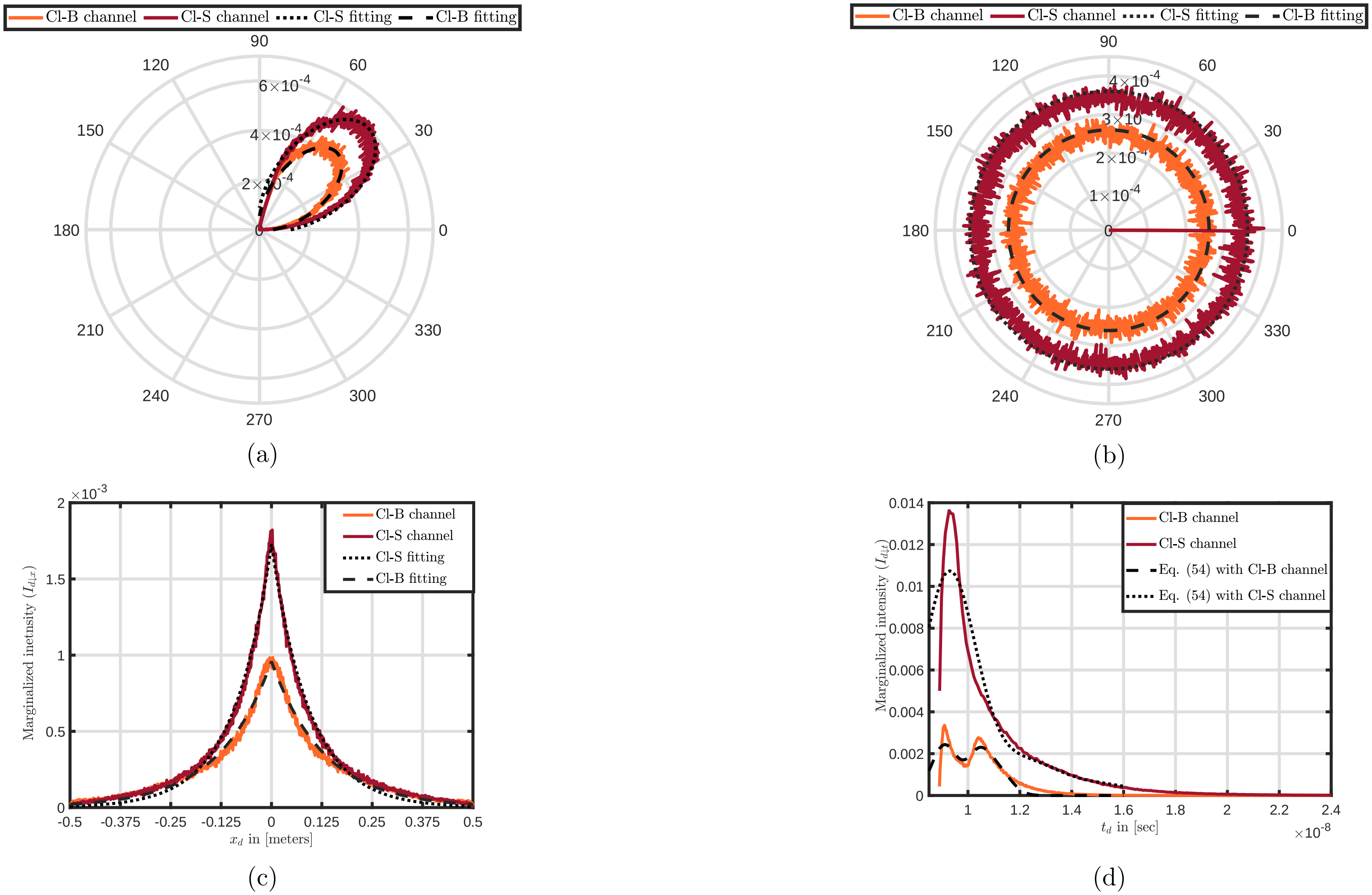

Figure 4.6: The marginalized diffusing patterns (a) $I_{d\downarrow\theta}(\theta_d)$, (b) $I_{d\downarrow\phi}(\phi_d)$, (c) $I_{d\downarrow x}(x_d)$, and (d) $I_{d\downarrow t}(t_d)$. The results are shown with the orange and maroon colors for the Cl-B and Cl-S channels, respectively. The fitting curves are indicated using black dashed and dot lines for the Cl-B and Cl-S channels, respectively.

intensity in case of Cl-S channel is relatively higher than the case of Cl-B channel. Specifically, the peaks of the marginalized intensities in Fig. 4.6a are 6×10^{-4} and 4×10^{-4} for Cl-S and Cl-B channels, respectively. Furthermore, the marginalized intensities in Fig. 4.6b are 3.5×10^{-4} and 2.5×10^{-4} for Cl-S and Cl-B channels, respectively. The pattern in these figures can be fit to two-dimensional Lambertian and uniform functions in θ_d and ϕ_d respectively, for both Cl-B and Cl-S channels [13]

$$I^{\text{Cl-S}}_{d\downarrow\theta,\phi}(\theta_d, \phi_d) = 4.438 \times 10^{-5} \cos^{6.6}(\theta_d - 0.248\,\pi)\,, \tag{4.5.1a}$$

$$I^{\text{Cl-B}}_{d\downarrow\theta,\phi}(\theta_d, \phi_d) = 6.032 \times 10^{-5} \cos^{6.5}(\theta_d - 0.242\,\pi)\,. \tag{4.5.1b}$$

Figure 4.6c shows the marginalized intensities $I_{d\downarrow x}$ versus the distance $x_d = [-0.5, 0.5]$ m. The intensities decay exponentially with peaks 1×10^{-3} and 1.8×10^{-3} at the center, $x_d = 0$ m, for the Cl-B and Cl-S SSCL channels, respectively, and almost zero value at $|x_d| = 0.5$ m. Due to the uniform value of the marginalized intensities w.r.t. ϕ_d, the intensity profiles for x_d and y_d are similar and can be fitted with the following two-dimensional functions for the Cl-B and Cl-S SSCL channels

---

[13] In this paper, the fitting is accomplished using the tool of curve fitting in Matlab [97, CFTOOL]. The goodness of the fit R-square= $\{0.8574, 0.8714\}$ and RMSE= $\{5.95 \times 10^{-6}, 7.606 \times 10^{-6}\}$ for Cl-B and Cl-S channels, respectively.

as[14]

$$I_{d\downarrow x,y}^{\text{Cl-B}}(x_d, y_d) = \frac{0.591}{10^3}\exp(-10.95\,|x_d| - 11.3\,|y_d|)\,, \tag{4.5.2a}$$

$$I_{d\downarrow x,y}^{\text{Cl-S}}(x_d, y_d) = \frac{1.466}{10^3}\exp(-15.41\,|x_d| - 15.46\,|y_d|). \tag{4.5.2b}$$

Though, the diffusing pattern has a small spot on the bottom of the sea ice sheet (i.e., $|x_d|$ and $|y_d| \leq 0.5$ m), due to the orientation with angle 45^o, the spot expands out with the propagation in the seawater as shown in the next subsection.

Figure 4.6d shows the marginalized diffusing pattern $I_{d\downarrow t}$ (i.e., temporal dispersion patterns of the upward transmission) with $t_d = [2, 24]$ ns. The pattern of the Cl-S channel has a high peak with amplitude 14×10^{-3} and it decays slowly with a long dispersion time due to the thickness and much particle scattering occurred for the laser beam in the channel as can be seen from Table 4.2b (i.e., a larger thickness, and higher temperature and salinity values). In contrast to the Cl-S channel, the pattern of the Cl-B channel has two peaks with amplitudes 32×10^{-4} and 26×10^{-4}. The time interval between the two peaks is nearly equal to the time taken by the optical ray to propagate from the bottom to the surface of the ice sheet. Thus, the shown dispersion pattern can reveal information about the thickness of the bare sea ice sheets whilst performing a communication function. The shown time dispersion

---

[14] The corresponding goodness of the fit criteria are; R-square= $\{0.9053, 0.9261\}$ and RMSE= $\{1.522 \times 10^{-5}, 2.505 \times 10^{-5}\}$ for Cl-B and Cl-S channels, respectively.

patterns can be fitted to a sum of Gaussian functions in t_d as[15]

$$I_{d\downarrow t}(t_d) = \sum_{i=1}^{3} \alpha_i \exp\left(-\left(\frac{t_d - \beta_i}{\gamma_i}\right)^2\right). \tag{4.5.3}$$

Equations (4.5.1)-(4.5.3) serve as a guide for a future analytic model for the upward transmission. The equations are shown with dotted lines in Fig. 4.6. We notice a good agreement between the equations and MCNRT results in space but less accuracy for the temporal dispersion patterns. Note that we also tested other fitting functions proposed in the literature for underwater CIRs in other scenarios (such as double gamma weighted [53], combination of exponential and arbitrary power [54], and Beta Prime distributions [55]), however, Eq. (4.5.3) provided a much better in fit for SDOC. In fact, the fitting is challenging due to the dense scattering taken place in the channel. Thus, further investigation is required to obtain more accurate equation as a future work.

4.5.2 Results for Downward Transmission

In this subsection, we demonstrate numerical results for the CIR, DC gain H_o, and the delay spread τ_{RMS}. The results are obtained using equations (4.3.23)-(4.3.26), and take into account the effects of the type of the sea ice, seawater, Rx configuration, and the position of the AUV-Rxs. The position and FOV parameters in the following were chosen to show there scope of operating characteristics for the SSCL channel. The optimization of these parameters for maximize communication performance is

---

[15] For Cl-B channel, the coefficients α_i, β_i and γ_i are $\{2.405 \times 10^{-3}, 1.931 \times 10^{-3}, 1.025 \times 10^{-3}\}$, $\{9.093 \times 10^{-9}, 1.041 \times 10^{-8}, 1.121 \times 10^{-8}\}$, $\{7.041 \times 10^{-10}, 6.492 \times 10^{-10}, 7.043 \times 10^{-10}\}$, respectively. As well, For Cl-S channel, the coefficients α_i, β_i and γ_i are $\{1.059 \times 10^{-2}, 1.547 \times 10^{-3}, 5.333 \times 10^{-4}\}$, $\{9.274 \times 10^{-9}, 1.206 \times 10^{-8}, 1.492 \times 10^{-8}\}$, $\{1.465 \times 10^{-9}, 1.817 \times 10^{-9}, 2.262 \times 10^{-9}\}$, respectively.

left as future work.

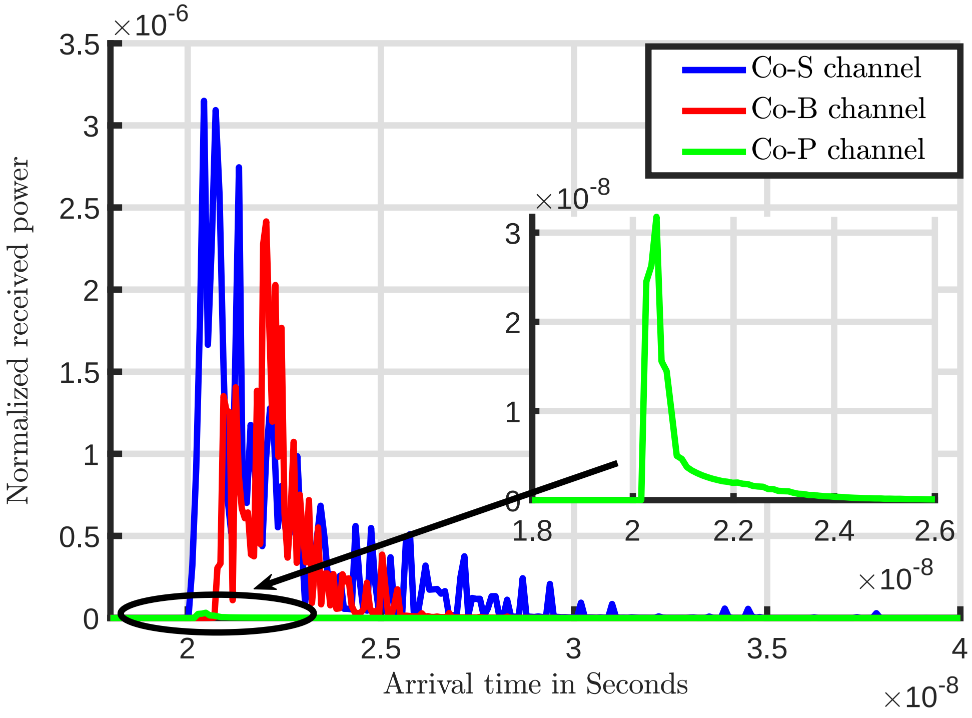

Figure 4.7: The effects of the sea ice on CIR with ($\theta_{FOV} = 140^o$, $D_r = 15\,\text{cm}$) and position $\{\Delta_x, \Delta_y, \Delta_z\} = \{2, 0, 3\}\,\text{m}$.

Impact of Sea Ice

Figures 4.7 shows the normalized received power versus arrival time (i.e., CIR) for the case of coastal seawaters and different types of ice sheet, namely, Co-S, Co-B and coastal-pure (Co-P)[16] channels. The AUV-Rx has the parameters $\theta_{FOV} = 140^o$ and $D_r = 15\,\text{cm}$, and is located at the position ($\Delta_x = 2, \Delta_y = 0, \Delta_z = 3\,\text{m}$). As shown in

---

[16] Co-P SSCL channel is the coastal seawater cascaded with a free-impurity sea ice, i.e., a perfect transparent sea ice. This pure sea ice rarely exists on the frozen oceans, and it is considered here just as benchmark.

the figure, the snow-covered sea ice sheet records the highest CIR amplitude and the largest dispersion thanks to the dense scattering occurring through its layers, as given in Table 4.2b. The Co-B channel shows a lower CIR amplitude and a relatively narrow dispersion due to a lower scattering coefficient as compared to the Co-S channel, see Tables 4.2a and 4.2b. The CIR of the pure sea ice sheet channel records the smallest amplitude and dispersion because there are no particles to scatter from inside the sheet. This result is likely to arise when the sea ice is thinned, such as when a part of the sea ice sheet melts in the summer season. The channel time delay, τ_d, takes its smallest value in the case of Co-S channel, which due to the fact that the second layer in the Co-S channel ($m = 2$) has a larger scattering coefficient with contrast to the second layer in the Co-B channel, see Tables 4.2b and 4.2a. Numerically, the peaks of the CIRs are 3.1×10^{-6}, 2.4×10^{-6} and 3.2×10^{-8}, and the delay spreads are 15×10^{-9}, 8×10^{-9} and 4×10^{-9} sec for the Co-S, Co-B and Co-P SSCL channels, respectively.

Impact of Seawater

Figure 4.8 shows the CIR for an AUV-Rx with $\theta_{FOV} = 90^o$ and $D_r = 15\,\text{cm}$ at position $(\Delta_x = 3, y = 0, \Delta_z = 2\,\text{m})$ bellow a bare sea ice sheet. The CIRs are shown for the Co-B, Cl-B and a Pu-B SSCL channels, where Pu-B denotes pure seawater cascaded with the bare sea ice sheet[17] (i.e., $a(m = 1) = 0.053\ \text{m}^{-1}, b(m = 1) = 0.003\,\text{m}^{-1}$) [159]. Here, we used the bare-sea ice which has less scattering compared to snow-covered sea ice, this makes the effect of the seawater on the channel more significant.

---

[17] The pure seawater rarely exists underneath the frozen oceans, and it is considered here for comparison.

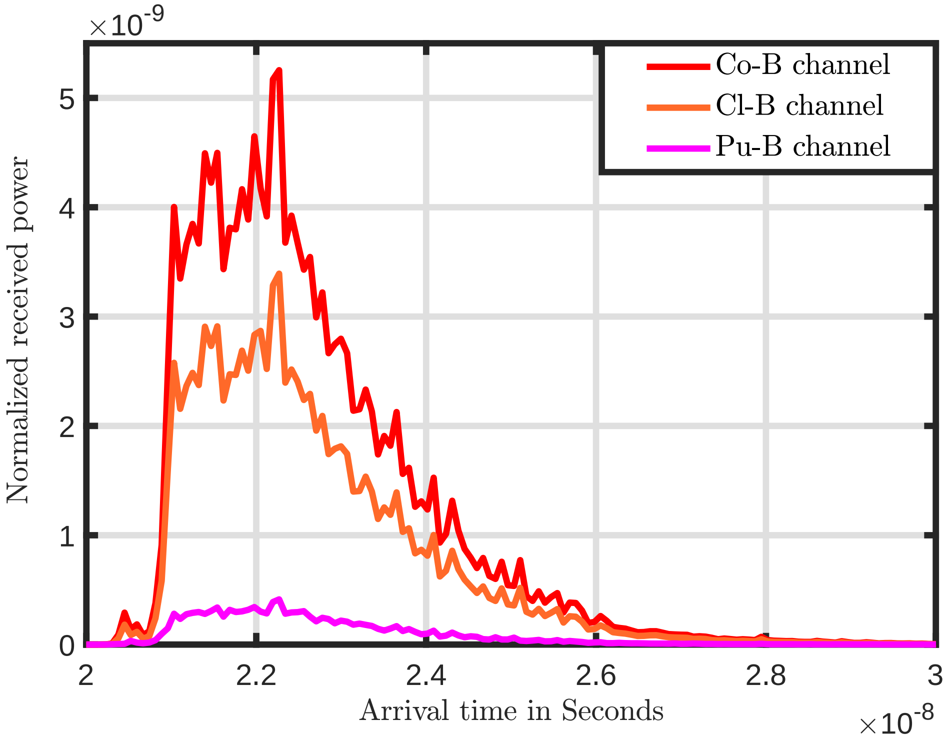

Figure 4.8: The effects of the seawater on CIR with ($\theta_{FOV} = 90^o, D_r = 15\,\text{cm}$) and position$\{\Delta_x, \Delta_y, \Delta_z\} = \{3, 0, 2\}\,\text{m}$.

At a distance of $\Delta_x = 3$ m from the AUV-Tx, the FOV does not see the diffusing spot on the bottom of the sea ice. Thus, the amplitude of the CIR depends on beam scattering in the sea water. As shown in the figure, the case of coastal seawater has the highest amplitude and largest dispersion due to particle scattering. However, pure seawater provides the AUV-Rx with the less significant CIR. Numerically, the peaks of the CIRs are 5.2×10^{-9}, 3.4×10^{-9} and 2×10^{-10}, as well, and the delay spreads are 8×10^{-9}, 8×10^{-9} and 4×10^{-9} sec for the Co-B, Cl-B, and P-B SSCL channels, respectively.

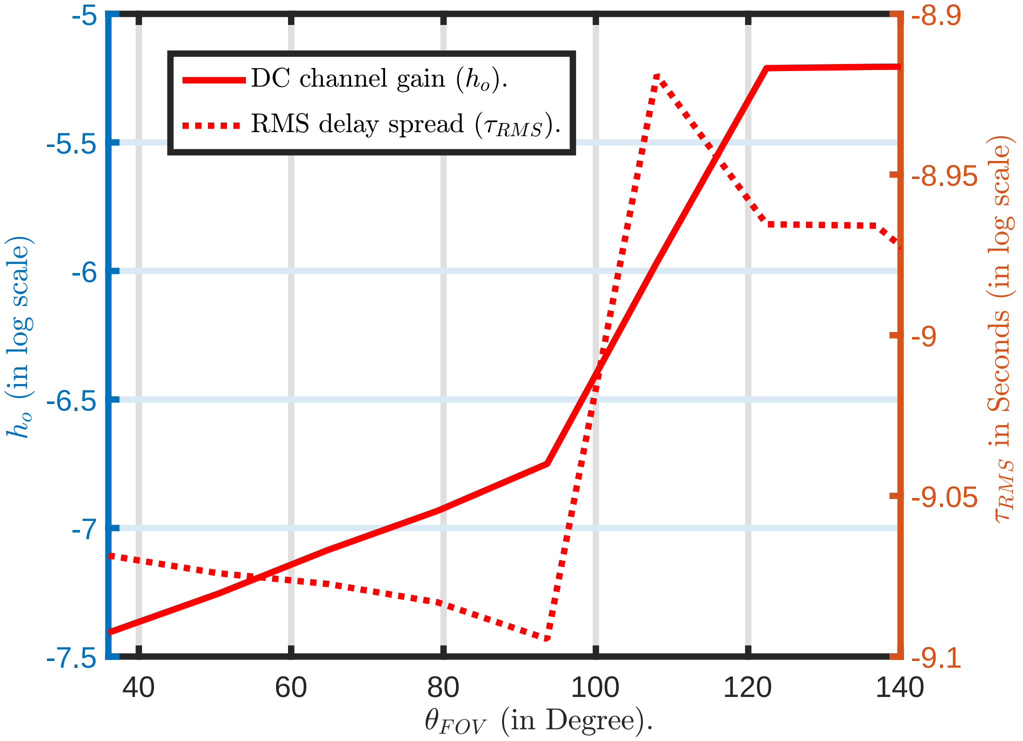

Figure 4.9: The effects of the FOV on h_o and τ_{RMS} with $D_r = 10$ cm at position $\{\Delta_x, \Delta_y, \Delta_z\} = \{3, 0, 2\}$ m and Co-B channel.

Effects of FOV

Figure 4.9 shows the DC gain and delay spread of the channel versus the Rx FOV for AUV-Rx located at position ($\Delta_x = 3, \Delta_y = 0, \Delta_z = 2\,\text{m}$). In general, increasing the FOV leads to the collection of more rays and improves the DC gain. However, the rate of change in the DC gain with the FOV ($\partial h_o/\partial\text{FOV}$) depends on the location of the AUV-Rx with respect to the diffusing surface. For the given case study in Fig. 4.9 and according to the geometry of the topology, the receiver aperture begins to receive a direct signal from the diffusing surface at a computed FOV $= 102.7^o$ and receives signals from the complete diffusing surface at a computed FOV $\geq 120.5^o$. The computed FOVs are shown in the figure with values 93^o and 122^o, respectively, due to the impacts of the orientation of the diffusing beam with angle 45^o and scattering occurring in the coastal seawater. This observation can help explain the results given in the figure as follows. When the FOV changes from 36^o to 93.6^o, the rate of change in $\partial h_o/\partial$FOV is 0.0456 per degree. As the FOV increases further, it starts to collect rays with high energy from the diffusing surface. Thus, when the FOV changes from 93.6^o to 122^o, the rate of change increases to $\partial h_o/\partial$FOV is 0.2137 per degree. Increasing the FOV further (FOV $\geq 122^o$), there is no additional improvement in the DC gain since nearly all power is collected.

On the other hand, the RMS delay spread depends on the time of diffusing t_d (4.3.9) in addition to the time taken to propagate from the bottom of the sea ice to the lens of the Rx (i.e., the distance $\mu_{d_o} + \mu_{d_1}$, see Fig. 4.4). In general, the value of t_d is a smaller for diffused rays that leave the sea ice close to the origin of the diffusing spot than for those rays that are further away. However, the propagation time from the sea ice to Rx for rays near the diffusing spot is longer than those further away. The RMS delay spread of the link is thus impacted by the balance of diffusing and propoagation times. Qualitatively, when $\theta_{FOV} \leq 97^o$, the Rx does not see the diffusing spot origin directly and the RMS delay spread is dominated by t_d. That is, the total time of propagation will be close to the mean value resulting in a smaller RMS delay spread. However, as FOV increases, i.e., $97^o \leq \theta_{FOV} \leq 107^o$, the received rays from the diffusing spot with longer propagation time dominate increasing the delay spread. Finally, for $\theta_{FOV} \geq 107^o$, the AUV-Rx receives diffused rays arriving from both the origin of the diffusing spot, $\{x_d, y_d\} \approx 0$, as well as diffused rays over a wider area of the ice sheet which contributes to a reduction in the delay spread.

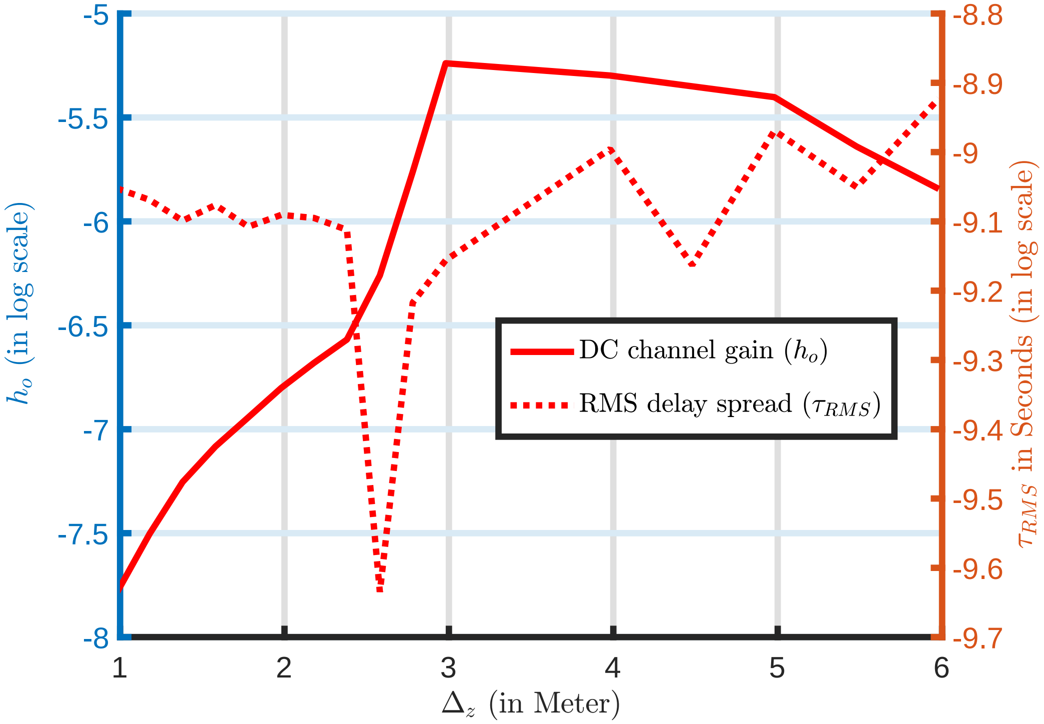

Figure 4.10: The effects of the depth on h_o and τ_{RMS} with ($D_r = 10$ cm, $\theta_{FOV} = 90^o$) at x-y position $\{\Delta_x, \Delta_y\} = \{3, 0\}$ m and Co-B channel.

Impact of Depth

Figure 4.10 shows the DC gain and delay spread of the channel versus the depth, Δ_Z, for an AUV-Rx with lens diameter $D_r = 10$ cm and $\theta_{FOV} = 90^o$. The AUV-Rx is located at a relatively long distance from the origin of the sea ice, ($\Delta_x =$ 3m, $\Delta_y = 0$) m. The AUV-Rx captures more diffused rays with increasing depth in the rang $\Delta_z = [1, 3]$ m, then, the power captured decays with range for $\Delta_z \geq 3$ m, as shown. This phenomena can be interpreted as follows. The spatial coverage of the diffusing pattern, in the x-y plane, extends with the depth due to two reasons. Firstly, the orientation of the diffusing pattern with the polar angle as shown in Fig. 4.6a. Secondly, the scattering taking place in coastal seawater contributes more in extending the spatial coverage of the diffusing pattern. However, for $\Delta_z \geq 3$ m, the DC gain decays with the depth, due to the absorption taking place in the coastal seawater which dominates the impact of scattering. Numerically, the rate of change in the gain with the depth, $(\partial h_o/\partial(\Delta_z))$, is fixed in the range $\Delta_z = [1.5, 2.5]$ m with value $\partial h_o/\partial(\Delta_z) = 0.6860$ per meter, however, it is higher in the range $\Delta_z = [2.5, 3]$ m with value $\partial h_o/\partial(\Delta_z) = 2.1419$ per meter. On the other hand, the delay spread reaches to its minimum value at depth $\Delta_z = 2.7$m as shown. This occurs since the lens (with $\theta_{FOV} = 90^o$ and at location $\Delta_x = 3$) captures the LOS rays diffused from points close to the diffusing spot on the bottom of the sea ice. These LOS rays arrive with high amplitude and small propagation times, resulting in the RMS delay spread attaining its minimum value.

The Spatial Distributions of H_o and τ_{RMS}

Figure 4.11 shows the spatial distributions of the DC channel gain and the RMS delay spread versus the position of the AUV-Rx in the x-y plane. The results are shown for Co-S channel within the area of $6 \times 6\,\mathrm{m}^2$. As well, Table 4.3 summarizes statistical values of the DC and RMS delay spread and contrasts the results with the case of the Co-B channel. The results are associated to an AUV-Rx located at $\Delta_z = 3$ and equipped with a lens with $D_r = 15$ andcm, $\theta_{FOV} = 140^o$. These settings for the

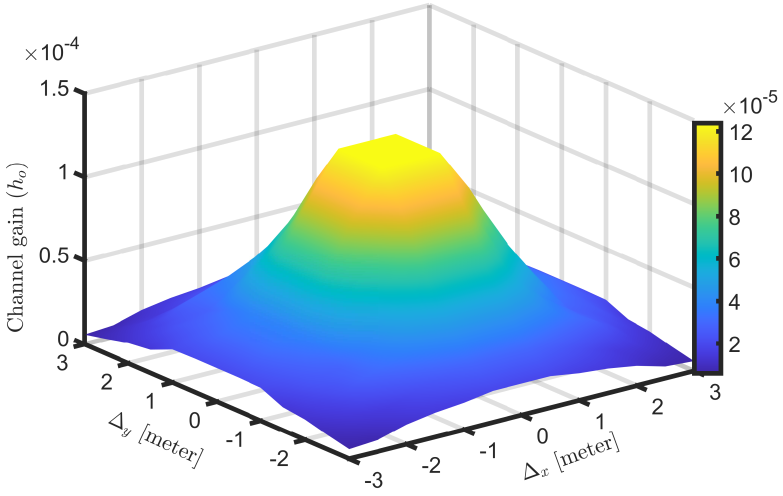

(a)

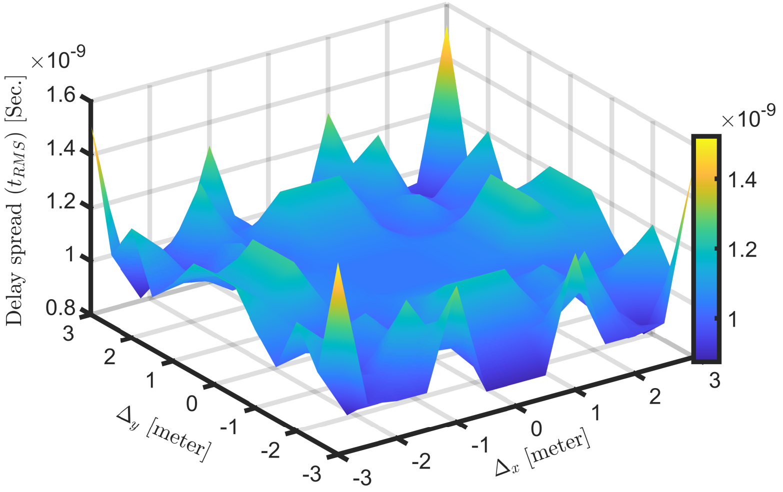

(b)

Figure 4.11: The distributions of h_o and τ_{RMS} with ($D_r = 15\,\text{cm}$, $\theta_{FOV} = 140^o$, $\Delta_z = 3$) for the Co-S channel.

AUV-Rx are used in the remainder of the numerical results.

As shown in Fig. 4.11a, the DC gain distribution is symmetric in the x-y plane around the center ($\Delta_x = 0, \Delta_y = 0$) and the DC gain value decreases monotonically

Table 4.3: Extracted statistics from Fig. 4.11

Parameters	The Co-S channel	The Co-B channel
Minimum h_o	5.82×10^{-6}	6.2×10^{-6}
Maximum h_o	1.239×10^{-4}	0.7×10^{-4}
Average h_o	3.587×10^{-5}	2.33×10^{-5}
Minimum τ_{RMS}	8.74×10^{-10}	5.50×10^{-10}
Maximum τ_{RMS}	1.53×10^{-9}	1.085×10^{-9}
Average τ_{RMS}	1.073×10^{-9}	0.77×10^{-9}

with Δ_x and Δ_y. The shown distribution matches with the average response from the results in Figs. 4.6b and 4.6c. As well, as given in the table, the DC gain values in case of the Co-S channel are higher than that in case of the Co-B channel due to the dense scattering taking place in the snow cap. Numerically, from Table 4.3, the maximum values of the DC gain are 0.7×10^{-4} and 1.239×10^{-4} and the average values are 2.33×10^{-5} and 3.587×10^{-5} for the Co-B and Co-S channels, respectively.

In Fig. 4.11b, the RMS delay spread spatial distribution is shown. In the area under the diffusing surface, the main amount of the power arrives from the LOS rays from the diffusing spot. Thus, these rays take the shortest path and the corresponding RMS delay spread has the lowest value in this area. At the edge of the considered area, the majority of received power arises from scattered rays. Thus, the corresponding RMS delay spread has the highest value. In the intermediate area, the RMS delay spread value fluctuates with the position of the AUV-Rx depending on whether a LOS or scattering components dominate. As well, from Table 4.3, the RMS delay spread is on the order of nanoseconds, however, the values in case of the Co-S channel are higher than that in case of the Co-B channel. Numerically, the maximum values of the RMS delay spread are 1.085×10^{-9} s and 1.53×10^{-9} s and the average values are 0.77×10^{-9} s and 1.073×10^{-9} s for the Co-B and Co-S channels, respectively.

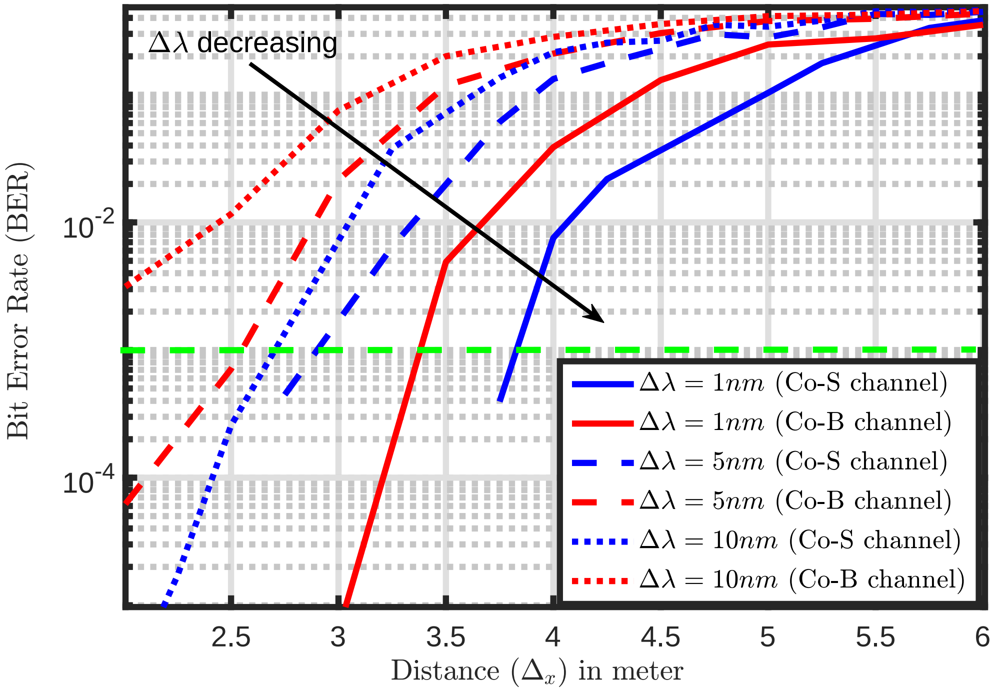

Figure 4.12: The BER for the Rx-PE (perfect equalization) system versus the distance x with $R_b = 50$ Mbps and $P_o = 100$ mW.

4.5.3 Link Performance

In this subsection, we numerically investigate the BER performance and maximum achievable bit rate for proposed system. The AUV-Rx is equipped with $D_r = 15$ cm with $\theta_{FOV} = 140^o$ and located at y-z position $\{\Delta_y, \Delta_z\} = \{0, 3\}$ m, load resistance is $R_L = 200\ \Omega$, and the electrical bandwidth of the Rx is considered as 0.7 GHz. A DFE equalizer is implemented using 15 taps T_b-spaced branches. The coefficients of the taps are obtained using 2024 training symbols, and the LMS algorithm runs with control value equal to 0.15.The ISI, shot, and thermal noises are evaluated using Eqs. (4.4.7)-(3.3.19). For the background radiation, clear weather is assumed with the sun at zenith angle equal to $\approx 60^o$ [167, 62]. For the thermal noise, the temperature of the seawater is assumed zero Celsius, see Fig. 4.2.

Figure 4.12 shows the average BER performance versus the distance Δ_x for a perfect equalizer receiver (Rx-PE), i.e., $v_{isi} = 0$, where performance limitation only arises from the Rx noise, dominated by background radiation. Here, we consider Co-B and Co-S channels, and the Rxs are equipped with optical filters with bandwidths $\Delta\lambda \in \{1, 5, 10\}$ nm. The average transmitted optical power is $P_o = 100$ mW and the bit rate is $R_b = 50$ Mbps. As shown, the BER performance degrades with distance and improves by decreasing the bandwidth of the optical filter. As well, the BER performance in the case of the Co-S channel is better than Co-B channel for two reasons. Firstly, the Co-S channel has a higher upward transmission DC gain; secondly, the Co-S channel reduces impact of the solar radiations much more than the Co-B channel. For example, considering a BER threshold of 10^{-3} as indicated by the green line in the figure, the AUV-Tx can communicate with the Rx-PE at ranges $\Delta_x = \{4, 3, 2.75\}$ and $\{3.5, 2.75, 1\}$ m with the bandwidth $\Delta\lambda = \{1, 5, 10\}$ in cases of the Co-S and Co-B channels, respectively. In other words, scaling $\Delta\lambda$ down by 10 times raises the communication range by 45% and 250% in cases of Co-S and Co-B channels, respectively.

Figure 4.13 compares the normalized optical power penalty (NOPP) versus the normalized RMS delay spread (NRDS) defined as

$$\text{NRDS} = \frac{\tau_{RMS}}{T_b}$$

at BER$= 10^{-3}$ for receivers with equalization (Rx-E) and unequalized (Rx-UE). The NOPP is defined as the required transmitted optical power to achieve the desired FEC limit in cases of Rx-E and Rx-UE systems normalized by that required in case

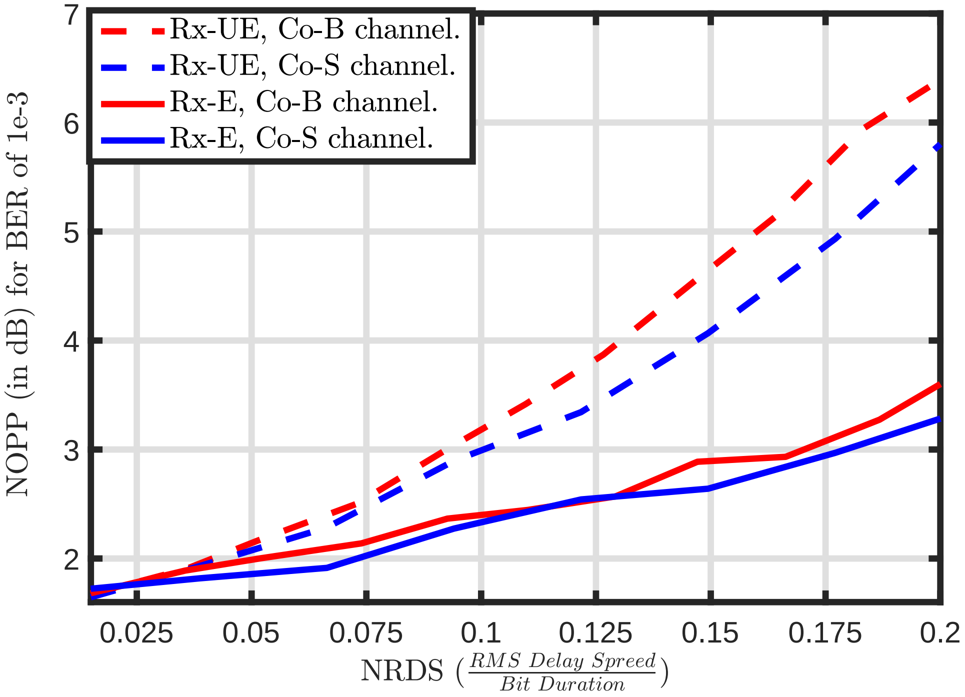

Figure 4.13: The normalized optical power penalty (NOPP) versus the normalized RMS delay spread (NRDS) for Rx-E and Rx-UE (no equalization) cases.

of the Rx-PE system. The RMS delay spread τ_{RMS} is computed for the AUV-Rx at position $\Delta_x = 2$ m, where $\tau_{RMS} = 1.1 \times 10^{-9}$ s and 8.5×10^{-10} s for the Co-S and Co-B SSCL channels, respectively. As well, the bit duration is varied in the range $T_b \in [2, 100]$ ns, i.e., [18] $R_b \in [10, 500]$ Mbps. The case of Rx-UE is used as a benchmark to highlight the benefit of channel equalization.

At low data rates, e.g., (NRDS $\leq$ 0.05), where the bit duration is much larger than the RMS delay spread, the effect of ISI on the system performance is limited and the performance of Rx-UE and Rx-E are nearly the same. As the data rate increases,

---

[18] At distance $\Delta_x = 2$ m, a data rate of 500 Mpbs is considered as a maximum since the average transmitted power is limited to 200 mW for the Rx-E systems, as indicated in the simulation parameters.

the impact of ISI increases and Rx-E gradually outperforms Rx-UE. Specifically, for the Co-B channel at NRDS= 0.075, Rx-E and Rx-UE require NOPP= 2.15 dB and NOPP= 2.52 dB, respectively. For the Co-S channel at the same NRDS, Rx-E and Rx-UE require NOPP= 2 dB and NOPP= 2.5 dB, respectively. At higher data rates of NRDS= 0.2, Rx-E and Rx-UE require NOPP= 6.3 dB and NOPP= 3.5 dB, respectively, for the Co-B channel. For the Co-S channel at the same NRDS, Rx-E and Rx-UE require NOPP= 3.2 dB and NOPP= 5.8 dB, respectively. These results indicate that the equalizer improves the power efficiency of the systems by nearly 3 dB, which means the required transmitted power is reduced roughly by a factor of two. In other words, the AUV with the equalized system enhances the power-efficiency of the AUVs which means more lifetime for the battery.

Figure 4.14 shows the maximum achievable bit rate under the constraint BER$\leq 10^{-3}$ versus the distance Δ_x with average transmitted optical power $P_o \in \{100, 200\}$ mW. As shown in the figure, the maximum achievable bit rate ($R_b \approx 700$ Mpbs) is achieved directly under the diffusing surface ($\Delta_x \leq 1$ m). However, as Δ_x increases, the maximum achievable bit rate decreases; the proposed system can achieve broadcast data rates on the order of $R_b = 1$ Mpbs over communication ranges of $\Delta_x = 6$ m. As indicated by the green dashed line, to maintain a communication rate of 10 Mbps, scaling the transmitted power by 2 increases the communication range by 18% and 10% in cases of Co-B and Co-S channels, respectively. This trade off between data rate and coverage distance should be considered during planning stage of the AUV swarms, based on the required data rate and range.

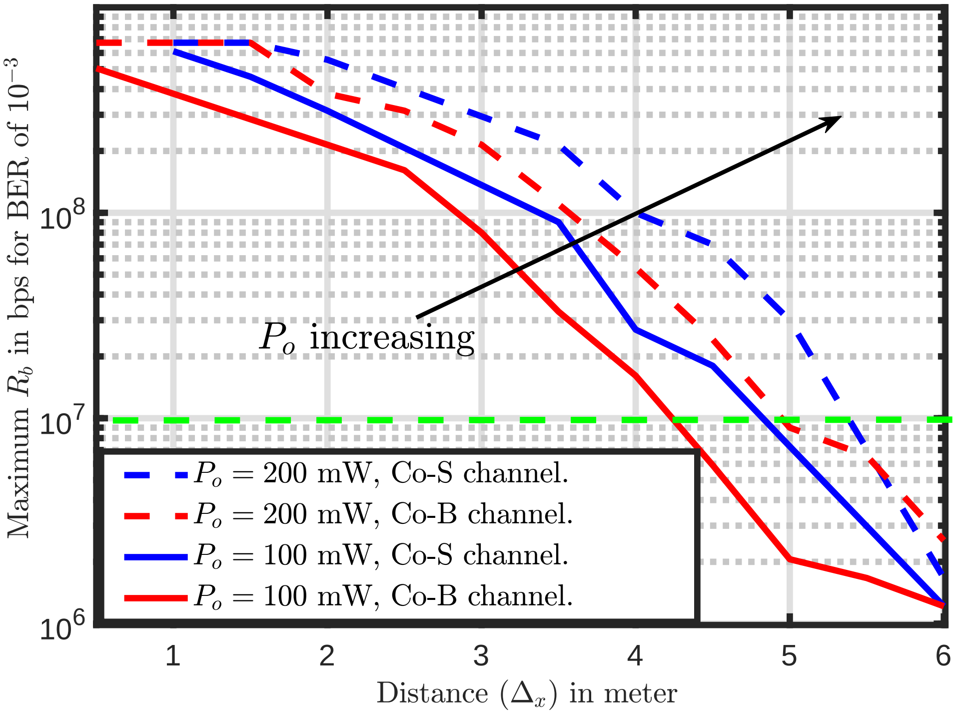

Figure 4.14: The maximum achieved bit rate for the Rx-E system versus the distance with FEC limit of BER$= 10^{-3}$.

4.6 Conclusions

In this paper, for first time, we propose a broadband-broadcast approach suitable for networking AUVs under sea ice, albeit with limited range. We take advantage of existing ice sheets on the sea surface to establish a diffusing communication systems. The SSCL model was introduced in which the channel is represented in the form of cascaded layers with uniform optical characteristics. Due to the challenge of analytic modeling of optical signal scattering inside the ice sheet, MCNRT is used to evaluate the diffusing pattern of upward transmission. For downward transmission, the CIR was derived in the form of a quasi-analytic equation assuming single scattering light propagation. Due to the expected effects of ISI and relatively high background solar power noise, we propose a new transceiver architecture that helps in mitigating the effects of these factors. We also provide extensive numerical results to investigate the effects of water and ice types, Rx parameters i.e., FOV and optical filter bandwidth, and the Rx location on the system performance.

The challenges in implementing SDOC systems includes the transceiver size which must be carefully chosen depending on the size of the AUV. The transmitted power must also be determined according to battery-life and eye-safety constraints. Lastly, the SDOC approach is not appropriate bellow transparent sea ice sheets which rarely exist in practice on frozen oceans. Future work includes further investigations for quasi-analytic forms of the diffusing patterns, investigating a better fit for the temporal diffusing pattern as well as experimental validation of the obtained results.

Chapter 5

Conclusions

5.1 Summary

Recent underwater applications require reliable high-speed short-range communications systems. This thesis has proposed three novel wireless optical systems: A-MIMO, TA-MIMO, and SDOC. These systems have taken advantage of optical wireless systems' reliability and high speed. They have been adopted for short-range applications such as video surveillance in shallow seawater, data muling, and real-time signaling exchange for AUV-swarms. A detailed description of the work is as follows:

In **Chapter 2**, in contrast to C-MIMO systems, A-MIMO systems are robust against link displacements and length variation. In addition, they have been implemented with smaller sizes. These features are essential for applications with low costs and small sizes, e.g., tiny sensors and small AUVs. Due to window truncation, A-MIMO systems provide communications with short ranges, e.g., 6 meters. However, A-MIMO systems could be adopted for short-range applications, e.g., data muling links between AUVs and sensor nodes fixed on the seabed.

In **Chapter 3**, TA-MIMO systems have been proposed to offer tracking and localization functions besides the communication jobs. TA-MIMO systems are good candidates for video links between AUVs and buoyed nodes on seawater surfaces. However, TA-MIMO systems require imaging receivers that reflect on the cost and complexity of the implementations.

In **Chapter 4**, SDOC systems have been proposed for broadband-broadcast communications under sea ice. In contrast to multi-LED systems, SDOC systems are robust against the blockage, shadowing, and misalignment. SDOC systems provide high-speed on the order of Gbps, and they are implemented with simple hardware. However, SDOC systems should be adopted for short-range applications, e.g., AUVs swarm.

5.2 Conclusions

The work in this thesis was centered around reliable high-speed point-to-point and broadcast communications systems for UWOSN. Three novel systems were proposed for UWOC, which is the unifying theme of the thesis. Throughout the development of this thesis, several contributions were introduced, and several observations and insights were obtained from each chapter. The contributions, observations, and insights are summarized in the following:

Firstly, A-MIMO systems have offered solutions for the challenges of UWOC links, e.g., misalignment, opto-electronic non-linearity, and eye safety. However, A-MIMO systems are not robust against relative tilt between the ends of links. According to models of A-MIMO systems, the systems should be adopted for short-range applications to avoid window truncation impacts. Though communication ranges can be increased, this leads to an increase in system sizes. Implementing LD and PD arrays with smaller inter-spaces extend communication ranges while keeping small system sizes. However, small inter-spacing in LD and PD arrays degrade systems capacities due to increasing spatial interference between adjacent channels. Due to spatial interference, C-MIMO and A-MIMO systems are not recommended to be implemented in high turbidity seawaters. A-MIMO systems are good candidates for high-speed or latency-sensitive applications, e.g., video surveillance, real-time signaling, and data muling.

Secondly, in addition to the merits offered by A-MIMO systems, TA-MIMO systems have offered reliability against relative disorientation between the ends of links. TA-MIMO systems could also perform localization functions besides reliable communications, which is very important where the global position system (GPS) does not cover underwater environments. In contrast to tracking C-MIMO systems, TA-MIMO systems are much simpler in computation and implementation due to their robustness against off-axis misalignment. TA-MIMO systems have the same drawbacks as A-MIMO systems, e.g., window truncation, short-range, severe spatial interference between the adjacent channels in turbidity seawater. In addition, TA-MIMO systems require imaging receivers with high resolutions, which may increase the hardware and costs of the systems. However, performing localization and communication functions using one system may compensate for these drawbacks. Though, a choice between A-MIMO and CMIMO systems depends on the link misalignment conditions. However, TA-MIMO systems are good choices in many underwater misalignment cases, e.g., F2M, F2B, and M2M links. In order to assist the future design and implementation of A-MIMO and TA-MIMO systems, robust analysis and comprehensive models have been provided with details. Several points are still open for the research in TA-MIMO and A-MIMO systems, e.g., contrasting with tracking C-MIMO systems, implementation, testing in the laboratory, multi-carrier with high-order modulations, and system optimization.

Thirdly, SDOC systems have been introduced as simple models for broadband-broadcast communications under sea ice, e.g., Arctic and Antarctica zones, rather than multi-LED systems. SDOC systems are more robust against misalignment, blockage, and shadowing. As well, they are implemented with small hardware and low costs. The number of layers should be sufficient for the channel model to obtain accurate results. However, the thesis compromised the accuracy of results and the complexity of the computations. Though the communication range is short, beam steering can increase this range, as indicated in the system model. Beam steering requires the AUV-Tx to know the locations of AUV-Rxs, which can be achieved by using localization techniques. Systems of equations have been provided to guide the feature implementation for SDOC systems. The proposed transceiver setup using DFE enhanced the link performance. For a well-designed DFE, the number of taps should be selected according to the RMS delay spread of the channel, i.e., a longer delay spread requires more taps. RMS delay spread could be estimated using the proposed quasi-analytic model. Though the proposed transceiver mitigated the channel impairments, more forward steps are required for a better setup. For example, using LD sources increases the system cost, and LD speed is restricted due to ISI induced by the diffusing. Hence, LED sources should be contrasted to LD for lower-cost systems. SDOC approaches require more investigation where several points are still open for the research, e.g., mobility model, multiple access techniques, beam steering, relays, localization, and link optimization.

5.3 Future Work

This thesis proposed A-MIMO, TA-MIMO, and SDOC systems for reliable high-speed short-range underwater communications. The thesis provided a comprehensive treatment of the subject through analytic derivations and numerical analysis, analytic and numerical validation, and numerical simulations. However, several future research directions and extensions can be motivated by the work in this thesis and the vision behind it. Future directions and extensions are suggested in the following.

5.3.1 Tracking C-MIMO Systems Versus TA-MIMO Systems

In this thesis, we have shown link performances for TA-MIMO systems which dramatically enhances channel capacities in cases of B2F links. Due to the space limit in **Chapter 3**, results for tracking C-MIMO (TC-MIMO) systems have not been considered. TC-MIMO systems could be implemented using one of the tracking techniques mentioned in **Chapter 1**, e.g., Gimbal-based and mirror-based systems, and Smart transceivers [71, 72, 73, 74]. TC-MIMO systems have some advantages, such as they do not have phenomena of window truncation, and they can provide high-speed communications with longer ranges. Thus, they may be better solutions for some communication scenarios and applications than TA-MIMO systems. The future works consider contrasting TA-MIMO with TC-MIMO systems and highlighting which one outperforms under different conditions.

5.3.2 Experimental Verification for SDOC Approach

In SSCL channels, channels are modeled using vertical cascaded layers of seawater, ice, snow then the air. For precise models, sea ice and snow mediums are divided into multi-layers due to nonhomogeneity for the optical properties within the mediums. The precision of results for CIRs depends on the number of layers of SSCL models. However, in this thesis, we compromised between the number of layers and the model complexity. The compromising may not be sufficient to get robust results for CIRs. In future work, aiming to verify the obtained CIRs, we may implement SDOC systems and measure the CIRs in the laboratory.

5.3.3 Optimized Configurations of SDOC Links

In system designs of SDOC links, there is a trade-off between configuration parameters of the link, e.g., working wavelength, lens diameter, and FOV of AUV-Rxs. In configurations of AUV-Txs, using green wavelengths minimize the attenuation of optical beams. On the other hand, background radiations also reach their peaks at these wavelengths. Rather than using green wavelengths, other wavelengths in the range of 400-1500 nm may offer a better compromise. In configurations of AUV-Rxs, enlarged receiver sizes and FOVs enhance channel gains. On the other hand, these settings signify background noise as payments. Optimal configurations for the links should be obtained given some network constraints such as coverage ranges, depths, FEC limits, and channel parameters.

5.3.4 Mobility Models for SDOC Networks

In the numerical results of SDOC systems, it is assumed that the AUV-Tx is fixed at the origin, and instance performance for links are evaluated at different positions and orientation for AUV-Rxs. However, this is not the case in practical scenarios, and the average performances of links depend on the mobility models of AUV-Tx and AUV-Rxs. In the extension of this work, we consider mobility models that include intended motions of AUVs and non-intended motions due to seawater currents and waves.

5.3.5 Multiple Access Schemes for SDOC Networks

SDOC approaches have been proposed for broadcast communications which means the same information is transmitted from AUV-Tx to all AUV-Rxs. However, in general scenarios, each AUV-Rx is associated with different information, and this requires multiple access techniques (MAT) to avoid the mutual interference between AUV-Rxs. MATs adapt the transmitted power of each AUV-Rx according to the channel conditions, e.g., small transmitted power to close AUV-Rxs and higher transmitted power to fare AUV-Rxs. In future work, appropriate MATs are investigated for SDOC systems according to the particular characteristics of SDOC channels.

5.3.6 Virtual Relaying for SDOC Networks

Though, SDOC systems provided high-speed communications with high reliability. However, the systems are limited in communication ranges to a few meters, e.g., 7 meters. The systems have achieved BER less than 10^{-3} with typically range 6 meters and speed on the order of 1 Mbps as shown in [9]. Though the transmitted power can be raised to extend communication ranges, the eye-safety, eco-friend, and power-efficiency conditions must be considered. In the future research step, we extend the communication ranges of SDOC systems using the concept of the virtual relay. Virtual relays are AUVs that perform the role of the relays besides their role as transceivers. After the decoding and amplification process, the virtual relay receives the information and re-transmits it to its neighbors. With well-designed relay architectures, we aim to provide high-speeds with a fraction of Gbps with communication ranges on the order of tens of meters and transmitted powers more minor than the threshold of MPE.

Appendix A

Proofs of Closed-Form Equations

A.1 Introduction

Chapter 3 provides closed-form equations, Eq. (3.3.10)-(3.3.14), that compute AoA distributions with high time efficiency and accuracy. The closed-form equations have been verified using the MCNR method, as shown in Figs. 3.8-3.10. These equations serve as guides for the feature implementations of A-MIMO and TA-MIMO systems. In this appendix, due to the importance of these equations, we provide detailed proofs for readers' convenience.

Note that this appendix has been published in [9], and IEEE only owns the copyright of the material presented in this part.

A.2 Proof of Equation (3.3.10)

Assuming that the beam spot on the transmitter lens is relatively small ($w \ll l_t$), the m_t^{th} LD can be well approximated as a single-ray source. According to this assumption, the double integration over (x_t, y_t) in Eq. (3.3.9), i.e., $\int_{x_t} \int_{y_t} I_{m_t}(x_t, y_t)\, dy_t\, dx_t$, is reduced to the transmitted optical power P_o.

Moreover, the integration over μ_0 in Eq. (3.3.9) can be solved for the central LD ($x_t = 0, y_t = 0$) with on-axis alignment assumption ($\Delta_x = 0, \Delta_y = 0$) as follows. The geometric loss function $G_{m_t}\,(x_r^s, y_r^s)$ depends on μ_0 as indicated in Eqs. (3.3.5), (3.3.7) and (3.3.8). Thus, the inequality in Eq. (3.3.5) can be rewritten in terms of μ_0 using Eqs. (3.3.7) and (3.3.8) assuming: $x_t = y_t = \Delta_x = \Delta_y = 0$. The solution of μ_0 lies in the range $\mu_{s_1} \leq \mu_0 \leq \mu_{s_2}$, where μ_{s_1} and μ_{s_2} are given as

$$\begin{aligned} &\{\mu_{s_1}(\theta_r, \phi_r), \mu_{s_2}(\theta_r, \phi_r)\} = \\ &\quad \frac{f_3(\theta_r, \phi_r)}{2\, f_4(\theta_r, \phi_r)} \pm \sqrt{\left[\frac{f_3(\theta_r, \phi_r)^2}{4\, f_4(\theta_r, \phi_r)^2} - \frac{L^2\, \tan(\theta_r)^2 - l_r^2/4}{f_4(\theta_r, \phi_r)}\right]}, \end{aligned} \tag{A.2.1}$$

where functions $f_3(\theta_r, \phi_r)$ and $f_4(\theta_r, \phi_r)$ are defined as

$$\begin{aligned} f_3(\theta_r, \phi_r) &= 2\, L\, \left[\sin(\phi_{m_t})\, \sin(\phi_r) + \cos(\phi_{m_t})\, \cos(\phi_r)\right] \\ &\qquad \times \tan(\theta_r)\, \sin(\theta_{m_t}) - 2\, L\, \tan(\theta_r^2)\, \cos(\theta_{m_t}), \\ f_4(\theta_r, \phi_r) &= \sin(\theta_{m_t})^2 + \tan(\theta_r)^2\, \cos(\theta_{m_t})^2 - 2\, \tan(\theta_r) \\ &\qquad \times \cos(\phi_r - \phi_{m_t})\, \sin(\phi_{m_t})\, \cos(\phi_{m_t}). \end{aligned} \tag{A.2.2}$$

The common range between the limits of the integration over μ_o, i.e., $0 \leq \mu_0 \leq$

$L/\cos(\theta_t)$, and $\mu_{s_1} \leq \mu_0 \leq \mu_{s_2}$ can be defined by two optimization functions as follows:

$$\begin{aligned} f_1(\theta_r, \phi_r) &= \max\{0, \mu_{s_1}(\theta_r, \phi_r)\}, \\ f_2(\theta_r, \phi_r) &= \min\left\{\frac{L}{\cos(\theta_t)}, \mu_{s_2}(\theta_r, \phi_r)\right\}. \end{aligned} \tag{A.2.3}$$

Therefore, integrating the first term of Eq. (3.3.9) over $f_1(\theta_r, \phi_r) \leq \mu_0 \leq f_2(\theta_r, \phi_r)$ yields a closed-form AoA distribution for the central LD with on-axis alignment as shown in Eq. (3.3.10).

A.3 Proof of Equation (3.3.12)

Equation (3.3.11) can be rewritten in a simpler form with zero launching angle, i.e., $\theta_{m_t} = 0$. By substituting $\theta_{m_t} = 0$ in Eq. (A.2.1), the solutions of the inequality and the scattering angle are obtained as

$$\begin{gathered} \{\mu_{s_1}(\theta_r), \mu_{s_2}(\theta_r)\} = \\ \left[-(L + l_r \ \cot(\theta_r)/4), (l_r \ \cot(\theta_r)/4 - L)\right], \\ \theta_s = \theta_r. \end{gathered} \tag{A.3.1}$$

Thus, the integration over ϕ_r in Eq. (3.3.11) can be computed analytically as shown in Eq. (3.3.12).

A.4 Proof of Equation (3.3.14)

In case of the central LD ($x_t = 0$, $y_t = 0$) at on-axis transmission ($\Delta_x = 0$, $\Delta_y = 0$) and zero launching angle ($\theta_{m_t} = 0$), the azimuthal AoA distribution is uniform as shown in Fig. 3.10, and is computed as

$$P_{\phi_r}(\phi_r|\theta_{m_t} = 0) = \frac{P_r}{2\,\pi}, \tag{A.4.1}$$

where P_r is the total received power on the receiver lens which is obtained by integrating Eq. (3.3.12) over θ_r using the following integral forms [170]

$$\begin{aligned} &\int \exp\left[-a\,x^2\right]dx = \sqrt{\frac{\pi}{4\,a}}\;\mathrm{erf}\left(\sqrt{a}\,x\right), \\ &\int x^m\,\exp\left[-\beta\,x^n\right]dx = \frac{1}{(n\,\beta^{\gamma})}\varGamma(\gamma, n\,\beta x^n), \end{aligned} \tag{A.4.2}$$

where $\gamma = (m+1)/n$ and $\{\beta, n\} \neq 0$. The ingratiation in Eq. (A.4.2) is calculated using the following approximations

$$\begin{aligned} \left[\frac{\sin(\theta_r)\,(\sec(\theta_r)-1)^{-1}}{(2+2\,g^2-4\,g\cos(\theta_r))^{3/2}}\right] &\approx \left[156.3\,\theta_r^{-1.519} - 1802\right], \\ \sec(\theta_r) &\approx \left[\theta_r^2/2 + 1\right]. \end{aligned} \tag{A.4.3}$$

The first approximation in Eq. (A.4.3) is done at $g = 0.91$ by using curve fitting tool (i.e. cftool tool box) in Matlab [97]. The second one is done by using Taylor series expansion. So, the approximated closed-form is given in Eq. (3.3.14).

Appendix B

Dependency of SSCL Models on Temperature and Salinity

B.1 Introduction

As shown in **Chapter 4**, SSCL models are cascaded layers; seawater, ice, snow, and atmosphere. In each layer, optical parameters (i.e., absorption and scattering coefficients, asymmetry parameter, and refractive index) depend on hosting mediums and values of temperature and salinity. In this appendix, we discuss in more detail SSCL models and Table 4.1 for readers' convenience. We also show the dependence of the optical parameters on values of temperature and salinity.

Note that this appendix has not been published in [10] due to limited space, and the thesis owns the copyright of the material presented here.

B.2 Layers of SSCL Models

In SSCL models, equations (4.2.5)-(4.2.9) are used to obtain absorption and scattering coefficients, asymmetry parameters, and refractive index values. Equations (4.2.5)-(4.2.9) depend on parameters $\{a_j, b_j, g_j\}$ which are challenge in the computations or measurements. These parameters are not obtained exactly, however, they are approximated depending on the hosting media and values of temperature and salinity as the following.

B.2.1 Seawater Layer $(m = 1)$

Morel's model [140, 144] is adopted here for the seawater layer, where the seawater is composed of; pure water, chlorophyll-a, and yellow substance particles. All particles contribute to the absorption; however, the scattering occurs due to particles of pure water and chlorophyll-a matter. The absorption and scattering coefficients are calculated in [144] and [140], respectively. The chlorophyll-a concentration, C, governs the turbidity of the seawater, where the pure, clear, coastal, and turbid seawaters are contaminated by $C \leq 0.15$, $0.15 \leq C \leq 0.42$, $0.42 \leq C \leq 2.7$, and $2.7 \leq C$ in milligram/m^3, respectively [32]. An increase in turbidity leads to higher absorption and scattering coefficients. The phase scattering function is defined using the OTHG function shown in Eq. (4.2.7) [90]. The asymmetry parameter of the seawater varies with type of the seawater, specifically, asymmetry parameters are $g(m = 1) = 0.87$, $g(m = 1) = 0.94$, and $g(m = 1) = 0.92$ for the pure and clear seawaters, the coastal seawater, and turbid seawater, respectively [141]. Also, refractive indices of pure water, chlorophyll-a and yellow substance are $n_1(m = 1) = 1.333$, $n_2(m = 1) = 1.54$ and $n_3(m = 1) = 1.54$, respectively [38], [34].

B.2.2 Ice and Snow Layers ($m = [2, 3, ..., 1 + m_i + m_s]$)

Hamre's model [37] is adopted here for ice and snow layers, where $a_j(m, \lambda)$, $b_j(m, \lambda)$, $p_{\theta_s,j}(m, \lambda)$ and $g_j(m, \lambda)$ can be approximated with two assumptions, the imaginary part of the refractive index is small and the radius of the particle is large relative to the wavelength, as demonstrated in [37]. Rather than using Eq. (4.2.5), the absorption coefficient of m^{th} layer is well approximated as [37]

$$\begin{aligned} a(m, \lambda) = \frac{4\,\pi\, n_{i_o}(m, \lambda)\, f_{v_o}(m)}{\lambda} &+ \sum_{j=1}^{J_m} \frac{4\,\pi\, n_{i_j}(m, \lambda)\, f_{v_j}(m)}{\lambda} \\ &\times \frac{(\hat{n}_j^3(m, \lambda) - (\hat{n}_j^2(m, \lambda) - 1)^{3/2})}{\hat{n}_j(m, \lambda)}\,, \end{aligned} \tag{B.2.1}$$

where, n_{i_j} is the imaginary part of the refractive index (i.e. $n_j(m, \lambda) = n_{r_j}(m, \lambda) + \sqrt{-1}\, n_{i_j}(m, \lambda)$) of the material that j^{th} particle is made from. The symbol of $\hat{n}_j(\lambda, m)$ presents the ratio of the real part of the refractive index of the particle relative to the hosting medium of that layer, $\hat{n}_j(\lambda, m) = n_{r_j}(\lambda, m)/n_{r_o}(\lambda, m)$.

Rather than using Eq. (4.2.6), the scattering coefficient of m^{th} layer is well approximated as [37]

$$b(m) = \frac{3}{2} \sum_{j=1}^{J_m} \frac{f_{v_j}(m)}{r_{e_j}(m)}, \tag{B.2.2}$$

where, $f_{v_j}(m)$ and $r_{e_j}(m)$ are volume fraction and the effective radius of j^{th} particle, respectively, where $0 \leq f_{v_j}(m) \leq 1$ and $\sum_{j=1}^{J_m} f_{v_j}(m) = 1$.

The phase scattering function is approximated using OTHG function with $-1 \leq g(m, \lambda) \leq 1$. Eqs. (B.2.1)-(B.2.2) depend on parameters $\{f_{v_j}(, m), r_{e_j}(m), g_j(\lambda, m), n_j(\lambda, m)\}$. These parameters will be quantified for the ice and snow layers, respectively, as the following.

Ice Layers (m=$[2, ..., m_i + 1]$):

According to Hamre's model [37], pure ice is typically contaminated by brine pockets (i.e., dissolved salts), solid salts particles, air bubbles, algae (i.e., green matters of the seawaters), and soot (i.e., black carbons falls from the atmosphere). The absorption is occurred due to pure ice, algae, and soot matters. The absorption coefficient of the pure ice is assumed uniform along with the ice layers. The presence of algae matters is assumed only in the first ice layer (i.e., $m = 2$); however, soot matters are assumed only in the last ice layer (i.e., $m = 1 + m_i$). Absorption coefficients of pure ice, alga, and soot matter are measured and given in [145, 37]. The scattering is occurred due to brine pockets, air bubbles, and solid salts particles [33]. The scattering coefficient depends on the volume fraction and the effective radius given in Eq. (B.2.2). Volume fractions are related to the layer temperature, salinity, and ice density. For brine pockets, the volume fraction $f_{v_b}(m)$ is calculated as [128]

$$f_{v_b}(m) = \frac{S(m)\,\rho_i(m)}{F_1(T(m))}\,, \tag{B.2.3}$$

where, $F_1(T(m))$ is a functions in ice temperature and it is given in [128]. Also, $\rho_i(m)$ is the bulk density of the ice in that layer, and it is measured in unit of $\mathrm{Mg/m^3}$ (i.e. megagram per cubic meter). For instance, first year ice, the bulk density varies in the range $0.89\,\mathrm{Mg/m^3} \leq \rho_i(m) \leq 0.93\ \mathrm{Mg/m^3}$ [146]. For air bubbles, the volume fraction $f_{v_a}(m)$ is calculated as [128]

$$f_{v_a}(m) = 1 - \frac{\rho_i(m)}{(0.917 - 1.4 \times 10^{-4} T(m))} + \frac{\rho_i(m)\,S(m)\,F_2(T(m))}{F_1(T(m))}, \tag{B.2.4}$$

where $F_2(T(m))$ is a function in ice temperature of the m^{th} layer and it is given in [128]. For particles of solid salt, the volume fraction $f_{v_s}(m)$ is calculated as [128]

$$f_{v_{ss}}(m) = \frac{1}{1.5}\, C_s(T(m))\, f_{v_b}(m)\, (1 + 8 \times 10^{-4} S_{br}(T(m)))\,, \tag{B.2.5}$$

where, $C_s(T_i(m))$ and $S_{br}(T_i(m))$ are functions in ice temperature and are given in [128].

The effective radius is quantified in cases of brine pockets and air bubbles, and is measured in case of solid salts particles. For the brine pockets, the effective radius $r_{e_b}(m)$ is computed as [37]

$$r_{e_b}(m) = \left(\frac{3\, f_{v_b}(m)}{2.4\pi\, S(m)}\right)^{1/3}, \text{(mm)} \tag{B.2.6}$$

For air bubbles, the effective radius $r_{e_a}(m)$ is computed as [33]

$$r_{e_a}(m) = 2.315\, \times \frac{r_2(m)^{(2.76)} - r_1(m)^{(2.76)}}{r_2(m)^{(1.76)} - r_1(m)^{(1.76)}},\ \text{(mm)} \tag{B.2.7}$$

where r_1 and r_2 are the minimum and the maximum radius in that layer. Experimentally, it is shown that $r_1 = 0.1\,\text{mm}$ and $r_2 = 2\,\text{mm}$ [29]. For the solid salt, the effective radius $r_{e_{ss}}(m)$ is not quantified, however it is shown that it varies in range of $0.015\,\text{mm} \leq r_{e_{ss}}(m) \leq 0.14\,\text{mm}$ according to the measurement on the first year ice [146].

The asymmetry parameter and the refractive index vary with the temperature of the ice layers, and they are independent on the wavelength according to Mie theory (i.e. large and sphere particles assumptions). For the range of $T(m) = [-33, 0]$ °C, asymmetry parameters of the brine pockets and solid salts vary linearly in the ranges $g_b(m) = [0.98, 0.997]$ and $g_{ss}(m) = [1, 0.99]$, respectively. However, for air bubbles, the asymmetry parameter is fixed at $g_a(m) = 0.856$ [38, 36]. In the same temperature range, $T(m) = [-33, 0]$ °C, refractive indices of brine pockets and solid salts vary linearly in the following ranges $n_b(m) = [1.4, 1.34]$, and $n_{ss}(m) = [1.31, 1.37]$, respectively. However, refractive indices of the pure ice[1] and air bubbles are fixed at $n_{o_i}(m) = 1.309$ and $n_a(m) = 0.999999$, respectively [38, 142].

Snow Layers (m=$[m_i + 1, ..., m_i + m_s + 1]$):

According to Hamre's model [37], the snow is composed of air and ice particles contaminated by algal and non-algal impurities and soot. The absorption occurs due to all the snow ingredients, and it is assumed uniform along with the snow layers. The total absorption of the algae and the non-algal matter is computed in [37]. The results are shown for pure snow grains and soot impurities in [34, 37]. The scattering is occurred due to the snow grains. The volume fraction of the snow grains is computed as [37]

$$f_{v_s}(m) = \frac{\rho_s(m)}{(0.917 - 1.4 \times 10^{-4} T(m))}, \tag{B.2.8}$$

where $\rho_s(m)$ is the snow density, and it is measured in unit of Mg/m^3.

The effective radius of the snow grain $r_{e_s}(m)$ is not quantified, however it is measured with the depth and it varies in the range of $r_{e_s} = [0.05, 2.5]\,\text{mm}$ [37].

The asymmetry parameter of the snow grain depends on its effective radius, and it varies in the range $g_s = [0.8, 1]$ [56]. Also, refractive indices of the air[2] and snow

---

[1] The pure sea ice is the hosting media of the ice layers.

[2] The air is the hosting media of the snow layers.

grains are $n_{o_s}(m) = 0.999999$ and $n_s(m) = 1.309$, respectively [38, 142].

B.2.3 Atmosphere Layer $(m = m_i + m_s + 2)$

For the last layer of the SSCL model, it is assumed that the layer is a free space (i.e., gases of Earth atmosphere) contaminated by weather components; dust, rain droplet, and snowflakes. The free space is assumed an ideal medium with no absorption or scattering effects. The presence of weather components changes according to the weather condition; clear, foggy, rainy, or snowy weather. The weather components absorb the light according to the empirical model given in [148, 171]. Also, the weather components scatter the light according to the Mie model, and the model parameters are associated with the type of weather condition [132, Ch. 3]. However, rather than using the Mie model, the OTHG function can be used as a good approximation with a small error under assumptions, as demonstrated in [153, 172]. Grabner *et al.* [152] investigated the effects of rain and fog scattering on optical beam propagation. Results show that the scattering should be considered in dense fog or heavy rain conditions.

Appendix C

Additional Numerical Results for SDOC Systems

C.1 Introduction

In **Chapter 4**, due to the limit of space, some results and figures are not included. In addition to what we have shown in **Chapter 4**, we provide additional numerical results and figures for readers' convenience. In particular, we show the temperature and salinity profiles of the bare sea ice sheet. Then, we show the effect of receiver radius on DC gain and delay spread, the effect of receiver positions on CIRs, and the effect of receiver tilt on CIRs. Two-dimension profiles of DC gain and delay spread in the x-y plane are shown for the Co-B channel. Finally, BER performances are evaluated for SDOC systems with different speed and power rates.

Note that this appendix has not been published in [10] due to limited space, and the thesis owns the copyright of the material presented here.

C.2 Temperature and Salinity Profiles of the Bare Sea ice Sheet

Figure C.1 shows measured temperature and salinity profiles of the bare sea ice sheet with thickness 12 cm, where T is the temperature in C^o, S is the salinity *ppt*, and $0 \leq z \leq 120$ mm. The measured profiles are fitted with equations (4.2.3) and (4.2.4) as shown, and there is a good agreement between the measured profiles and the fitting equations. Although the shown profiles are for specific ice sheets, they hold the standard linear and C-Shape for temperature T and salinity S, respectively, like the case of the snow-covered sea ice sheet shown in Fig. 4.2.

C.3 Effects of Receiver Diameter

Figure C.2 shows DC gain and delay spread versus receiver diameter with $\theta_{FOV} = 90^o$. The shown results are associated with an AUV-Rx navigating at position ($\Delta_x = 3, \Delta_y = 0, \Delta_z = 2\,\mathrm{m}$) and the Co-B channel. An increase in the diameter raises the DC gain monotonically because an increase in the diameter decreases the geometric loss. As shown, a scaling for the diameter by three times, from $D_r = 5$ cm to $D_r = 15$ cm, leads to an enhancing in the DC gain by almost 4 times, from $h_o = 4.2 \times 10^{-8}$ to $h_o = 1.77 \times 10^{-7}$. However, the delay spread fluctuates with an increase in the diameter, the delay spread depends on both the intensity and the traveling time taken by the ray to reach the receiver. As shown, the change in the delay spread with the

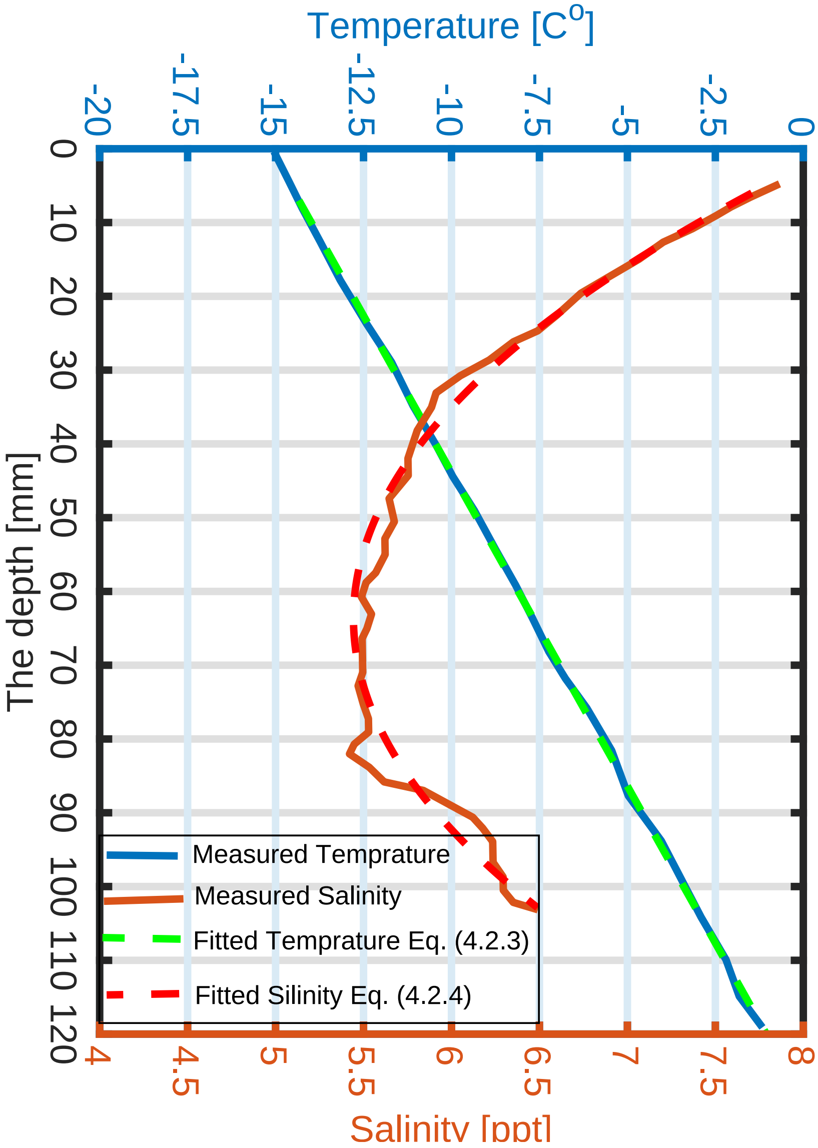

Figure C.1: Temperature and salinity profiles versus sea ice depth for a bare sea ice sheet as show in [131, Fig. 3].

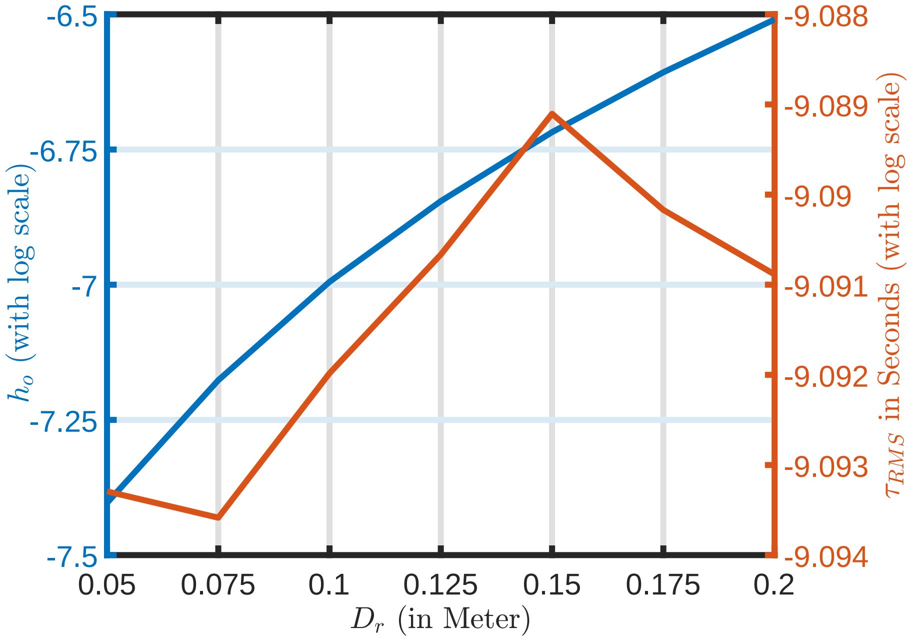

Figure C.2: The effects of the diameter on h_o and τ_{RMS} with $\theta_{FoV} = 90^o$ at position ($\Delta_x = 3, \Delta_y = 0, \Delta_z = 2\,\mathrm{m}$) and Co-B channel.

increase in the diameter is not significant. The delay spread changes in the range of 8.14×10^{-10} and 8.063×10^{-10}.

C.4 Effects of Communication Range

Figure C.3 shows CIR distributions for three communication ranges, $\Delta_x = \{3, 3.5, 4\}\,\mathrm{m}$. The results are associated with AUV-Rx configured with ($D_r = 10\,\mathrm{cm}$, $\theta_{FOV} = 90^o$) and navigates in the Co-B channel at y-z position of ($\Delta_y = 0, \Delta_z = 2\,\mathrm{m}$). Due to absorption and scattering taken place in the Co-B channel, longer communication range achieves less received power, however, more pulse dispersion and delay time. For the communication ranges, $\Delta_x = \{3, 3.5, 4\}\,\mathrm{m}$, the DC gains are obtained as

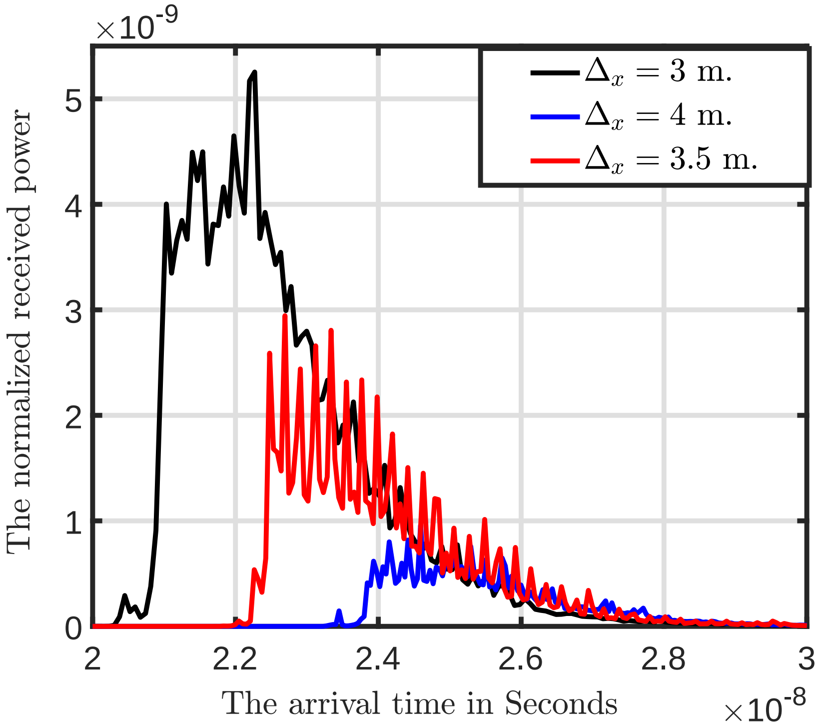

Figure C.3: Effects of the position on CIR with ($D_r = 10\,\text{cm}$, $\theta_{FOV} = 90^o$) at ($\Delta_y = 0, \Delta_z = 2\,\text{m}$) and Co-B channel.

2.5×10^{-7}, 1×10^{-7} and 5×10^{-8}, respectively. These values indicate that an increasing in the communication range with 0.5 meters, scales the gain down by two times. The computed RMS delay spreads are 7.9×10^{-10}, 8.0×10^{-10} and 8.7×10^{-10} sec for $\Delta_x = \{3, 3.5, 4\}$ m, respectively.

C.5 Effects of Receiver Disorientation

Figure C.4 shows variations in DC channel gain and RMS delay spread with receiver

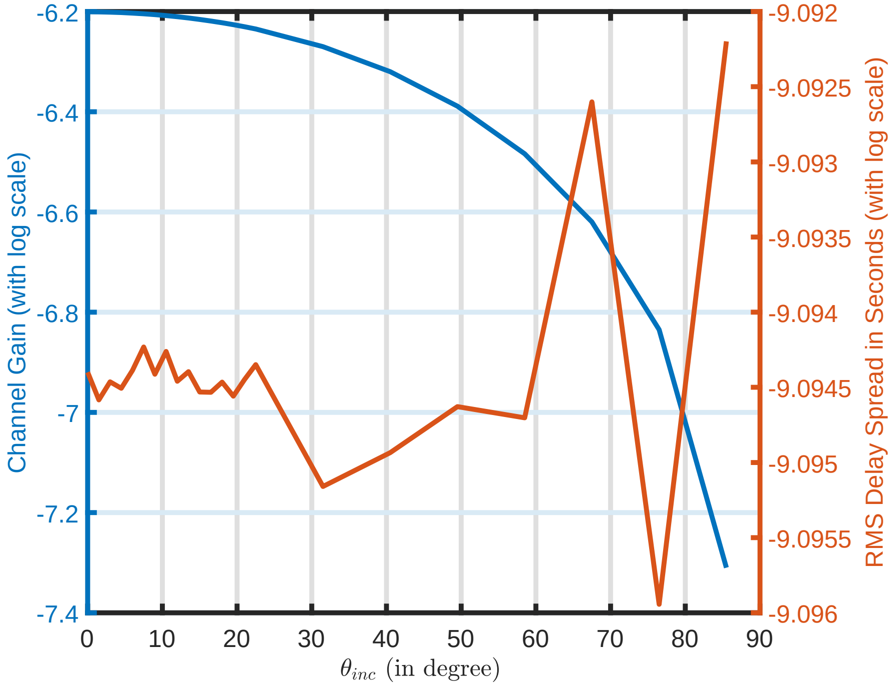

Figure C.4: Effects of the orientation on CIR, H_o and τ_{RMS}.

disorientation, $\theta_{inc} = [0^o, 90^o]$. The shown results are associated with AUV-Rx configured with ($D_r = 10\,\text{cm}$, $\theta_{FOV} = 90^o$), located at ($\Delta_x = 3, \Delta_y = 0, \Delta_z = 2\,\text{m}$), azimuthal angle $\phi_{inc} = 0^o$, in the Co-B channel. The disorientation leads to an increase in geometric loss. Thus, the DC gain decreases monotonically versus the inclination angle, $\theta_{inc} = [0^o, 90^o]$. The rate of the decreasing is slow in the range of $\theta_{inc} = [0^o, 20^o]$, however, the rate of the decreasing is fast in the range of $\theta_{inc} = [60^o, 90^o]$. The disorientation effectively impacts the DC gain when the angle exceeds 20^o. However, the channel gain is fixed with a disorientation angle less than 10^o. However, the delay spread fluctuates with increasing in the inclination angle. As shown, changes in the delay spread with increasing in the diameter are not significant, where the delay spread changes on the range of $[8.08 \times 10^{-10}, 8.01 \times 10^{-10}]$. Results indicate the robustness of SDOC approaches against disorientation which is not the typical case of LOS communications. SDOC systems inherit this robustness due to the Co-B channel's wide spots and omni-directional diffusing patterns.

C.6 Spatial Distributions of H_o and τ_{RMS}

Figure C.5 shows spatial distributions for DC gain and RMS delay spread versus position of the receiver on the x-y plane. The results are shown for the Co-B channel, and distributions cover an area of $6 \times 6\,\mathrm{m}^2$. The results are associated to AUV-Rx configured with: $D_r = 15\,\mathrm{cm}$, $\theta_{FOV} = 140^o$, $\Delta_z = 3$ and $\theta_{inc} = \phi_{inc} = 0$. These configuration compromises between receiver sizes and DC gains according to results shown in Figs. C.2-C.4. Specifically, lens with diameter $D_r = 15$ cm is an appropriate to AUV-Rx with size $60 \times 25\ cm^2$ [82]. Rather than full FOV (i.e., $\theta_{FOV} = 180^o$), a relatively narrow angle (i.e., $\theta_{FOV} = 140^o$) eliminates background radiations. Comparative with the depth of AUV-Tx (i.e., $z_o = 2$ m), AUV-Rxs can navigate more deeper under sea ices (i.e., $\Delta_z = 3$) to increase the communication range, see Fig. 4.10.

Figure C.5a shows the spatial distribution of DC gain. The distribution is symmetric in the x-y plane around the center ($\Delta_x = 0, \Delta_y = 0$) due to the symmetry of the diffusing pattern under the sea ice in spatial and angular domains as shown in Figs. 4.6a, b and c. Values of the DC gain decrease monotonically with Δ_x and Δ_y. As well, shown values are smaller than that have been shown for the case of the Co-S channel, Fig. 4.11, due to dense scattering taking place in the snow. Numerically, the maximum, average, and minimum values for the DC gain are 0.7×10^{-4}, 2.33×10^{-5}

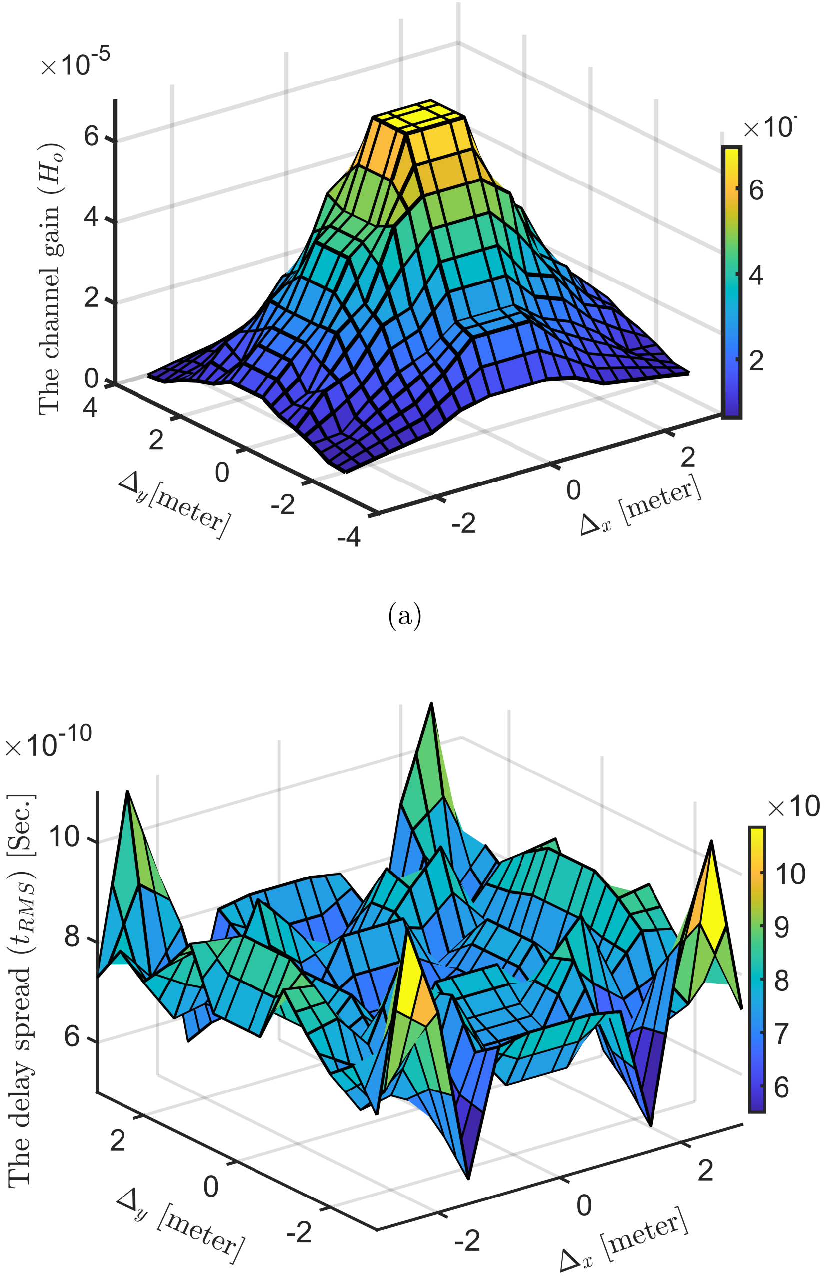

(a)

(b)

Figure C.5: (a) Spatial distribution of the channel gain and (b) Spatial distribution of delay spread for the Co-B channel.

and 6.2×10^{-6} respectively.

Figure C.5b shows the spatial distribution of RMS delay spread. Values of delay spread are not a monotonic function with distances as the case of the DC channel gain. However, the values fluctuate with the position of AUV-Rx. The lowest and the highest values for the delay spread are observed nearby the center ($\Delta_x = \Delta_y = \pm 0.5$) and the corners ($\Delta_x = \Delta_y = \pm 3$), respectively. The delay spread is on the order of the nano-seconds scale. However, the values being observed in the Co-B model are smaller than that have been observed in the case of the Co-S model. Numerically, the maximum, average, and minimum values for the delay spread are 1.085×10^{-9} Sec, 0.77×10^{-9} Sec, and 5.5×10^{-10}, respectively.

C.7 Bit Error rates (BER) Versus Transmitted Power and Bit Rates

Figure C.6 shows BER performances versus the distance Δ_x with different values for the bit rate and average transmitted power, i.e., $R_b = \{10, 50, 100, 200, 300\}$ Mpbs $P_{av} = \{50, 250\}$ mW. As well, the FEC limit is indicated using the green line with BER value 10^{-3}. The results are associated with AUV-Rx with the equalized receiver, i.e., $i_{isi} \neq 0$, where both residual ISI and receiver noise impairs the received signals.

As shown, higher communication speed can be achieved with a smaller communication range and vice versa. Also, the AUV-Tx can send more transmitted power to extend the communication range and raise the communication speed with AUV-Rxs.

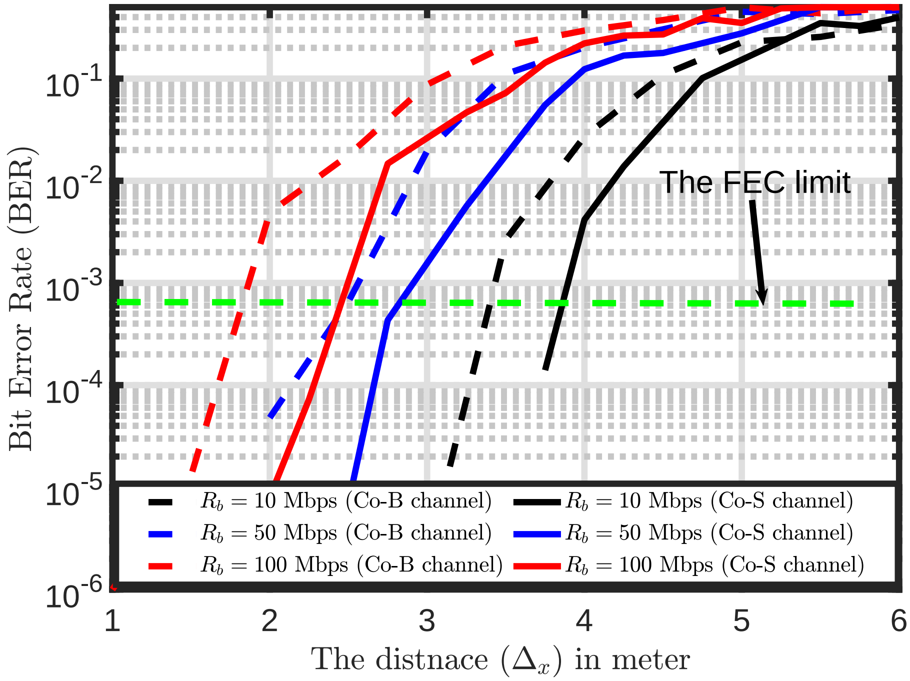

(a) $P_{av} = 50$ mW.

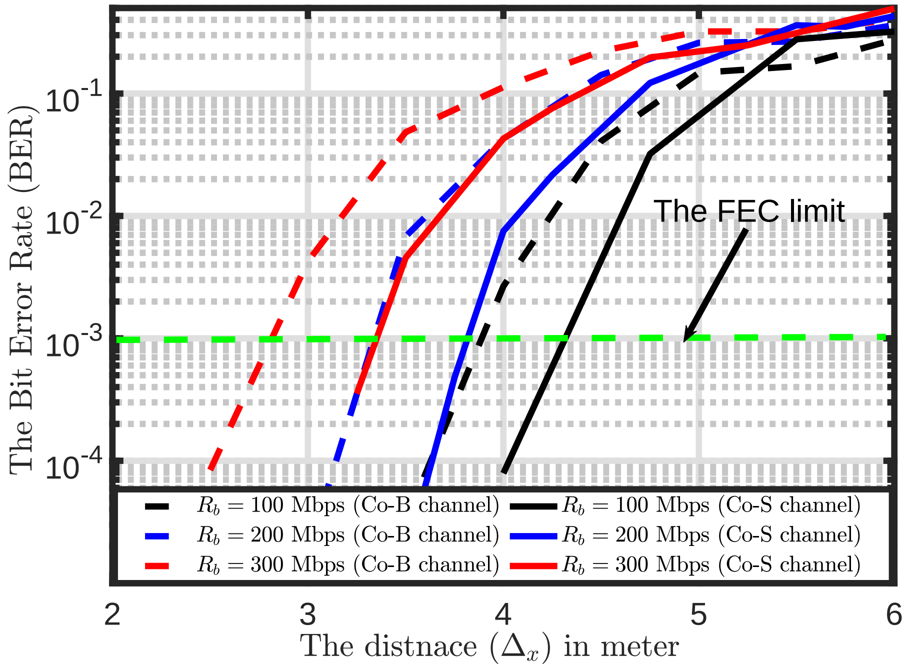

(b) $P_{av} = 250$ mW.

Figure C.6: BERs versus the distance Δ_x with different transmitted powers.

However, the transmitted power is usually restricted due to limitations of the lifetime of the battery and eye-safety standards. In contrast to the Co-B channel, the Co-S channel provides a better performance, where the AUV-Tx can communicate with AUV-Rxs at a more extended range and higher speed.

In the Co-B channel, the AUV-Tx can extend the communication range and increase the speed by increasing the transmitted power as shown in Figs. C.6a and C.6b. In Fig. C.6a, the AUV-Tx communicates with the AUV-Rx at speed of $R_b = 10$ Mbps and range up to $\Delta_x = 3.5$ m, however, at speed of $R_b = 100$ Mbps and range up to $\Delta_x = 1.8$ m. In Fig. C.6b, the transmitted power is raised to $P_{av} = 250$ mW, the AUV-Tx communicates with the AUV-Rx at speed of $R_b = 100$ Mbps and range up to $\Delta_x = 3.9$ m, however, at speed of $R_b = 300$ Mbps and range up to $\Delta_x = 2.75$ m. At communication range 3.5 meters, we observe that scaling the transmitted power by 5 times (i.e., from $P_{av} = 50$ mW to $P_{av} = 250$ mW) increases the communication speed by twenty times (i.e., from 10 Mbps to 200 Mbps).

Note that, in the Co-B and Co-S channels, with speed 100 Mbps, scaling the transmitted power by 5 times (i.e., from $P_{av} = 50$ mW to $P_{av} = 250$ mW) increases the communication range roughly by two times (i.e., from 1.8 m to 3.9 m in Co-B channel and 2.5 m to 4.5 m in Co-S channel).

Bibliography

[1] "How Much Water is in the Ocean?" https://oceanservice.noaa.gov/facts/oceanwater.html, accessed: 2021-3-23.

[2] "Earth's Ocean is 95% Unexplored: So what?" https://oceanexplorer.noaa.gov/okeanos/explorations/10index/background/edu/media/so_what.pdf, accessed: 2021-3-23.

[3] K. K. A. Zolich, D. Palma, "Survey on Communication and Networks for Autonomous Marine Systems," *Journal of Intell Robot Syst*, vol. 95, p. 789–813, 2019.

[4] Z. Zeng, S. Fu, H. Zhang, Y. Dong, and J. Cheng, "A Survey of Underwater Optical Wireless Communications," *IEEE Communications Surveys Tutorials*, vol. 19, no. 1, pp. 204–238, 2017.

[5] H. Kaushal and G. Kaddoum, "Underwater Optical Wireless Communication," *IEEE Access*, vol. 4, pp. 1518–1547, 2016.

[6] M. Jouhari, K. Ibrahimi, H. Tembine, and J. Ben-Othman, "Underwater Wireless Sensor Networks: A Survey on Enabling Technologies, Localization Protocols, and Internet of Underwater Things," *IEEE Access*, vol. 7, pp. 96 879–96 899, 2019.

[7] C. Osterloh, T. Pionteck, and E. Maehle, "MONSUN II: A Small and Inexpensive AUV for Underwater Swarms," in *ROBOTIK 2012; 7th German Conference on Robotics*, 2012, pp. 1–6.

[8] A. S. Ghazy, S. Hranilovic, and M.-A. Khalighi, "Angular MIMO for Underwater Wireless Optical Communications: Channel Modelling and Capacity," in *2019 16th Canadian Workshop on Information Theory (CWIT)*, 2019, pp. 1–6.

[9] ——, "Angular MIMO for Underwater Wireless Optical Communications: Link Modeling and Tracking," *IEEE Journal of Oceanic Engineering*, vol. 46, no. 4, pp. 1391–1407, 2021.

[10] A. S. Ghazy, H. S. Khallaf, S. Hranilovic, and M.-A. Khalighi, "Under-sea ice diffusing optical communications," *IEEE Access*, pp. 1–21, 2021.

[11] Dreamstime, "Dreamstime," [Available at] https://www.dreamstime.com, [Accessed on]: 2021-10-13.

[12] Gograph, "Gograph," [Available at] https://www.gograph.com, [Accessed on]: 2021-10-13.

[13] Pngtree, "Pngtree," [Available at] https://pngtree.com, [Accessed on]: 2021-10-13.

[14] C. Albaladejo, F. Soto, R. Torres, P. Sánchez, and J. A. López, “A Low-Cost Sensor Buoy System for Monitoring Shallow Marine Environments,” *Sensors*, vol. 12, no. 7, pp. 9613–9634, 2012.

[15] B. Cochenour, L. Mullen, and A. Laux, “Phase Coherent Digital Communications for Wireless Optical Links in Turbid Underwater Environments,” in *OCEANS 2007*, 2007, pp. 1–5.

[16] G. W. Marsh and J. M. Kahn, “Performance Evaluation of Experimental 50-Mb/s Diffuse Infrared Wireless Link Using On-Off Keying with Decision-Feedback Equalization,” *IEEE Transactions on Communications*, vol. 44, no. 11, pp. 1496–1504, 1996.

[17] M. A. Khalighi, C. J. Gabriel, L. M. Pessoa, and B. Silva, *Visible Light Communications: Theory and Applications.* CRC-Press, 2017, ch. Underwater Visible Light Communications, Channel Modeling and System Design, pp. 337–372.

[18] ThorLab, “Unmounted LEDs,” [Available at] https://www.thorlabs.com/newgrouppage9.cfm?objectgroup_id=2814, [Accessed on]: 2021-11-15.

[19] ——, “Collimated LED Light Sources for Microscopy,” [Available at] https://www.thorlabs.com/newgrouppage9.cfm?objectgroup_id=2615, [Accessed on]: 2021-11-15.

[20] ——, “LED Array Light Sources,” [Available at] https://www.thorlabs.com/newgrouppage9.cfm?objectgroup_id=2853, [Accessed on]: 2021-11-15.

[21] ——, “Laser Diodes by Wavelength,” [Available at] https://www.thorlabs.com/navigation.cfm?guide_id=2164, [Accessed on]: 2021-11-15.

[22] ——, “Laser Modules,” [Available at] https://www.thorlabs.com/navigation.cfm?guide_id=2097, [Accessed on]: 2021-11-15.

[23] ——, “Single-Frequency Lasers,” [Available at] https://www.thorlabs.com/navigation.cfm?guide_id=2455, [Accessed on]: 2021-11-15.

[24] B. Cochenour, L. Mullen, and J. Muth, “Temporal Response of the Underwater Optical Channel for High-Bandwidth Wireless Laser Communications,” *IEEE Journal of Oceanic Engineering*, vol. 38, no. 4, pp. 730–742, Oct. 2013.

[25] D. Karunatilaka, F. Zafar, V. Kalavally, and R. Parthiban, “LED Based Indoor Visible Light Communications: State of the Art,” *IEEE Communications Surveys Tutorials*, vol. 17, no. 3, pp. 1649–1678, 2015.

[26] Y. Dong, J. Liu, and H. Zhang, “On Capacity of 2-by-2 Underwater Wireless Optical MIMO Channels,” in *2015 Advances in Wireless and Optical Communications (RTUWO), Riga*, Nov 2015, pp. 219–222.

[27] ThorLab, “Molded Glass Aspheric Lenses: 350 - 700 nm or 400 - 600 nm AR Coating,” [Available at] https://www.thorlabs.com/newgrouppage9.cfm?objectgroup_id=3810, [Accessed on]: 2021-04-01.

[28] R. A. Leathers, T. V. Downes, C. O. Davis, C. D. Mobley, R. A. Leathers, T. V. Downes, C. O. Davis, and C. D. Mobley, “Monte Carlo Radiative Transfer Simulations for Ocean Optics: A Practical Guide,” [Available at] http://www.dtic.mil/docs/citations/ADA426624, 2004.

[29] T. C. Grenfell, “A Theoretical Model of the Optical Properties of Sea Ice in the

Visible and Near Infrared," *Journal of Geophysical Research: Oceans*, vol. 88, no. C14, pp. 9723–9735, 1983.

[30] R. Millard and G. Seaver, "An Index of Refraction Algorithm for Seawater over Temperature, Pressure, Salinity, Density, and Wavelength," *Deep Sea Research Part A. Oceanographic Research Papers*, vol. 37, no. 12, pp. 1909–1926, 1990.

[31] N. Anous, M. Abdallah, M. Uysal, and K. Qaraqe, "Performance Evaluation of LOS and NLOS Vertical Inhomogeneous Links in Underwater Visible Light Communications," *IEEE Access*, vol. 6, pp. 22 408–22 420, 2018.

[32] C. Gabriel, M. A. Khalighi, S. Bourennane, P. Leon, and V. Rigaud, "Monte-Carlo-Based Channel Characterization for Underwater Optical Communication Systems," *IEEE/OSA Journal of Optical Communications and Networking*, vol. 5, no. 1, pp. 1–12, Jan. 2013.

[33] T. C. Grenfell, "A Radiative Transfer Model for Sea Ice with Vertical Structure Variations," *Journal of Geophysical Research: Oceans*, vol. 96, no. C9, pp. 16 991–17 001, 1991.

[34] B. Light, H. Eicken, G. Maykut, and T. Grenfell, "The Effect of Included Participates on the Spectral Albedo of Sea Ice," *Journal of Geophysical Research: Oceans*, vol. 103, no. C12, pp. 27 739–27 752, 1998.

[35] A. Glaciers, "Antarctic Glaciers," [Available at] http://www.antarcticglaciers.org/antarctica-2/photographs/ice-textures-and-patterns/, [Accessed on]: 2021-04-01.

[36] B. Light, “Structural-Optical Relationships in First-Year Sea Ice,” Ph.D. dissertation, 2000.

[37] B. Hamre, J.-G. Winther, S. Gerland, J. J. Stamnes, and K. Stamnes, “Modeled and Measured Optical Transmittance of Snow-Covered First-Year Sea Ice in Kongsfjorden, Svalbard,” *Journal of Geophysical Research: Oceans*, vol. 109, no. C10, 2004.

[38] B. Light, G. Maykut, and T. Grenfell, “A Temperature-Dependent, Structural-Optical Model of First-Year Sea Ice,” *Journal of Geophysical Research: Oceans*, vol. 109, no. C6, 2004.

[39] H. Zhang, J. Cheng, Z. Wang, and Y. Dong, “On the Capacity of Buoy-Based MIMO Systems for Underwater Optical Wireless Links with Turbulence,” pp. 1–6, May 2018.

[40] L. Zeng, D. C. O’Brien, H. L. Minh, G. E. Faulkner, K. Lee, D. Jung, Y. Oh, and E. T. Won, “High Data Rate Multiple Input Multiple Output (MIMO) Optical Wireless Communications Using White LED Lighting,” *IEEE Journal on Selected Areas in Communications*, vol. 27, no. 9, pp. 1654–1662, Dec. 2009.

[41] Y. Li, H. Qiu, X. Chen, J. Fu, M. Musa, and X. Li, “Spatial Correlation Analysis of Imaging MIMO for Underwater Visible Light Communication,” in *Optics Communications, Elsevier*, vol. 443, no. 4, Jul. 2019, pp. 221–229.

[42] J. R. Barry and J. M. Kahn, “Link Design for Nondirected Wireless Infrared Communications,” *Appl. Opt.*, vol. 34, no. 19, pp. 3764–3776, Jul 1995. [Online]. Available: http://ao.osa.org/abstract.cfm?URI=ao-34-19-3764

[43] T. Hamza, M.-A. Khalighi, S. Bourennane, P. Léon, and J. Opderbecke, "Investigation of Solar Noise Impact on the Performance of Underwater Wireless Optical Communication Links," *Opt. Express*, vol. 24, no. 22, pp. 25 832–25 845, Oct 2016. [Online]. Available: http://www.opticsexpress.org/abstract.cfm?URI=oe-24-22-25832

[44] T. Komine, J. H. Lee, S. Haruyama, and M. Nakagawa, "Adaptive Equalization System for Visible light Wireless Communication Utilizing Multiple white LED Lighting Equipment," *IEEE Transactions on Wireless Communications*, vol. 8, no. 6, pp. 2892–2900, 2009.

[45] S. Nadarajah, X. Fernando, and R. Sedaghat, "Adaptive digital predistortion of laser diode nonlinearity for wireless applications," in *CCECE 2003-Canadian Conference on Electrical and Computer Engineering. Toward a Caring and Humane Technology (Cat. No. 03CH37436)*, vol. 1. IEEE, 2003, pp. 159–162.

[46] A. Rainal, "Laser Clipping Distortion in Analog and Digital Channels," *Journal of Lightwave Technology*, vol. 15, no. 10, pp. 1805–1807, 1997.

[47] K. Hinton and T. Stephens, "Modeling High-Speed optical Transmission Systems," *IEEE Journal on Selected Areas in Communications*, vol. 11, no. 3, pp. 380–392, 1993.

[48] H. M. Oubei, J. R. Duran, B. Janjua, H.-Y. Wang, C.-T. Tsai, Y.-C. Chi, T. K. Ng, H.-C. Kuo, J.-H. He, M.-S. Alouini, G.-R. Lin, and B. S. Ooi, "4.8 Gbit/s 16-QAM-OFDM Transmission Based on Compact 450-nm Laser for Underwater Wireless Optical Communication," *Opt. Express*, vol. 23, no. 18, pp. 23 302–23 309, Sep. 2015.

[49] R. T. Mihran, “Interaction of Laser Radiation with Structures of the Eye,” *IEEE Transactions on Education*, vol. 34, no. 3, pp. 250–259, 1991.

[50] H. C. Van de Hulst, *Light Scattering by Small Particles*, H. C. Van de Hulst, Ed. Wiley, New York., 1957.

[51] “Laser Products and Instruments,” https://www.fda.gov/radiation-emitting-products/home-business-and-entertainment-products/laser-products-and-instruments, accessed: 2020-8-7.

[52] S. Khoo, E. Zyambo, G. Faulkner, D. O’Brien, D. Edwards, M. Ghisoni, and J. Bengtsson, “Eyesafe optical link using a holographic diffuser,” in *IEE Colloquium on Optical Wireless Communications (Ref. No. 1999/128)*, 1999, pp. 3/1–3/6.

[53] S. Tang, Y. Dong, and X. Zhang, “Impulse Response Modeling for Underwater Wireless Optical Communication Links,” *IEEE Transactions on Communications*, vol. 62, no. 1, pp. 226–234, 2014.

[54] Y. Li, M. S. Leeson, and X. Li, “Impulse Response Modeling For Underwater Optical Wireless Channels,” *Appl. Opt.*, vol. 57, no. 17, pp. 4815–4823, Jun 2018. [Online]. Available: http://ao.osa.org/abstract.cfm?URI=ao-57-17-4815

[55] R. Boluda-Ruiz, P. Rico-Pinazo, B. Castillo-Vázquez, A. García-Zambrana, and K. Qaraqe, “Impulse Response Modeling of Underwater Optical Scattering Channels for Wireless Communication,” *IEEE Photonics Journal*, vol. 12, no. 4, pp. 1–14, 2020.

[56] W. J. Wiscombe and S. G. Warren, “A Model for the Spectral Albedo of Snow. I: Pure Snow,” *Journal of the Atmospheric Sciences*, vol. 37, no. 12, pp. 2712–2733, 1980.

[57] Z. Vali, A. Gholami, Z. Ghassemlooy, M. Omoomi, and D. G. Michelson, “Experimental Study of the Turbulence Effect on Underwater Optical Wireless Communications,” *Appl. Opt.*, vol. 57, no. 28, pp. 8314–8319, Oct 2018.

[58] M. V. Jamali, A. Mirani, A. Parsay, B. Abolhassani, P. Nabavi, A. Chizari, P. Khorramshahi, S. Abdollahramezani, and J. A. Salehi, “Statistical Studies of Fading in Underwater Wireless Optical Channels in the Presence of Air Bubble, Temperature, and Salinity Random Variations,” *IEEE Transactions on Communications*, vol. 66, no. 10, pp. 4706–4723, 2018.

[59] M. Vahid Jamali, A. Mirani, A. Parsay, B. Abolhassani, P. Nabavi, A. Chizari, P. Khorramshahi, S. Abdollahramezani, and J. A. Salehi, “Statistical Studies of Fading in Underwater Wireless Optical Channels in the Presence of Air Bubble, Temperature, and Salinity Random Variations (Long Version),” *arXiv e-prints*, pp. arXiv–1801, 2018.

[60] M. V. Jamali, J. A. Salehi, and F. Akhoundi, “Performance Studies of Underwater Wireless Optical Communication Systems With Spatial Diversity: MIMO Scheme,” *IEEE Transactions on Communications*, vol. 65, no. 3, pp. 1176–1192, 2017.

[61] R. M. G. S. Karp, “Optical Communications,” in *John Wiley and Sons*, feburary, First 1995, pp. 249–519.

[62] C. Mobley, E. Boss, and C. Roesler, "Ocean Optics Web Book (2016)," [Available at] https://www.oceanopticsbook.info, [Accessed on]: 2021-07-06.

[63] H. Zhang, J. Cheng, Z. Wang, and Y. Dong, "On the Capacity of Buoy-Based MIMO Systems for Underwater Optical Wireless Links with Turbulence," in *2018 IEEE International Conference on Communications (ICC)*, 2018, pp. 1–6.

[64] H. Zhang, Y. Dong, and L. Hui, "On Capacity of Downlink Underwater Wireless Optical MIMO Systems With Random Sea Surface," *IEEE Communications Letters*, vol. 19, no. 12, pp. 2166–2169, Dec. 2015.

[65] "World's Largest Swarm of Miniature Robot Submarines," https://spectrum.ieee.org/automaton/robotics/artificial-intelligence/worlds-largest-swarm-of-miniature-robot-submarines, accessed: 2021-07-10.

[66] F. Miramirkhani and M. Uysal, "Visible Light Communication Channel Modeling for Underwater Environments With Blocking and Shadowing," *IEEE Access*, vol. 6, pp. 1082–1090, 2018.

[67] A. A. El-Fikky, M. E. Eldin, H. A. Fayed, A. A. E. Aziz, H. M. H. Shalaby, and M. H. Aly, "NLoS Underwater VLC System Performance: Static and Dynamic Channel Modeling," *Appl. Opt.*, vol. 58, no. 30, pp. 8272–8281, Oct 2019. [Online]. Available: http://ao.osa.org/abstract.cfm?URI=ao-58-30-8272

[68] N. Saeed, S. Guo, K.-H. Park, T. Y. Al-Naffouri, and M.-S. Alouini, "Optical Camera Communications: Survey, Use Cases, Challenges, and Future Trends," *Phyisical Communications*, vol. 37, Dec. 2019.

[69] S. Hranilovic and F. R. Kschischang, “A pixelated MIMO Wireless Optical Communication System,” *IEEE Journal of Selected Topics in Quantum Electronics*, vol. 12, no. 4, pp. 859–874, July 2006.

[70] B. Han and S. Hranilovic, “A fixed-Scale Pixelated MIMO Visible Light Systems,” *IEEE Journal on Selected Areas in Communications*, vol. 36, no. 1, pp. 203–211, Jan 2018.

[71] S. D. Milner, J. Llorca, and C. C. Davis, “Autonomous Reconfiguration and Control in Directional Mobile ad Hoc Networks,” *IEEE Circuits and Systems Magazine*, vol. 9, no. 2, pp. 10–26, 2009.

[72] Y. Kaymak, R. Rojas-Cessa, J. Feng, N. Ansari, M. Zhou, and T. Zhang, “A survey on acquisition, tracking, and pointing mechanisms for mobile free-space optical communications,” *IEEE Communications Surveys Tutorials*, vol. 20, no. 2, pp. 1104–1123, 2018.

[73] R. Nalbandian, “Enhanced pointing gimbal mechanisms for next generation communication antennas,” in *Proc. 15th European Space Mechanisms & Tribology Symposium*, 2013.

[74]

[75] J. A. Simpson, B. L. Hughes, and J. F. Muth, “Smart Transmitters and Receivers for Underwater Free-Space Optical Communication,” *IEEE Journal on Selected Areas in Communications*, vol. 30, no. 5, pp. 964–974, 2012.

[76] W. Liu, D. Zou, Z. Xu, and J. Yu, “Non-Line-of-Sight Scattering Channel Modeling for Underwater Optical Wireless Communication,” in *2015 IEEE International Conference on Cyber Technology in Automation, Control, and Intelligent Systems (CYBER)*, 2015, pp. 1265–1268.

[77] Z. Pan, Y. Xiao, L. Zhou, Y. Cao, M. Yang, and W. Chen, “Non-line-of-sight Optical Information Transmission Through Turbid Water,” *Opt. Express*, vol. 29, no. 24, pp. 39 498–39 510, Nov 2021.

[78] S. Arnon and D. Kedar, “Non-Line-of-Sight Underwater Optical Wireless Communication Network,” *J. Opt. Soc. Am. A*, vol. 26, no. 3, pp. 530–539, Mar 2009.

[79] X. Quan and E. S. Fry, “Empirical Equation for the Index of Refraction of Seawater,” *Applied optics*, vol. 34, no. 18, pp. 3477–3480, 1995.

[80] Z. Jin, K. Stamnes, W. Weeks, and S.-C. Tsay, “The Effect of Sea Ice on the Solar Energy Budget in the Atmosphere-Sea Ice-Ocean System: A Model Study,” *Journal of Geophysical Research: Oceans*, vol. 99, no. C12, pp. 25 281–25 294, 1994.

[81] C. D. Mobley, G. F. Cota, T. C. Grenfell, R. A. Maffione, W. S. Pegau, and D. K. Perovich, “Modeling Light Propagation in Sea Ice,” *IEEE Transactions on Geoscience and Remote Sensing*, vol. 36, no. 5, pp. 1743–1749, 1998.

[82] U. Behrje, A. Amory, B. Meyer, and E. Maehle, “System identification and sliding mode depth control of the micro AUV SEMBIO,” in *ISR 2018; 50th International Symposium on Robotics.* VDE, 2018, pp. 1–8.

[83] N. Vedachalam, R. Ramesh, V. B. N. Jyothi, V. Doss Prakash, and G. Ramadass, “Autonomous Underwater Vehicles-Challenging Developments and Technological Maturity Towards Strategic Swarm Robotics Systems,” *Marine Georesources & Geotechnology*, vol. 37, no. 5, pp. 525–538, 2019.

[84] E. Sahin and A. F. Winfield, “Special Issue on Swarm Robotics,” *Swarm Intelligence*, vol. 2, no. 2-4, pp. 69–72, 2008.

[85] B. Han, “A fixed-Scale Pixelated MIMO Visible Light,” Master’s thesis, McMaster University, 2017.

[86] Zemax, “Opticstudio,” [Available at] https://www.zemax.com, [Accessed on]: 2021-04-01.

[87] A. Mohan, G. Woo, S. Hiura, Q. Smithwick, and R. Raskar, “Bokode: Imperceptible Visual Tags for Camera Based Interaction from a Distance,” *ACM Trans. Graph.*, vol. 28, no. 3, pp. 98:1–98:8, July 2009. [Online]. Available: http://doi.acm.org/10.1145/1531326.1531404

[88] H. Zhang and Y. Dong, “General Stochastic Channel Model and Performance Evaluation for Underwater Wireless Optical Links,” *IEEE Transactions on Wireless Communications*, vol. 15, no. 2, pp. 1162–1173, 2016.

[89] C. Li, K. H. Park, and M. S. Alouini, “On the Use of a Direct Radiative Transfer Equation Solver for Path Loss Calculation in Underwater Optical Wireless Channels,” *IEEE Wireless Communications Letters*, vol. 4, no. 5, pp. 561–564, Oct 2015.

[90] J. L. Henyey and L. G. Greenstein, "Diffuse Radiation in the Galaxy," in *Astrophysical Journal*, Jan. 1941, pp. 70–83.

[91] J. S. L. and W. L., *Monte Carlo Modeling of Light Transport in Tissues.* Boston, MA: Springer US, 1995, pp. 73–100.

[92] "Oceaneering," https://www.Oceaneering.com, accessed: 2019-02-19.

[93] K. Nakamura, I. Mizukoshi, and M. Hanawa, "Optical Wireless Transmission of 405 nm, 1.45 Gbit/s Optical IM/DD-OFDM Signals Through a 4.8 m Underwater Channel," *Opt. Express*, vol. 23, no. 2, pp. 1558–1566, Jan 2015.

[94] P. Zou, Y. Zhao, F. Hu, and N. Chi, "Underwater Visible Light Communication at 3.24 Gb/s Using Novel Two-Dimensional Bit Allocation," *Opt. Express*, vol. 28, no. 8, pp. 11 319–11 338, Apr 2020.

[95] M. A. Khalighi, H. Akhouayri, and S. Hranilovic, "Silicon-Photomultiplier-Based Underwater Wireless Optical Communication Using Pulse-Amplitude Modulation," *IEEE Journal of Oceanic Engineering*, vol. 45, no. 4, pp. 1611–1621, Octuber 2020.

[96] R. Xu, Y. Chen, Z. Wei, H. Fu, J. Cheng, and Y. Dong, "On BER of Fixed-Scale MIMO Underwater Wireless Optical Communication Systems," in *2020 IEEE 17th Annual Consumer Communications Networking Conference (CCNC), Las Vegas, NV, USA*, 2020, pp. 1–6.

[97] Mathwork, "Matlab: MCNRT and Curve Fitting," [Available at] https://www.mathworks.com, [Accessed on]: 2021-04-01.

[98] M. Pisani, “Four Quadrant Photo-Detector with Ultra High Common Mode Rejection Ratio and Ultra Narrow Gap,” in *The 17th Annual Meeting of the IEEE Lasers and Electro-Optics Society, 2004. LEOS 2004, Rio, Grande, Pureto Rico*, vol. 1, 2004, pp. 51–52 Vol.1.

[99] G. F. Simmons, “Calculus with Analytic Geometry,” in *McGraw-Hill.*, Oct 1996, pp. 249–519.

[100] G. Xu and J. Lai, “Average Capacity Analysis of the Underwater Optical Plane Wave over Anisotropic Moderate-to-Strong Oceanic Turbulence Channels with the Malaga Fading Model,” *Opt. Express*, vol. 28, no. 16, pp. 24 056–24 068, Aug. 2020.

[101] “Gaussian Beam Optics,” accessed: 2020-01-04. [Online]. Available: https://web.pa.msu.edu/courses/2010fall/phy431/PostNotes/PHY431-Notes-GaussianBeamOptics.pdf

[102] J. Thompson and W. O. Popoola, “Effects of Turbulence Induced Scattering on Underwater Optical Wireless Communications,” *arXiv preprint arXiv:2008.01152*, 2020.

[103] G. J. Foschini and M. J. Gans, “On Limits of Wireless Communications in a Fading Environment when Using Multiple Antennas,” *Wireless Personal Communications*, vol. 6, no. 3, pp. 311–335, 1996.

[104] J. Xu, Y. Song, X. Yu, A. Lin, M. Kong, J. Han, and N. Deng, “Underwater Wireless Transmission of High-Speed QAM-OFDM Signals Using a Compact Red-Light Laser,” *Opt. Express*, vol. 24, no. 8, pp. 8097–8109, Apr. 2016.

[105] C. Cox and W. Munk, "Measurement of the Roughness of the Sea Surface from Photographs of the Sun's Glitter," *J. Opt. Soc. Am.*, vol. 44, no. 11, pp. 838–850, Nov 1954.

[106] I. Vasilescu, K. Kotay, D. Rus, M. Dunbabin, and P. Corke, "Data Collection, Storage, and Retrieval with an Underwater Sensor Network," in *Proceedings of the 3rd International Conference on Embedded Networked SensorSystems, San Diego, Californiam USA*, 2005, pp. 154–165.

[107] T. I. Fossen, *Guidance and Control of Ocean Vehicles.* Wiley, 1994.

[108] B. S. Reddy and B. N. Chatterji, "An FFT-Based Technique For Translation, Rotation, and Scale-Invariant Image Registration," *IEEE Transactions on Image Processing*, vol. 5, no. 8, pp. 1266–1271, Aug. 1996.

[109] C. A. Wilson and J. A. Theriot, "A Correlation-Based Approach to Calculate Rotation and Translation of Moving cells," *IEEE Transactions on Image Processing*, vol. 15, no. 7, pp. 1939–1951, July 2006.

[110] G. Tzimiropoulos, V. Argyriou, S. Zafeiriou, and T. Stathaki, "Robust FFT-based scale-invariant image registration with image gradients," *IEEE Transactions on Pattern Analysis and Machine Intelligence*, vol. 32, no. 10, pp. 1899–1906, Oct 2010.

[111] E. E. Zelniker and I. V. L. Clarkson, "Maximum-Likelihood Estimation of Circle Parameters via Convolution," *IEEE Transactions on Image Processing*, vol. 15, no. 4, pp. 865–876, Apr. 2006.

[112] C. Mobley, "Light and Water: Radiative Transfer in Natural Waters," in *San Diego, CA: Academic Press/Elsevier Science*, Jan. 1994, pp. 249–519.

[113] L. J. Johnson, R. J. Green, and M. S. Leeson, "Underwater Optical Wireless Communications: Depth Dependent Variations in Attenuation," *Appl. Opt.*, vol. 52, no. 33, pp. 7867–7873, Nov. 2013.

[114] G. J. HAHN, "Sample Sizes for Monte Carlo Simulation," *IEEE Transaction on Systems, Man, and Cybernetics*, vol. SMC-2, no. 5, pp. 219–222, Nov 1972.

[115] H. Bear, "A Primer of Lebesgue Integration," in *Academic Press,*, Sep. 2002, pp. 249–519.

[116] National Snow and Ice Data Center, "All About Sea Ice," [Available at] https://nsidc.org/cryosphere/seaice/index.html, [Accessed on]: 2021-04-01.

[117] P. Wadhams, J. Wilkinson, and A. Kaletzky, "Sidescan Sonar Imagery of the Winter Marginal Ice Zone Obtained from an AUV," *Journal of Atmospheric and Oceanic Technology*, vol. 21, no. 9, pp. 1462–1470, 2004.

[118] N. Milard, P. Stevenson, M. Brandon, C. Banks, K. Heywood, M. Price, P. Dodd, A. Jenkins, K. Nicholls, D. Hayes *et al.*, "Instruments and Methods Autonomous underwater vehicles (AUVs) and Investigations of the Ice–Ocean Interface in Antarctic and Arctic Waters," *Journal of Glaciology*, vol. 54, no. 187, p. 661, 2008.

[119] T. Maksym, H. Singh, C. Bassett, A. Lavery, L. Freitag, F. Sonnichsen, and J. Wilkinson, "Oil Spill Detection and Mapping Under Arctic Sea Ice Using

Autonomous Underwater Vehicles," *Final Report BSEE Contract E12PC00053*, 2014.

[120] F. R. Gfeller and U. Bapst, "Wireless in-House Data Communication Via Diffuse Infrared Radiation," *Proceedings of the IEEE*, vol. 67, no. 11, pp. 1474–1486, 1979.

[121] G. Yun and M. Kavehrad, "Spot-Diffusing and Fly-Eye Receivers for Indoor Infrared Wireless Communications," in *IEEE International Conference on Selected Topics in Wireless Communications*, 1992, pp. 262–265.

[122] ——, "Indoor Infrared Wireless Communications Using Spot Diffusing and Fly-Eye Receivers," *Canadian Journal of Electrical and Computer Engineering*, vol. 18, no. 4, pp. 151–157, 1993.

[123] S. T. Jovkova and M. Kavehard, "Multispot Diffusing Configuration for Wireless Infrared Access," *IEEE Transactions on Communications*, vol. 48, no. 6, pp. 970–978, 2000.

[124] A. G. Al-Ghamdi and J. M. H. Elmirghani, "Line Strip Spot-Diffusing Transmitter Configuration For Optical Wireless Systems Influenced By Background Noise And Multipath Dispersion," *IEEE Transactions on Communications*, vol. 52, no. 1, pp. 37–45, 2004.

[125] W. Liu, D. Zou, Z. Xu, and J. Yu, "Non-line-of-sight Scattering Channel Modeling for Underwater Optical Wireless Communication," in *2015 IEEE International Conference on Cyber Technology in Automation, Control, and Intelligent Systems (CYBER)*, 2015, pp. 1265–1268.

[126] R. W. Preisendorfer, "Secchi Disk Science: Visual Optics of Natural Waters 1," *Limnology and Oceanography*, vol. 31, no. 5, pp. 909–926, 1986.

[127] Z. Lee, K. Du, R. Arnone, S. Liew, and B. Penta, "Penetration of Solar Radiation in the Upper Ocean: A Numerical Model for Oceanic and Coastal Waters," *Journal of Geophysical Research: Oceans*, vol. 110, no. C9, 2005.

[128] G. F. Cox and W. F. Weeks, "Equations for Determining the Gas and Brine Volumes in Sea-Ice Samples," *Journal of Glaciology*, vol. 29, no. 102, pp. 306–316, 1983.

[129] G. Carnat, T. Papakyriakou, N. Geilfus, F. Brabant, B. Delille, M. Vancoppenolle, G. Gilson, J. Zhou, and J.-L. Tison, "Investigations on physical and textural properties of Arctic first-year sea ice in the Amundsen Gulf, Canada, November 2007–June 2008 (IPY-CFL system study)," *Journal of Glaciology*, vol. 59, no. 217, p. 819–837, 2013.

[130] M. Shokr and N. K. Sinha, *Sea ice: physics and remote sensing.* John Wiley & Sons, 2015.

[131] D. K. Perovich and A. J. Gow, "A Statistical Description of the Microstructure of Young Sea Ice," *Journal of Geophysical Research: Oceans*, vol. 96, no. C9, pp. 16 943–16 953, 1991.

[132] M. Uysal, C. Capsoni, Z. Ghassemlooy, A. Boucouvalas, and E. Udvary, *Optical Wireless Communications: an Emerging Technology.* Springer, 2016.

[133] A. P. Worby, C. A. Geiger, M. J. Paget, M. L. Van Woert, S. F. Ackley, and

T. L. DeLiberty, "Thickness Distribution of Antarctic Sea Ice," *Journal of Geophysical Research: Oceans*, vol. 113, no. C5, 2008.

[134] M. R. Drinkwater, "LIMEX '87 Ice Surface Characteristics: Implications for C-Band SAR Backscatter Signatures," *IEEE Transactions on Geoscience and Remote Sensing*, vol. 27, no. 5, pp. 501–513, 1989.

[135] A. Manninen, "Surface Roughness of Baltic Sea Ice," *Journal of Geophysical Research: Oceans*, vol. 102, no. C1, pp. 1119–1139, 1997.

[136] J. C. Landy, D. Isleifson, A. S. Komarov, and D. G. Barber, "Parameterization of Centimeter-Scale Sea Ice Surface Roughness Using Terrestrial LiDAR," *IEEE Transactions on Geoscience and Remote Sensing*, vol. 53, no. 3, pp. 1271–1286, 2015.

[137] J. C. Landy, A. S. Komarov, and D. G. Barber, "Numerical and Experimental Evaluation of Terrestrial LiDAR for Parameterizing Centimeter-Scale Sea Ice Surface Roughness," *IEEE Transactions on Geoscience and Remote Sensing*, vol. 53, no. 9, pp. 4887–4898, 2015.

[138] W. Hibler, "Modeling a Variable Thickness Sea Ice Cover," *Monthly weather review*, vol. 108, no. 12, pp. 1943–1973, 1980.

[139] R. Pope and E. Fry, "Absorption Spectrum (380-700 nm) of Pure Water. II. Integrating Cavity Measurements," *Appl. Opt.*, vol. 36, pp. 8710–8723, (1997).

[140] A. Morel, "Light and Marine Photosynthesis: a Spectral Model with Geochemical and Climatological Implications," *Progress in Oceanography*, vol. 26, no. 3, pp. 263–306, 1991.

[141] Y. I. Kopilevich, M. Kononenko, and E. Zadorozhnaya, "The Effect of the Forward-Scattering Index on the Characteristics of a Light Beam in Sea Water," *Journal of Optical Technology*, vol. 77, no. 10, pp. 598–601, 2010.

[142] W. M. Irvine and J. B. Pollack, "Infrared Optical Properties of Water and Ice Spheres," *Icarus*, vol. 8, no. 1-3, pp. 324–360, 1968.

[143] A. Morel and S. Maritorena, "Bio-optical properties of oceanic waters: A reappraisal," *Journal of Geophysical Research: Oceans*, vol. 106, no. C4, pp. 7163–7180, 2001.

[144] A. Bricaud, A. Morel, and L. Prieur, "Absorption by Dissolved Organic Matter of the Sea (Yellow Substance) In the UV and Visible Domains 1," *Limnology and oceanography*, vol. 26, no. 1, pp. 43–53, 1981.

[145] T. C. Grenfell and D. K. Perovich, "Radiation Absorption Coefficients of Polycrystalline Ice from 400–1400 nm," *Journal of Geophysical Research: Oceans*, vol. 86, no. C8, pp. 7447–7450, 1981.

[146] B. Light, G. Maykut, and T. Grenfell, "Effects of Temperature on the Microstructure of First-Year Arctic Sea Ice," *Journal of Geophysical Research: Oceans*, vol. 108, no. C2, 2003.

[147] J. Felske, T. Charalampopoulos, and H. Hura, "Etermination of the Refractive Indices of Soot Particles from the Reflectivities of Compressed Soot Pellets," *Combustion Science and Technology*, vol. 37, no. 5-6, pp. 263–283, 1984.

[148] I. I. Kim, B. McArthur, and E. J. Korevaar, "Comparison of Laser Beam Propagation at 785 nm and 1550 nm In Fog and Haze for Optical Wireless

Communications," in *Optical Wireless Communications III*, E. J. Korevaar, Ed., vol. 4214, International Society for Optics and Photonics. SPIE, 2001, pp. 26 – 37. [Online]. Available: https://doi.org/10.1117/12.417512

[149] M. Mellor, "Light Scattering And Particle Aggregation In Snow-Storms," *Journal of Glaciology*, vol. 6, no. 44, pp. 237–248, 1966.

[150] A. Macke, J. Mueller, and E. Raschke, "Single Scattering Properties Of Atmospheric Ice Crystals," *Journal of Atmospheric Sciences*, vol. 53, no. 19, pp. 2813–2825, 1996.

[151] T. Nousiainen, "Scattering of Light by Raindrops With Single-Mode Oscillations," *Journal of the Atmospheric Sciences*, vol. 57, no. 6, pp. 789–802, 2000.

[152] M. Grabner and V. Kvicera, "Multiple Scattering in Rain and Fog on Free-Space Optical Links," *Journal of Lightwave Technology*, vol. 32, no. 3, pp. 513–520, 2014.

[153] O. Boucher, "On Aerosol Direct Shortwave Forcing and the Henyey–Greenstein Phase Function," *Journal of the Atmospheric Sciences*, vol. 55, no. 1, pp. 128–134, 1998.

[154] M. C. Al Naboulsi, H. Sizun, and F. de Fornel, "Fog Attenuation Prediction for Optical and Infrared Waves," *Optical Engineering*, vol. 43, no. 2, pp. 319–329, 2004.

[155] L. Gate, "Light-Scattering Cross Sections in Dense Colloidal Suspensions of Spherical Particles," *Journal of Optical Society of America*, vol. 63, no. 3, pp. 312–317, 1973.

[156] Y. Cocheril and R. Vauzelle, “A New Ray-Tracing Based Wave Propagation Model Including Rough Surfaces Scattering,” *Progress In Electromagnetics Research*, vol. 75, pp. 357–381, 2007.

[157] P. Yeh, *Optical Waves in Layered Media*, Hoboken, Ed. NJ, USA: Wiley, 2005.

[158] Jacques, S. L., Wang, and Lihong, *Monte Carlo Modeling of Light Transport in Tissues*. Boston, MA: Springer US, 1995, pp. 73–100.

[159] C. Gabriel, M.-A. Khalighi, S. Bourennane, P. Leon, and V. Rigaud, “Monte-carlo-based Channel Characterization for Underwater Optical Communication Systems,” *IEEE/OSA Journal of Optical Communications and Networking*, vol. 5, no. 1, pp. 1–12, 2013.

[160] J. M. Kahn, W. J. Krause, and J. B. Carruthers, “Experimental Characterization of Non-Directed Indoor Infrared Channels,” *IEEE Transactions on Communications*, vol. 43, no. 2/3/4, pp. 1613–1623, 1995.

[161] L. J. Johnson, R. J. Green, and M. S. Leeson, “The Impact Of Link Orientation In Underwater Optical Wireless Communication Systems,” in *2014 Oceans - St. John’s*, 2014, pp. 1–8.

[162] T. Sakurai, H. Chosrowjan, T. Somekawa, M. Fujita, H. Motoyama, O. Watanabe, and Y. Izawa, “”Studies of Melting Ice Using CO_2 Laser for Ice Drilling”,” *Cold Regions Science and Technology*, vol. 121, pp. 11 – 15, 2016. [Online]. Available: http://www.sciencedirect.com/science/article/pii/S0165232X15002116

[163] J. Kahn and J. Barry, "Wireless Infrared Communications," *Proceedings of the IEEE*, vol. 85, no. 2, pp. 265–298, 1997.

[164] T. Hamza and M. Ali Khalighi, "On Limitations of Using Silicon Photo-Multipliers for Underwater Wireless Optical Communications," in *2019 2nd West Asian Colloquium on Optical Wireless Communications (WACOWC)*, 2019, pp. 74–79.

[165] J. Proakis and M. Salehi, *Digital Communications.* McGraw-Hill, 2008.

[166] F. Xu, M.-A. Khalighi, and S. Bourennane, "Impact of different noise sources on the performance of PIN- and APD-based FSO receivers," in *Proceedings of the 11th International Conference on Telecommunications*, 2011, pp. 211–218.

[167] I. Juszak, W. Eugster, M. M. Heijmans, and G. Schaepman-Strub, "Contrasting Radiation and Soil Heat Fluxes in Arctic Shrub and Wet Sedge Tundra," *Biogeosciences*, vol. 13, no. 13, pp. 4049–4064, 2016.

[168] S. Haykin, *Communication Systems.* John Wiley & Sons, 2008.

[169] J. A. Ogilvy and J. R. Foster, "Rough Surfaces: Gaussian or Exponential Statistics?" *Journal of Physics D: Applied Physics*, vol. 22, no. 9, pp. 1243–1251, sep 1989.

[170] D. Zwillinger, V. Moll, I. Gradshteyn, and I. Ryzhik, "Table of Integrals, Series, and Products," in *Academic Press*, Oct. 2015, pp. 249–519.

[171] I. RP, "Prediction Methods Required for the Design of Terrestrial Free-Space Optical Links," *International Telecommunication Union, Geneva, Switzerland*, pp. 1–12, 2007.

[172] K. Louedec and R. Losno, “Atmospheric Aerosols at the Pierre Auger Observatory and Environmental Implications,” *The European Physical Journal Plus*, vol. 127, no. 8, pp. 1–16, 2012.